Characterisation and Calibration of ZEPLIN III - A Dark Matter Detector

Claire Thorne

High Energy Physics Group
Blackett Laboratory
Department of Physics
Imperial College London

Thesis submitted for the Degree of
Doctor of Philosophy
to Imperial College London
and the Diploma of Imperial College

· March 2009 ·

Abstract

The ZEPLIN III liquid xenon dark matter detector is designed to potentially discover the WIMP - a supersymmetric galactic dark matter candidate. This thesis presents experimental results of the ZEPLIN III commissioning studies, in preparation for the first and second underground science runs.

Data acquired on the surface, at the Imperial College London laboratories, were used to characterise the instrument's response in terms of light yield (LY) and single photoelectron (SPE) spectra. A zero-field LY was measured as 7.42±0.37 phe/keV and 18.12±0.91 phe/keV in dedicated single- and dual-phase high yield configurations, respectively, consistent with Monte Carlo simulations. Mean SPE measured pulse areas ranged from 41.78±1.55 Vps to 52.37±1.59 Vps, depending on the method employed. A 3-D position reconstruction was verified and, significantly, no evidence of a potentially-contaminating background α-population was observed. This study directly lead to critical development of the DAQ software and hardware configuration. The PMT array was confirmed as responsive and, crucially, the particle discrimination principle was demonstrated. Zero-field LYs of (4.6-4.7) ±0.5 phe/keV were recovered from the centre of the chamber, exceeding simulation predictions. With-field (3.01 kV/cm in the liquid) LYs of (1.2-1.8) ±0.3 phe/keV from the liquid scintillation (S1) and an electroluminescence yield (S2) of (98-140) ±35 phe/keV from the gas phase were also determined.

ZEPLIN III was deployed in the Boulby Underground Laboratory, UK and demonstrated successful operation at high field (up to 3.79 kV/cm in the liquid), in situ. An alternative Poisson method for obtaining single photoelectron distributions was developed by the ZEPLIN collaboration. The origin of long-τ events in surface data was investigated and ultimately resolved as an artefact of early versions of the data reduction software. An S1 zero-field LY of 4.72±0.10 phe/keV, obtained with a ^{57}Co external source, was recovered for the centre of the chamber. The instrument's energy resolution was evaluated and a novel parameterisation approach, developed by the author, yielded σ=1.08±0.06$\sqrt{E(keV)}$ with a dominant stochastic term. A 'flat-fielding' method was established, proving to minimise the resolution significantly, yielding 8.6% and 7.3% for S1 and S2, respectively, in the fiducialised anti-correlated energy channel. This flat-fielding recipe, along with construction of the light collection correction matrices, formed the basis of the final procedures subsequently applied to first science run data-sets.

To Nan & Grandad, and Vadim.

Acknowledgements

When I embarked on this research, over four years ago, my Astro peers made the inevitable task less daunting and were a source of tremendous fun, namely: Markos - the only person who can stomach tens of coffee breaks a day, though he did tire of tuna and cucumber baguettes (eventually); Jeremy - a real ray of light in what could sometimes be a rather muted environment, (I now know what the 'secret lab' is!); and Joe - provider of hours of endless amusement, his wackiness never failed to amaze, nor the extent of his caffeine highs. Many more have passed up through the ranks, all contributing to my fantastic experience within the Astro and HEP groups, and moved on to greater things - too many to mention.

Members of the ZEPLIN III collaboration - Henrique, Richard, Vitaly and Francisco - have assisted me greatly throughout my studies, strengthened my enthusiasm for scientific research,... and nurtured my love of Whitby cuisine!

I owe a great deal to my supervisor, Tim. The patience and commitment he has demonstrated in guiding me to this end point is phenomenal. I would also like to thank STFC for the funding I have received, without which this thesis could not have been written.

The significance of the unconditional support my family has provided me can not be underestimated. I thank Mum and Dad for the exceptional education and enormous opportunities they have afforded me, along with David, Daniel and Bethan for their parts in my inspirational upbringing. Ultimately, it is my family that has allowed me to pursue this research. The devotion of my partner Matthew, his reassurance and his unfaltering belief in me have maintained my motivation throughout, long before the end was in sight. For all of these good fortunes I am eternally grateful.

Finally, my thanks and thoughts go out to those who never got to see this: Nan, Grandad and Vadim.

Declaration and Copyright

This thesis is my own work, except where explicitly indicated in the text.

Claire Thorne
March 2009

Contents

List of Figures

List of Tables

Chapter 1

Introduction

A general overview of the evidence for dark matter, its place in a supersymmteric framework, plausible candidates and the two experimental approaches currently seeking to detect it are introduced.

Chapters 2 and 3 are also introductory but provide a more in depth discussion of the direct detection of WIMPs and the ZEPLIN III instrument, respectively. The work chapters that follow do so in chronological order: the analyses conducted on ZEPLIN III surface data-sets, pre-deployment 1070 m underground, are described in Chapter 4; in Chapter 5 ^{57}Co γ energy calibration, on underground data, is presented; the analyses of science data, conducted by the ZEPLIN collaboration but to which the author has made direct contributions, are detailed in Chapter 6 and, finally, the main conclusions are drawn.

1.1 The Dark Matter

Just 4.6%[2] of the mass-energy density of the Universe can be attributed to visible matter. Of the remaining 95.4%, approximately one quarter is believed to be elusive 'dark matter'.[2] These two kinds of matter combine to make up 28%[2] of the total mass-energy of the Universe, with the remaining 72%[2] being dark energy, a mysterious negative pressure pervading all space. Therefore, it is now widely accepted that 83.5%[2] of the mass of the Universe exists in some non-luminous,

invisible form.

Until just over a century ago non-luminous matter played no role in the description of the mass composition of the Universe. Stars, visible matter alone were thought to account for almost its entire mass.[3] Our current knowledge of the mass composition may therefore seem progressive. Yet, with regard to the precise nature of this non-luminous matter, only revealing its presence through gravitational effects, we remain in the 'dark'. It is this, the form of dark matter which remains one of the biggest unanswered questions in modern astronomy, cosmology and particle physics. If this question could be solved solutions to many other astrophysical problems, such as complete understanding of galaxy formation, could follow.

The field remains varied in many respects; the list of proposed candidates is vast, the detection techniques currently employed globally are diverse and the effects of dark matter are not confined to large scales.

1.2 Evidence for Dark Matter

Dark matter is thought to exist both in and around galaxies. Not only does it cluster with stellar matter to form galactic halos, but it also exists as a background density over the entire Universe: its presence is 'felt' on all scales. In contrast, its distribution is believed to vary significantly with scale.

The list of plausible and compelling arguments for the existence of dark matter is extensive. Thus, a non-exhaustive discussion follows on the evidence provided by: galactic rotation curves, the Oort discrepancy, central mass measurements, intracluster plasma X-ray emission, gravitational lensing, large scale structure (LSS), Type 1a supernovae and cosmic microwave background (CMB) anisotropies. Finally, for completeness an alternative to the dark matter hypothesis is supplied.

1.2.1 Dark Matter in Galaxies

It is now understood that galaxies have dark matter halos extending beyond their visible limits and that without this extra mass galaxies would fail to exist. Nevertheless, why no dark matter is observed on scales smaller than galaxies remains unknown.

Galactic Rotation Curves

A spiral galaxy may be represented by a central bulge with a rotating disk of stars in circular orbit around the galactic centre. The velocity profile of such a galaxy can be estimated by applying Newton's second law if the mass distribution of the galaxy is approximated to be spherical or ellipsoidal. If a spherically symmetric bulge is assumed, with constant density, the mass M at small r from the galactic centre is proportional to r^3. This implies a velocity distribution where the average orbital velocity $\nu(r) \propto r$. However, for the outer region of the galaxy $M(r) \sim M_{gal}$, suggesting that at large r, $\nu(r) \sim 1/\sqrt{r}$.

Strong evidence for the existence of dark matter is provided in the form of galactic rotation curves which suggest a massive dark matter halo is a major component of almost every spiral galaxy, contributing ∼90% of the galaxy's total mass.[4]

After obtaining spectra of the Andromeda galaxy in 1939 Babcock[5] demonstrated that the outer regions of M31 rotated at velocities higher than expected. In an attempt to explain this he concluded that either the outer mass-to-light ratio was higher, or strong dust absorption occurred. In 1940 Oort remarked that "the distribution of mass in this system appears to bear almost no relation to that of light"[6] when referring to the S0 galaxy NGC3115.

In 1954 Schwarzschild[7] claimed that "in any one galaxy the mass distribution and luminosity distribution are identical". Crucially, inaccurate observations were not capable of disproving this. As a result Schwarzschild single-handedly delayed a dark matter component of the Universe from being widely-accepted by almost a decade.

In 1970 Rubin and Ford[8] demonstrated that, like Babcock and contrary to Schwarzschild's argument, the observed mass-to-light ratios do increase with increased enclosed volume; thus the rotation curves do not 'drop-off' at large distances, but instead remain flat. The implications of this, the apparent existence of matter in the absence of visible matter, are immense. It is this discrepancy between the expected velocity profile and the observed which accommodates a dark matter contribution.[9]

The amount of matter required to stabilise a spiral galaxy was studied in 1973 by Ostriker and Peebles with simulations.[10] They found that the only way of preventing it from flying apart was to factor in a halo, at least as massive as the

galaxy itself, in which the galaxy was immersed.

Interpretation of the Milky Way's rotation curve indicates that within the optical disk, $r \lesssim 25$ kpc, approximately 70%[11] of the total mass is in the form of dark matter. Furthermore, in excess of 90%[11] of the total mass is dark out to $\sim$230 kpc. This suggests that, for the Milky Way, the dominance of dark matter increases with radial scale. In 1993 Rubin[11] concluded that this trend is not unique to the Milky Way, but exists over all galactic scales.

Measurements of dark matter halo parameters by Kormendy and Freeman[12] indicate that smaller galaxies have larger dark matter densities. Indeed, the velocity dispersions (the spread in measured stellar velocities) of dwarf galaxies are very large - a direct indication of dark matter.

The Oort Discrepancy

Further evidence for dark matter, on both subgalactic and inter-galactic scales, is provided by the Oort discrepancy. In 1932 Oort computed the total matter density in the solar neighbourhood to be 0.092 $M_\odot$ pc^{-3} $\pm$ 20%[13]. Through the effect of the gravitational field on the motion of stars (normal to the plane of the Milky Way) Oort also estimated the local matter contribution from stars as 0.038 $M_\odot$ pc^{-3} and the total mass of nebulous or meteoric matter near the sun as $<<$0.05 $M_\odot$ pc^{-3}.[13] In 1960 Oort recalculated the total matter density in the solar neighbourhood to be 0.15 $M_\odot$ pc^{-3} $\pm$ 10%.[14] Hence, Oort's results revealed a discrepancy. To resolve this it was suggested that visible and unobserved 'missing' matter coexist in the solar neighbourhood.

It should be noted that although this discrepancy is significant on subgalactic scales it is amplified further on larger scales. Relative to the dark matter halo component however disk dark matter is less important.

1.2.2 Dark Matter in Galaxy Groups and Clusters

Dark matter is a major constituent of mass on both galactic-scales, and larger scales, i.e. clusters of galaxies. The derived value of the non-baryonic density, $\Omega_{nb}\sim$0.2-0.3, for clusters of galaxies is larger than that of individual galaxies.[15]

Central Mass Measurements

Estimates of the dynamical mass, M, of clusters of galaxies may by obtained through application of the Virial Theorem, and radii and velocity measurements. Approximately forty years prior to Rubins' observational evidence for dark matter, Zwicky used this method, comparing M with the luminosity, L, in 1933[16]; observing radial velocities of eight galaxies in the Coma Cluster. He found that the mean density of the cluster was significantly larger than that implied solely from luminous matter. In fact, the mean density was calculated to be $\sim$50 times greater. Zwicky concluded that the mutual gravitational attraction of individual galaxies is insufficient to bind clusters.[16] Thus, he proposed that only a small fraction of all mass in the Universe is in the form of visible matter: providing the first evidence for the presence of dark matter on large scales.

Within three years of Zwicky's remarkable discovery Smith too claimed to observe a mass, larger than expected, this time in the Virgo Cluster.[17] Later, in 1959, Kahn and Woltjer[18], oblivious to the findings of both Smith and Zwicky, suggested that most of the mass of the Local Group exists in some invisible form.[3]

Intracluster Plasma X-ray Emission

If no dark matter component exists within clusters of galaxies the hot gas, or intracluster plasma within them would have expanded outwards. This is not the case. X-ray telescopes have observed this intercluster medium, indicating that the measured gravitational force exceeds the pressure force of the hot gas in clusters.

Gravitational Lensing

Light from a distant object follows the path of space-time which appears curved by an intermediate massive object acting as a lens. This lens focuses the image of the background source to a different location, thereby distorting the positions and sizes of distant galaxies. This process, known as *gravitational lensing*, has many applications in astronomy including measurement of the Hubble constant and 'weighing' galaxies to estimate their dark matter content.[15] Computation of the

latter requires the source-to-observer distance, the lens-to-observer distance and the image positions to be known.[9]

Three strength regimes of gravitational lensing exist: strong lensing, weak lensing and microlensing. Strong lensing is the most extreme of the three lensing effects and requires a very massive lens close to the line of sight of the source to create more than one image. Although weak lensing, as the nomenclature suggests, is too weak to produce multiple images or arcs the source can still be stretched (shear) and magnified (convergence). The light from distant galaxies is weakly lensed or scattered by matter and dark matter clumps enabling the dark matter distribution to be mapped on large scales. When microlensing occurs the excess curved light seems to brighten the source and will occur if massive astronomical compact halo objects (MACHOs), such as brown dwarfs, intercept the line of sight between the observer and a distant star.[19]

Observations of strong lensing in clusters yield mass-to-light ratios consistent with other dark matter cluster measurements. Similarly, those obtained through weak lensing yield consistent results. As well as detecting more mass than is visible in clusters of galaxies, adding considerable weight to the argument for dark matter, gravitational lensing also provides a direct measurement of the dark matter density of the Universe.

1.2.3 Cosmological Dark Matter

Evidence of dark matter on cosmological scales is provided by the large scale structure (LSS), Type 1a supernovae (SNe) and, on the largest scale ($\sim 10^3$ Mpc), cosmic microwave background (CMB) anisotropies. On such scales dark energy and dark matter are thought to drive the accelerating expansion of the Universe.

Large Scale Structure

Small perturbations (or density irregularities) present in the early Universe evolve through gravitational growth, giving rise to the LSS we see today. Our understanding of the LSS is developed by surveys of distant galaxies and spatial distribution and peculiar motion measurements. Additionally, N-body numerical simulations of galaxy formation are applied to solve the mysteries associated with this evolution.

These simulations place constraints on particle velocities and cross sections, producing results which require a matter density higher than allowed by visible components alone.[20]

Type 1a Supernovae

The brightest class of SNe are Type 1a and are of particular cosmological use. This is because they can be seen up to such high redshifts as z=1 when the Universe was approximately half its present age since they are *standard candles*.

Type 1a SNe, of known luminosity, can act as effective standard candles determining distances. Therefore, the Hubble parameter (describing the current expansion rate of the Universe) can be monitored through comparison of brightness and redshifts of nearby and distant Type 1a SNe. When compared to those nearby, distant SNe at high redshifts are observed to be fainter than predicted. This provides direct evidence for a currently accelerating and expanding Universe and measures the dark energy component Ω_Λ to be finite.[21]

Cosmic Microwave Background

Following the Big Bang the early Universe entered a period of recombination, a hot, dense phase during which electrons get captured by ionised Hydrogen and Helium atoms. At the end of this stage the Universe consists, mostly, of neutral atoms, through which photons can travel freely. Background radiation from photon propagation is thought to be a remnant of this stage and is known as the CMB. Density irregularities give rise to temperature differences in the CMB across the sky. The CMB spectrum follows that of a black body, with a temperature T = 2.726 K, but is anisotropic to one part in 10^5; its temperature varies with direction in the sky and hence the brightness too varies.[22]

Not only are measurements of the CMB temperature useful but measurements of properties of the anisotropies also prove valuable. These provide constraints on cosmological parameters and hence on the total amount of dark matter in the Universe.

The Balloon Observations Of Millimetric Extragalactic Radiation and Geophysics (BOOMERanG)[23] and Millimeter Anisotropy eXperiment IMaging Array (MAX-

IMA) [24] experiments both measured the CMB properties using balloon-borne experiments. BOOMERanG first measured the CMB temperature in 1999[23], establishing that the Universe is indeed flat with Ω=1.

The Wilkinson Microwave Anisotropy Probe (WMAP)[2] satellite measures the temperature fluctuations with superior accuracy and therefore produces maps with greatly enhanced resolution. Combining data from the WMAP experiment and several smaller-scale experiments constrains the baryon and matter abundances in the Universe to values consistent with predictions from Big Bang Nucleosynthesis (BBN) - see Section 1.5.1 - and a flat Ω=1 Universe.[22]

A simple 6-parameter Ω=1 CDM cosmological model fits the 5-year WMAP temperature and polarization data alone where the cold dark matter density, Ω_c, is 0.214$\pm$0.027[2]. Hence the existence of dark matter is suggested from CMB anisotropy data alone, even without the wealth of alternative supporting evidence.

Combining these WMAP data with other experimental data-sets leads to cosmological density parameters, currently used to describe the generally accepted model, as discussed in Section 1.3.

1.2.4 An Alternative Explanation: MOND

Modified Newtonian Dynamics (MOND) was proposed by Milgrom in 1983[25]. In the limit of small acceleration MOND modifies Newton's second law: describing the proportionality between the observed acceleration, a, and mass, m, of an object, produced by a force, F, where $F = ma$.[25] MOND suggests that

$$F = m\mu\left(\frac{a}{a_0}\right)a \tag{1.1}$$

should be adopted instead, where the quantity $\mu(x)$ is a function of the ratio (a/a_0), a_0 is an acceleration constant, and has specified behaviour when x is large or small ($\mu(x >> 1) \approx 1$, $\mu(x << 1) \approx x$).[26]

On galactic scales the gravitational force is small because of the large distances between stars. Therefore MOND effects should be evident on such scales. This adjustment to Newton's law could imply a change to inertia or to the gravitational force. Verification of the latter maybe pursued using space experiments, performed where the force of gravity dominates.[25]

In 'ordinary' situations, here on Earth, $a >> a_0 \Rightarrow \mu(\frac{a}{a_0}) \approx 1$ and Newtonian dynamics is restored. However, over large distances r from the galactic centre to an outer star, $a << a_0 \Rightarrow \mu(\frac{a}{a_0}) \approx a/a_0$. Combining this with the equation for a star experiencing the gravitational force far from the galactic centre ($F = GMm/r^2$ where G is the gravitational constant and M is the mass of the galaxy) gives $GM/r^2 = a^2/a_0$. The acceleration from this expression is then equated to the acceleration defined for a circular orbit in the rotation law ($a = v^2/r$), yielding

$$v^4 = GMa_0 \tag{1.2}$$

This implies that the velocity of a star, on a circular orbit, far from the galactic centre, is independent of r. Thus, it is characterized by a flat rotation curve in the low acceleration limit. This validation of flat rotation curves is what presents MOND as an alternative to the dark matter hypothesis. Observations of v applied to this expression, by Milgrom, define the acceleration constant a_0 as 1.2×10^{-10}m s^{-2}.[27]

In order to confirm (or discredit) MOND as a theory compatible with observations, experiments have to be performed on physical process involving small accelerations i.e. the dynamics of galaxies or larger systems. Milgrom realised that this theory may be validated through observations of low surface brightness (LSB) galaxies. A large radius compared to their mass is one attribute of LSB galaxies. This property means that a significant majority of stars within LSB galaxies occupy the flat part of the rotation curve. Prior to the acquisition of actual data on the rotation curves of these galaxies being acquired, Milgrom predicted that the curves are predominantly flat. The anticipated effects of MOND allowed him to go further, saying that the proportionality factor in the $v^4 \propto M$ relation (Equation 1.2) is the same for these galaxies as for higher surface density galaxies.[26] Observations of LSB galaxies by the divided community later both confirmed and refuted MOND's validity.

Relativistic extensions to MOND, required for its application on large scales, to address gravitational lensing or cosmology, have recently been developed.[28] Experiments are being designed to test this and new predictions of MOND; such as the distortion of satellite dynamics, unexplained by a dark matter halo. However, strong challenges to this extension arise from recent observational discoveries: *the bullet cluster* and *the ring*.

The first direct empirical proof of the existence of dark matter, independent of the nature of the gravitational force law, was presented in 2006 following weak lensing

observations of the bullet cluster (IE0657-56)[29]. In a MOND scenario with no dark matter the gravitational potential would be expected to trace the baryonic matter. Instead, the derived map of gravitational potential exhibited an 8σ spatial offset between the peaks of the lensing and baryonic mass distributions. This observed displacement cannot be explained with a modification of the gravitational force law and proves the presence of a dominant collisionless dark matter component, questioning the MOND paradigm.

In 2007 lensing observations of the galaxy cluster Cl0024+17 revealed a ring-like dark matter substructure with a distribution that is not traced by the intracluster medium nor by the cluster galaxies.[30] Reconstructed mass maps showed the ring to be significant at the $\gtrsim 5\sigma$ level with respect to the background. The observational evidence agreed with the hypothesis that such a feature results from a high-speed line of sight collision with another massive cluster $\sim$1-2 Gyr ago. This work was accompanied by a collisionless N-body simulation of a collision of two massive clusters, demonstrating a possible explanation for the origin of the ring as radially expanding decelarating dark matter shells. Moreover, this was supported by the observed flat density profile. It has been argued that the offset of the ring from the gas and galaxies is difficult to explain within the MOND prescription.[30] However, this continues to be highly debated.[31][32]

For the majority of astronomers, MOND currently remains an ad-hoc and insufficient adaption to gravity, with the goal of replacing dark matter unsatisfied.[15]

1.3 The ΛCDM Model

Einstein's field equations are a fundamental part of the cosmological model, relating the geometry of the Universe with its matter and energy content. Therefore the Friedmann equation, which can be obtained by solving these, impacts enormously on our understanding of dark matter. Utilising this, cosmological models can be classified in the following way:

- $\rho < \rho_c \quad \Omega < 1 \quad k = -1$ **OPEN** (Universe expands forever)
- $\rho = \rho_c \quad \Omega = 1 \quad k = 0$ **FLAT** (critical case)
- $\rho > \rho_c \quad \Omega > 1 \quad k = +1$ **CLOSED** (leads to an inverse Big Bang)

where ρ_c is the critical density of the Universe ($\approx 10^{-29}$ gcm^{-3}) and k is a constant describing spatial curvature. The simplest case, where k=0, corresponds to a flat, Ω=1 Universe. This scenario is consistent with the proportions of density components, including that of dark matter in the Universe, detailed in Table 1.1. It forms part of the current widely-accepted and simplest cosmological description of the Universe: the Λ-Cold Dark Matter (ΛCDM) or *concordance model.*[22]

<table>
<tr><td>Ω_Λ
0.721±0.015[2]</td><td colspan="4">Ω_m
0.279±0.015[2]</td></tr>
<tr><td></td><td colspan="2">Ω_b
0.0462±0.0015[2]</td><td colspan="2">Ω_{nb}</td></tr>
<tr><td></td><td>Ω_{lum}
∼0.0231[33]</td><td>Ω_{nlum}
∼0.0231[33]</td><td>Ω_c
0.233±0.013[2]</td><td>Ω_h</td></tr>
</table>

Table 1.1: Density components of the Universe and the corresponding uncertainties at the 1σ level (∼68%) derived from the WMAP data and other experimental data-sets.[2] The dark energy or vacuum energy, Ω_Λ, constitutes over two thirds of the Universe's total mass-energy density. The non-baryonic matter component, Ω_{nb}, consists of cold, Ω_c, and hot, Ω_h, dark matter. The baryonic matter component, Ω_b, can be further classified as either luminous, Ω_{lum}, or non-luminous, Ω_{nlum}.

The ΛCDM model assumes a flat Universe, a significant dark energy term and a cold, non-baryonic and collisionless dark matter component. Here, *cold* refers to the dark matter particles being non-relativistic in the early Universe. Although proven successful and consistent, agreeing with observations as discussed in Section 1.2, this model offers no description of the origin of dark matter.

1.4 Supersymmetry

The supersymmetric extension to the standard model of particle physics is a convincing part of our description of nature. However, at present none of the additional particles predicted by supersymmetry (SUSY) have been observed and SUSY remains a hypothesis.

1.4.1 The Standard Model

The standard model of particle physics (SM) consists of three key elements: particles (six leptons and six quarks along with their corresponding anti-particles); interac-

tions (weak ($W^{\pm}$, Z^0), electromagnetic (γ) and strong (8 gluons)); the Higgs boson (H^0). A neutral scalar field, in the form of the Higgs boson, is necessary to introduce mass into the SM.

Proof of the success of the SM exists, such as its ability to make accurate predictions.[34] Indeed, the SM is an effective theory up to $\sim 10^2$ GeV. However, the description of the Universe provided by the SM so far is thought to be incomplete. Among others the SM does not explain: why quarks and leptons are grouped into *three* families; why it does not include a description of gravity; the matter dominance, over anti-matter, of the Universe; the Hierarchy problem. Many of these inadequacies can be resolved with the inclusion of a new type of symmetry - *Supersymmetry*.

1.4.2 SUPERsymmetry

SUSY is a symmetry between fermions (the constituents of matter) and bosons (the interaction mediators). This unification demands a complete set of new partner, or supersymmetric, particles associated with each of the known particles. These differ from ordinary particles in terms of spin and mass. The SM defines matter with non-integer spin S=1/2 and force carriers with integer spin S=1 whereas the reverse is true for SUSY.

The simplest extension to the SM and most widely-studied, plausible SUSY model is the *minimal supersymmetric standard model* (MSSM). The MSSM extension, with 124 associated parameters, contains the smallest possible field content necessary to give rise to all the fields of the SM.[22]

SUSY explains phenomena that the SM simply can not. As well as providing dark matter candidates and potentially enabling force-unification between gravity and the SM forces it undoubtedly owes its success to its stabilization of the Higgs mass and its resolution of the Hierarchy problem. The infinite Higgs mass, implied by the SM can indeed be redefined as finite with SUSY considerations. Also the huge difference between the electroweak and Planck energy scales together with the fact that the Higgs boson is considerably lighter than the Planck mass are stabilized by SUSY. Experimental verification of the existence of the heavy top quark is just one example of a confirmed SUSY prediction.[35] Despite all this, research spanning three decades has produced no direct evidence for the existence of superpartners - insisting SUSY, like the SM, is a broken symmetry - and it seems that even with

this extension we have still not arrived at a fundamental theory. Supersymmetry is unlikely to be the final word.

1.4.3 Supersymmetric Dark Matter Candidates

The multiplicative quantum number R-parity is conserved in SUSY and is given by $R = (-1)^{3B+L+2S}$ where B, L and S are baryon number, lepton number and spin, respectively. For ordinary particles $R = +1$ and for supersymmetric particles $R = -1$. This implies that supersymmetric particles can only be created and annihilated in pairs. In order for R-parity to be conserved one SUSY particle can not decay into ordinary particles only. A heavy SUSY particle may however decay into a lighter SUSY particle as well as ordinary particles. Therefore, by definition, the lightest supersymmetric particle (LSP), having no allowed state to decay into, is stable.

After the Big Bang, large quantities of supersymmetric particles (and their antiparticles) would have been produced. Then, following the cooling and expansion phase, almost all of these would have decayed through annihilation, except the LSP. The particle-antiparticle annihilation probability decreases with time, as the Universe expands and the interaction cross section naturally leads to a cosmologically significant population of LSPs which may still exist today as Big Bang relics. If neutral, they would interact very weakly and if massive, they could contribute to the dark matter content of the Universe.[36]

Although the original motivation for a supersymmetric extension to the SM was thought to be irrelevant to the problem of missing mass, in 1983 Goldberg[37] proposed the LSP, with absolute stability, to be a possible, neutral and colourless dark matter candidate.[15]

Four neutralinos $\tilde{\chi}_i^0 (i = 1, 2, 3, 4)$ are theoretically predicted as a consequence of SUSY. They are the physical superpositions of the fermionic partners of the neutral electroweak gauge bosons (bino and wino) and the fermionic partners of the two neutral Higgs bosons (Higgsinos). The $\tilde{\chi}_1^0$ is the lightest neutralino and is thus the LSP. [15]

1.5 Dark Matter Candidates

There is strong supporting evidence for the existence of dark matter. Furthermore, experimental evidence confirms that dark matter clusters with stellar matter forming galactic halos. Evidence also suggests that dark matter inhabits the entire Universe as a background density.[15] The question of which form(s) it takes however is the problem tackled in the current era.

In the 1970s the astronomical community recognized the significance of the 'missing' mass and by 1975 they were convinced of the existence of missing mass and its potential cosmological impact. At this time however the precise form of this missing mass remained unresolved with white and brown dwarfs, black holes and very hot gas provisionally nominated.[38] Over the last thirty years many potential candidates have been investigated and subsequently eliminated. With regard to those originally proposed the current short-list is somewhat more exotic.

1.5.1 Baryonic Dark Matter

Brown dwarfs, massive black holes, neutron stars and planets are all baryonic astrophysical objects. That is, they consist of baryonic matter (protons and neutrons). This group are collectively known as *massive astronomical compact halo objects* (MACHOs) and the former two are the main MACHO candidates for baryonic dark matter. There is no doubt that some of the dark matter content can be attributed to these. However, the limit on the number of baryons that can exist, set by Big Bang Nucleosynthesis (BBN), is simply too small to account for the whole dark matter fraction.[15]

The theory of BBN is now the generally accepted view of light-element production in the early Universe. It details how the light elements (^{2}H, ^{3}He, ^{4}He, ^{7}Li) were formed via fusion of protons and neutrons in the first $\sim$3 mins after the Big Bang. By this time the temperature of the Universe would have cooled from 10^{32} K, when all matter was fully ionized, to $\sim 10^9$ K. After this time, the temperature of the Universe along with the density dropped below that required for nuclear fusion. Elements heavier than Helium are believed to originate in star interiors, while some Helium is also formed there, considerably later than those formed by Nucleosynthesis.

BBN can be applied to estimate the present total baryonic matter content of the

Universe by comparison of the He/H abundance ratio observed today with the baryonic matter content at $t \lesssim 3$ mins. Such studies indicate that the majority of the He we observe today was created within this time, leading to a lower limit on the He abundance at $t \lesssim 3$ mins. A low, early baryon density, hindering the production of heavier elements, can not account for this He abundance. Confirmed by observations of MACHOs through gravitational lensing, more (non-baryonic) candidates are needed.[15]

1.5.2 Non-Baryonic Dark Matter

Non-baryonic particles, such as neutrinos, photons and free electrons, can either be 'hot' or 'cold' according to whether they were, or were not, moving with relativistic speeds when galaxy formation began. The three most promising non-baryonic dark matter candidates are neutrinos (hot), axions (cold) and *weakly interacting massive particles* (WIMPs) (cold).

The view that hot dark matter dominates the Universe is unpopular and inconsistent with the existence of the galactic halo. This would imply that clusters of galaxies form first, with individual galaxies only recently formed via fragmentation. Instead hierarchal clustering of smaller units agrees with the accepted ideas of galaxy formation.[19] Thus, neutrinos are not believed to be the prime non-baryonic dark matter candidate despite them being the only dark matter candidates actually known to exist.

The existence of axions, very light (10^{-6} eV-10^{-3} eV [36]) hypothetical bosons and a cold non-baryonic dark matter candidate, is currently being investigated. However so far no evidence for this has been found. Furthermore, the role they play in contributing to the dark matter content is still undefined.[9]

The supersymmetric extension to the SM predicts the neutralino, a particular WIMP, as a plausible cold dark matter candidate among others: sneutrinos, gravitinos and axinos. Neutralinos do not emit or absorb radiation and there are numerous final states into which they can annihilate. Even though the neutralino relic abundance is technically sufficient to be detected, it is because they interact weakly that they remain undetected. Since they are believed to be present in the Milky Way and to get trapped by and accumulate in massive dense objects in galactic halos (e.g. the Sun, Earth) a potentially detectable neutralino flux on Earth is assumed.

The lightest of the four neutralinos $\tilde{\chi}_1^0$ (see Section 1.4.3) is the most promising non-baryonic cold dark matter candidate, with mass $\gtrsim 37$ GeV[39]. For completeness, superheavy, weakly interacting and extremely massive ($> 10^{10}$ GeV) relic particles termed *wimpzillas* are also candidates for non-baryonic dark matter.[15]

While the SM itself does not allow non-baryonic particles to account for all dark matter, extensions to it do. Thus, identification of non-baryonic dark matter would encourage physics beyond the SM.[15]

1.6 Experimental Searches

Many experiments across the world are either currently operational or are in the development phase to detect dark matter directly in the form of WIMPs. Meanwhile an attempt to detect dark matter indirectly is also a global effort: seeking to detect the numerous products of WIMP annihilations in the galactic halo or the centre of the Sun.

1.6.1 Direct Detection

Direct detection of WIMPs does not demand the assumption of a specific dark matter candidate. It simply involves the detection of WIMPs in the mass range of $\sim$1 GeV - 1 TeV.[40] By definition the interaction of WIMPs with ordinary matter and thus detector materials is weak. Therefore a WIMP detection, which must be statistically significant, is more likely in larger detectors. For this reason most direct WIMP searches involve scalable detector designs, ideally seeking to upgrade to ton-scale target masses. Currently, the favoured method of directly detecting WIMPs is through nuclear scattering within the target volume. Direct detection experiments have constrained WIMP-nucleon interaction cross sections to low values, corresponding to high annihilation rates which theory predicts.

The first evidence for direct WIMP detection from the Italian DArk MAtter (DAMA) group in 2003[41] has still not been independently confirmed by other collaborations.[42] This is looking increasingly unlikely since other competing experiments such as Cryogenic Dark Matter Search (CDMS)[43], Experience pour DEtecter Les Wimps En SIte Souterrain (EDELWEISS)[44], XENON[45] and ZonEd Proportional scintillation in LIquid Noble gases (ZEPLIN)[46] have already probed

this area of parameter space without registering a positive signal. However, the annual variation signal detected by DAMA with a 100 kg detector during its first 7-year run has recently been reproduced by an upgraded, 250 kg second 4-year run.[47] Although this adds some weight to the unconfirmed and highly-refuted first result, the DAMA findings have not been reconciled with the lack of signal recorded by the rest of the field.

The Korea Invisible Mass Search (KIMS)[48] detector is currently operational at the Yangyang Underground Laboratory. Results from the KIMS CsI scintillation experiment offers a comparison with DAMA. In 2007[48] KIMS presented a limit on the spin-independent (and spin-dependent) WIMP-nucleon cross section, with 3409 kg×days data using four crystals, of $\sim 2\times10^{-6}$ pb. For the first time, the DAMA signal region[41] was ruled out by a fellow crystal detector also containing ^{127}I, for WIMP masses higher than 20 GeVc^{-2}.

Two examples of cryogenic phonon and scintillation experiments are Cryogenic Rare Event Search with Superconducting Thermometers (CRESST)[49] and Rare Objects SEarch with Bolometers UndergrounD (ROSEBUD)[50]. The CRESST experiment is located at the Gran Sasso Underground Laboratory, Italy. The second generation detector, CRESST II, returned a dark matter limit of 6×10^{-7} pb[49] with only 67 kg×days exposure and two, of a potential thirty-three (10 kg total mass[51]), detector modules. Using small sapphire (Al_2O_3) bolometers the initial ROSEBUD experiment at Canfranc Underground Laboratory, Spain, probed down to $\sim10^{-1}$ pb[50]. After experiencing difficulties in identifying contaminant sources[50], reflected in the sensitivity achieved, the ROSEBUD collaboration has switched to using alternative bolometers (see [52]).

The XENON experiment is among many currently utilising liquid xenon (LXe) technology. This predominantly USA collaboration has a 10 kg prototype, XENON10, running in Gran Sasso. Results published in 2007[53] make it the most sensitive detector in the race to detect dark matter, having set a new upper limit for the WIMP-nucleon spin-independent cross section. A 100 kg upgraded detector is planned and due to deliver more sensitive results in 2009. The Italian-American Wimp ARgon Programme (WARP) experiment is also operating underground at Gran Sasso, utilising liquid argon technology.[54]

The USA-based CDMS II and European EDELWEISS II phonon and ionisation, cryogenic experiments are currently operational in the Soudan mine, Minnesota and at the Modane underground laboratory, France, respectively. The 2008 CDMS II

limit, combining recent and previous data-sets, reaches the same minimum cross section as XENON10 but with more sensitivity at higher masses.[55]

The UK Dark Matter Collaboration (UKDMC) developed, installed and ran the ZEPLIN I[56] LXe WIMP detector 1070 m underground at the Boulby mine, North Yorkshire, in the initial phase of their continuous ZEPLIN programme. World-leading limits from the second generation detector within this programme, ZEPLIN II[57], were published in early 2007. Part of this group have formed the ZEPLIN collaboration, developing the ZEPLIN III[58] detector within the same, long-term, progressive programme. It is designed to be more sensitive to WIMPs than its predecessors by employing a more challenging discrimination technique and is the focus of this thesis.

Looking to the future worldwide efforts to detect dark matter directly are planned with the European LIquid Xenon Identification of Recoils (ELIXIR)[59] and Large Underground Xenon (LUX)[60] experiments, both exploiting LXe technology. The ZEPLIN III collaboration is leading the ELIXIR programme, with involvement from XENON10 whilst the LUX collaboration includes the XENON10 (USA) and ZEPLIN II (USA) teams. This co-ordinated 'big push' to detect dark matter draws on global expertise and cutting-edge technology on a large scale.

1.6.2 Indirect Detection

Evidence of WIMP–anti-WIMP annihilations, by their products and not the WIMPs themselves, is sought in the field of experimental WIMP indirect detection. The annihilation products may be in the form of protons, antiprotons, electrons, positrons or gamma-rays in the galactic halo, or as high-energy neutrinos at the centre of the Sun or Earth.

In contrast to the direct detection of dark matter, indirect detection does demand the assumption of a specific dark matter candidate. The current worldwide effort to indirectly detect WIMPs focuses specifically on the neutralino.

Non-relativistic neutralinos are hypothesized to accumulate in the centre of large astrophysical objects, like the Sun and the Earth, through elastic scattering with the object's nuclei. Each successive scattering event will reduce the neutralino's energy, transporting it further and further inside the body, in a process known as *gravitational capture*. Since they are their own anti-particles the neutralinos within

this captured population at the centre of the body could annihilate, producing a range of secondary particles. In these regions the high-energy neutrino fluxes (10-100 GeV) are enhanced above the background rate of solar neutrinos ($\sim$MeV). This potentially detectable signal is currently pursued by various neutrino telescopes. However, as neutrinos are weakly interacting particles detecting them is proving a great experimental challenge. Even so, current observations suggest neutrinos are neither sufficiently massive nor plentiful to account for the entire dark matter fraction.

Both neutrinos and γ-rays maintain their original direction. Exploiting this, examples of current neutrino experiments on the Earth's surface hoping to detect high-energy neutrinos through their directional signature include: Astronomy with a Neutrino Telescope and Abyss environmental RESearch (ANTARES)[61]; ICECUBE, the Antarctic Muon Neutrino Detector Array (AMANDA)[62] extension; Sudbury Neutrino Observatory (SNO)[63]; Super-Kamioka Nucleon Decay Experiment (SUPER-Kamiokande)[64]. Meanwhile cosmic γ-ray experiments can be classified into two types: space-based telescopes such as Energetic Gamma Ray Experiment Telescope (EGRET)[65] and Gamma-ray Large Area Space Telescope (GLAST)[66]; ground-based telescopes such as Collaboration of Australia and Nippon for a GAmma Ray Observatory in the Outback (CANGAROO)[67], and High Energy Stereoscopic System (HESS)[68]. Furthermore, experiments which are searching for evidence of dark matter annihilations in the spectra of positrons, antiprotons, or both also exist, such as Alpha Magnetic Spectrometer (AMS)[69].

A very different experiment, the Large Hadron Collider (LHC)[70] particle accelerator at CERN will search for supersymmetric particles, including the predicted neutralino, studying its production. It is due to be operational this year and release physics results before 2010: anticipated to coincide with reaching the lowest predicted neutralino limits by alternative methods. This highlights the fact that diverse approaches and technologies are being utilised. For instance, direct detection experiments are not rendered obsolete by the possibility of detecting high mass WIMPs with greater sensitivity in indirect detection experiments. Instead, the two avenues of investigation are deemed complementary.

Chapter 2

Direct Detection of WIMPs

This chapter focusses on the direct detection of a specific type of supersymmetric dark matter candidate: the WIMP. A detailed discussion of WIMP signatures and detection principles follows. In addition, a review of the two categories of WIMP detectors, single and dual channel, is provided.

2.1 WIMP Signatures

The hypothesis that the galactic halo is filled with WIMPs, which routinely pass through the Earth, can be tested directly by studying: the recoil energy of nuclei, annual modulation of events, or diurnal modulation of recoil direction. Each of these is detailed below, with focus given to the nuclear recoil strategy as employed in ZEPLIN III.

A more thorough description of the ZEPLIN III instrument design, detection principles and microphysics can be found in Chapter 3.

2.1.1 Nuclear Recoils

WIMPs are expected to scatter off detector target nuclei either through an elastic or inelastic scattering process.[42] In the former case the energy deposited to the recoil nucleus E_R depends on the interaction itself, the WIMP mass, m_w, and the WIMP velocity distribution, v.[71] In general this energy can then give rise to photon

emission, charge release and phonon production. Low-background detectors looking for these signals may prove capable of directly detecting WIMPs.

The positive identification of a WIMP signal via WIMP-nucleon scattering would require the study of nuclear recoils at low energies $\lesssim$100 keV. The maximum energy transferred in a nuclear recoil, from a head-on collision of equal masses, is equal to the WIMP's kinetic energy, E_0, where:

$$E_0 = \frac{1}{2} m_w c^2 \left(\frac{v}{c}\right)^2 \tag{2.1}$$

and $v \sim 10^2$ km s^{-1}, $c \sim 10^5$ km s^{-1}, $\frac{1}{2} m_w c^2 \sim$GeV, implying that $E_0 \sim$keV.[71]

The physics associated with WIMP direct detection can be explained more completely within the following framework. For the simplest case of a detector stationary in the Galaxy the differential energy spectrum, or expected number of counts per recoil energy bin, is given by:

$$\frac{dR}{dE_R} = \frac{R_0}{E_0 r} e^{-E_R/E_0 r} \tag{2.2}$$

where R, E_R, R_0 and r are the event rate per unit mass, the recoil energy, the total event rate and the target nucleus kinematic factor, respectively.[71] Here, E_0 is the mean kinetic energy of a distribution. Experiments measure the differential rate on the left-hand side of Equation 2.2, allowing a corresponding value for R_0 to be calculated, from the right-hand side, as a function of m_w.[72] To describe the dark matter differential energy spectrum more accurately modifications to Equation 2.2 are required. These account for: the Earth's motion, recoil detection efficiency, instrumental resolution and threshold, the use of multiple target elements, spin-dependent and coherent factors as well as the *nuclear form factor*, F. The form factor correction is due to the actual size of the nucleus being finite and is dependent on the recoil energy.[72] With the above modifications Equation 2.2 takes the following form

$$\frac{dR}{dE_R} = 2N_T \frac{n_0 \sigma_0}{m_w r} F^2(E_R) \int_{v_{min}}^{v_{esc}} \frac{f(v)}{v} dv \tag{2.3}$$

$$v_{min} = \sqrt{\frac{2E_R}{m_w r}} \tag{2.4}$$

$$r = 4 \frac{m_w m_n}{(m_w + m_n)^2} \tag{2.5}$$

where $f(v)$, n_0, v_{esc}, N_T and m_n are the WIMP velocity distribution, the mean dark

matter particle number density, the escape velocity (∼600 km s^{-1}), the number of target nuclei and the target nucleus mass, respectively. Here $f(v)$, v_{esc}, and n_0 are astronomical terms, associated with the WIMP's source and location. The unknown WIMP-nucleus interaction cross section, σ_0, and WIMP mass are to be determined by direct detection. Variables relating to the physics of the detector itself are N_T, E_R, m_n and $F^2(E_R)$. Note that the number of counts per recoil energy (see Equation 2.3) is clearly dependent the mass of the target nucleus m_n and thus on the target material.[42] It is this WIMP-nucleus interaction rate equation, together with the approximate, known galactic dark matter density and flux, which enables a limit on R_0 to be converted to one on the particle interaction strength, or cross section. Hence, results of experimental direct detection experiments can be plotted in the m_w-σ_0 plane.[72]

Detector Sensitivity

The fundamental process involved in WIMP-nucleus scattering is WIMP-quark scattering. When summed over the quarks present in all nucleons this yields an effective WIMP-nucleus cross section defined as:

$$\sigma_0 = \frac{signal\ event\,[s^{-1}]}{total\ flux\,[cm^2\ s^{-1}]} \tag{2.6}$$

WIMPs are expected to scatter off nuclei rarely, at a rate of less than one kg^{-1} day^{-1} (assuming $\sigma_0 \sim 10^{-42}$ cm^2).[73] The current aim of direct detection instruments is to test down to sensitivities of 10^{-44} cm^2 (or 10^{-8} pb, equivalent to ∼1 event kg^{-1} $year^{-1}$). The next generation of detectors seek to improve this further, aiming to reach 10^{-46} cm^2 (or 10^{-10} pb, ∼1 event ton^{-1} $year^{-1}$).

Interactions between target nuclei and neutrons result in a nuclear recoil signature, mimicking that of a WIMP-nucleon interation. In addition, there are background electron recoil events from γ or β particles from the natural radioactivity background of the detector and its environment of which distributions can overlap those of nuclear recoils. Therefore, the successful detection of extremely rare WIMP-nucleon interactions demand high particle discrimination.

When a detector, designed to probe down to a certain cross section sensitivity, excludes some region of the m_w-σ_0 parameter space, it places constraints on the WIMP cross section and mass at certain confidence levels. Rescaling the WIMP-nucleus to a WIMP-nucleon cross sections allows comparison between different experiments.

Each null experimental result then places limits on the WIMP-nucleon interaction rate, which is lower, or more rare. Consequently, the next generation of detector seeks to probe cross sections of lower orders of magnitude. The iterative nature of progressively improving detector technologies in this way favours scalable detectors.

Coupling

WIMP-nucleon interaction rates or detector sensitivities can be expressed in terms of spin-independent or spin-dependent coupling. The cross section of the lightest supersymmetric particle (LSP) for elastic scattering off nuclei contains both spin-independent and spin-dependent terms.[72]

As the name suggests *spin-dependent* coupling describes the interaction between WIMPs and the spin of the target nuclei, where it effectively involves only unpaired nucleons. In this case the cross section is not proportional to the number of nucleons or the quark mass but is dependent on the assumed WIMP type. Only nuclei with an odd number of protons and/or an odd number of neutrons can show spin-dependent interactions.[72] Thus the main consideration when measuring spin-dependent WIMP-nucleon cross sections is to use odd-p, odd-n, or odd-p and odd-n target nuclei to maximize the number of unpaired nucleon spins. [73]

Spin-independent, scalar (coherent) coupling σ_{SI}, where all coupling occurs equally to all nucleons, is dependent on the number of target nucleons N_{nuc}; $\sigma_{SI} \propto N_{nuc}^2$.[74] Equivalently $\sigma_{SI} \propto A^2$, where A is the target's atomic mass number. Thus rates or cross sections should be divided by A^2 to normalise (i.e. convert from WIMP-nucleus to WIMP-nucleon) for different target elements across different experiments and σ_{SI} is greatly enhanced for heavy nuclei.[72] In detectors with heavy target nuclei ($A \gtrsim 30$), such as xenon (A=131) spin-independent dominates over spin-dependent scattering.[74]

2.1.2 Annual Modulation

A second type of WIMP signature that direct detection methods can potentially identify is the annual modulation of event count rates (see Figure 2.1). This is due to the Earth's orbital velocity around the Sun, v_{orb}=30 km s^{-1}[75]. The movement of the Sun, with velocity v_{Sun}= 232 km s^{-1}[75], generates a 'WIMP wind'. The average WIMP velocity can be seen to vary by approximately +15 km s^{-1} in summer and

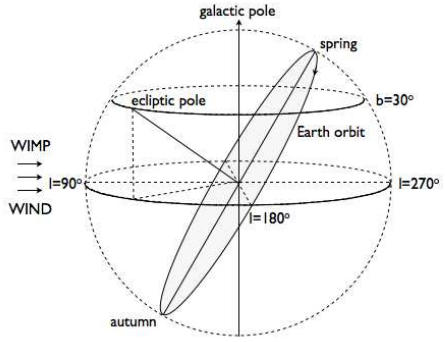

Figure 2.1: Schematic detailing the annual modulation WIMP signature. The WIMP wind induced by the Sun's motion and the relative velocity changes in summer and winter produce a yearly modulation of count rates. Adapted from [42]

-15 km s^{-1} in winter by the following:

$$v_{Earth} = v_{Sun} + v_{orb}\cos\gamma\cos[\omega(t-t_0)] \quad (2.7)$$

$$= v_{Sun} \pm 30\cos(60)\cos((2\pi/365)153) \quad (2.8)$$

$$\approx v_{Sun} \pm 15 \quad (2.9)$$

where v_{Earth} is the velocity of the Earth through the Galaxy, γ=60^o is the angle of inclination of the Earth's orbital plane relative to the galactic plane and $\omega \approx 2\pi/365$ radian day^{-1}, with the phase, t_0=152.5 days, corresponds to June 2^{nd}.[75] The second term in Equation 2.7 together with the WIMP wind leads to variations in the mean kinetic energy for approaching WIMPs. Hence, a predicted annual asymmetry rate of a few %[76] in the WIMP flux and spectrum is expected. Controversially, in 1998[75] a WIMP signal was hinted at, later announced in 2003[77] and confirmed in 2008[78]; the DAMA group claimed to have successfully detected this asymmetry, witnessing the first detection of dark matter! This is discussed further in Section 2.3.

2.1.3 Diurnal Modulation

A third, potential WIMP signature is the diurnal modulation of recoil direction (see Figure 2.2). On a daily basis a high directional asymmetry of WIMP scattering events is expected. This is because of the WIMP wind and *sidereal rotation*, the daily rotation of the Earth. By recording the track directions of the recoil nuclei

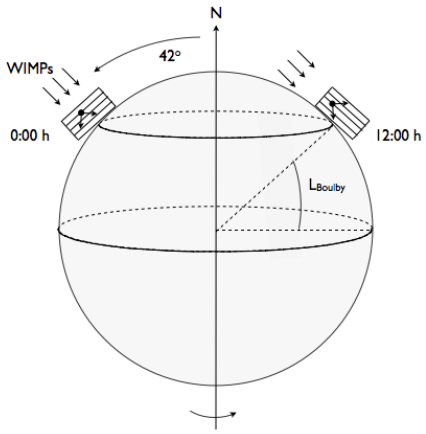

Figure 2.2: Schematic showing the diurnal modulation WIMP signature measured at the Boulby mine, North Yorkshire, with latitude L_{Boulby}. The WIMP wind induces a strong asymmetry of nuclear recoil directions which are modulated daily. Adapted from [42]

one can look for evidence of this time-dependent asymmetry. Such evidence would indicate dark matter interactions within the detected signal. However, at the very low energies involved in WIMP interactions, successful detection using this technique is highly ambitious.

A UK-USA collaboration are developing the Directional Recoil Identification From Tracks (DRIFT)[79] *time projection chamber* (TPC) programme of detectors, designed to observe the strong diurnal modulation signal. Ionisation track recoil energies and ranges ∼mm[80] are measured with two 1 m long *multi-wire proportional chambers* (MWPCs) of 1 m^3 sensitive volume in low-pressure CS_2 gas, allowing potential correlation of the direction of nuclear recoils with our motion through the Galaxy.[79]

The CS_2 gas acts both as an effective dark matter target material and as an electronegative molecule which captures the electrons and preserves the tracks as they are drifted along the chamber, until separated again by the electric field, inducing an avalanche. Discrimination of electron recoil and alpha versus nuclear recoil tracks is achieved through their relative track lengths.[80]

DRIFT I[81] was originally operated underground at Boulby in 2001 in the high-pressure search mode to discriminate between nuclear recoils and gamma-background. The alternative, low-pressure mode of operation to investigate directionality was planned to take over if a signal was detected. During operation no

positive WIMP signal was found.

DRIFT II, offering 3D instead of 2D track reconstruction[82], is expected to reach sensitivities of 10^{-7}pb[83]. Laboratory space and facilities exist to increase the size of the array to include up to 20 adjacent modules.[82]

Adopting a similar approach to DRIFT, the NEw generation WIMP search with an Advanced Gaseous tracking device Experiment (NEWAGE)[84] is a directional experiment with a CF_4 gaseous micro-pixel readout TPC. Pilot runs of small-volume ($10 \times 10 \times 10$ cm^3) and large-volume ($23 \times 28 \times 30$ cm^3) TPCs on the Earth's surface[84], yielded the first directional limit on the spin-dependent WIMP-nucleon cross section of 1.36×10^4 pb[85]. An underground measurement was initiated in the Kamioka Observatory in 2007.[84]

2.2 Detection Principles

Low energy nuclear recoils induced by WIMP scattering, can be detected via the phonon, charge or light signals generated in the target material. These, along with the main requirements of direct WIMP detection technology, are detailed below.

2.2.1 Signal Channels

The preferred experimental techniques for detecting WIMPs by WIMP-nucleon scattering currently involve bolometric, ionisation and scintillation devices, or a combination of any two and can be classified as in Figure 2.3.[42]

Ionisation can occur by several routes: in the case of a γ-ray interaction the electron produced will scatter inelastically from the surrounding atoms causing further ionisation as bound electrons are 'knocked out' of the atoms; in the case of a nuclear recoil, either from a WIMP or a neutron scatter, the recoiling atom will collide with other atoms and this process can release bound electrons or excite them to higher states. Detectors utilising the technique of ionisation alone are incapable of distinguishing nuclear recoils from electron recoils (background). Detectors using scintillation (light) and/or ionisation (charge) principles can attempt event-by-event discrimination of nuclear and electron recoils.[42]

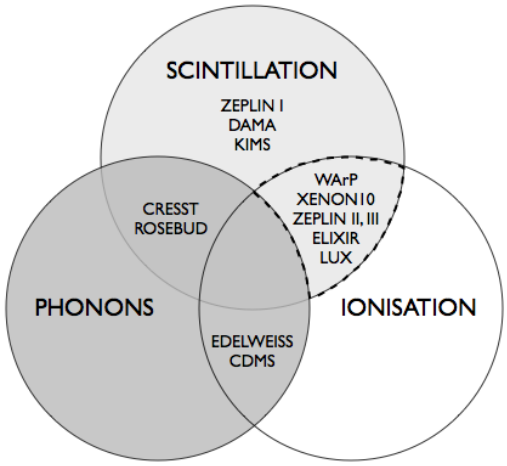

Figure 2.3: Schematic showing the three primary approaches to the detection of recoil energy depositions: ionisation, scintillation and phonon detection. Any one, or combination of two, of these principles may potentially result in successful WIMP detection. The technologies associated with some past, present and future experiments are also shown. Those utilising noble liquids lie in the region enclosed by the broken line.

When an excited electron falls back to its ground state a photon is emitted. This is the process of *scintillation*. Often WIMP detectors adopting this method, measuring the emitted photons, employ photomultiplier tubes to produce a pulse of current for every scintillation detected. Either crystal or liquid noble gas scintillators can successfully discriminate between nuclear and electron recoils using statistical pulse shape analysis. This is possible since nuclear recoils have higher energy loss per unit track length (linear energy transfer (LET), $\mathrm{d}E/\mathrm{d}x$) which alters the timescale of the processes leading to scintillation.[86]

2.2.2 Detector Requirements

The constraints placed on WIMP direct detection technology have inspired a vast number of detector designs and experiments around the world. The three main constraints on detector design - target mass, energy threshold and background minimisation - may be summarised as follows.

The target mass should be as large as possible in order to maximise interaction probability. To achieve competitive detector sensitivities at the moment target masses should exceed the order of a kilogram.

The WIMP signal produced from elastic scattering is expected to give rise to an energy spectrum that is featureless and decreases exponentially (see Equation 2.2). Furthermore, the dark matter region of interest lies in the $\lesssim$100 keV energy range[87]. Thus, the energy threshold should be minimised in order to maximise the signal strength.

Minimisation of the internal and external sources of background is crucial for WIMP detectors. At the design stage careful consideration must be given to detector materials including those of the auxiliary systems. Locating WIMP detectors in underground laboratories can significantly reduce the level of external backgrounds. More specifically, cosmic ray muons produce a neutron flux of $\sim 10^6$ counts $\mathrm{kg}^{-1}\mathrm{yr}^{-1}$ at the Earth's surface which is negligible $\sim$1 km below the Earth's surface.[88] Additional shielding can be fitted around the detector. Particle discrimination also plays a major role in effective background minimisation and event rejection. The choice of signal channel(s) determines which discrimination technique is adopted while useful event rejection can be achieved by the inclusion of a veto system. For a comprehensive list of background sources present in the ZEPLIN III setup see Section 3.1 and Table 3.1.

2.3 Single Channel Detectors

Several of the current global WIMP detection experiments can be classified as single channel detectors: adopting only one, not a combination of the detector techniques of ionisation, scintillation and phonon detection. A description of two such detectors follows (see also Table 2.1).

Scintillation

The DAMA experiment is one example of a dark matter detector utilising scintillation detection (see Section 1.6.1). The original DAMA experiment used 100 kg Sodium Iodide (NaI) detectors with temporal analysis in a bid to detect an annual modulation WIMP signature (see Section 2.1.2). It is located underground at the Gran Sasso National Laboratory, Italy. The acquired data appeared to show a modulated cosine-like behviour and after seven years of running the DAMA group claimed a 6.3σ positive WIMP-signal detection with a fitted t_0 of 140$\pm$22 days.[89] This suggested the existence of WIMPs, assuming a mass of 60 GeVc^{-2}, with an

interaction cross section of 7.0×10^{-6} pb, corresponding to a rate of $\sim$ 1 event day^{-1} kg^{-1}.[89] However, according to other groups e.g. CDMS and EDELWEISS, the events in question should not have been attributed to scattering events from dark matter. They concluded cosmic rays producing background neutrons and penetrating their laboratory were the most likely culprit with the general view of either some background contributions or detector systematics being accountable.[90][91][92] The controversial nature of the DAMA result was heightened by the other searches failure to detect dark matter interactions at apparently better sensitivities.

In 2003 the DAMA successor Large sodium Iodide Bulk for RAre processes (LIBRA) started operating at the Gran Sasso site. This second generation detector is a $\sim$250 kg NaI detector, with 25 crystal scintillators and improved radiopurity[77]. Like DAMA, it is based on the technique of scintillation with temporal analysis. Meanwhile, a 1-ton, third generation detector remains in its research and development phase.[77]

In 2008 the DAMA/LIBRA collaboration announced a revised dark matter result, through the combination of DAMA/LIBRA and DAMA/NaI (first generation) data, claiming the detection of dark matter particles in the galactic halo with a 8.2σ CL.[47]

It was shown that, looking at single-hit events (a class to which the dark matter particle induced events belong), a clear modulation is present and statistically well distributed in all the crystals, in all the data taking periods and in all of the considered energy intervals. The 2-6 keV energy interval is shown in Figure 2.4. Furthermore, the periods and phase of the modulation amplitudes agreed with those expected in the case of a dark matter particle induced effect. The collaboration also excluded many effects either from systematics or side processes (such as temperature, radon background and noise amongst others). As with the previous DAMA/NaI result, controversy resides over the combined result since no experiment exists whose results can be directly compared[47] as, if correct, the WIMPs involved are not the neutralinos expected from within SUSY, and worries about the systematics remain.

A second example of a solid scintillator detector, of which recent performance has yielded a null-signal in the DAMA region which should be noted, is KIMS. The KIMS collaboration developed low background CsI(Tl) crystals to detect the signals from the elastic scattering of WIMPs off the target nuclei, exploiting the detection approach of scintillation.[48] Both ^{133}Cs and ^{127}I nuclei are sensitive to the spin-independent and spin-dependent interactions of WIMPs. From 2004, the KIMS

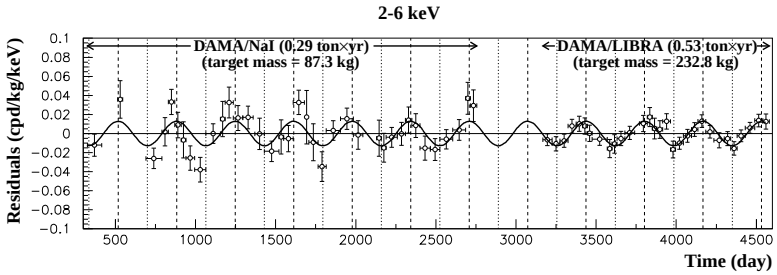

Figure 2.4: The time behaviour of the model-independent residual rates for single-hit events collected by the new DAMA/LIBRA experiment (over 4 annual cycles) and those by the former DAMA/NaI experiment (over 7 annual cycles) in the 2-6 keV energy interval. The zero of the time scale is January 1^{st} of the first year of data taking of the DAMA/NaI experiment. The superimposed curve represents the cosinusoidal functions behaviours $A\cos w(t-t_0)$ with a period T=1 year and a phase t_0=152.5 day (June 2^{nd}). [47]

detector has been operational[93] and consists of four 8.7 kg[48] CsI(Tl) crystals used in conjunction with eight PMTs, with a view to progressively upgrading the target mass, up to 250 kg[93].

2.4 Dual Channel Detectors

Dual channel detectors adopt two information read-out channels. These types of detector are becoming increasing popular in the worldwide race to detect WIMPs since they offer high nuclear recoil discrimination. Such experiments include CDMS II, EDELWEISS II, CRESST II, ROSEBUD, XENON, WARP, ZEPLIN II and ZEPLIN III (see Section 1.6.1). These experiments are described briefly below and a synopsis of their main characteristics is given in Table 2.1.

Phonons & Ionisation

The CDMS II[55] and EDELWEISS II[95] heat and ionisation cryogenic experiments are currently both operational. For increased sensitivity, the second-generation CDMS detector, CDMS II, uses 2-7 kg of Germanium (Ge) and Silicon (Si) semiconductor crystals to collect the phonon and ionisation signals simultaneously. Its predecessor, CDMS I[43], used only 1 kg of Ge and Si and ran at Stanford, California. This novel approach, using Ge and Si crystals, has equipped the CDMS group with the potential to discriminate between nuclear recoils due to neutrons and WIMP induced events.

Detector Type	Readout Channels	Experiment	Location	Detector Target	Target Mass (kg)	Exposure (kg×days)	σ_{SI} (pb)
liquid noble gas	scintillation	ZEPLIN I[94]	UK[a]	LXe	5 (3.2 fid.)	293	1.1×10^{-6}
solid scintillator	temporal analysis	DAMA/LIBRA[78][89]	Italy[b]	NaI(Tl)	100	57986	5.4×10^{-6}
	scintillation	KIMS[48]	Korea[c]	CsI(Tl)	34.8	3409	$\sim2\times10^{-6}$
cryogenic	phonons & scintillation	CRESST II[49]	Italy[b]	$CaWO_4$	0.6	67	6×10^{-7}
		ROSEBUD[50]	Spain[d]	Al_2O_3	0.05	0.105	$\sim10^{-1}$
	phonons & ionisation	CDMS II[55]	USA[e]	Ge	3.75	121.3	6.6×10^{-8}
		EDELWEISS II[95]	France[f]	Ge	35		$\sim10^{-7}$
liquid noble gas	ionisation & scintillation	XENON10[53]	Italy[b]	L/GXe	10 (5.4 fid.)	316	8.8×10^{-8}
		WARP[96]	Italy[b]	L/GAr	(1.83 fid.)	96.5	$\sim10^{-6}$
		ZEPLIN II[57]	UK[a]	L/GXe	31 (7 fid.)	225	6.6×10^{-7}
		ZEPLIN III[58][97]	UK[a]	L/GXe	12 (8 fid.)	3000	$\sim10^{-9}$
		ELIXIR[59][98]	Europe	L/GXe	∼1000	∼365000	$\sim10^{-10}$
		LUX[60]	USA[g]	L/GXe	300 (100 fid.)	∼36500	7×10^{-10}
gas detector	ionisation track resolved	DRIFT II[83]	UK[a]	CS_2	0.167	207	$\sim10^{-7}$
		NEWAGE[85]	Japan[h]	CF_4	0.009	0.151	$^{\dagger}1.36\times10^{4}$

Table 2.1: Comparison of several, different past, present and future direct dark matter (single and dual channel) detectors. Projected limits on the spin-independent WIMP-nucleon cross section, σ_{SI}, and exposures are given in *italics*. In the Location column: a refers to *Boulby mine, North Yorkshire (2800 mwe)*; b *Laboratori Nazionali del Gran Sasso (4000 mwe)*; c *Yangyang Underground Laboratory (Y2L) (∼2000 mwe)*; d *Laboratorio Subterrneo de Canfranc (2450 mwe)*; e *Soudan mine, Minnesota (2090 mwe)*; f *Underground Laboratory of Modane (4800 mwe)*; g *Deep Underground Science and Engineering Laboratory (DUSEL), Homestake mine, South Dakota (4300 mwe)*; and h *Kamioka Observatory (2700 mwe)*. Note that, in the final, cross section column, † denotes a spin-dependent limit obtained pre-deployment with NEWAGE located in a surface laboratory.

Analogous to the scaling-up of CDMS, the original EDELWEISS I[99] detector (1 kg Ge) has been upgraded to increase the sensitivity by a factor of 100 to EDELWEISS II (35 kg Ge).

Phonons & **Scintillation**

The CRESST II detection principle is based on both phonon and scintillation readout channels, using two calorimeters per module; a heat detector (300 g $CaWO_4$ dielectric crystals as absorbers) and a separate light detector (Silicon (Si) wafer), respectively.[51] Two, independent *Tungsten Superconducting Phase transition Thermometers* (W-SPTs) are used in both channels. A thin film of Tungsten (W) is evaporated onto the scintillating crystals and another is located on the Si light-absorbing wafers.[49] Following the early commissioning stages ten detector modules have been installed, are operational (at ∼10 mK) and their energy response calibrated. A dark matter exclusion limit, updating that obtained with the earlier run with two detector modules[49], has recently been achieved.[100]

Deployed in its original form in 1999[101], the ROSEBUD cryogenic experiment adopts a similar WIMP detection approach to that of CRESST II. The ROSEBUD detector consists of a double scintillating bolometer configuration (a scintillating crystal and a Ge disk), achieving simultaneous measurement of heat and light produced in particle interactions.[52] The temperature increases - as a direct result of the heat produced in the scintillating crystal and, indirectly, through the emitted light escaping from it and evenutally absorbed in the Ge - are measured by Ge thermistors glued onto each crystal. In its current, second phase, an assembly of two double bolometers of BGO and sapphire are used in the same experimental setup.[52]

Ionisation & **Scintillation**

The XENON, ZEPLIN II, ZEPLIN III and WARP experiments are all based on mixed, cryogenic, noble liquid/gas detector designs with both ionisation and scintillation readout channels. The prompt scintillation and delayed ionisation signals, both seen as vacuum ultra-violet (VUV) light pulses, are measured simultaneously.

The current XENON experiment, XENON10, has ∼3 kg and ∼10 kg of active and fiducial mass, respectively. The chamber consists of a LXe bulk, above which there is gaseous xenon (GXe) in which an array of photomultiplier tubes (PMTs) are mounted. The proposed, upgraded detector would have a 1000 kg fiducial mass.[45]

The design of the ZEPLIN II detector is similar to XENON10 in that 7 PMTs are mounted in the gas phase, viewing the LXe phase from above, with a 31 kg xenon target mass.[57] By analogy with the XENON and ZEPLIN II approach, the WARP detector has an array of 12 PMTs mounted in the gas phase with the bulk, liquid phase sitting below ∼1.83 kg fiducial volume.[96] Unlike in XENON and ZEPLIN, WARP's choice of target material offers an additional rejection method, providing an independent background discrimination. This is based on the slope of the scintillation signal since the singlet and triplet time constants, ∼6 ns[86] and ∼1.6 μs[86], respectively, are much longer in liquid argon (LAr) than in LXe.

Chapter 3

ZEPLIN III

This chapter describes the detection principle and key sub-systems of the two-phase liquid xenon WIMP dark matter detector, ZEPLIN III. Details of the xenon purity, PMT array, electric field, DAQ system and the detector shielding and Veto are included. Finally, discussions of the ZEPLIN III Monte Carlo model and the adopted method of instrument monitoring are presented.

Although most of the material presented in this Chapter has inevitably been derived from work of the ZEPLIN collaboration, Figures 3.3-3.4, 3.6-3.17 and Tables 3.2 and 3.3 were constructed by the author alone.

3.1 Detection Principle

The ZEPLIN III Dark Matter detector exploits both scintillation and electroluminescence processes in the xenon WIMP target (Figures 3.1 and 3.2). An array of thirty-one photo-detectors, photomultiplier tubes (PMTs), are used to detect the vacuum ultraviolet (VUV) 175-nm[57] scintillation photons from both the liquid and gaseous xenon. Hence, good light collection by the PMTs is critical. The light yield of the fast, prompt primary scintillation signal (S1) in the liquid xenon (LXe), with time constant of $\sim$10 ns[87] is caused by direct excitation. The energy density is proportional to the type of interacting particle and the energy deposited in the LXe depends on the kinematics of the scattering process. The secondary signal (S2) produced in the gaseous xenon (GXe), is due to electroluminescence. This is

caused after the ionisation charge, released at the interaction site, has been drifted up towards the liquid surface and extracted into the gaseous phase by the uniform, applied electric field, suppressing recombination in the liquid. Once in the gas phase, excitation, enabled by the sufficiently strong electric field there, follows, leading to a second, delayed burst of photons.[87] The ratio of S2/S1 depends on particle type which is exploited in particle discrimination. S2 is also used for position reconstruction of the events.

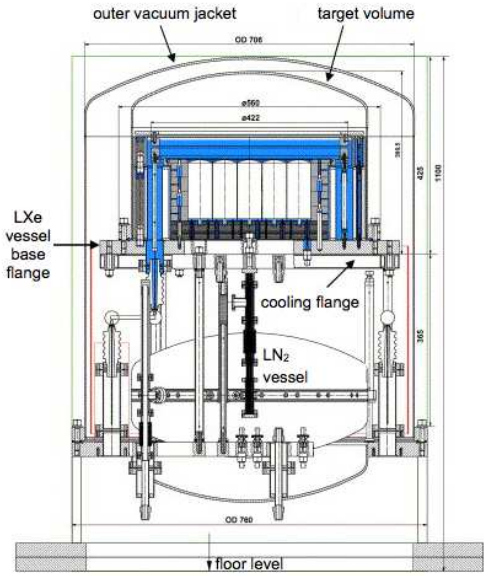

Figure 3.1: Cross sectional view of the ZEPLIN III detector showing the key components. All scale dimension are in mm. The instrument is 1100 mm tall with a diameter of 760 mm and the bulk of the parts are made of C103 OFHC copper. The target vessel stands above the liquid nitrogen (LN_2) reservoir which cools it to $-100\,^{\circ}C$.[87]

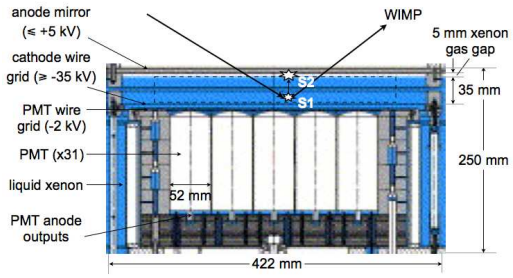

Figure 3.2: Cross section of the ZEPLIN III LXe target region viewed by the array of 31, immersed photomultipliers along with the event interaction process. The broken line defines the fiducial volume boundary.[87]

The singlet and triplet states of the xenon excimer can be formed in one of two ways; either directly by atoms which have been excited by the interacting particle or by recombination into an excited state (Figure 3.3).[87] It is the decay of these excimer states to the ground state which produces the VUV luminescence, with characteristic decay times of 3 ns and 27 ns, respectively.[57]

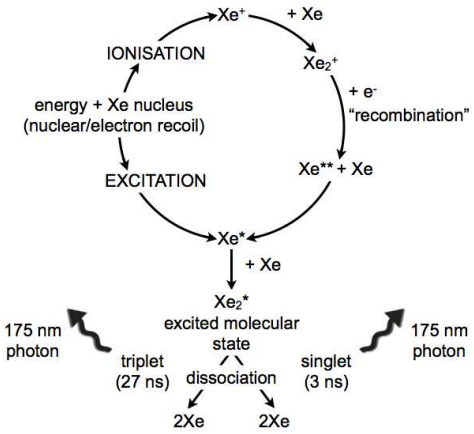

Figure 3.3: Schematic showing scintillation and ionisation processes in LXe.[102] The ratio of light produced by direct excitation to ionisation recombination depends on the linear energy transfer (LET) or energy loss rate, dE/dx, of an interaction. The population of triplet and singlet states also depends on the LET. The LET of a 1 MeV electron is less than that of an alpha particle. Hence the recombination time of the electron is significantly greater than that of an alpha particle. Consequently, electron recoil and nuclear recoil scintillation light have different time profiles.[57]

When recombination is allowed to occur, at zero-field, the recombination time is determined by the energy loss rate, dE/dx, of the interacting particle. For nuclear recoils this is fast (<1 ns) compared with electron recoils (∼40 ns). This forms the basis of the particle discrimination approach employed in ZEPLIN I which operated at zero-field.[57]

In the case where recombination is suppressed and an electric field is applied the electron drift velocity in liquid xenon, v_d, slowly increases with the electric field strength, E, up to $v_d \sim 10^5$ cm s^{-1}, with $E \sim 10^2$ V cm^{-1}. At electric fields above this value i.e. the 'saturation region', v_d is approximately constant.[103] All electrons that are extracted into the GXe elastically collide with the gas atoms. At high enough field strengths the electrons have sufficient energy to produce xenon excitation leading to scintillation or electroluminescence. This secondary signal (amplified with respect to that of the primary) is proportional to the number of electrons extracted.

The number of electrons produced is partly dependent on the ionisation separation efficiency which, in turn, is dependent upon the initial linear ionisation density. In γ-ray interactions the electric field is more effective in separating the free electrons from the ions. This is because the ionisation track is less dense. As a result, the electron extraction is strengthened and the observed S2 is larger.[57] The probability of charge extraction, from the liquid to the gas, which is dependent on the electric field at the L/GXe interface, also affects the S2 signal.

As discussed, the total S1 at zero-field includes a contribution from recombination of the ionisation. Suppression of the recombination redirects this contribution into the S2 channel instead, with the total energy deposited in the xenon conserved.[57] Thus, on an event-by-event basis S1 and S2 are *anti-correlated*.[104] With this in mind, some linear combination of S1 and S2 may be used to characterise the interaction more generally, tightening peaks in the energy distributions.[57]

In ZEPLIN III the S2 signal lasts longer than S1, and this is related to the gas gap thickness and the electric field in the gas. As the charge drifts across the gap the secondary emission levels off. The time delay between S1 and S2 is dependent upon the interaction depth and the drift velocity ($\sim$2.5 mm μs^{-1}) in the liquid.[87] Extraction dynamics, charge diffusion and the gas scintillation time constant all influence the signal rise and decay times. Figure 3.4 shows a typical S1 and S2 signal from a γ-ray interaction in the LXe.[87]

Utilising LXe technology within WIMP detectors has numerous advantages: since LXe can be obtained through the fractional distillation of air it is readily available in large quantities; the high atomic number of xenon ($Z_{Xe} = 54$) and thus high atomic mass ($A_{Xe} = 131.29$), together with $\sigma_0 \propto A^2$ for spin-independent scattering, yields an increased interaction rate compared to lower mass targets; xenon can be purified to give a long free-electron lifetime ($\sim$ms); the high density of liquid xenon, at $\sim$3.052 g cm^{-3}, is particularly favourable as the large target mass sought can be achieved in a small volume; a high light and ionisation yield is achievable; xenon has no contaminating, long-lived radioisotopes; LXe offers low energy threshold and high background discrimination;[105] and at $\sim$47.6 % the odd iostope abundance (^{129}Xe, ^{131}Xe) is high enough for it to be sensitive to spin-dependent WIMP interactions.

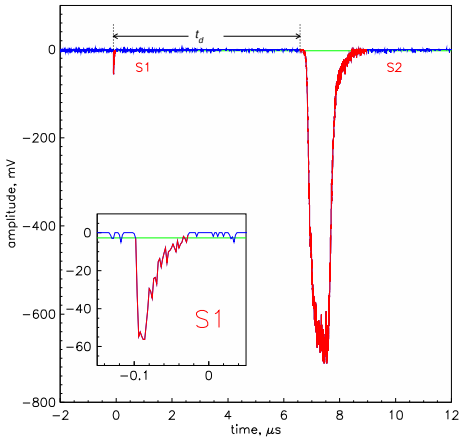

Figure 3.4: A typical S1 and S2 signal (amplitude, mV vs time, μs) from a γ-ray interaction in the LXe acquired in the LS SUM channel with an external ^{57}Co source placed on top of the vacuum vessel, at 17 kV (3.8 kV/cm in the liquid). The fast, primary scintillation S1 pulse in the liquid is followed in time by the wider, secondary S2 pulse from electroluminescence in the gas phase. The S1-S2 separation here corresponds to a drift time in the LXe, t_d, of 6.7 μs.

Low Energy Threshold

By placing the PMT array in the liquid phase ZEPLIN III optimises its sensitivity to S1, the primary scintillation signal, lowering the S1 energy threshold. This is realised by the removal of two interfaces - in deciding against mounting the array in the gaseous phase - together with the adoption of a planar geometry. The former improves the S1 light collection by replacing the two interfaces, with large refractive index mismatches, with a single interface exploiting total internal reflection. The latter weakens the dependence on surface reflectivities with a large solid angle acceptance.[87]

A high electric field in the gas region generates a low threshold for S2 by enhancing the photon yield (photon emission per electron emitted from the surface). Furthermore, refraction at the liquid surface 'focuses' the light on to the PMTs below.[87]

ZEPLIN III has sufficient sensitivity to the scintillation light to provide a usable electron recoil equivalent energy (keVee) threshold of ∼1-2 keVee and sensitivity to single electrons extracted from the liquid surface.[87]

Particle Discrimination

The two-phase design of ZEPLIN III enables S1 and S2 measurements for each event. The S2/S1 ratio of deposited energy is known to differ depending on the incident particle type: differing for nuclear recoil (incident neutrons and WIMPs) and electron recoil (photon backgrounds and alpha particles) interactions.

The scintillation yield of LXe for nuclear recoils is quantified by the *quenching factor*, q, or *scintillation efficiency*, normalised to that for γ-rays; q is defined as the ratio of the light produced by a nuclear recoil to the light produced by an electron recoil of the same energy.[106] Knowledge of q is important for the determination of the sensitivity of LXe based detectors to WIMP dark matter.[106] This ratio has been measured as 0.19 ± 0.02, on average, in the recoil energy range from 140 keV down to 5 keV.[107]

The S2/S1 ratio is measured through separate integration of the two signal pulse timelines. Comparison of calibrated signals, from neutron and γ-ray sources of known activity, with this ratio for each interaction makes the powerful technique of event-by-event particle discrimination possible.

The width and separation of the distributions for each incident particle species determines the effectiveness of the discrimination. Two distinct populations of nuclear and electron recoil events in ZEPLIN III, highlighting their separation, above the threshold energy, are shown in Figure 3.5 (see Section 4.3.8 for further discussion).

Both WIMPs and neutrons elastically scatter off the xenon target nuclei. Successful discrimination between these requires good 3-D position reconstruction (see below) since neutrons are distinguishable from WIMP-induced nuclear recoils by their multiple scattering nature. This is because the scattering cross section of neutrons is significantly higher than that of WIMPs.[87]

ZEPLIN III operates with a higher electric field ($\sim$4 kV/cm in the liquid) than its predecessor, ZEPLIN II. Its design differs from ZEPLIN II further in that the array of thirty-one PMTs are situated in the liquid phase.

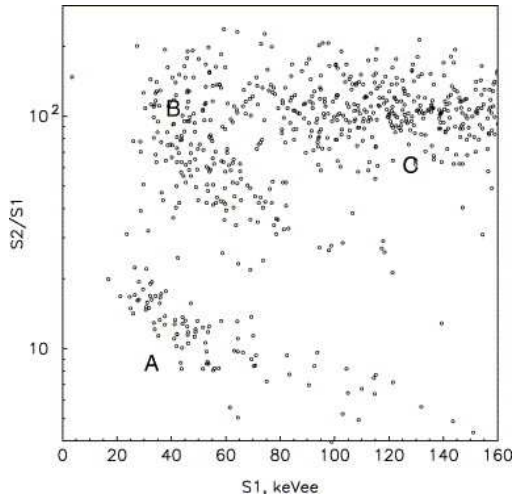

Figure 3.5: Scatter plot of the S2/S1 ratio as a function of electron-equivalent energy, keVee, ($\propto$S1) for single scatter events in the inner 7 PMTs obtained with a 10 mCi (370 MBq) Am-Be (α,n) source located above the detector (operated at 3.01 kV/cm in the liquid). For elastic nuclear recoil events (population A) the energy scale must be multiplied by 1.95, which comes from the combination of the inverse quenching factor, and the relative S1 suppression factor at our operating field ($\sim$0.37). Population B corresponds to the de-excitation of the 40 keV ^{129}Xe inelastic level (plus some nuclear recoil energy). Population C is the γ-ray population, also associated with the source.[87]

3-D Position Reconstruction

As mentioned previously, the ability to resolve the position of each interaction site in three dimensions is crucial in discriminating neutron background from potential WIMPs and for identifying multiply scattered γ-ray interactions. The r, θ and z co-ordinates of the 3-D interaction point can be constructed from: application of a position reconstruction algorithm (see [108]) in the horizontal (r, θ) plane; and the time delay between S2 and S1, the drift time in the liquid (z). The former provides sub-cm spatial resolution and, in general, the larger S2 signal produces the best (r,θ) reconstruction. When used in conjunction with S1 as well though, the two signals can act as a cross check and as a useful diagnostic tool, identifying multi-site events. The latter gives resolution at the 50 μm level. The accurate reconstruction of event positions in 3-D allows a $\sim$300-mm diameter fiducial volume, enclosing $\sim$8 kg of xenon, to be defined independent of any physical surfaces.[87]

Low Background

The sensitivity to the rare WIMP-nucleon scattering events which ZEPLIN III seeks to detect is optimised by minimising the level of background events within the fiducial volume. This is achieved through: deployment of the detector underground, below 1070 m of rock, removing cosmic-ray induced backgrounds; and by choosing detector materials from a restricted range of materials at the design stage, including stainless steel, C103 oxygen-free high conductivity (OFHC) copper, quartz and high-purity ceramic.

An itemised radioactivity budget for ZEPLIN III is detailed below (Table 3.1). The 31 PMTs are the largest specific contributor to the background.[87] Upgrading the PMT array is expected to reduce the γ-ray activity attributable to the array itself by a factor of thirty.[87]

As well as background events associated with the internal, external and auxiliary detector components three other sources may be observed: γ-rays and neutrons emitted by Uranium/Thorium (U/Th) decays from the surrounding rock, via the (α,n) reaction, with $\sim$MeV energies; partial energy loss of Radon progeny (α-particles) through nuclear recoils, depositing energies down to the keV range; and β-decays from a Krypton isotope, ^{85}Kr, contributing to the electron recoil γ-ray background population.[57] Installing shielding and veto systems immediately around the detector (Section 3.6), applying timing cuts thereby rejecting events and opting to use a low-Kr xenon target is intended to reduce these contributions.

3.2 Xenon Purity

For efficient S2 measurement, two-phase detectors require high xenon purity with electronegative impurities removed or minimised in order to preserve the number of electrons, or charge, during drift. The impurities, from species such as H_2O, O_2, N_2, CO, CO_2 and H_2, should be maintained below ppb levels. This is addressed in two ways; the target volumes must be manufactured as high vacuum vessels and it is crucial that purification systems are incorporated into the auxiliary systems.[87]

In ZEPLIN III the xenon is purified using one of two available SAES getters[110][111], removing impurities (e.g. O_2). Measurement of the average electron lifetime, τ_e, is used to monitor the xenon purity. For full electron extraction into the gas phase,

allowing one to 'see' events with interaction sites as far down as the bottom of the target volume, an electron lifetime of $\gtrsim$17 μs is demanded.[87] The *electron lifetime monitor* (ELM)[112] is a purpose built system designed to perform this measurement.

The Electron Lifetime Monitor

The ELM is a stand-alone, portable two-phase system dedicated to quantifying the purity of xenon (Figure 3.6). This is measured through ionisation in the gas phase, producing electrons, which are then drifted down towards the anode and into the liquid phase where they continue to drift, until captured by electronegative impurities. An internal 30 kBq ^{241}Am source mounted within the cathode emits α-particles which generate ionisation at an interaction rate of 11 s^{-1}. This independence from cosmic-ray induced ionisation enables it to be operated in underground, or shielded conditions.[112]

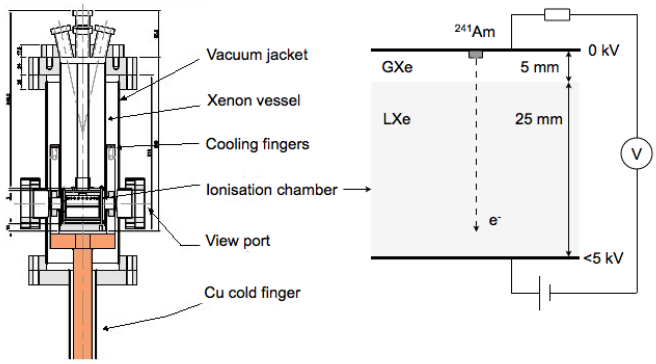

Figure 3.6: Engineering drawing showing components of the ELM (left panel). The copper cold finger is placed in a dewar of LN_2, cooling the xenon while heaters provide thermal control. A magnified schematic of the working principles of the ionisation chamber, housed within a xenon vessel, is also shown (right). Electrons are drifted through the liquid, towards the anode. Measurement of the induced potential difference across the plates enables the electron drift time, t_d, to be measured. The xenon purity is assessed by analysing the deviation from the linear induction otherwise expected.[112]

The xenon is zoned into a liquid and gas phase, with thickness of 25 mm and 5 mm, respectively. The applied anode voltage can vary up to 5 kV, corresponding to maximum electric fields of 1.4 kV/cm in the liquid and 2.9 kV/cm in the gas.[112]

Exploiting the method of pulse shape variation, the data are analysed following the acquisition of event timelines (Figure 3.7). The percentage deviation of the actual

charge collected at the anode from the ideal, pure xenon scenario, d, is assessed. The maximum drift time in the liquid, t_d, may be determined from the trace itself. The trace deviation from the perfect case is directly proportional to the xenon purity and relates to τ_e, in the following way:

$$\tau_e = \frac{-t_d}{\ln(1-d)} \tag{3.1}$$

where

$$d = \frac{N_0 - N}{N_0} \tag{3.2}$$

and N_0 and N are the initial number of electrons present and the number of electrons present at time t_d, respectively. For convenience, this measurement can be carried out on a small volume of LXe ($\sim$100 cm^3) sampled from the target, if and when required.[112]

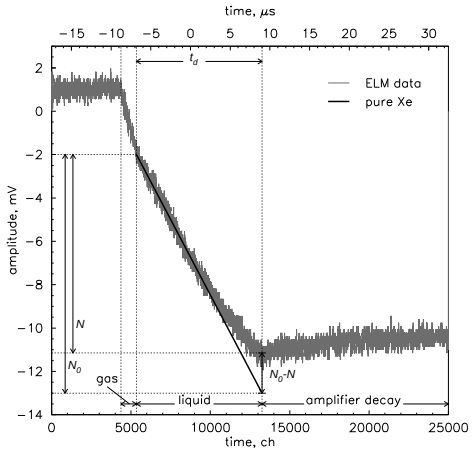

Figure 3.7: An ELM digitised trace (amplitude, mV vs time, μs). The three regions of the two-phase signal are clearly marked on the 071218 'data' signal, for the typical, impure xenon case. The superposed solid line represents the theoretical extrapolation of the ideal, pure xenon case where no electron capture takes place. The drift time in the liquid, t_d, and deviation, $N_0 - N$, parameters are used in a direct measurement of the xenon purity.[112] For this particular example, with an applied electric field of 0.29 kV/cm in the liquid of 2.5 cm, the LXe purity, τ_e, was measured as 100$\pm$29 μs.

For a more thorough description of the ELM operating principles, design and performance see [112].

3.3 Photodetectors: The PMT Array

PMTs satisfy the dark matter detector requirements for good light collection detection, ultra-fast response speeds (∼ns) and for background rates to be minimised making them a popular photodetector choice in this field. Thirty-one 52-mm diameter (ETL D730/9829Q)[1] high performance 12-stage PMTs are used for simultaneous detection of S1 and S2 in ZEPLIN III.

PMT Operating Principle

A schematic of the operating principle of a PMT is shown in Figure 3.8. There are two basic processes to consider: *photoemission* and *secondary emission*. When the PMT is exposed to light photons are incident on the photocathode, k. In ZEPLIN III k is at -2.15 kV. Photoelectrons are then emitted, via the photoelectric effect (photoemission). These are accelerated towards the series of dynodes, where charge multiplication occurs at each successive dynode (secondary emission). The resulting, amplified current signal is collected at the anode (at 0 kV in the case of ZEPLIN III). This is then converted into a voltage signal and fed into the data acquisition (DAQ) pipeline. The pulse shape and amplitude are subsequently analysed.

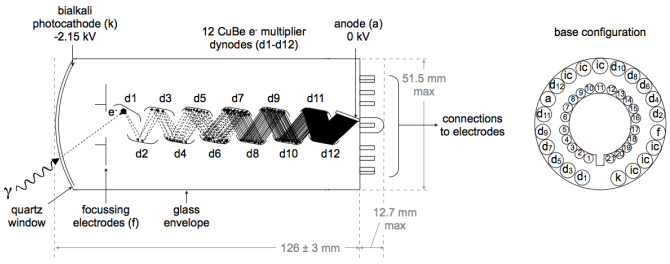

Figure 3.8: Schematic of a PMT (ETL D730/9829Q)[1] showing key components and the operating principle (left panel) and the base configuration, as viewed from above (right). Essentially, a PMT converts an optical signal into an electrical one which is subsequently amplified.

The probability that a photoelectron will be released at the photocathode is, neglecting some potential position and/or angular dependence, the same for all incident photons of the same wavelength. The photoelectrons are emitted in all directions and this process of photo-emission is very fast ($<10^{-11}$ s). The photocathode conversion efficiency for producing electrons, termed the *quantum efficiency*, QE(%), is a measurable characteristic for each PMT. More specifically, the QE is the average

percentage of incident photons that convert to photoelectrons and the statistics of the number of photoelectrons released follows a binomial distribution.[113]

Similarly, secondary electrons are emitted instantaneously, in all directions when a photoelectron is incident on any one dynode. The secondary current is proportional to the primary current. The statistical distribution of the number of secondary electrons, δ, is assumed to be Poisson-like.[113]

For an ideal n-stage PMT one assumes that: all emitted electrons do arrive at the next stage; and the QE and mean number of secondary electrons, $\bar{\delta}$, are constant on the surface of each electrode. If the inter-dynode voltage is the same for all stages the mean output charge collected at the anode, for a photoelectron generated at the photocathode, is given by

$$q = G.\, e \tag{3.3}$$

where e is the charge on an electron and G is the overall gain of the system. The latter is the product of the individual n dynode contributions to the incident electron amplification:

$$G = (\delta)^n \tag{3.4}$$

The QE and G parameters are used to describe the performance of a PMT. Measurement of the PMTs response, q, and prior knowledge of G and QE enables the number of incident photons, or true signal size, to be determined.[113]

The form of Equation 3.4 means that PMTs are extremely sensitive photodetectors. Thus the PMT response may be subject to fluctuations in environmental parameters, such as temperature, and electric and magnetic fields.[113] When normalising the PMTs response for different acquired data-sets the corresponding applied voltages must be taken into account.

The statistics of the photo- and secondary emission response processes are based on fluctuations in the number of output pulses per second and in the amplitude of output pulses, respectively. In general, signal statistics are limited by the multiplication of the charge at the first dynode, $d1$, where a relatively high gain is required.[113]

Single Photoelectrons

The single photoelectron (SPE) signal - in response to a single incident photon - arises when the PMT photocathode emits one electron. This one electron is then amplified according to Equation 3.3.

The signal strength, or energy deposited in the target, must be calibrated to be of any practical use. Therefore measurements of SPE spectra are crucial. However, this can prove challenging since the sensitive SPE distribution may be masked by the *dynode noise*; spontaneous emission of electrons from dynodes.

When the mean SPE pulse size is known for a particular experimental setup, the size of the corresponding S1 and S2 can be converted from pulse area (Vns), into the number of photoelectrons, *nphe*. The ratio of the VUV scintillation and SPE signal sizes is proportional to the product of the total number of photons produced, *nph*, the QE and the photodetector's light collection efficiency, ϵ:

$$nphe \equiv \frac{VUV}{SPE} \propto nph \cdot QE \cdot \epsilon \tag{3.5}$$

The detector's characteristic sensitivity (phe/keV) and energy resolution, σ(E)/E, can be measured through energy calibration with specific lines of known energy from external sources such as ^{137}Cs, ^{57}Co, ^{60}Co and ^{241}Am. Furthermore, comparison of lines of different energies from one or more sources may be used to investigate xenon (non)linearity, to photons.

The ZEPLIN III PMT Array

A hexagonal close-packed array of thirty-one PMTs, with a pitch spacing of 53 mm, is located within the ZEPLIN III target volume (Figure 3.9).[87] The ZEPLIN III array has an average QE of $\sim$30 % and typical gain of $\sim 10^7$ at 2.2 kV.[114] It is immersed in the LXe phase for maximum light collection (see Section 3.1).

Since the PMT array is situated in the LXe phase it must be able to operate at LXe temperature ($-100\,^{\circ}$C). Hence, the original batch of 35 PMTs were subject to a series of cold tests on the surface, prior to installation inside the target volume (see [114]). The batch was calibrated at low temperature with xenon UV scintillation light.[87] As a result of this work 31 PMTs were selected and their relative placement decided upon (Figure 3.10). The other four PMTs were rejected on the basis of low QE, $d1$ gain, or overall gain or large dark current.

The PMTs' intrinsic radioactivity is expected to generate the largest contribution to the background, mainly due to γ-contamination in the glass body. This will be significantly reduced following the scheduled upgrade whereby these PMTs (Phase I) will be replaced with 31 52-mm diameter (ETL D766QA)[115] low background ones

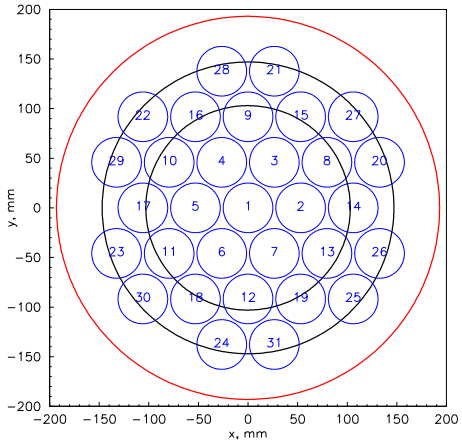

Figure 3.9: The ZEPLIN III hexagonal close-packed PMT array consisting of 31 52-mm diameter (ETL D730/9829Q) high performance PMTs (Phase I). The two black lines represent a fiducial volume of ∼4 kg and ∼8 kg with a radius of 103 mm and 147 mm, respectively. This assumes a target depth of approximately 40 mm. The boundary of the detector target, with a ∼12-kg enclosed full active volume, corresponding to a corrected radius of 193 mm, is also shown.

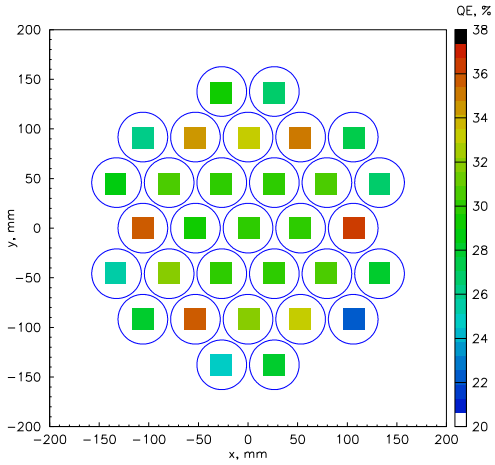

Figure 3.10: The PMT array was constructed with PMTs of relatively high characteristic QE positioned at larger radii, optimising the uniformity of response across the array. This was realised through low temperature calibrations conducted on the surface, prior to the target assembly. The resulting measurements of QE at −100 °C are shown. The square bin entries do not reflect the true, circular response areas of the PMT photocathodes and are an artefact of the histogram plotting.[114]

for Phase II of the science run. The upgrade is expected to decrease the γ-ray contribution to the differential rate by a factor of $\sim \times 35$, to $\sim$0.29 events/kg/day/keVee (see Table 3.1).

ITEM	neutrons/yr >10 keVnr	neutrons/yr 5-50 keVnr	γ dru evt/kg/d/keV	γ evt/yr 2-20 keVee
Rock γs				
n-shield only			25	1314000
			100	5256000
n-&γ-shield			0.001	53
Rock ns				
n-&γ-shield		1.5		
μ-induced ns				
GEANT4 total	0.1			
Solar ν (n+A)				
		$\sim$0	<0.001	
Solar ν (n+e)				
			1.2x10^{-5}	0.6
			2.0x10^{-6}	0.1
γ-shield				
Lead			0.7	36792
		0.04		
Steel boxing			0.06	3104
n-shield				
Polypropylene		0.4		
Radon (air)				
			0.5	26280
Xe				
^{136}Xe			1.00x10^{-5}	0.5
^{85}Kr				
			0.2	10512
PMTs				
D730Q			10.5	551880
	25	44		
		72		
D766Q			0.35	18396
	0.13	0.27		
	0.35	0.80		
		0.8		
		2		
Copperware				
	0.14	0.27		
	0.33	0.63		
Feedthroughs				
	0.9	2		

Table 3.1: The estimated ZEPLIN III itemised background budget. Contributions are grouped into four distinct categories, from top to bottom: *External* (rock γs, ns, μ-induced ns, solar neutrinos), *Shielding* (γ- and n shields, radon), *Xenon* (Xe, Kr contributions), and *Detector Hardware* (PMTs, copperware, feedthroughs). Other items, such as nuts, bolts and cabling, may also contribute to the radioactivity budget but no values are available.[109]

3.4 The Electric Field

For the successful two-phase operation of ZEPLIN III a uniform and sufficiently high electric field should be maintained in three different regions: the *drift field* in the active volume, the *extraction field* at the liquid/gas interface and the *electroluminescence field* in the gas phase.[87]

In the active volume the applied electric field prevents recombination. It separates the ionisation charge released from the track of the interacting particle, drifting the electrons towards the LXe surface. Hence this is termed the drift field. The extraction field must be adequate to extract electrons from the LXe into the gas phase. This field serves to enable the S2 signal. It also prevents charge build-up at the liquid/gas interface. In the GXe, the electroluminescence field is required for the accelerated electrons to produce excitation in the gas atoms.[87]

All three of these distinct field regions are created simultaneously using a single pair of electrodes: the *anode mirror* and *cathode grid*. The anode mirror is a solid, flat, polished copper plate located above the gas gap. The cathode grid is a metal wire plane positioned 35 mm below the LXe surface, within the LXe. At most, 40 kV can be applied between these electrodes, defining the active region (see Figure 3.2).

A second wire plane, the *PMT grid*, mounted just above the PMT array and 5 mm below the cathode grid, is used to create the dual-purpose reverse field region: the S2 from low-energy background photons from the PMTs is suppressed; and the PMT photocathode fields are isolated and protected from the external high electric field.[97]

The electric field determines how much ionisation is extracted from the interaction site, the charge drift time to the LXe surface, the emission probability and location, and the light yield in the GXe.[97]

With 20 kV applied the maximum operating drift field of ZEPLIN III is 4.4 kV/cm (in the LXe). However, the electroluminescence field in the GXe is approximately twice this.[97] Both the field in the LXe and the GXe can be approximated by parallel plate formulae. Within the fiducial volume, a description of the former is given by

$$E_l = \frac{\Delta V}{\epsilon_r L - (\epsilon_r - 1)D} \tag{3.6}$$

where ΔV, ϵ_r, L and D are the voltage difference applied between the electrodes, the

relative permittivity of LXe (ϵ_r=1.96[116]), the electrode separation and the depth of LXe above the cathode grid, respectively.[87] The latter, within the fiducial volume, is simply:

$$E_g = \epsilon_r E_l \tag{3.7}$$

The fraction of charge extracted from the LXe into the gas phase is determined by the E_l component normal to the LXe surface. The S2 signal strength is proportional to the number of charge carriers extracted. Hence, operating ZEPLIN III at high field is crucial for effective particle discrimination.[97]

The Uniform Electric Field

The absence of any physical electrode structure between the anode mirror and the cathode grid in the active volume is an intentional design feature. This aims to prevent any 'surface' effects such as surface charge trapping, embedded radioactivity or photoelectric feedback. The 'open plan' nature of the target volume does however mean that a significantly higher, individual voltage must be used. Thus, the separate fields can not be independently controlled.[87]

The disk-like LXe target extends out beyond the PMT array (340 mm in diameter). The diameter of the electrode structure is ∼400 mm, ensuring the electric fields directly above the PMT array are uniform.[97] The fiducial volume is defined within this uniform field region through application of timing and position cuts. The uniformity in E_l (Equation 3.6) over the fiducial volume is limited by variations in L and D:

$$\frac{\Delta E_l}{E_l} = \frac{\epsilon_r \Delta L + (\epsilon_r - 1)\Delta D}{\epsilon_r L - (\epsilon_r - 1)D} \tag{3.8}$$

Although variations in the electric field affect the S1 and S2 amplitudes as well as the time delay between them the impact on the S2 signal size is most significant.[87]

The Detector Levelling System

Three capacitive sensors are placed around the detector circumference, equidistantly. Simultaneous measurement of these enables ZEPLIN III to be levelled with sub-mm precision (see also Section 3.8). This allows the LXe depth D within the fiducial volume to be known to $\Delta D \sim \pm 500$ μm. Combining this with Equation 3.8 and assuming ϵ_r= 2, L= 40 mm and D= 35 mm corresponds to a fractional variation

in the electric field in the liquid, $(\Delta E_l)/E_l$, of <15 %.[87] Therefore, the operating field in the liquid, E_l ∼20 kV/cm, may vary by up to 0.7 kV/cm.

3.5 Data Acquisition

The thirty-one PMT signals are fed into wideband Phillips Scientific amplifiers[117] and split into a dual range data acquisition (DAQ) system. Sensitivity to both very small S1 (∼few photoelectrons) and comparatively large, unsaturated S2 signals is achieved with the large dynamic range of the low and high sensitivity (LS and HS) channels, respectively.[87]

Electronic gain is added to the thirty-one PMT signals in two stages. All output channels go via the first stage amplifier, with ×10 gain, and thirty-one adjustable attenuators. The Phillips Scientific manual attenuators[118] equalise the single photoelectron response for each PMT given a common HV supply is used. The outputs are then split here where they feed into thirty-one 8-bit ACQIRIS digitisers (LS) and the second stage ×10 amplifiers. Similarly, the outputs from this stage feed into another thirty-one digitisers (HS). Thus, there is a factor of 10 difference in the gain between the HS and LS channels. Adjusting the full-scale ranges of the digitisers can increase this factor further.[87]

For different calibration and background data-sets the LS and HS full-scale (FS) are typically chosen between 0.2-1.0 V and 0.1-0.5 V, respectively. However, for single photoelectrons (SPEs) the LS and HS FS are considerably smaller at 0.05 V.

All sixty-two channels are sampled at 500 MS/s by the digitisers with 2 ns sampling. In total, sixty-four channels are sampled, with the additional two being SUM LS and HS channels.[87] The acquired data-sets are all labelled according to the YYMMDD convention, i.e. 070316 refers to a data-set acquired on 16^{th} March 2007.

Initially, before the DAQ was fully operational, a multi-channel analyser (MCA) was used to read out individual PMT signal channels during surface operation at the Imperial College London laboratories. This was accompanied by pulse height analysis. During the latter stages of surface operation this was superseded by a WINDOWS-based software application used to read out the digitiser crates. This was, in turn, upgraded to a LINUX-based one prior to deployment underground. Two different voltage dividers (#1 and #2), supplying power to the PMT array, have been used at different stages. In order to reduce data rates to more manageable

levels, a cut on signals saturated in LS channels has been implemented. This is performed in software before writing to disk and when 'on' the DAQ application rejects events with ten consecutive time samples (20 ns) saturated in LS. The various DAQ hardware configurations used at different phases of instrument operation are detailed in Figures 3.11-3.15.

An external threshold trigger signal for the ACQIRIS digitisers is derived from the output of the HS SUM amplifier, with inputs from all PMTs, and fed into a discriminator.[87] For acquisition of all data types, excluding SPEs, the external trigger mode is used. For each PMT, SPEs are acquired by internal triggering on the corresponding PMT channel.

In order to synchronise the triggering of channels within all three of the ACQIRIS crates a logic 'veto' signal is used. This is powered through the parallel port on the DAQ computer and was developed by the author. It inhibits the trigger before all of the crates and the DAQ computer are ready to acquire data.[119] The DAQ can support a data acquisition rate of 100 events/s.[87]

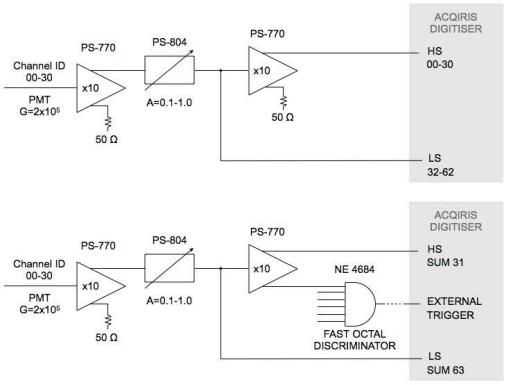

Figure 3.11: Schematic of the ZEPLIN III DAQ circuit for the acquisition of surface data at the Imperial College London laboratories (pre-061206) with voltage divider #1: individual HS and LS channels (upper panel); HS and LS SUM channels (lower). Details of the trigger, a logic 'veto' signal derived from the DAQ computer, are not included here.

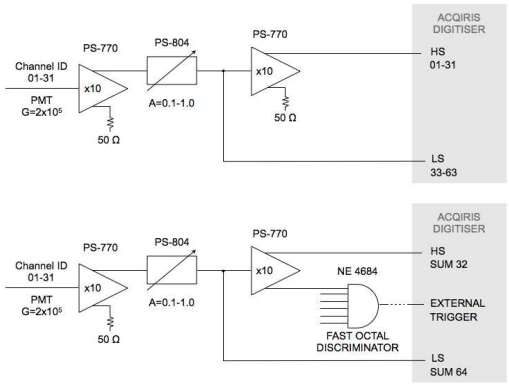

Figure 3.12: Schematic of the ZEPLIN III DAQ circuit for the acquisition of underground data, post deployment (070316-070614) with voltage divider #1 and a cut on signals saturated in LS (from 070306 onwards): individual HS and LS channels (upper panel); HS and LS SUM channels (lower).

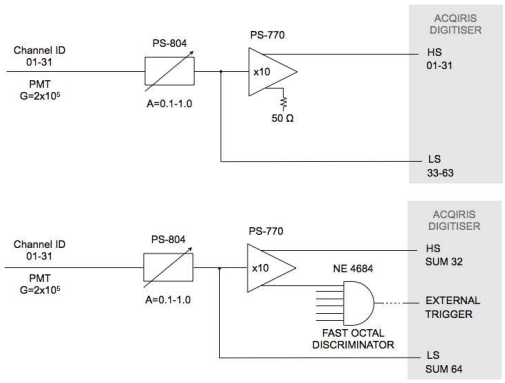

Figure 3.13: Schematic of the ZEPLIN III DAQ circuit for the acquisition of underground data (070614-070723) with voltage divider #2 (from 070717 onwards) and a cut on signals saturated in LS: individual HS and LS channels (upper panel); HS and LS SUM channels (lower).

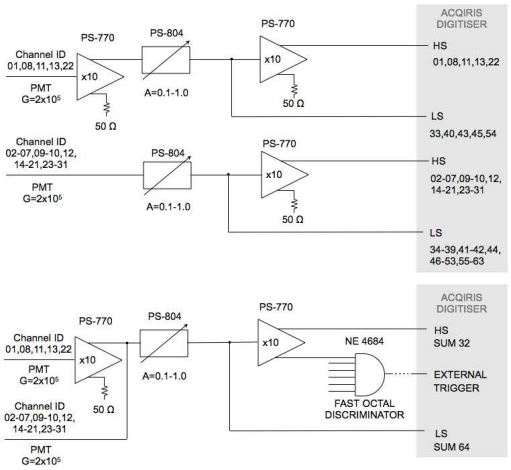

Figure 3.14: Schematic of the ZEPLIN III DAQ circuit for the acquisition of underground data (070723-080304) with voltage divider #2 and a cut on signals saturated in LS: individual HS and LS channels (upper panel); HS and LS SUM channels (lower).

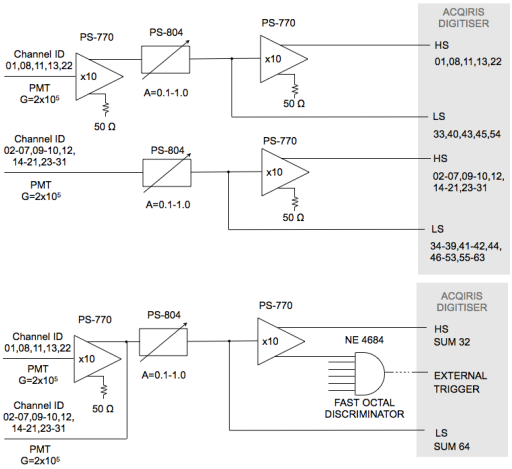

Figure 3.15: Schematic of the ZEPLIN III DAQ circuit for the acquisition of underground science data, first run (080304-present) with voltage divider #2 and a cut on signals saturated in LS: individual HS and LS channels (upper panel); HS and LS SUM channels (lower).

Reduction & Analysis Software

The purpose-built ZEPLIN III reduction and analysis software, ZE3RA[120], successfully identifies and characterises acquired pulses. It enables the individual pulses to be identified using baseline correction, adaptive running average smoothing, pulse matching and cluster algorithms. Also, ZE3RA allows users to visualise acquired raw data and results from reduction analyses in a graphical mode. The ZE3RA code was written by the ZEPLIN III Coimbra group.

The reduction process is where information in the raw data files is extracted and used to produce a set of quantities for subsequent use. The form of the reduced data has an ntuple structure that is compatible with Physics Analysis Workstation (PAW)[121] for post-processing data analyses. The ZE3RA output parameters used to characterise the pulse shape are illustrated in Figure 3.16.

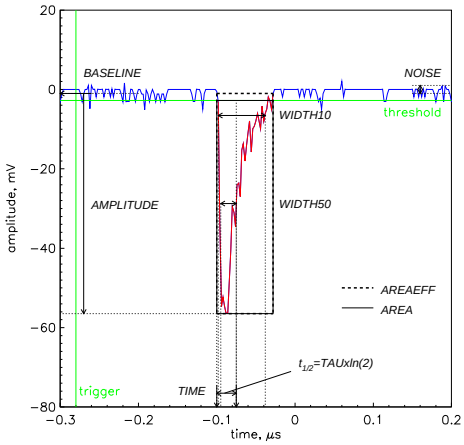

Figure 3.16: Typical scintillation pulse (or event) acquired in the LS SUM channel. Parameters used to characterise the pulse shape in post acquisition reduction and analysis software are also shown. The $AREA$ and $AREAEFF$ parameters differ in that calculation of the latter includes summation over both positive and negative bins. Note that this TAU relation (Equation 3.9) only holds for an exponential pulse shape.

ZE3RA is capable of handling all data types relevant to ZEPLIN III including calibration, background and SPE data. Reduction with ZE3RA demands the input of several parameters such as *pre-trigger* and *threshold* which are adjusted accordingly.

The pre-trigger ZE3RA parameter is defined as the percentage of the DAQ delay time that is used to calculate the baseline mean and rms. The threshold defines the

level below which the negative going signal is considered to be pulse-like.

The ZEPLIN III *golden code* is essentially a series of FORTRAN functions which act on the reduced ZE3RA ntuples, enforce *the golden rule* and produce *golden ntuples*. The code simplifies and eases the data analysis procedure which is complicated by the two dynamic DAQ ranges. It does this by acting as a filter, retaining only 'good' events. Such events would contain a single valid S1 and a single valid S2. In addition, it is particularly useful for calculating efficiencies.

The golden code contains: all analysis cuts; all selection rules, including the position reconstruction algorithm(s); and input and output file handling. Cuts are applied to the reduced data in a first- (coarse) and second-pass (fine). These are performed on the ZE3RA output ntuple flags, or parameters, such as pulse *AMPLITUDE*, *AREA* or *WIDTH50* (full width half maximum, FWHM) and can be fine tuned according to the specific data type and experimental configuration.

Iterative versions of the ZE3RA reduction software and the golden code processing software were developed during both surface and underground instrument operation. Improvements made to ZE3RA, from v1 to v2, included upgrading the raw data smoothing, pulse matching and (small) pulse clustering algorithms and introducing an algorithm for baseline reconstruction/correction. The evolution of the main features of the golden code is summarised in Table 3.2.

	Golden Code
v05	23 basic ntuple pulse parameters ntuple parameters for first 5 pulses in each timeline centroid position reconstruction algorithm
v10	accounts for PMT after-pulsing (ion feedback)
v11	centroid and template position reconstruction algorithms correction and calibration for energy spectra Xe purity (lifetime) correction
v15	flat-fielding, SPE and QE coefficients PMT#31 killed (pulse area set to 0) DAQ/ZE3RA time-stamps for event (DAQ readout time) slow control time factor charge going into scintillation data-quality cuts (voltages, fields)
v20	flat-fielding coefficients revised summary information on data-set (exposure, etc)
v21	ntuple parameters for first 10 pulses in each timeline set day '0' for first science run (FSR) data to 27th February 2008 Xe purity, detector levelling and tilt correction factors
v22	first pass energy cut reducing number of events for some data-sets light collection correction arrays to correct S1 and S2 pulse area S1 depth-dependent light collection correction revised SPE mean area values
v23	HS/LS pulse time consistency checks S1 and S2 area saturation cuts after-pulsing cut remove S1 depth-dependent light collection correction
v24	disallow S1 events in last place (#10) on ntuple S2 area: LS used when HS saturated and pulse not too small
v25	105 ntuple pulse parameters S1 and S2 HS-LS integration parameters centroid, template and least-squares position reconstruction algorithms

Table 3.2: Summary of the main developments in versions of the golden code analysis software.

Time Constant Analysis of S1 Pulses

Nuclear recoil S1 pulses have a shorter characteristic time constant than that of electron recoils, at zero-field. This difference is lessened as the applied E-field is increased as the electron recoil time constant reduces due to less recombination. The time constant can be characterised by: the mean arrival time (relative to the first photoelectron) at the photocathode; the interpolated median time; the rise time

to reach some chosen percentage of the maximum amplitude; or the best fit to an exponential rise.[17]

Considering the mean arrival time approach, the time of arrival of half the total number of photoelectrons at the photocathode, $t_{1/2}$, corresponds to half of the total integrated pulse area. This is related to the mean arrival time, τ, (or pulse width) according to

$$\tau = t_{1/2}/ln(2) \tag{3.9}$$

Here τ is the characteristic decay time constant in a single exponential approximation. This is the characteristic time quoted in the literature, by convention, and is one of the ntuple flags output by the ZE3RA reduction software (TAU).

For completion, the time constant of S2 pulses is determined by the drift time across the xenon gas gap and exceeds that of S1.

3.6 Shielding & Veto Principles

During the early commissioning period the ZEPLIN III instrument was located on the Earth's surface, at the Imperial College London laboratories. In this scenario, no detector shielding or veto system was implemented. The lead γ-shielding, or 'castle', should only be considered an integral detector component from the start of Phase I of its underground operation onwards. In contrast, the veto is to be retrofitted 19 months after deployment, coinciding with the PMT upgrade.[1] Therefore, its performance is only relevant for Phase II of the underground science run.

Background Sources & Underground Operation

The ZEPLIN III detector is deployed in an underground laboratory in the Boulby salt and potash mine. It is located at a vertical depth of 1070 m (2805 m water-equivalent shielding).[57]

The cosmic-ray muon flux and the radioactive decay of the cavern rock (mainly NaCl) and detector components (U/Th decay chains) all contribute to the nuclear recoil background in the underground laboratory environment. The neutron pro-

[1] The ZEPLIN III instrument was deployed to the Boulby Underground Laboratory, North Yorkshire, UK, arriving underground on 6th December 2006. Disassembly of the shielding systems and LXe target, along with the PMT upgrade began on 1st July 2008.

duction associated with the radioactive decay in the rock walls dominates over those produced through cosmic-ray muon spallation.[97] This level of neutron background is unacceptable for a dark matter detector, motivating the installation of a passive hydrocarbon neutron shield around the detector, inside the lead γ-ray shield.

Deep underground operation reduces the cosmic-ray muon flux by a factor of $\sim 10^6$ to a level $(4.09 \pm 0.15) \times 10^{-8}$ muons cm^{-2} s^{-1}[122] thereby significantly reducing muon-induced, nuclear recoil background contributions. Nevertheless, muons interacting in the detector materials and the cavern rock still generate a few neutrons.

The third source of nuclear recoil backgrounds is from the detector components and this was minimised through the choice of detector manufacture materials. Additionally, the active neutron veto, rejecting approximately solely such events, will provide a diagnostic for these events in Phase II.

There are two internal and two external sources of electron recoil backgrounds in the ZEPLIN III experiment. The former are due to: γ-rays from ^{40}K and from the ^{238}U and ^{232}Th chains, emitted from the PMTs, mainly from the glass, at a predicted low-energy rate of 10 dru (differential rate unit, 1 event/keV/kg/day) during Phase I (see Table 3.1); and β-decay of ^{85}Kr contamination of the xenon target[97]. The external sources arise from short-lived γ emitters (^{214}Bi and ^{214}Pb) from ^{222}Rn and its progeny found in the air around the detector; and from the γ-rays emitted by the cavern walls.[97]

Sourcing old xenon for the target volume reduces the background contribution from ^{85}Kr ($T_{1/2}$=10 yr) to the relatively small level of $\sim$5 ppb ^{85}Kr contamination. This corresponds to a simulated rate of $\sim$0.1 dru at low energies. The ^{222}Rn γ background level is believed to be comparable to this.[97]

The average radioactive contamination of the Boulby rock is 67 ppb U, 127 ppb Th and 1300 ppm K, from measurements conducted prior to deployment.[123] The 15-cm thick lead passive shield, or castle, should attenuate the γ background to $<$0.01 dru.[123] Thus, the overall electron recoil background level, for the shielded detector in Phase I, is calculated to be $\sim$10 dru.

Passive Shielding

The ZEPLIN III instrument is surrounded by an inner 30 cm thick polypropylene neutron shield and an outer 20 cm Pb γ-ray shield.[124] These are necessary to at-

tenuate the neutron and γ-ray backgrounds from residual muons and radioactivity in the cavern walls, respectively.

The lead γ castle is constructed from blocks of high-purity lead, cast within steel casing, and fully surrounds the detector. The hydrocarbon neutron shield consists of solid hydrocarbon blocks (with 20-30 g cm^{-2}).This is believed to attenuate the neutron flux from the cavern walls to $\sim$1 nuclear recoil yr^{-1}. Similarly, the neutrons from the muon flux interacting in the detector materials or in the rock are attenuated to $\lesssim$1 single nuclear recoil yr^{-1} (above 10 keVnr, in a 8 kg fiducial volume).[97]

Active Veto System

The active veto will record neutrons in coincidence with the target. These are neutrons which might be generated from the radioactive decay of detector components since the veto sits within the detector shielding. Most internal neutrons will scatter in the LXe target and then either pass into or through the scintillator veto, producing a signal. A veto efficiency of 50 % for internal neutrons is predicted and within one year of operation the veto, together with the upgraded PMT array, is expected to improve the detector's sensitivity to WIMPs, down to 10^{-9} pb.[97]

An effective veto system should not generate significant additional background itself and should provide 4π detector coverage. The goal to minimise the veto's intrinsic background contributions naturally demands for the minimum number of PMTs to be used, while maintaining as low an energy threshold as possible and maximising light collection. In addition, a high efficiency, for both neutrons and γ-rays, is a key requirement.

The ZEPLIN III cylindrical veto system consists of two elements: thirty-two Gd-loaded sections, each of five sheets of 30-mm thick hydrocarbon and thirty-two PMT/plastic scintillator slab sections. Gd-loading is employed to enhance the neutron efficiency, capturing neutrons and releasing detectable 8 MeV γ-rays. Within the PMT/slab sections, a total of fifty-two 78-mm diameter PMTs (ETL 9302 KB)[125] are used to observe the scintillator.

In addition to neutrons, the veto also records signals from cosmic-ray muons. These can further assist in rejection of the muon-induced background and simulations suggest a γ-ray veto efficiency of $\simeq$70 % is achievable.[126]

3.7 Monte Carlo Simulations: *ZepIII*

ZepIII is a GEANT4-based Monte Carlo (MC) tool developed for realistic simulations of the ZEPLIN III detector performance. It is required to: model the path and interactions of particles both internal and external to the detector, down to the production of electron and nuclear recoils; simulate the physical processes involved in the generation of the optical response to scintillation and electroluminescence; generate the electrical response for all channels; allow the operating parameters to be easily modified by the user and be user friendly.[97] A non-exhaustive list of typical ZepIII user-defined input parameters includes the incident particle type, energy, position and direction, the LXe depth and the applied electric field.

ZepIII can be run in two modes, batch or interactive, with either the *full* or *light geometry* implemented. The full geometry includes most detector components above the LN_2 vessel and up to the dome of the outer vacuum vessel and is used for intensive calculations. The energy and polarisation of optical photons, generated by scintillation and electroluminescence, is taken into account by optical tracking (ray tracing) within an optical model of the detector. The reduced or light geometry only describes the (optically) active region defined between the PMT photocathodes and the anode mirror. This less computationally demanding option is used, for example, in light collection calculations.[97]

In the standard version of ZepIII the PMTs, LXe and GXe zones, electric fields, electrode grids and the DAQ are all modelled. However, neither the scintillator veto system nor the hydrocarbon and lead shielding are represented. These were subsequently appended.

For each event, *hits* and *optical hits* are recorded, corresponding to energy deposition in the xenon target and in the PMT array, respectively. These are then output to an ascii file for future analysis or stored in ntuples and histograms. For each event a position reconstruction (template[108]) algorithm is invoked.[97]

The following information is contained in the output file: event number; primary particle type and energy; number of hits in the LXe; total energy deposited in the LXe; x, y and z positions of the first hit in the LXe; total number of hits in the PMT array; number of primary and secondary hits; time between the first and secondary signals; PMT with the highest score and the associated number of hits; number of hits in a 7-PMT cluster, centered on the PMT with the highest score;

the reconstructed x and y event co-ordinates; and the random event seeds.[97]

Some key primary zero-field optical response, $S1_{zero-field}$, or *light yield* (LY) results from ZepIII are summarised in Table 3.3.

t_{GXe}, mm	t_{LXe}, mm	μ_{LXe}, cm	R_m, %	$S1_{zero-field}$, phe/keV
5	35	34.6	15	3.4
5	35	34.6	90	4.2
0	40	34.6	15	2.3
0	40	100.0	15	4.0

Table 3.3: Summary of results of MC simulations of the primary zero-field optical response for various configurations, all assuming a photon yield of 60 photons/keV (compiled from [97]). A copper reflectivity of 15 %, LXe refractive index of 1.69 and average PMT quantum efficiency of 30 % are also assumed[97]. The GXe and LXe thickness' are given by t_{GXe} and t_{LXe}, while μ_{LXe} and R_m denote the LXe absorption length and mirror reflectivity, respectively. The $S1_{zero-field}$ figures where R_m=15 % relate to a more conservative case. The lower half of the table describes a full detector target, with no gas gap.

ZepIII has been used to assess the local background contributions from instrument components and calculate particle event rates both pre- and during the design phase. Furthermore, ZepIII generated realistic data-sets, which proved crucial in the planning of the DAQ electronics and data analysis software.

The ZepIII model promises to be essential at the post design phase too, during data acquisition, and even beyond the science run. Here, simulated data-sets can be compared and contrasted with acquired data in order to confirm, or question, our understanding of the detector physics and, more generally, xenon physics. Comparisons of simulated and real calibration data are detailed throughout Chapters 4 - 5.

For a more thorough description of the ZepIII tool and full performance simulations for the ZEPLIN III instrument, see [97].

3.8 Instrument Monitoring

Due to the continuous development of both the hardware and software systems, from the initial point of instrument construction through to acquisition of the science data post upgrade, the configuration of the ZEPLIN III experiment has evolved greatly.

Operating parameters (such as the target temperature and pressure, xenon purity and detector levelling) and DAQ parameters (such as the DAQ rate and cumulative exposure) were monitored throughout the surface and underground runs and, more rigorously, during the science runs. The evolution of some parameters during the first science run (FSR) is shown in Figure 3.17.

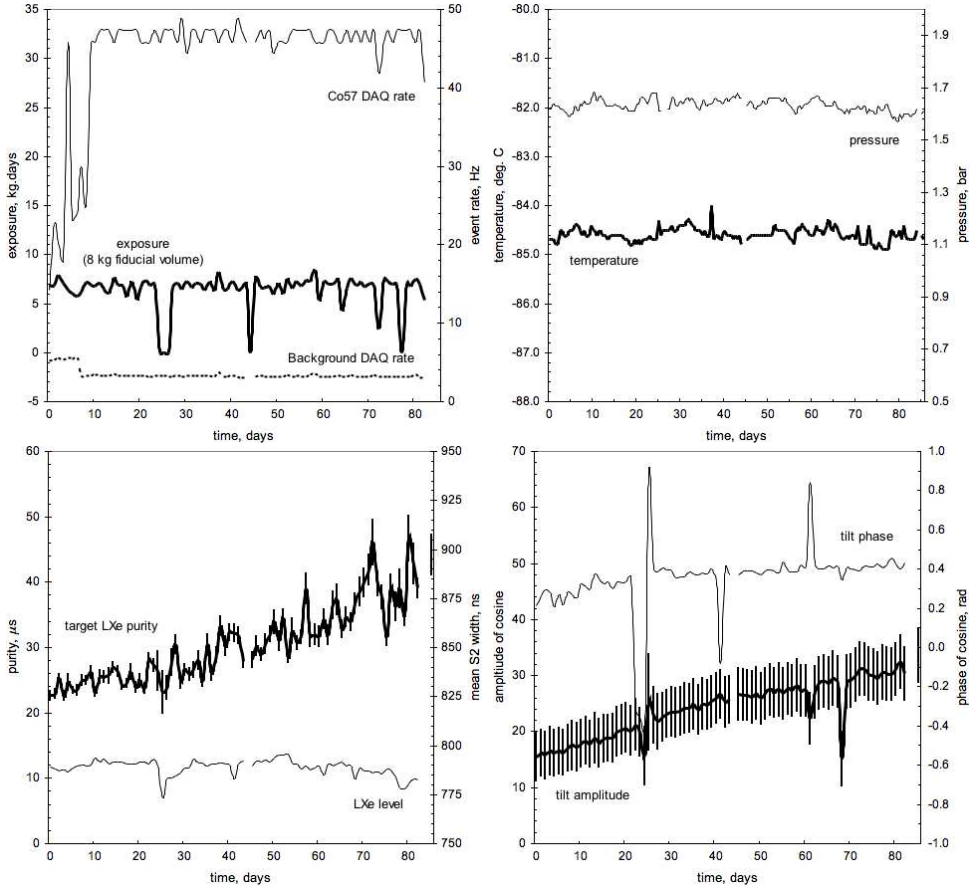

Figure 3.17: The evolution of some typical DAQ monitoring (upper left panel) and detector operating (remaining panels) parameters with time, t. The x-axis spans the underground first science run (FSR) phase where, here, t=0 is defined as 29th February 2008.

The locations of the feedthroughs for the high voltage supplies and environmental monitoring and the GXe and cryogenic connections are indicated in the ZEPLIN III structure diagram (Figure 3.18). These are shown to emerge through the bottom of the target and vacuum vessels and pass through the shielding systems.[87] Temperature sensors are also used to monitor critical points.

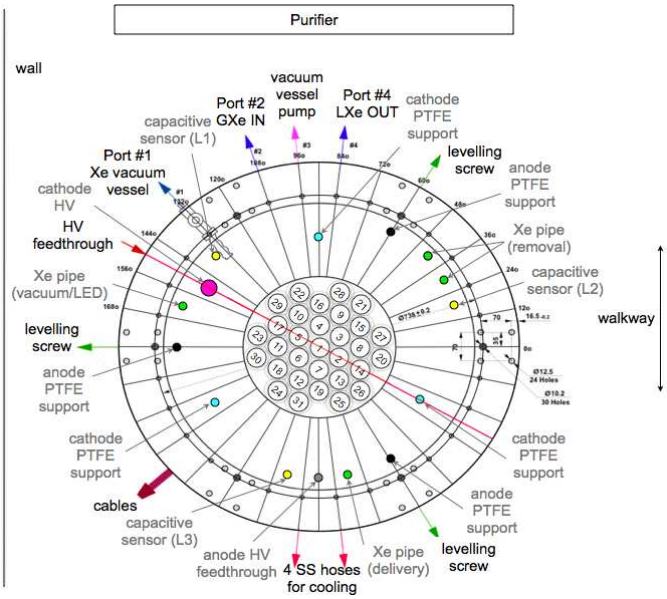

Figure 3.18: ZEPLIN III structure diagram detailing the location of the PMT array with respect to connections to/from the target and vacuum vessels and key components. The instrument's orientation relative to the underground laboratory environment is also shown. Adapted from [127]

Slow Control

The *slow control* system was developed to enable automatic readout and logging, every ∼60 s, of the: temperature (*T1-T16*), capacitive level (*L1-L3*) and environment sensors; the purifier, 'dumps' and target pressure transducers; and high voltage data. It also offers some safety features including being capable of raising the pressure alarm, monitoring the vacuum jacket and purifier vacuum probes, automatically updating (ramping up/down) the high voltage supplies and managing the LN_2 reservoir filling.[128]

The LXe target is maintained at the constant temperature of -97 ^{o}C by LN_2 and heaters (for thermal stability). The LN_2 reservoir sits directly below the target, containing up to 36 litres of LN_2 and the maximum time between refills is ∼2 days.[87]

The ZEPLIN III target vessel, vacuum jacket and the dumps (the large-volume safety reservoirs) are certified to 6.0, 4.3 and 6.0 bar absolute, respectively. The vacuum jacket, pumps and purifier system can be evacuated down to $\sim 10^{-8}$ mbar.[87]

The environmental parameters monitored by the slow control are the ambient tem-

perature and pressure measured in the underground laboratory, outside of the detector and shielding systems but in close proximity to the ZEPLIN III instrument. These are typically ∼1.16 bar absolute and ∼25-30 ^{o}C, respectively and are stable except for, on the rare occasion, when the Boulby mine fans are switched off.

Chapter 4

ZEPLIN III Surface Data

Prior to ZEPLIN III being deployed underground, two commissioning phases, or cool-down tests, took place in the surface laboratories. During this time the detector was fully operational (although unshielded) and surface commisssioning data were acquired in various setups. These tests were necessary to have confidence in the readiness of the instrument for deployment in anticipation of the science runs.

Analyses of these data were performed with the aim being to: validate the detector functioning; characterise its response in terms of the light yield and single photoelectron spectra; assist in the development of the DAQ readout, reduction and analysis pipeline; demonstrate a 3-D position reconstruction sensitivity; and verify the critical particle discrimination principle.

For distinction, details of all analyses conducted with these surface commissioning data are confined solely to this chapter. All subsequent chapters refer to data-sets acquired underground post-deployment, during more extensive preparatory studies.

4.1 Surface Operation

The first cool down test was designed to test the response of the PMT array and verify the thermal control system. Thirty-one ^{241}Am γ-sources were mounted inter-

nally directly above the PMTs allowing an artificially-enhanced light collection to be measured. These were removed and the full electric field system was installed in its final configuration on entering the second commissioning phase. Additional cool down tests followed, confirming successful two-phase operation.

Pulse height spectra, pulse waveforms and single photoelectron spectra were collected from, initially, a couple and later, all PMTs during the first cold run both with the DAQ electronics (ACQIRIS digitiser and a Windows or Linux DAQ programme) and with a multichannel analyser (MCA), utilising pulse height analysis (PHA). The instrument was operated with: no applied electric field and no GXe gap (single-phase); no applied electric field and ∼2-5 mm GXe (dual-phase); an applied electric field and ∼2-5 mm GXe (two-phase). The DAQ configuration was just a linear amplification setup with no attenuator present for these early tests, prior to the PMT outputs being normalised.

The data reduction and analysis pipeline, in place post-deployment, was not available at this time. Instead, the raw data files were 'reduced'; that is the event parameters calculated and output to PAW *ntuples*, entirely within PAW code, developed by the author. Within these, five parameters, *TAU, AREA, BASELINE, WIDTH* and *AMPLITUDE* characterise PMT response on an event-by-event basis.

A simplistic pulse-finding algorithm was invoked within the PAW reduction code where the pulse parameters are defined as:

$$BASELINE = \sum_{i=1}^{45} A(t)_i/45 \tag{4.1}$$

$$AMPLITUDE = A(t)_{min} - BASELINE \tag{4.2}$$

$$AREA = \sum_{i=t_{start}}^{t_{end}} (A(t)_i - BASELINE) \cdot (t_{i+1} - t_i) \tag{4.3}$$

$$TAU = (AREA/2)\,/ln(2) \tag{4.4}$$

$$WIDTH = t_{end} - t_{start} \tag{4.5}$$

and $A(t)_{min}$ is the minimum amplitude value across all bins, i. Here, $A(t)_{min}$ and not $A(t)_{max}$ is used since the signals are negative going pulses. Some small threshold voltage value, $A(t)_{thresh}$, ≤0.01 V below the calculated baseline was defined in order to determine the start and end times of the pulse, t_{start} and t_{end}, respectively. These are given by:

$$t_{start} = i - 1 \qquad i > 0;\ A(t)_i < A(t)_{thresh} \tag{4.6}$$

$$t_{end} = i \quad i > t_{start};\ A(t)_i \geq A(t)_{thresh}; \tag{4.7}$$

$$A(t)_i \geq BASELINE \tag{4.8}$$

The Windows DAQ and the author's reduction code were upgraded to a Linux DAQ programme and the ZE3RA reduction code (see Section 3.5), respectively, for the later stages.

4.2 Commissioning Phase I: Single-Phase Operation

Replacement of the anode and cathode electrodes by a copper plate 5.5 mm above the array enabled thirty-one ^{241}Am radioactive sources to be vacuum-sealed, one above each PMT (Figure 4.1). A thin copper foil overlay was also incorporated into this plate to prevent α-particles from interacting in the xenon target. The ^{241}Am internal sources (0.8 μCi, 0.3 MBq) delivered low-energy photons (main line at 59.5 keV[129] with 35.9 % intensity) to the target volume. Mounted in close proximity to each PMT, the sources allowed the response of every PMT to be tested and measurement of an enhanced S1 LY to be carried out.

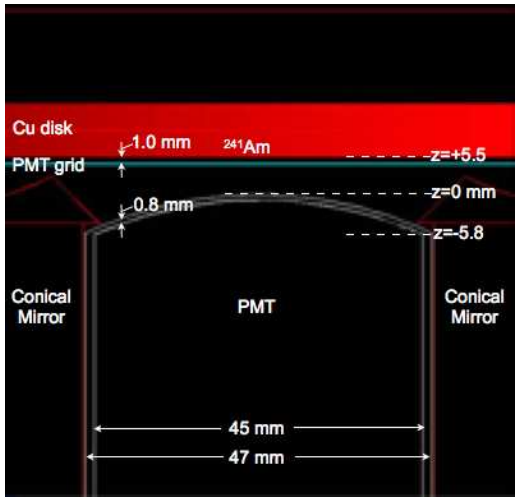

Figure 4.1: Schematic adapted from the GEANT4 ZepIII code showing the location of the temporary, internal ^{241}Am sources above each PMT. The Cu disk is positioned 1 mm above PMT grid. Each ^{241}Am source is vacuum-sealed 120 μm within the Cu disk covered with a thin Cu foil overlay. The distance between the top of the PMT window and the source is 5.5 mm.[130]

4.2.1 Xenon Linearity

The 051207 surface zero-field background data-set was acquired with the Windows ACQIRIS DAQ and with the ^{241}Am sources mounted internally in the LXe, with no external Am-Be n-source present. The response of a single PMT (#11), with relatively high QE (32%), was examined to determine which spectral features could be resolved and to study the linearity of response, or not, exhibited by the xenon target.

Comparison of the single-phase (no GXe gap, with poor LXe purity $\sim$ ns, not $\sim \mu$s) experimental integrated pulse area (Vns) or energy spectrum (at PMT high voltage of -2.0 kV) with the equivalent high-statistics MC simulation[130] run (at PMT HV of -1.9 kV), following normalisation of number of events and energy calibration with respect to the 59.5 keV[129] (14.9 % full width half maximum, FWHM=$2.35\sigma/\mu$) ^{241}Am γ-ray line, is shown in Figure 4.2.

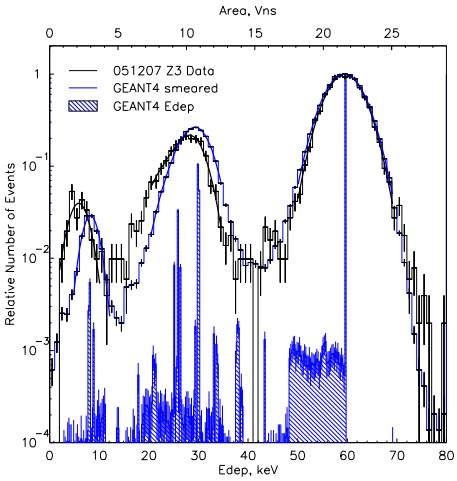

Figure 4.2: Comparison of the experimental (PMT #11 operated at -2.0 kV) and MC simulated[130] (at 1.9 kV) S1 energy spectrum, with thirty-one ^{241}Am sources mounted within the LXe. Both axes (relative number of events, energy deposited in LXe) are normalised with respect to the 59.5 keV γ-ray line. Single Gaussian functions fitted to the symmetric 59.5 keV and 8 keV lines, and two linearly-combined Gaussians to the blended feature, are also shown. Note that a saturation cut ($AMPLITUDE$ >-0.9 V) and a SPE cut ($AREA$ <-1 Vns) are applied, post-acquisition.

In the ZepIII simulation the Np X- and γ-rays are generated individually and isotropically 120 μm inside the Cu holder without the scintillation tracking invoked. Inputs of ZepIII include: a scintillation yield of 60 photons/keV; scintillation Fano factor

F=1.0; PMT QE=30%, subsequently scaled up to 32% for the case of PMT #11; and considering a vertical source-to-photocathode separation of (5.5 mm + 5.8 mm - 0.8 mm) ≈10 mm. The ZepIII simulation output energy spectrum (Figure 4.2) has been smeared with a Gaussian (σ=0.5).[130]

Features of both spectra include: the ^{237}Np daughter 59.5 keV, 26.3 keV[129] (2.40 % intensity) and 33.2 keV[129] (0.126 % intensity) γ-ray lines. The latter two appear merged, unresolved. The ∼8 keV[131] Cu Kα X-ray line can also be seen here. Single Gaussian functions are fitted to the two symmetric (8 keV and 59.5 keV) lines, in turn. Two linearly-combined Gaussians are used to fit the blended, asymmetric feature. The 13.9 keV[129] (9.6 % intensity) ^{237}Np daughter X-ray line is evident.

Conclusions regarding the linearity of xenon, at low energies, can be drawn from Figure 4.2. With respect to the 59.5 keV line, the 8 keV line is expected to appear at 2.886 Vns. However, this feature actually appears at 5.85±0.25 keV (2.109±0.091 Vns). Thus, xenon appears to behave non-linearly to within 36.8%, down to 8 keV, where

$$non-linearity(\%) = 100 \cdot \frac{(E_{exp} - E_{meas})}{E_{meas}} \quad (4.9)$$

$$e(non-linearity)(\%) = \sqrt{2}\left(\frac{e(E_{meas})}{E_{meas}}\right) \cdot non-linearity(\%) \quad (4.10)$$

Therefore, it is reasonable to conclude that the 8 keV line is non-linear with respect to the 59.5 keV line (see Figure 4.3). It should also be noted that the 26.3-33.2 keV feature (expected at 26.7 keV) is linear with respect to the 59.5 keV line to within 8.3%.

The non-linearity of the 26.3-33.2 keV feature with respect to the 59.5 keV line can be assessed further, analytically, using the model detailing the conversion of radiation energy in Xe presented in Reference [132]. Since the incident 26.3-33.2 keV photons (26.7 keV weighted average) have energy less than the Xe K shell binding energy (at 34.56 keV[133]), they only produce the photoelectric effect in the L_I shell (at 5.45 keV[133]). A vacancy in the L_I shell is then filled by an electron in the L_{II} shell (at 5.10 keV[133]), emitting an 0.35 keV (=5.45-5.10 keV) X-ray photon. This is accompanied by the emission of an Auger electron (with energy 4.78 keV[133] from the L_{III} shell). Thus, for incident 26.3 keV photons, the energy of the ejected L_I shell photoelectron is 20.85 keV (=26.3-5.45 keV) and similarly, for 33.2 keV photons it is 27.75 keV (=33.2-5.45 keV). For the 59.5 keV incident photons, the energy of the ejected K and L_I shell photoelectrons are 24.94 keV (=59.5-34.56 keV) and

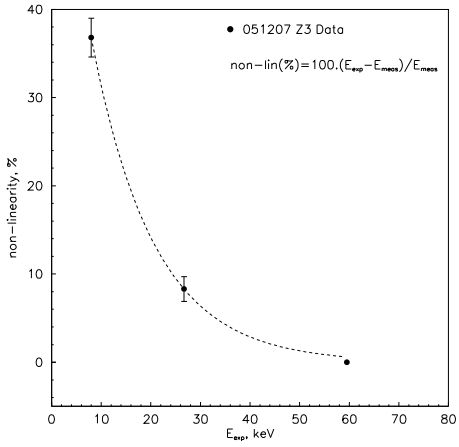

Figure 4.3: The percentage non-linearity in measured response E_{meas}, as a function of the known or expected deposited energy, E_{exp}, for four features of the acquired energy spectrum in the 051207 data-set: 8 keV Cu Kα X-ray; 26.3-33.2 keV ^{237}Np daughter γ-ray blended lines, with centroid at 26.7 keV; 59.5 keV ^{237}Np daughter γ-ray line. The y-error bars on the data points are derived from the error on the means, not the standard deviation of the distributions. The 8 keV line actually appears at 5.85±0.25 keV. Thus, with respect to the 59.5 keV line, the xenon target exhibited linearity to within 36.8%, down to 8 keV.

23.66 keV (=29.11-5.45 keV, where 29.11=34.56-5.45 keV), respectively. This yields a total deposited energy of 58.48 keV (=24.94+5.10+23.66+4.78 keV), implying an energy non-linearity of 1.74% (=(59.5-58.48)/58.48) which is inconsistent with the significantly larger value of 8.3% obtained above.

The thirty-one ^{241}Am source measurements at zero-field first demonstrated that all thirty-one PMTs were working and that there was a non-linearity in S1 response of a LXe target to the photoelectric absorption of γ-rays at low energies. However, this discovery was not considered conclusive at this stage since the ZEPLIN III instrument, the DAQ and the data pipeline were all in the early, unrefined commissioning phases and not fully understood. Nevertheless, the implications of such a finding should not be underestimated. This result may indicate the production of less light than expected for lower deposited energies i.e. an energy-dependent quenching factor or scintillation yield; an effect later confirmed within the with-field first science run (FSR), underground and shielded data-set (see Chapter 6).

Repetition of the tests described here, and other enhanced LY configurations, are proposed to be conducted with a better understood instrument, in a more systematic way, post deployment.[134]

4.2.2 Time Constant Analysis: Variation as a Function of Energy

The characteristic decay time constants, τ (ns), of individual S1 pulses in one PMT with high QE (i.e. PMT #11) were studied at zero-field as a function of energy using the mean photoelectron arrival time method (Equation 3.9) and the same data-set as that used to probe xenon linearity.

An S1 pulse from a low-energy γ-ray emitted by an ^{241}Am source, with a characteristic decay time of 40.4 ns is shown (Figure 4.4). For comparison, examples of typical 8 keV pulse and an SPE pulse (see Section 4.2.2.1), with characteristic decay times of 26.0 ns and 2.9 ns, respectively, are also shown.

S1 time constant distributions, for various energies, were compared by slicing the spectral response in energy (Figure 4.2), with slices centred on each of the peaks (see Figure 4.5). Here, the bin widths were optimised to avoid the inherent digitisation of the data, due to the sampling rate, from dominating or skewing the distributions. Single Gaussian functions were fitted to the time constant distributions associated with each energy slice, centred on the expected spectral features, although the fit to the $0 < E(keV) \leq 15$ slice is clearly poor. This investigation suggests that a higher energy slice yields a longer mean time constant.

Using this energy-slicing method two additional, finer slices were analysed. For comparison with published decay time constants of electron recoils in LXe[135] of 29.1±0.6 ns[135] at ∼13.5 keV and 34.0±0.6 ns[135] at ∼37.5 keV, these were chosen to be $12 < E(keV) \leq 15$ and $36 < E(keV) \leq 39$. The fitted means of the corresponding time constant distributions are 30.41±2.40 ns and 36.67±1.66 ns, respectively, where the errors quoted are those returned by the Gaussian fits. Figure 4.6 shows the comparison of these two, finer slices with the study in Reference [135] along with the associated values of the three coarser bins (Figure 4.5): The results are consistent.

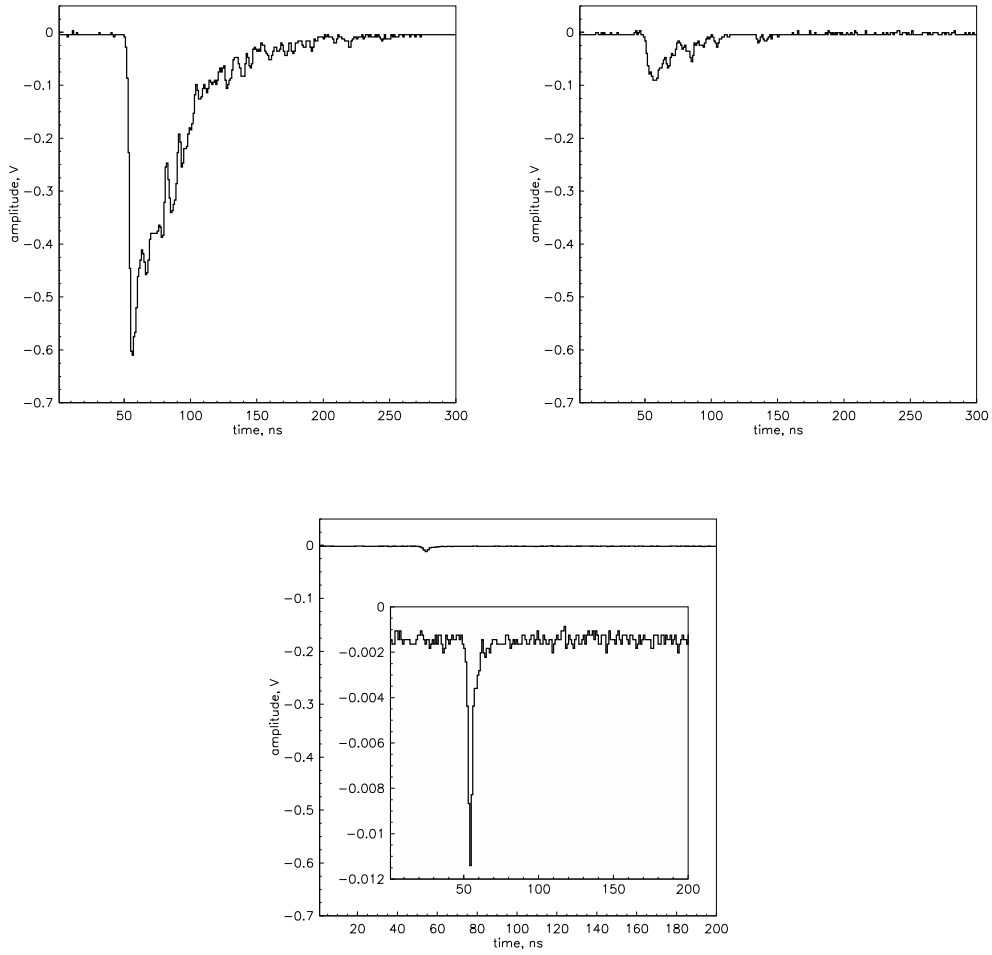

Figure 4.4: Typical primary scintillation pulse from a low-energy ^{241}Am γ-ray interaction (upper left panel), an 8 keV pulse (upper right) and a single photoelectron response (centre) from one of the PMTs (#11) with characteristic decay time constants of 40.4 ns, 26.0 ns and 2.9 ns, and amplitudes of 0.61 V, 86.81 mV and 9.95 mV, respectively. All were obtained with -2.0 kV on the PMT cathode; however there was an additional $\times$10 amplifier present for the single photoelectron measurement.

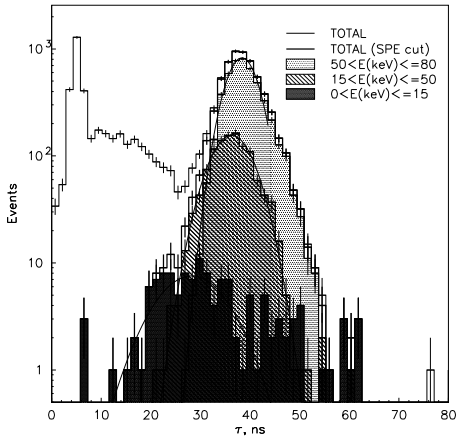

Figure 4.5: Comparison of decay time constant, τ (ns), distributions associated with the full, unsaturated energy spectrum (TOTAL with a saturation cut of $AMPLITUDE$ >-0.9 V) and with three energy slices, centred on the 59.5 keV γ-ray peak, the 26.3-33.2 keV blended feature and the 8 keV lines, with an SPE/noise cut ($AREA$ <-1 Vns) applied. These data were acquired with one of the PMTs (#11) operated at -2.0 kV. The mean time constants of the three populations, returned from single Gaussian fits, are 38.35±0.06, 36.25±0.13, and 28.23±0.79 ns, respectively.

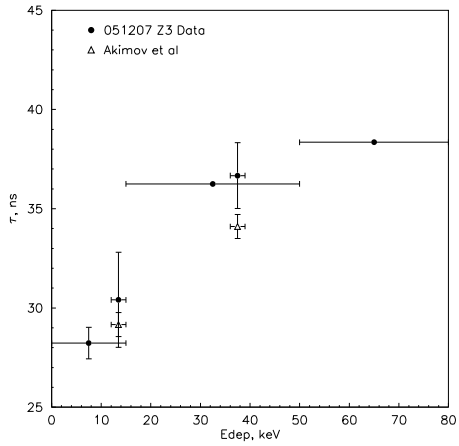

Figure 4.6: Measured decay time constant values, τ (ns), for electron recoil events as a function of deposited energy, E_{dep}. Results shown are obtained from τ distributions of the background data-set sliced in energy, along with an alternative set of experimentally obtained values[135], for comparison.

4.2.2.1 SPE Spectra

The 051207 surface zero-field SPE spectra (SES) data-set, a dedicated SPE run with decreased full scale settings and an additional factor of ×10 gain, was acquired in the same way as the corresponding background run, previously described. The SPE spectrum seen with PMT #11 was analysed to establish the detector's characteristic LY (see 4.2.3).

The 'true' SPE signal is considered to be that at the PMT output, which is read out after being passed through an amplifier, mimicking HS signal readout. Thus, the conversion factor from observed, or readout SPE to 'true' SPE response is simply ×0.1.

The normalised integrated pulse area (Vns), following energy calibration with respect to the 59.5 keV ^{241}Am γ-ray is shown in Figure 4.7. Here the SPE response peak is visible and has been fitted with a single Gaussian function indicating a mean area of 41.08±0.27 Vps (70 % full width half maximum, FWHM, where FWHM=2.35*σ/μ) corresponding to a mean energy of 0.11±(0.73×10^{-3}) keV, and similarly a mean pulse amplitude of 9.82±0.06 mV. Contrasting this mean energy value with Figure 4.2 indicates an apparent S1 LY at 59.5 keV of 8.78±0.44 phe/keV.

A measurable parameter used to characterise an SPE energy spectrum is the signal *peak-to-valley* ratio, P/V. For the particular distribution shown in Figure 4.7 this ratio is ∼10 and is significantly deeper than that measured prior to and independent of these tests (P/V=1.9[136]): indicating a probable efficiency loss at lower signals. Since both the pulse area and the equivalent pulse amplitude spectra exhibit the same, sharp drop-off in signal at low energy, this effect is not believed to be attributable to the digitization of the signal during acquisition.

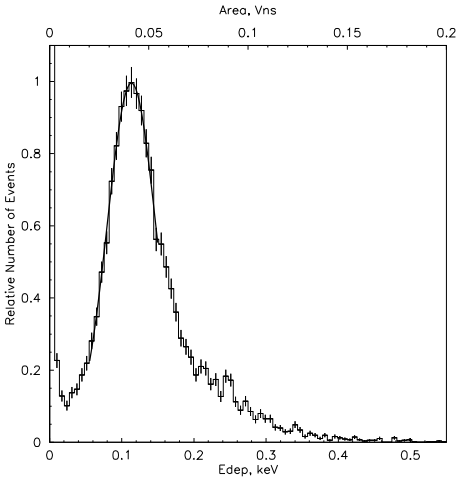

Figure 4.7: HS SPE energy spectrum from PMT #11 (PMT HV at -2.0 kV) in the 051207 dedicated SPE data-set with a mean of $0.11\pm(0.73\times10^{-3})$ keV (70 % FWHM) from a single Gaussian fit to the distribution. A cut on the decay time constant $\tau < 8$ ns has been applied, post-acquisition, to eliminate a feature due to two photoelectrons and saturation effects (due to the additional $\times10$ gain and the minimised amplitude range (full scale of 50 mV instead of 1 V). The measured P/V $\sim$10 suggesting some efficiency loss at lower energies.

4.2.3 Enhanced S1 Light Yield Runs

The close proximity of the thirty-one, temporary, ^{241}Am γ-sources to the PMT photocathodes enhanced the measured S1 LY. Within the cool down tests of the first commissioning phase various data-sets were acquired, in several different ways. These were all taken at zero-field and included combinations of: background and dedicated SPE runs; with applied PMT voltages ranging from -2.0 to -1.5 kV; with an 'empty' (air), full (LXe) and partially full (LXe and $\sim$2-5 mm GXe) target volume. Enhanced S1 LYs for a selection of these data were calculated and are contrasted below.

Single-Phase (LXe Only)

An S1 zero-field LY, with no gas gap and LXe depth of 5.5 mm above the PMT windows, of 8.78±0.44 phe/keV was determined from the 051207 fitted energy spectra of the SPE and 59.5 keV ^{241}Am γ-ray line (Sections 4.2.1 and 4.2.2.1).

Zero-field Windows ACQIRIS 051108 data for PMT #11 at 2.0 kV, acquired prior to the 051207 data-set, demonstrate an enhanced S1 LY of 7.42±0.37 phe/keV. This

value is consistent with that predicted by MC simulations, 7.1 phe/keV at 1.9 kV, but not with the second experimentally determined value of 8.78±0.44 phe/keV, above. Furthermore, MCA 051219 γ and 051215-16 SPE data-sets were acquired (at 1.9 and 2.0 kV) and analysed[137], and separate analyses of the ACQIRIS 051207 data were conducted[138]. All of these results are summarised in Table 4.1.

The single-phase MCA measurements used the amplitudes of pulser reference peaks, measured with an oscilloscope, to determine the gain ratio of the SPE peak and γ-spectrum, at different amplifier gains.[137]

The reason for the observed increase in S1 LY, measured over a period of ∼6 weeks, with consistent setups was unconfirmed although the poor (and at this stage unquantified), but potentially improving LXe purity (electron lifetime) is believed to have contributed significantly. Prior analyses of ZEPLIN II data demonstrated a strong correlation between the S1 zero-field LY and the LXe purity: an improvement in purity, from 10 μs to 100 μs was shown to correspond to an increase in measured LY of approximately 94% (from ∼0.80 phe/keV to ∼1.55 phe/keV).[139]

Dual-Phase (LXe with GXe Gap)

With the LXe level somewhere between the source and the PMT window (above or below the grid) and the xenon gas gap estimated to be ∼2-5 mm, the light collection increased. The improved light collection, attributable to total internal reflection at the liguid gas interface due to the refractive index mismatch, gave a LY of 18.12±0.91 phe/keV (the 59.5 keV line with 11 % FWHM energy resolution), with the interactions occurring mainly in the LXe phase. This was confirmed by an alternative approach, using data acquired with the MCA, giving ∼18.0 phe/keV (∼13 % FWHM) with a 4.2 mm LXe layer and 1.3 mm GXe gap[137].

The normalised, acquired ACQIRIS S1 energy spectrum, along with the equivalent MC prediction[130], are shown in Figure 4.8. In the MC G4 spectrum the 59.5 keV and blended 26.3-33.2 keV γ-ray lines are visible. Furthermore, the 8 keV line appears, but at ∼9 keV and the centroid of a stronger '8 keV in gas' peak is at 4.6 keV. In the ACQIRIS spectrum the 8 keV line is not evident, an additional feature appears at ∼12 keV, and the '8 keV in gas' peak at is centred at 4.7 keV. Identification of this '8 keV in gas' feature enables the undefined thickness of the GXe gap to be deduced, post-acquisition. The normalised MCA spectra, acquired with varying LXe depths and GXe gaps, but with no clear '8 keV in gas' feature,

DATA-SET	t LXe (mm)	GXe gap (mm)	S1 LY (-1.9 kV) (phe/keV)	S1 LY (-2.0 kV) (phe/keV)
051108 ACQIRIS Bkgd †‡ 051108 ACQIRIS SPE †‡	∼2-3	∼2.5-3.5	7.01±0.35	7.42±0.37
051207 ACQIRIS Bkgd †‡ 051207 ACQIRIS SPE †‡	5.5	0.0		8.78±0.44
051207 ACQIRIS Bkgd [138] † 051207 ACQIRIS SPE [138] †	5.5	0.0		7.32
051219 MCA Bkgd [137] † 051215-16 MCA SPE [137] †	5.5 <0.0	0.0 >5.0	11.5	11.3
G4 MC simulation [130]	5.5	0	7.1	

Table 4.1: Comparison of enhanced S1 LYs, determined from different experimental and simulated data-sets, for PMT #11 operated at -1.9 and/or -2.0 kV, in single-phase, with no applied electric field. Here † denotes data acquired and ‡ analyses conducted by the author.

are shown in Figure 4.9. All of these results are summarised in Table 4.2. Figure 4.10 shows the corresponding ACQIRIS SPE energy spectrum with P/V ~7 - again indicating some efficiency loss at low energies.

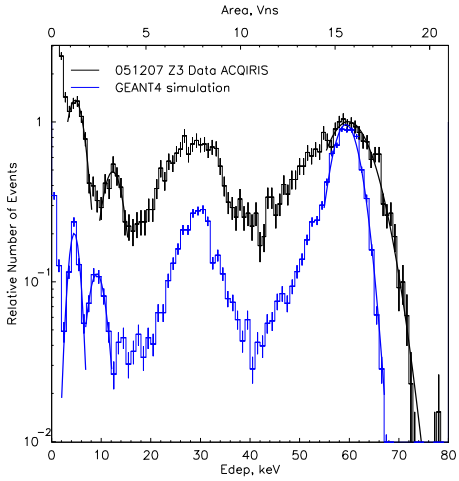

Figure 4.8: Comparison of the experimental ACQIRIS (PMTs operated at 2.0 kV) and G4 MC simulated[130] (at 1.9 kV) S1 dual-phase energy spectrum, with thirty-one ^{241}Am sources mounted in the LXe phase. Both axes (relative number of events, energy deposited in LXe) are normalised with respect to the 59.5 keV γ-ray line. Single Gaussian functions fitted to the symmetric 59.5 keV (ACQIRIS and G4) and 8 keV (G4) lines and the '8 keV in gas' peak (ACQIRIS and G4) are also shown.

The G4 MC simulation dual-phase data were generated with an exactly 5 mm GXe layer underneath the flat Cu holder. Furthermore, the grid was 'removed', a Cu reflectivity of 0%, QE=32% (PMT #11 at 1.9 kV), perfect optical match between the PMT and LXe phase and a photon yield of 60 photons/keV (15 eV/photon) were assumed.[130]

Following on from the single-phase MCA measurement with no GXe gap, xenon was systematically removed from the detector to collect dual-phase MCA data, as a function of gas gap. More specifically, the moment when the γ-peaks disappeared from the spectra was interpreted as the LXe surface reaching the level of the edge of the PMT spherical window (11.3 mm below the Cu disk, see Figure 4.1). This, together with the single-phase measurement, was used as a reference point to estimate the level of the LXe surface at each stage.[137]

The GXe gap, of unknown size, with the 051207 ACQIRIS data can be inferred from the spectral features, or rather those 'missing' or diminished. The '8 keV in

DATA-SET	t LXe (mm)	GXe gap (mm)	S1 LY (-1.9 kV) (phe/keV)	S1 LY (-2.0 kV) (phe/keV)
051207 ACQIRIS Bkgd †‡ 051207 ACQIRIS SPE †‡	-	-		18.12±0.91
051209 MCA Bkgd [137] 051209 MCA SPE [137]	4.9	0.6		17.3
051209 MCA Bkgd [137] 051209 MCA SPE [137]	4.2	1.3		18.0
051209 MCA Bkgd [137] 051209 MCA SPE [137]	3.8	1.7		19.1
G4 MC simulation [130]	<1.0	5.0	12.1	

Table 4.2: Comparison of enhanced S1 LYs, determined from different experimental and simulated data-sets, for PMT #11 operated at -1.9 and/or -2.0 kV, in dual-phase (with a GXe gap of ∼mm), with no applied electric field. Here † denotes data acquired and ‡ analyses conducted by the author.

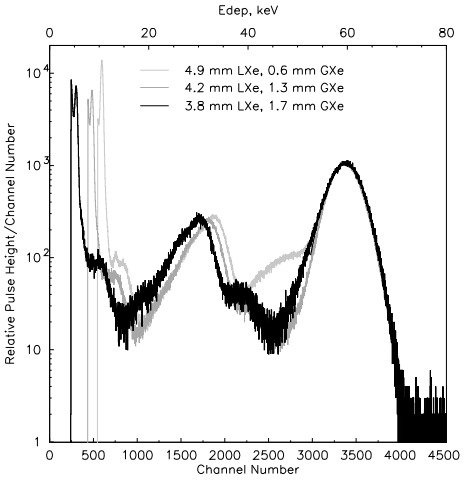

Figure 4.9: Comparison of the experimental MCA (PMTs operated at 2.0 kV) S1 dual-phase energy spectra, acquired as a function of LXe depth and GXe gap, with thirty-one ^{241}Am sources mounted within the LXe. The x-axis (energy deposited in LXe) is normalised with respect to the 59.5 keV γ-ray line. An additional background, ∼40-50 keV, is only seen during acquisition with the smallest GXe gap (0.6 mm). A single Gaussian function fitted to the symmetric 59.5 keV is also shown.

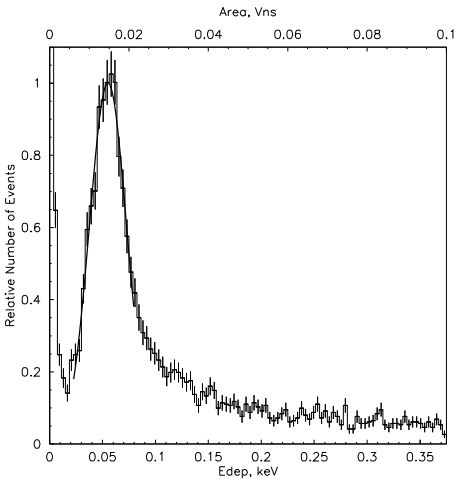

Figure 4.10: LS SPE energy spectrum from PMT #11 (PMTs operated at -2.0 kV) with a mean of 0.0552±0.0175 keV (75 % FWHM) from a single Gaussian fit to the distribution.

gas' feature, appearing at ∼5 keV in these dual-phase data is not present in any single-phase data, confirming its origins in the gas. Hence, using this, the GXe gap is estimated to be quite large, ∼5 mm or at least larger than the liquid layer, as the ∼5 keV line is shown to be strong, while the 8 keV (Cu X-rays in the LXe) seems

to be absent from the spectrum. The G4 MC simulated dual-phase data-set, at 1.4 bar (12.6 mg cm^{-3}), with 5 mm of GXe, was shown to cause significant absorption of the 8 keV line.[130]

The additional feature at ∼12 keV, is seen in both the MCA and ACQIRIS data-sets, but not in the G4 MC simulated spectrum, and only with the dual-phase configuration. Thus, it is associated with the GXe phase. Physically this must be the 8 keV line, but enhanced in some way.

A large GXe gap, relative to a small LXe layer, in the dual-phase setup supports the ∼×2.1 (8.78 phe/keV) and ∼×2.4 (7.42 phe/keV) factors between the measured ACQIRIS S1 zero-field single- and dual-phase LYs. A difference of ∼×2.4[140], for a 5 mm GXe gap, is predicted.

The SPE spectra used for calibration of the dual-phase MCA data-sets were acquired in single-phase. For the dual-phase system reflections from the Cu disk were expected to have a negligible, ∼1%, effect on the fraction of light escaping from the LXe to GXe phases. Ultimately, the MCA data-sets were employed to determine W_{ph}; the *photon yield* or energy expended per scintillation photon. A W_{ph} value of 9.06 eV was calculated, following solid angle and QE considerations, for the data acquired with a 4.9 mm LXe layer and a 0.6 mm GXe gap.[137]

The measured dual-phase zero-field S1 LY results indicate poor agreement between the experimental and simulations. This, along with the measured W_{ph} value, suggests that it is quite likely that W_{ph} <15 eV (i.e. photon yield >60 ph/keV), contrary to many published values[130][141]. However consistency between the two experimental setups, the ACQIRIS and MCA data-sets, is encouraging with the former being independent of any oscilloscope or pulser calibration.

In a separate series of tests, conducted by the author several weeks later, the stability of the pulser reference and MCA setup were investigated over an ∼3 hr period. Although the pulse generator and amplifier used were deemed stable following the repetition of five such identical tests, the MCA was observed to drift significantly.[142]

The factor of ∼×2 improvement in dual-phase LY, with respect to single-phase, can be explained by significantly more efficient light collection in dual-phase mode as ∼80% of the light that comes to the LXe surface is reflected back and the scintillation occurs closer to the PMT's photocathode.

4.2.4 Am-Be Neutron Run at Zero-Field

Elastic scattering of monoenergetic neutrons can be used to determine the response of a dark matter detector to nuclear recoils. Using this technique, a study of scintillation pulse shapes, or event decay time constants, in the LXe was conducted at zero-field.

A 10 mCi (370 MBq) Am-Be (α, n) source was placed centrally on top of the detector, externally, to assess the response of ZEPLIN III to nuclear recoils. Placing the n-source directly on top of the instrument vacuum jacket minimised the PMT-source separation, maximising the detector solid angles and thus the number of neutrons interacting in the target volume. At this stage all thirty-one internally-mounted ^{241}Am sources remained in situ and the detector target was completely filled with xenon, with no gas gap. The response of PMT #11 at -2.0 kV, as before, during the 80 minute total exposure was studied.

The characteristic τ of individual S1 pulses in PMT #11 were calculated using the method of pulse integration to determine the mean photoelectron arrival time (Equation 3.9), as for the data acquired with no external Am-Be source present. Additionally, individual pulses were fitted with a single exponential function, assuming a single dominant decay component to the scintillation pulse shape, verifying the τ values and thus providing two independent methods of computing τ. These two methods proved consistent for a range of τ values and are demonstrated by the example given in Figure 4.11. Calculating the uncertainties associated with these is non-trivial. For the integration approach the uncertainty in $\tau(int)$ is dependent on three factors: the pulse-finding algorithm and the determined time corresponding to the end of the pulse; the noise in each time bin impacting on the integrated area calculation; and the digitization (bin sampling time) contributing to calculation of the area, half of the area and ultimately the mean arrival time. Looking at τ distributions, of constant area (or energy), the uncertainty in $\tau(int)$ is estimated to be $\lesssim \pm 2$ ns, but is of course energy-dependent (see Figure 4.6). For the exponential fit approach, although an error on the gradient is returned by the fit ($-1/\tau(fit)$=-0.0258$\pm$0.0095 ns^{-1} for the specific case shown in Figure 4.11), systematic effects will also contribute to the uncertainty in $\tau(fit)$. Such effects include the uncertainty in the determined end time of the pulse and the uncertainty in defining the start time of the pulse as the minimum fit range, rather than the time corresponding to the maximum amplitude. Neglecting systematic considerations, the uncertainty in $\tau(fit)$ is estimated to be $\lesssim \pm 5$ ns.

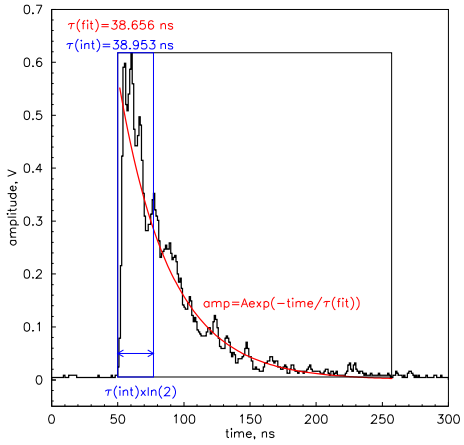

Figure 4.11: Typical zero-field primary scintillation pulse from a low-energy (21.51 Vns) ^{241}Am γ-ray interaction from one of the PMTs (#11, operated at -2.0 kV) with characteristic decay time constants computed from the integrated pulse area ($\tau(int)$) and an exponential fit to the pulse rise time ($\tau(fit)$). Consistent time constants of 38.953($\lesssim \pm 2$) ns and 38.656($\lesssim \pm 5$) ns were calculated from the two independent methods, respectively. Note that the, normally negative going signal, has been inverted for the purpose of performing the fit.

Comparison of the single-phase S1 background (pre-neutron) and Am-Be (neutron) integrated pulse area (Vns) or energy spectrum, with PMT 11 HV at -2.0 kV, following normalisation and energy calibration with respect to the 59.5 keV ^{241}Am γ-ray line, is shown in Figure 4.12. Acquisition of the neutron data (2×10^6 events, a 20 minute exposure subset of the total run) was at a significantly increased event rate than the pre-neutron data (10^4 events) due to the presence of the n-source. Hence the error bars on the two distributions reflect this. Single Gaussian functions are fitted to the two symmetric (8 keV and 59.5 keV) lines, in turn. A small excess of events, with 40$< E(keV) <$50, in the background data is suggested but probably statistical in nature. Also, an excess of events, with $E(keV) \lesssim$15, in the Am-Be data is shown. This is the region where events would be expected given the quenching factor of 0.19$\pm$0.02[107] for nuclear recoils. These potential neutron events may be identified by utilising energy slicing and time constant analysis.

Distributions of the pulse decay time constant, τ, for data acquired prior to and during the surface neutron (Am-Be) runs, are shown in Figure 4.13. This is using the pulse area integration approach, not by fitting an exponential function to individual pulses. The full, unsaturated ($AMPLITUDE >$-0.9 V) τ distributions are plotted and the y-axis normalised with respect to the γ population centred on $\sim$40 ns.

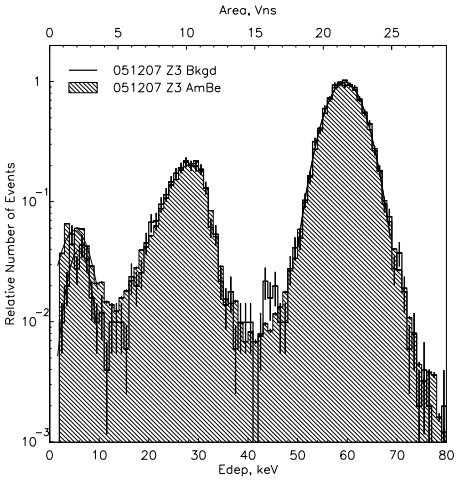

Figure 4.12: Comparison of the single-phase S1 background (pre-neutron) and Am-Be (neutron) energy spectrum, with thirty-one ^{241}Am sources mounted within the LXe. Both axes (relative number of events, energy deposited in the LXe) are normalised with respect to the 59.5 keV γ-ray line. Single Gaussian functions fitted to the symmetric 59.5 keV and 8 keV lines are also shown. Note that a saturation ($AMPLITUDE$ >-0.9 V) and SPE cut ($AREA$ >1 Vns) are applied, post-acquisition.

The same two distributions, but with analysis cut on SPEs/noise ($AREA$ <-1 Vns) applied, are also shown. The SPE/noise cut significantly removes low-τ events; the saturation cut cleans up the τ tail of the γ-peak, at high-τ.

Two distinct τ-distributions, with means of ∼22 ns (21.0±0.5 ns, 6<$E_{ee}(keV)$<30)[135] and ∼40 ns (38.5 ns, E_{ee} ∼59.5 keV[1])[135], associated with neutron and γ populations respectively, were expected to be observed within these data-sets. A γ population was subsequently observed at ∼38 ns. However, although a low-τ 'shoulder' was seen, centred at ∼20-25 ns, no apparent excess with the Am-Be n-source was observed here, to within errors. An excess of events in the Am-Be data was only seen at high-τ. It was believed that the internal ^{241}Am γ-sources, combined with the high γ background of an unshielded surface-operated detector, could 'mask' any indication of a smaller neutron population.

The values presented in Figure 4.14 were obtained by slicing the τ distributions in energy across several, fine energy ranges and fitting the peaks with a Gaussian function in an attempt to identify a neutron excess. Results of the fit to each sliced

[1] τ ∼38.5 ns: extrapolating the observed increase in τ from E_{ee} ∼13.5 keV to ∼37.5 keV up to ∼59.5 keV using published values of 29.1±0.6 ns (E_{ee} ∼13.5 keV) and 34.0±0.6 ns (E_{ee} ∼37.5 keV)

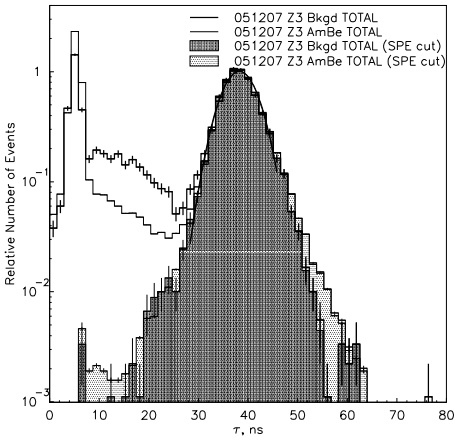

Figure 4.13: Comparison of decay time constant, τ (ns), distributions of data acquired prior to and during the surface neutron (Am-Be) runs. These data were acquired with one of the PMTs (#11) operated at -2.0 kV. The distributions are plotted with saturation (TOTAL) or saturation and SPE/noise (SPE cut) analysis cuts applied. The y-axis is normalised with respect to the γ population centred on 38.20±0.05 ns (22.7% FWHM) and 38.30±0.26×10^{-2} ns (22.7% FWHM) for the pre-neutron and neutron runs, respectively.

γ population for both the background (pre-neutron) and Am-Be (neutron) data-sets are summarised in Figure 4.14.

The general trend of fitted decay time constant values for zero-field electron recoil events over the ∼10-70 keV energy range is consistent with those obtained from the alternative experimental data-set (Reference [135]). However, Figure 4.14 indicates an apparent offset, with τ values retrieved by the author being systematically longer. The 051207 data-points have larger associated error bars over the ∼34-50 keV energy range due to the less tight distributions containing fewer events.

To clarify the described procedure, and to further search for a low-energy neutron excess in the Am-Be data around τ ∼22 ns, the τ distributions corresponding to two, more coarse ranges (a low-energy, 3< $E(keV)$ <=9 and a slightly higher energy interval, 9< $E(keV)$ <=15) can be seen in Figure 4.15.

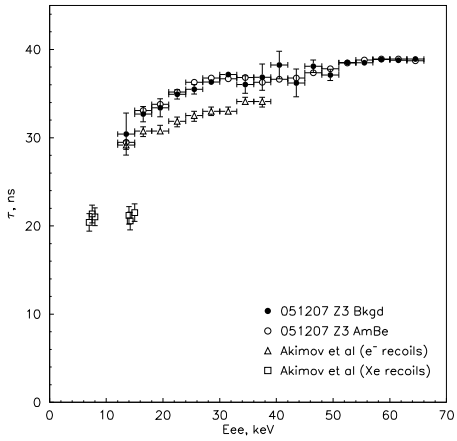

Figure 4.14: Fitted decay time constant values, τ (ns), for zero-field electron recoil events and for an alternative set of experimentally obtained values[135], for both electron and nuclear recoils as a function of electron equivalent energy, E_{ee}, are shown for comparison. The 051207 Z3 fitted values are obtained from τ distributions of both the background (pre-neutron) and Am-Be (neutron) data-sets sliced in energy. The horizontal error bars on the nuclear recoil points (6< $E_{ee}(keV)$ <30) are not shown for clarity.

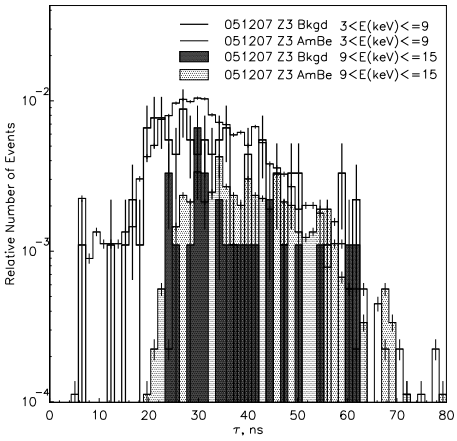

Figure 4.15: Comparison of decay time constant, τ (ns), distributions of data acquired prior to and during the surface neutron (Am-Be) runs. The data shown here are sliced in energy below 15 keV to look for a low-energy neutron excess around τ ∼22 ns in the Am-Be (neutron) data. No such statistically significant excess can be seen here, to within errors.

In these early Am-Be laboratory calibrations too few neutron events were observed to conclusively identify a convincing neutron population up to ∼70 keV. Follow-

ing energy-slicing down to low-energies, no such statistically significant excess with τ ~22 ns was seen in the Am-Be data distributions, to within errors. At best, the γ time constants variation as a function of energy was probed.

4.3 Commissioning Phase II: Two-Phase Operation & Optical Response

After the temporary ^{241}Am sources were removed, the anode and cathode grids were replaced and subsequent cold runs were done, filling the detector with LXe: the second commissioning phase. Here both zero-field and with-field data-sets were acquired during dedicated background, SPE, ^{57}Co, ^{60}Co, ^{137}Cs and Am-Be runs.

During Phase II a conservative but sufficiently-high electric field was successfully applied between the grids, the maximum being -13.50 kV across the anode and the cathode, generating 3.11 kV/cm in the liquid with a GXe gap of ~3-4 mm. Furthermore, the PMTs were operated with a maximum applied voltage of -1.9 kV.

4.3.1 Single Photoelectron (SPE) Spectra

Several dedicated SPE data-sets with minimised full scale ranges were acquired at zero-field, with no external source present during the second commissioning phase. These include 060526 and 060707 data runs. For both of these the PMTs were operated at a conservative voltage of -1.8 kV and the upgraded, Linux ACQIRIS DAQ was used together with the ZE3RA (v1.2) reduction code. The earlier, 060526 data were used to propose attenuation adjustments for each channel in order to equalise the SPE areas in each channel. Analysis of the later, more refined 060707 SPE data were then used to characterise the zero and with-field S1 and S2 LY (Sections 4.3.4-4.3.7) with all channels normalised to the same overall gain. The acquisition setup was consistent with Figure 3.11 (Section 3.5).

The dual-phase target volume consisted of the LXe phase with a GXe gap of ~3 mm during acquisition of the 060707 data.

The ZE3RA reduction tool and the 'SPE tab' within it is not designed specifically for the reduction of SPE pulses. This function within ZE3RA is just designed to handle small signals, in general. Nevertheless, the ZE3RA SPE reduction was adapted

by applying carefully considered reduction parameters and by enforcing a constant right-hand integration time to accommodate long tails, even if the tail is buried within noise.

Using the 060707 data-set, well resolved SPE area peaks for each HS PMT channel were acquired. The mean SPE pulse area in each HS channel was derived from the mean of the distribution (not the fit) of the SPE area after defining some 'threshold' in amplitude. Examples of two typical area distributions are shown in Figure 4.16 with their associated thresholds. An average SPE mean area across the array of 52.37±1.59 Vps was determined where the error quoted on this value is given by the 'standard error of the mean'.

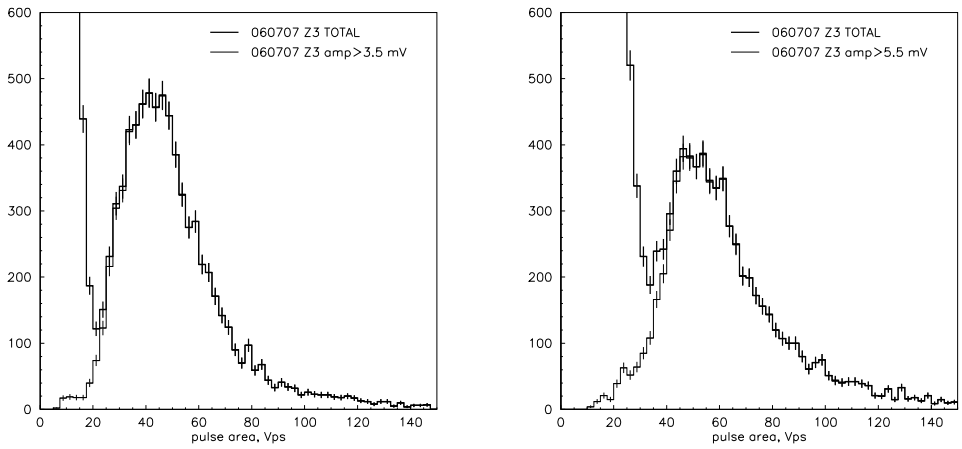

Figure 4.16: Two typical example histograms of SPE pulse area for PMTs #7 (left panel) and #22 (right) from HS channels in the 060707 zero-field data-set (PMTs at -1.8 kV). The area distributions were considered above amplitude thresholds of 3.5 mV and 5.5 mV, respectively. The means of these distributions are 50.27±0.24 Vps (σ=20.74 Vps) for PMT #7 and 62.27±0.29 Vps (σ=23.67 Vps) for PMT #22. The error quoted on the means is given by the 'standard error of the mean'.

Several functions, to be fitted to the SPE peak and the dynode noise, were considered to better estimate the SPE value, that is, the most probable SPE pulse area. The linear combination of two Gaussian functions was first considered.

The functions fitted to the pulse area spectra, performed within PAW, were defined in the following way with six free parameters:

$$g(x) = a_1 e^{\frac{-(x-\mu_1)^2}{2\sigma_1^2}} + a_2 e^{\frac{-(x-\mu_2)^2}{2\sigma_2^2}} \quad (4.11)$$

$$a_{1,2} = \frac{1}{\sigma_{1,2}\sqrt{2\pi}} \tag{4.12}$$

where the peak amplitude, mean and standard deviation of each are denoted by $a_{1,2}$, $\mu_{1,2}$ and $\sigma_{1,2}$, respectively. Examples of two typical area distributions, fitted by $g(x)$, are shown in Figure 4.17. Since the SPE peaks are asymmetric, possibly due to some efficiency loss at low areas, the Gaussian function does not appear to fit the right-hand tail of the distributions. Therefore, it is preferable to fit the full distributions. This suggests some additional function, i.e. a second-order polynomial, may be required in order to accommodate the tail and any baseline shift. This is something considered in the Wolfs fit function[143], discussed below.

The results of fitting the function $g(x)$ to the individual spectra, enabled an average SPE fitted area across the array of 44.70±1.40 Vps to be determined.

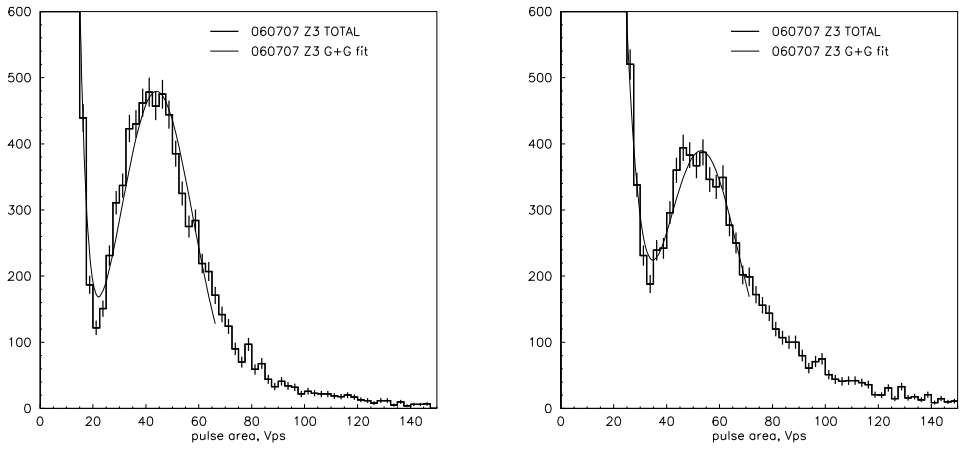

Figure 4.17: Two typical example histograms of SPE pulse area for PMTs #7 (left panel) and #22 (right) from HS channels in the 060707 zero-field data-set (PMTs at -1.8 kV). For each PMT, the dynode noise and SPE peak distributions were simultaneously fitted with a linearly combined two-Gaussian function, $g(x)$. For PMT #7 this SPE mean is 44.02±0.23 Vps (σ=13.68±0.26 Vps, χ^2=8.57) for the combined function. Similarly, the mean is 52.99±0.34 Vps (σ=14.11±0.48 Vps, χ^2=3.98) for PMT #22.

A selection of alternative functions, to suitably describe the area distributions, were considered. These included the Polya[144], 'negative Binomial' or 'compound Poisson' distribution, $p(x)$, and the Wolfs, $w(x)$, functions. In both approaches, the function of choice was fitted to the SPE peak distribution, after application of the threshold cut previously mentioned.

The Polya function contains both Poisson and exponential functions as special extreme cases and allows for the non-uniformity of the PMT dynodes. Such dynode inhomogeneities may include cases where: the emitted electrons do not all have the same probability of reaching the following dynode; or the effective secondary emission ratio varies with position on each dynode. Thus, the Polya describes secondary emission from a dynode of finite area for which the average number of secondaries per incident electron for the dynode as a whole is the mean, μ. Although dynode inhomogeneities are found to contribute to the effectively non-Poissonian dynode statistics in PMTs, the study in Reference [144] makes no distinction as to whether it is these alone which account for the non-Poissonian shape, or whether the secondary emission process itself differs from Poissonian. The Polya function is defined as:

$$p(x) = \frac{N(xb)^a e^{-bx}}{x\Gamma(a)} \tag{4.13}$$

$$a = \left(\frac{\mu}{\sigma}\right)^2 \tag{4.14}$$

$$b = \frac{\mu}{\sigma^2} \tag{4.15}$$

$$\mu = \frac{a}{b} \tag{4.16}$$

$$\sigma = \frac{\sqrt{a}}{b} \tag{4.17}$$

where N is a normalisation factor (number of events $\times$ bin width) and a and b are free parameters of the fit. The errors on the fitted μ and σ, $e(\mu)$ and $e(\sigma)$, are combined in quadrature, according to:

$$e(\mu) = \mu\sqrt{\left(\frac{e(a)}{a}\right)^2 + \left(\frac{e(b)}{b}\right)^2} \tag{4.18}$$

$$e(\sigma) = \sigma\sqrt{\left(\frac{2e(a)}{a}\right)^2 + \left(\frac{e(b)}{b}\right)^2} \tag{4.19}$$

An example of a typical area distribution, fitted by $p(x)$, for PMT #7 is shown in Figure 4.18. The Polya fit function successfully describes the tail of the SPE, out to $\sim$80 Vps, for PMT #7. It was not possible to fit the SPE distribution of PMT #9. Note that the Polya function, as defined in Reference [144], assumes a certain emission probability distribution over the surface of the PMT dynode which may not accurately reflect the ZEPLIN III case, for these particular PMTs.

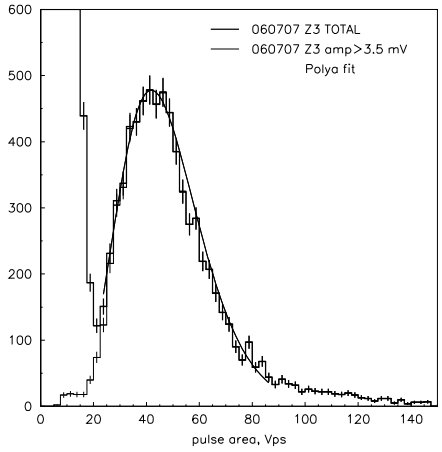

Figure 4.18: An example histogram of SPE pulse area for PMT #7 from HS channels in the 060707 zero-field data-set (PMTs at -1.8 kV). For each PMT, the SPE peak distribution was fitted with a Polya function, $p(x)$. For PMT #7 the Polya SPE mean is 47.32±1.78 Vps (σ=16.04±0.94 Vps, χ^2=3.07).

The Wolfs function, designed to reliably fit a wide range of spectral shapes, is simply the combination of a Gaussian and a second-order polynomial and is defined as:

$$w(x) = ae^{\frac{-(x-\mu)^2}{2\sigma^2}} + bx + c \tag{4.20}$$

where a is the peak amplitude and b and c correspond to the gradient and offset of the linear background, respectively. Incorporating the polynomial term better equips the fit function to handle the tails of the distributions. The SPE peaks were fitted with the lower fit limit defined as 75% of the peak amplitude and the upper fit limit as 150 Vps. The relatively high chosen lower limit ensures the structure at low SPE areas, and any potential efficiency loss, does not bias the fit or influence its stability.

An example of a typical area distribution, fitted by $w(x)$, for PMT #7 is shown in Figure 4.19. As with the Polya, the Wolfs fit function also successfully describes the tail of the SPE, out to ∼100 Vps, for PMT #7. The average fitted SPE area, across the area, of 41.78±1.55 Vps was found using this. Similarly, the average fitted SPE area, across the array, of 49.06±1.71 Vps was found using the Polya function.

All results from the four different approaches are summarised in Figure 4.20. Also shown are the finalised attenuator settings. Applying the fit functions to the distributions clearly gives a systematically lower average SPE pulse area, ∼3-11 Vps

smaller, than the mean values.

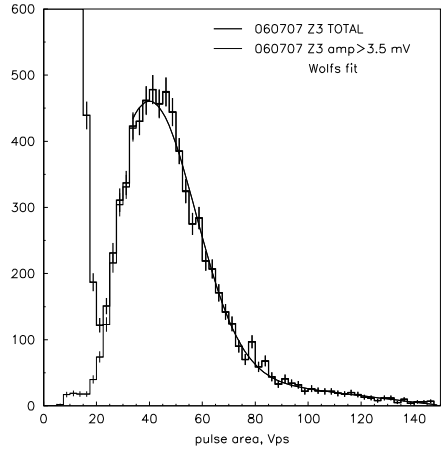

Figure 4.19: An example histogram of SPE pulse area for PMT #7 from HS channels in the 060707 zero-field data-set (PMTs at -1.8 kV). For each PMT, the SPE peak distribution was fitted with a Wolfs function, $w(x)$. For PMT #7 the Wolfs SPE mean is 40.36±0.94 Vps (σ=17.10±0.72 Vps, χ^2=1.19).

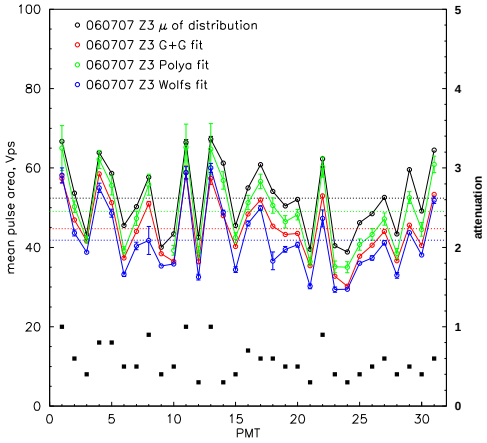

Figure 4.20: Plot summarising the thirty-one SPE mean pulse area and SPE fitted peak pulse area values (open circles). The y-error bars on the 'mean of the distribution' data points are given by the standard error of the mean. All other y-error bars are determined from the errors returned by the fits. The average mean SPE area, calculated across the full array, is 52.37±1.59 Vps, 44.70±1.40 Vps, 49.06±1.71 Vps and 41.78±1.55 Vps using the mean of the distribution and the two-Gaussian, Polya and Wolfs fit functions, respectively (broken lines). In addition, the attenuation settings for each channel, finalised in order to equalise the PMT gains across the array, are shown (closed squares).

The robustness of the Wolfs function to different spectral shapes, was demonstrated (see Figure 4.21). It succeeded where the Polya function failed: to perform a reasonable fit to the SPE distribution of PMT #9. Furthermore, the Wolfs function appears to describe the width of the distributions better (yielding larger σs), coping well with fitting to the tails of the distributions, out to larger areas, as expected.

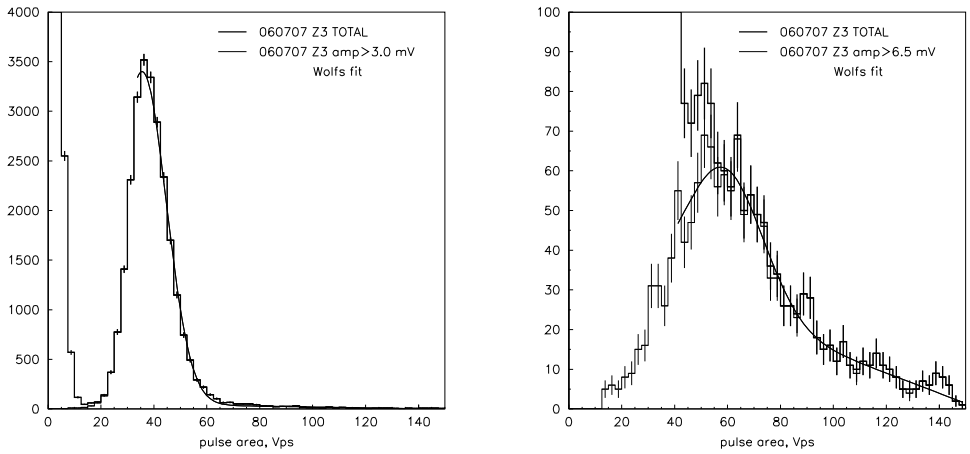

Figure 4.21: Two typical example histograms of SPE pulse area for PMTs #9 (left panel) and #11 (right) from HS channels in the 060707 zero-field data-set (PMTs at -1.8 kV). For each PMT, the SPE peak distribution was fitted with a Wolfs function, $w(x)$. For PMT #9 this SPE mean is 35.53±0.26 Vps (σ=9.19±0.15 Vps, χ^2=4.70). Similarly, the mean is 58.81±1.52 Vps (σ=14.70±2.05 Vps, χ^2=0.78) for PMT #11.

The Polya function approach to fitting the SPE peak, in order to determine a mean SPE value, is consistent with the value returned by the mean of the distribution, to within errors. Similarly, there is consistency between the two-Gaussian and the Wolfs fits. The averaged reduced χ^2 values calculated for the different fit functions investigated here suggest the Wolfs fit performs the best, for this particular data-set. Incidentally, the associated average SPE mean area is the lowest of all the methods. These results are summarised in Table 4.3. The large averaged reduced χ^2 value corresponding to the Polya function can be attributed to the significantly lower fit limit employed.

The success of the two-Gaussian, Polya and Wolfs fit functions may have been limited by the possibility of two photoelectron signals comprising the tail of the SPE distributions. The inclusion of two photoelectrons in the tail is unavoidable when acquiring SPE spectra in the manner employed here. In which case, a fit to the SPE peak will always be preferable over the mean of the distribution (an average).

method	average SPE mean area (Vps)	average χ^2/ndf
mean of distribution	52.37±1.59	
G+G fit, $g(x)$	44.70±1.40	12.87±1.78
Polya fit, $p(x)$	49.06±1.71	14.66±2.05
Wolfs fit, $w(x)$	41.78±1.55	4.32±0.62

Table 4.3: Summary of the performance of different approaches to determine the SPE mean area, via either calculating the mean of the distribution or fitting a function to the SPE peak (or a combination of functions to the dynode noise and the SPE peak). All values shown are averaged across the full array (31 PMTs) except the Polya function where no fit was performed to PMT #9 (30 PMTs). The errors on the average SPE mean area and reduced χ^2 quoted are given by the 'standard error of the mean'.

Exploring the possibility of fitting a combination of three functions - one to the dynode noise, a second to the SPE and a third to a two photoelectron peak[145] - may prove useful in characterising the entire distribution. For completeness, the suitability of a Polya (or Wolfs) function to fit the full SPE peak (with no applied threshold), possibly in conjunction with a Gaussian fit to the dynode noise, should be investigated.

The development of an alternative method of measuring the SPE response is discussed in Chapter 5, Section 5.2 in the context of data-sets acquired subsequently, during the underground runs.

4.3.2 Unshielded Surface Background Run at Zero Field: ^{222}Rn α Contamination

The identification of sources of α-particle interactions - a special case of nuclear recoils where the incident particles are not uncharged, nor monoenergetic - was conducted using the two-phase zero-field 060519 and with-field (3.01 kV/cm in the liquid) 060520 background run data-sets, with no external calibration source present. Presentation of the with-field work follows in Section 4.3.3. For the purpose of this analysis only the LS SUM channel was used.

Such a search was motivated by α-like events having previously been observed within the ZEPLIN II experiment as a significant limiting background. These were believed to have been due to a constant supply of ^{222}Radon into the detector, at a rate of $\sim$2.2 Hz.[146] This was hypothesised to be from U/Th decays in the PTFE, vessel walls,

the PMTs or the construction materials of the laboratory itself, producing ^{222}Rn. Following investigation, the source was found to most likely be from the getters used within the Xe purification system and once produced, the ^{222}Rn contaminant moved into the fiducial volume. As the supply of ^{222}Rn was cut i.e. the Xe recirculation was switched off, the α rate was shown to drop accordingly, decaying with the associated half-life of 3.82 days. Although α-energy, E_α, is $\sim$MeV energies, small energy deposits down to the keV range by boundary walls or close to grid wires occurred in ZEPLIN II. The most important sources of these events, mimicking nuclear recoils, were from the cathode and field grids. A timing cut was used to reject such events, located at the top and bottom of the chamber while a radial cut based on S2 removed low-energy recoil events from the walls.[57] Note that ZEPLIN III did not inherit the internal structure of ZEPLIN II, with walls and boundaries but does use the same getters. See References [147] & [146] for studies of the α-background in ZEPLIN II.

Any incident αs - heavy, charged particles - will interact continuously with the Xe target atoms through the Coulomb force, with their interactions being very localized. The α-particle interaction range is significantly less than the dimensions of the chamber, at $\sim$45μm in LXe (assuming a continuous-slowing-down approximation range of 1.343×10^{-2} g cm^{-2}[148] in Xe, at E_α=5.5 MeV; LXe density ρ_{LXe}=2.953 g cm^{-3}[116]).

If confirmed, the presence of a background α-population in ZEPLIN III would impact on its sensitivity to WIMP searches with the low energy ($\sim$keV) range impinging on the dark matter region of interest with the ZEPLIN III getters being the most obvious culprit. Hence, it is crucial to study and identify the α-particle sources in ZEPLIN III. Conversely, if no αs are observed and the decay time constant, τ, calculation in ZE3RA verified, this would suggest the getters are not injecting ^{222}Rn contaminants into the system, as ZEPLIN III does not use continuous circulation in the way that ZEPLIN II did.

Diagnostics of a significant α-particle background contribution include the analysis of energy spectra and decay time constant distributions. One would expect to observe clear separation of the γ-ray and α-particle populations, with the latter present at comparatively higher energies (E_α=4.987 MeV and 5.489 MeV[149], with 0.078% and 99.92% relative intensities, respectively). Similarly, two, semi-separate distributions would be expected in the time constant, τ, parameter, where τ_γ $\sim$50 ns and τ_α $\sim$15 ns, at zero-field.[150]

The zero-field 060519 data-set was acquired for all readout channels, with no external calibration source present, over a period of ∼16 minutes with -1.8 kV applied to the PMTs. It was subsequently reduced with ZE3RA v1.3.

Firstly, to confirm the quality of the data and to check that most events are not saturated in the LS dynamic range the amplitude in an individual LS channel (not the SUM) was histogrammed. A populated bin, at large amplitudes around the acquisition FS value of 1.0 V, demonstrated some degree of saturation in the LS channels; with 1.5% of events being saturated in the LS SUM; thus, confirming the need for the saturation cut ($nsaturated(64) = 0$) to be applied.

The time constant distribution, in the LS SUM channel is shown in Figure 4.22. Three analysis cuts employed here demand at least one, unsaturated pulse ($npulses(64)>0$, $nsaturated(64)=0$) with $WIDTH50(1,64)$ <50 ns. The cut on the pulse $FWHM$ <50 ns is applied to remove wider events in order to focus on low-energy S1 pulses and has a visible effect in Figure 4.22.

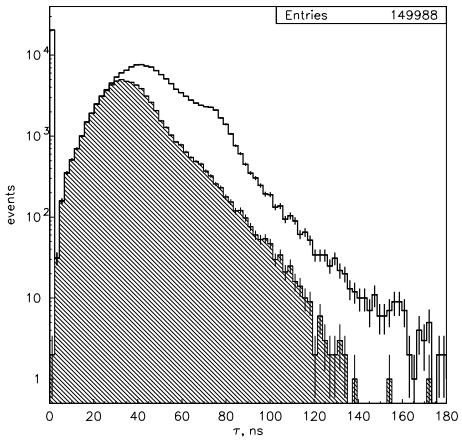

Figure 4.22: Histogram of the first pulses in the LS SUM channel of the time constants, τ, ns. The bold line corresponds to all reduced data with no applied cuts. Only events satisfying the demand for one, unsaturated pulse with $FWHM$ <50 ns are plotted in the shaded region.

In order to identify α-particle interactions a plot of τ vs the S1 energy was produced (see Figure 4.23). The data-set was calibrated in energy using the ^{57}Co 060519 zero-field data (see Section 4.3.4) and the measured pulse area value of the ∼125 keV photopeak, for the inner 7 PMTs, at 583.17±0.34 phe. According to work previously conducted (see Reference [150]) one expects the zero-field decay time constants of αs and γs to be 15.40±0.08 ns and 47.4±0.4 ns, respectively. The upper left panel

of Figure 4.23 shows how a high-τ population of events appear extended over this energy range, up to ∼25 MeV. The lower panel suggests that the main population seen here are γ events. No population, separate in S1 energy from the main, γ-population is visible in the upper right panel, particularly within the expected E_α region of ∼4.9-5.5 MeV and τ_α ∼15.40±0.08 ns.

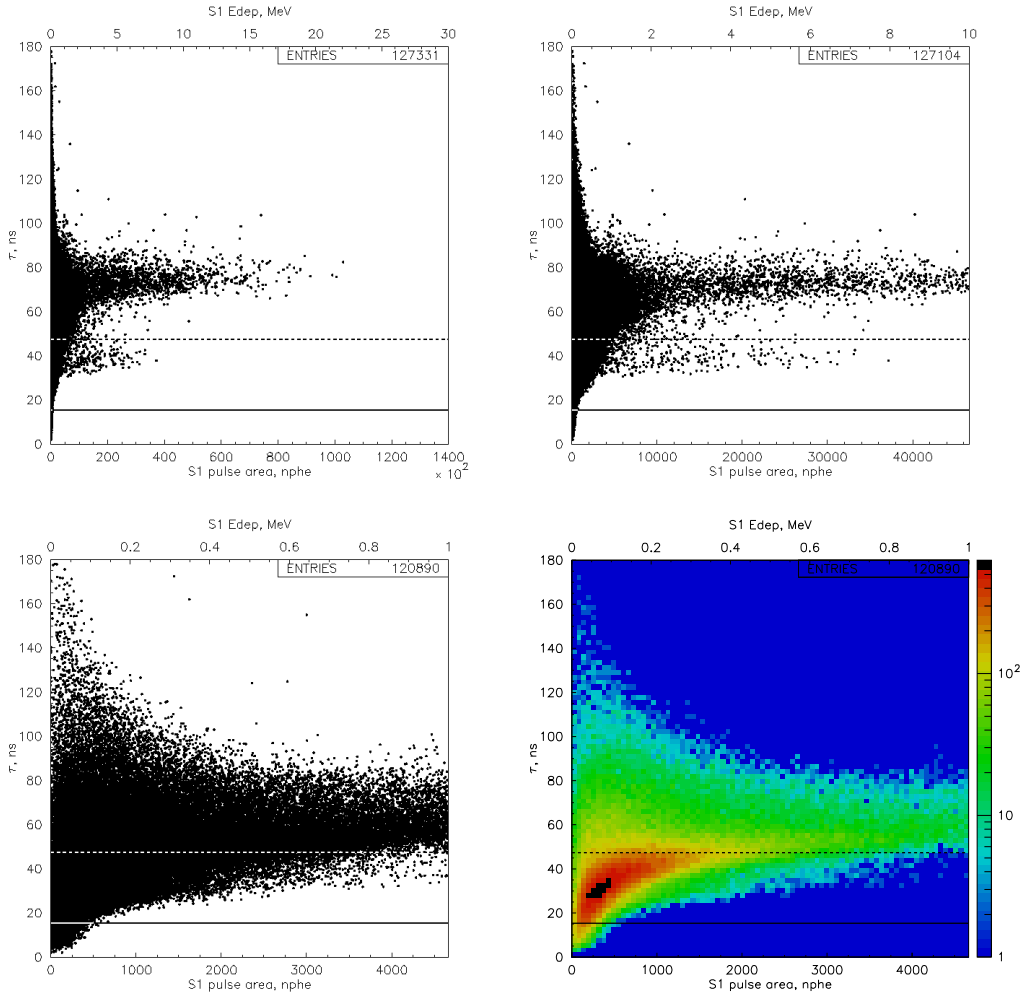

Figure 4.23: Scatter plots of τ vs S1 energy, E_{dep}, for all unsaturated, first pulses in the LS SUM channel, with each S1 energy scale successively zoomed (upper left, upper right and lower left panel). The density plot (lower right, equivalent to the lower left panel) is also shown for clarity, revealing the structure of the distribution. Expected τ_α and τ_γ values[150] are represented by the solid and broken lines, respectively.

4.9-5.5 MeV Events

If a significant α-particle population is present in the data it should be readily identifiable from the S1 energy spectrum (see Figure 4.24). Indeed, there does appear to be a feature around 4.9-5.5 MeV, to within errors. However, although this suggests the presence of a possible small α population is it not yet conclusive.

There are 124498 events with E_{dep} <500 keV in this data-set (considering the first bin of the solid-line histogram in Figure 4.24). Since the total acquisition time of these data files is ∼16 minutes this implies an event rate of ∼0.26 events/keV/s.

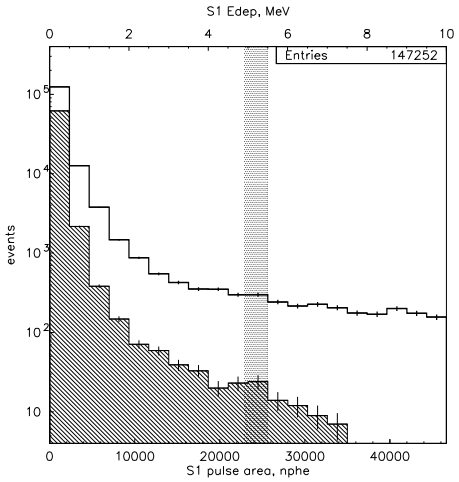

Figure 4.24: Histogram of S1 energy, E_{dep}, for the first pulses in the LS SUM channel up to 10 MeV. The bold line corresponds to all reduced data with no applied cuts. Only events satisfying the demand for one, unsaturated pulse with $FWHM$ <50 ns are plotted in the shaded region. A possible hint of a α population can be seen in the expected 4.9-5.5 MeV energy band here, to within errors.

Event Identification

Focusing back on which type of events the high-τ population (seen in Figure 4.23, upper panels) could be composed of, their characteristics, and specifically the pulse shape, were probed. Four boxes (labelled A-D) were strategically placed on the plot shown in the upper right panel of Figure 4.23 to sample events of different decay time constants and energies in order to investigate the diversity (or not) of pulse shapes being observed (see Figure 4.25). Boxes A-D are defined by: 4.7≤ E_A(MeV)≤5.7 and 10≤ τ_A(ns)≤20; 0.5≤ E_B(MeV)≤0.6 and 38≤ τ_B(ns)≤40; 5.5≤ E_C(MeV)≤6.5 and 55≤ τ_C(ns)≤85; 5.5≤ E_D(MeV)≤6.5 and 25≤ τ_D(ns)≤55. No events were found

within the expected α region, as defined by box A. Boxes B, C and D were found to contain 54, 195 and 10 events, respectively. A typical event, sampled within each box (B-D), was individually viewed in ZE3RA to assist in event identification and that of box B is presented in Figure 4.26. The uneven shape of the pulse tails of the three events sampled from boxes B, C and D appear well-behaved and may be indicative of cosmic ray events.

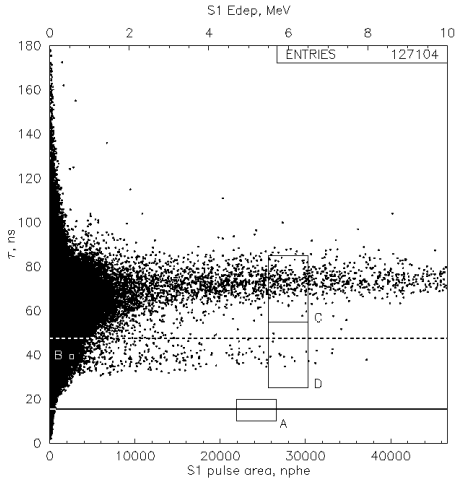

Figure 4.25: Scatter plot of τ vs S1 energy, E_{dep}, for all unsaturated, first pulses in the LS SUM channel with four, event sampling boxes positioned (A-D). Expected τ_α and τ_γ values[150] are represented by the solid and broken lines, respectively.

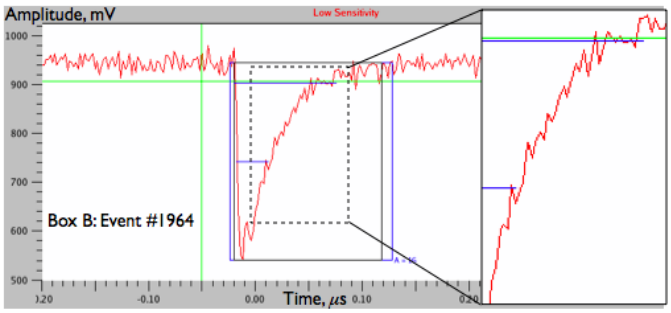

Figure 4.26: Pulse screenshot taken from the ZE3RA v1.3 reduction software in the LS SUM channel (pulse amplitude, mV vs time, μs) for box B, zooming in on the uneven shape of the pulse tail.

'Upper' and 'Lower' (High- and Low-τ) Populations

Two regions with 4.0$\leq$ $E_{dep}(MeV)$ $\leq$6.0 have been defined on Figure 4.23 (upper right) in an attempt to compare and contrast event locations in the high-

(55≤ $\tau_{upper}(ns)$ ≤90) and low-τ (20≤ $\tau_{lower}(ns)$ ≤55) populations, marked as boxes U and L respectively, utilising the peak PMT parameter (see Figure 4.27). The peak PMT is defined as the channel with the largest deposited energy response, $AREA$, for each event and is implemented using a PAW function. Figure 4.27 (upper left panel) reveals that events in the high-τ region (544 events) have interaction sites located, mainly, around the edge of the array. In contrast, low-τ events (36 events) appear more confined to the central PMTs (upper right).

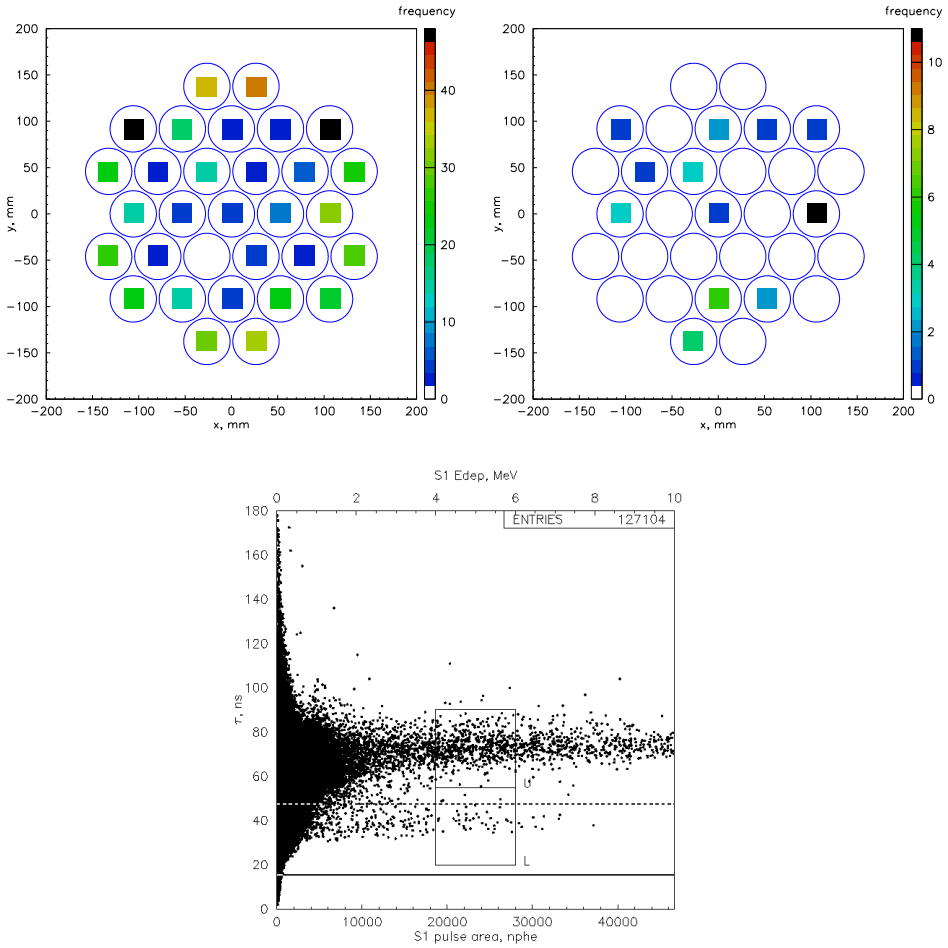

Figure 4.27: S1 zero-field 060519 background density distributions of the LS peak PMT frequency (z-axis) for the upper and lower (high- and low-τ) populations (upper panels), boxes U and L respectively. The square bins do not reflect the true, circular response areas of the PMT photocathodes and are an artefact of the histogram plotting. Scatter plot of τ vs S1 energy, E_{dep}, for all unsaturated, first pulses in the LS SUM channel (lower) displaying the selection regions for the upper and lower populations, sampled for 4≤ $E_{dep}(MeV)$ ≤6 and 55≤ $\tau_{upper}(ns)$ ≤90 and 20≤ $\tau_{lower}(ns)$ ≤55. Expected τ_α and τ_γ values[150] are represented by the solid and broken lines, respectively.

Amplifier 'Distortion' and DAQ 'Saturation'

The γ population seen in the τ vs E_{dep} scatter plots (Figure 4.23) is not well defined. This may be due to distortion effects; distortion of the signal by the amplifiers, above certain threshold voltages, V_{dist1}. It is important to note that these events, 'distorted' in the amplifiers may not necessarily appear 'saturated' in ZE3RA. The setup with which these data were acquired is consistent with Figure 3.11 (Section 3.5).

Amplifier distortion effects may be due to: the input voltage (or signal amplitude) being too large, causing the amplifier to limit; amplification not taking place over the whole signal cycle (incorrect biasing); or amplification not being linear over the entire frequency range of inputs.

In order to estimate the voltages above which amplifier signals are 'distorted' and full scale channel settings, FS (V), are 'saturated', the PMT output voltages at different stages of acquisition, $P0$-$P3$ (V) were calculated and are defined in Figure 4.28. The output voltage of the attenuator, $P2$, is simultaneously split into the second stage amplifier input and the LS readout channel, defining the first stage distortion amplitude voltage, V_{dist1} (V), for the LS channels. Similarly, the output voltage of the second stage amplifier, $P3$, defines V_{dist2} (the HS readout channel). The distortion voltage of $P3$ (2.0 V) is less than that of $P1$ (2.5 V), due to $P2$ being positioned at a junction and the cascade of amplifiers. Additional definitions include: the OS (V) and OS' (V) offset values in the LS and HS respectively, corresponding to 80% of $FS/2$; and $G1$ and $G2$ are the gains of the first and second stage amplifiers, respectively. The voltages at which the LS and HS channels 'saturate' are dependent upon the FS and OS (or OS') ACQIRIS settings and occurs above 90% of the FS values. For this particular data-set FS_{LS}=1.0 V and FS_{HS}=0.1 V.

Figure 4.29 reproduces Figure 4.23 (upper right panel) but with additional cuts, plotting events that only distort at the first stage amplifier in PMT #2 i.e. satisfying $AMPLITUDE(1, 34) > V_{dist1}(34)$ where $V_{dist1}(34)$=0.75 V (see Table 4.4 and similarly, for the second stage, Table 4.5). From this, just two events (of 1065 events which, up to 30 MeV, suffer distortion in any one LS PMT channel) are shown to be distorted at the amplifiers, in PMT #2 (LS channel #34) only. It is clear the total 1065 events do contribute to the high-τ events seen in the complete data-set but do not occur in significant numbers. Similar plots for all, individual channels have been produced (not shown), confirming that this is the case for any one particular

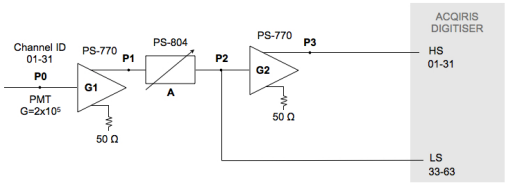

Figure 4.28: Schematic of the ZEPLIN III DAQ circuit for the acquisition of surface data and definition of the PMT output voltages at different stages of acquisition, $P0$-$P3$ (V): $P0$ is the PMT output; $P1$ is the output voltage of the first stage amplifier, prior to attenuation, A; $P2$ is the output voltage of the attenuator, simultaneously split into the second stage amplifier input and the LS readout channel; $P3$ is the output voltage of the second stage amplifier; and $G1$ and $G2$ are the gains of the first and second stage amplifiers, respectively.

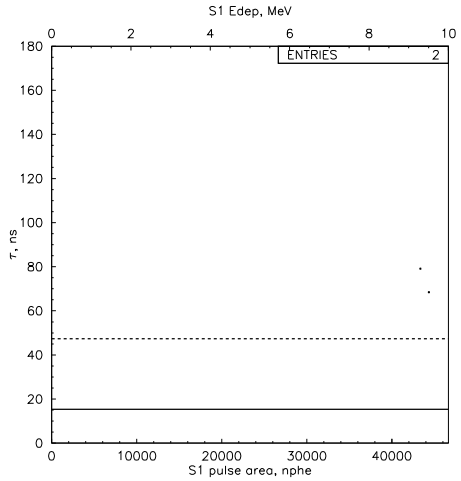

Figure 4.29: Scatter plots of τ vs S1 energy, E_{dep}, for all unsaturated, first pulses in the LS SUM channel. Expected τ_α and τ_γ values[150] are represented by the solid and broken lines, respectively. The events satisfy additional cuts ($AMPLITUDE(1,34) > V_{dist1}(34)$; $AMPLITUDE(1,[33,35{-}63]) \leq V_{dist1}([33,35-63])$) and thus, only those which are distorted at the amplifier in channel #34 (PMT #2) are shown here.

readout channel.

A scatter plot of pulse FWHM vs τ for all, unsaturated, first pulses in the LS SUM channel, is shown in Figure 4.30 (left panel). Note that no cut on the pulse FWHM has been applied here. Comparison of data with the superposed $WIDTH50{=}\tau\ln(2)$ function may prove useful when attempting to quantify distortion of pulse signals by the amplifier, or saturation within the acquisition settings or reduction software. This asymmetric plot shows a region of events which deviate from the expected

PMT#	PMT Output $P0$ (V)	$P1$ (V) $P0 \times G1$	A	$P2$ (V) (P1*A)/2	$P3$ (V) $P2 \times G2$	$dist(1)$	sat_{LS}	$dist(2)$	sat_{HS}	total
1	0.25	2.5	1.0	1.25	12.50	1	1	1	1	1
2	0.25	2.5	0.6	0.75	7.50	1	0	1	1	1
3	0.25	2.5	0.4	0.50	5.00	1	0	1	1	1
4	0.25	2.5	0.8	1.00	10.00	1	1	1	1	1
5	0.25	2.5	0.8	1.00	10.00	1	1	1	1	1
6	0.25	2.5	0.5	0.63	6.25	1	0	1	1	1
7	0.25	2.5	0.5	0.63	6.25	1	0	1	1	1
8	0.25	2.5	0.9	1.13	11.25	1	1	1	1	1
9	0.25	2.5	0.4	0.50	5.00	1	0	1	1	1
10	0.25	2.5	0.5	0.63	6.25	1	0	1	1	1
11	0.25	2.5	1.0	1.25	12.50	1	1	1	1	1
12	0.25	2.5	0.3	0.38	3.75	1	0	1	1	1
13	0.25	2.5	1.0	1.25	12.50	1	1	1	1	1
14	0.25	2.5	0.3	0.38	3.75	1	0	1	1	1
15	0.25	2.5	0.4	0.50	5.00	1	0	1	1	1
16	0.25	2.5	0.7	0.88	8.75	1	0	1	1	1
17	0.25	2.5	0.6	0.75	7.50	1	0	1	1	1
18	0.25	2.5	0.6	0.75	7.50	1	0	1	1	1
19	0.25	2.5	0.5	0.63	6.25	1	0	1	1	1
20	0.25	2.5	0.5	0.63	6.25	1	0	1	1	1
21	0.25	2.5	0.3	0.38	3.75	1	0	1	1	1
22	0.25	2.5	0.9	1.13	11.25	1	1	1	1	1
23	0.25	2.5	0.4	0.50	5.00	1	0	1	1	1
24	0.25	2.5	0.3	0.38	3.75	1	0	1	1	1
25	0.25	2.5	0.4	0.50	5.00	1	0	1	1	1
26	0.25	2.5	0.5	0.63	6.25	1	0	1	1	1
27	0.25	2.5	0.6	0.75	7.50	1	0	1	1	1
28	0.25	2.5	0.4	0.50	5.00	1	0	1	1	1
29	0.25	2.5	0.5	0.63	6.25	1	0	1	1	1
30	0.25	2.5	0.4	0.50	5.00	1	0	1	1	1
31	0.25	2.5	0.6	0.75	7.50	1	0	1	1	1

Table 4.4: Calculations of the voltages at which the first stage amplifiers are estimated to 'distort' the LS and HS signal amplitude in each individual channel, $P2 = V_{dist1}(LS)$ and $P3 = V_{dist1}(HS)$, respectively. The last five columns of the table provide information on whether distortion or saturation occurs and the overall effect ('yes'=1, 'no'=0). For this scenario, all HS channels suffer distortion and all HS channels are saturated.

well-behaved exponential shape, around τ ∼70 ns and $WIDTH50$ >80 ns. The digitization effect apparent in the data is due to the ACQIRIS digitization and the 2 ns sampling rate. The plot in Figure 4.30 (right panel) is similar. However, only events which are distorted, in one or more channels, by the amplifiers are shown here.

PMT#	PMT Output $P0$ (V)	$P1$ (V) $P0 \times G1$	A	$P2$ (V) (P1*A)/2	$P3$ (V) $P2 \times G2$	$dist(1)$	sat_{LS}	$dist(2)$	sat_{HS}	total
1	0.04	0.40	1.0	0.20	2.00	0	0	1	1	1
2	0.07	0.67	0.6	0.20	2.00	0	0	1	1	1
3	0.10	1.00	0.4	0.20	2.00	0	0	1	1	1
4	0.05	0.50	0.8	0.20	2.00	0	0	1	1	1
5	0.05	0.50	0.8	0.20	2.00	0	0	1	1	1
6	0.08	0.80	0.5	0.20	2.00	0	0	1	1	1
7	0.08	0.80	0.5	0.20	2.00	0	0	1	1	1
8	0.04	0.44	0.9	0.20	2.00	0	0	1	1	1
9	0.10	1.00	0.4	0.20	2.00	0	0	1	1	1
10	0.08	0.80	0.5	0.20	2.00	0	0	1	1	1
11	0.04	0.40	1.0	0.20	2.00	0	0	1	1	1
12	0.13	1.33	0.3	0.20	2.00	0	0	1	1	1
13	0.04	0.40	1.0	0.20	2.00	0	0	1	1	1
14	0.13	1.33	0.3	0.20	2.00	0	0	1	1	1
15	0.10	1.00	0.4	0.20	2.00	0	0	1	1	1
16	0.06	0.57	0.7	0.20	2.00	0	0	1	1	1
17	0.07	0.67	0.6	0.20	2.00	0	0	1	1	1
18	0.07	0.67	0.6	0.20	2.00	0	0	1	1	1
19	0.08	0.80	0.5	0.20	2.00	0	0	1	1	1
20	0.08	0.80	0.5	0.20	2.00	0	0	1	1	1
21	0.13	1.33	0.3	0.20	2.00	0	0	1	1	1
22	0.04	0.44	0.9	0.20	2.00	0	0	1	1	1
23	0.10	1.00	0.4	0.20	2.00	0	0	1	1	1
24	0.13	1.33	0.3	0.20	2.00	0	0	1	1	1
25	0.10	1.00	0.4	0.20	2.00	0	0	1	1	1
26	0.08	0.80	0.5	0.20	2.00	0	0	1	1	1
27	0.07	0.67	0.6	0.20	2.00	0	0	1	1	1
28	0.10	1.00	0.4	0.20	2.00	0	0	1	1	1
29	0.08	0.80	0.5	0.20	2.00	0	0	1	1	1
30	0.10	1.00	0.4	0.20	2.00	0	0	1	1	1
31	0.07	0.67	0.6	0.20	2.00	0	0	1	1	1

Table 4.5: Calculations of the voltages at which the second stage amplifiers are estimated to 'distort' the LS and HS signal amplitude in each individual channel, $P2 = V_{dist2}(LS)$ and $P3 = V_{dist2}(HS)$, respectively. The last five columns of the table provide information on whether distortion or saturation occurs and the overall effect ('yes'=1, 'no'=0). For this scenario, all HS channels are saturated but the LS channels are undistorted and unsaturated.

Although any of these pulses, when viewed in ZE3RA, would appear to have a well-behaved, exponential tail (observed symmetry about $WIDTH50{=}\tau\ln(2)$), deeming them trustworthy, their signal has in fact been distorted and therefore should not be relied upon.

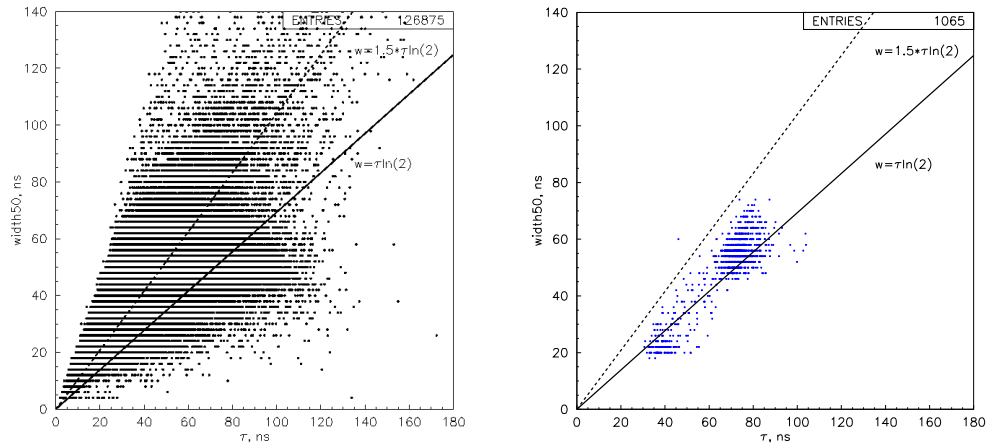

Figure 4.30: Scatter plot of pulse $WIDTH50$ (ns) vs decay time constant, τ (ns) for all unsaturated, first pulses in the LS SUM channel (left panel). The solid line shows how the pulse FWHM varies with τ for a well-behaved exponential pulse shape obeying $WIDTH50{=}\tau\ln(2)$ while the broken line corresponds to $WIDTH50{=}1.5{\times}\tau\ln(2)$. The latter is used to force symmetry of the distribution of events. It is clear the events are distributed asymmetrically about the solid line. The same plot, but with an additional amplifier distortion cut whereby only (blue) events which are distorted in one or more channels, is also shown (right). Here, the distribution is symmetric about the $WIDTH50{=}\tau\ln(2)$ function.

Although accounting for the amplifier 'distortion effect' can remove large numbers of events at high energies it does not make the high-τ γ population more clearly defined below 1 MeV (see Figure 4.31). The black data points shown correspond to events which are not suffering distortion in any of the readout channels. The events plotted in blue correspond to those which are distorted by the first amplifier in one or more channels, have time constants in the range $30 \lesssim \tau(ns) \lesssim 60$, with E_{dep} >0.5 MeV and appear to populate two distinct regions. Hence, any amplifier distortion effect does not fully account for the observed high-τ events.

Quantifying 'Saturation'

Figure 4.30 (left panel) shows some possible evidence for saturation of pulse signals where the pulse tail deviates from the expected, well-behaved, exponential shape defined by $WIDTH50{=}\tau\ln(2)$ since the scatter is not symmetric about this function. This saturation would have occurred within the acquisition (ACQIRIS) or reduction (ZE3RA) software and is an effect that should be considered distinct from the previously described 'amplifier distortion' effect. Quantifying the satura-

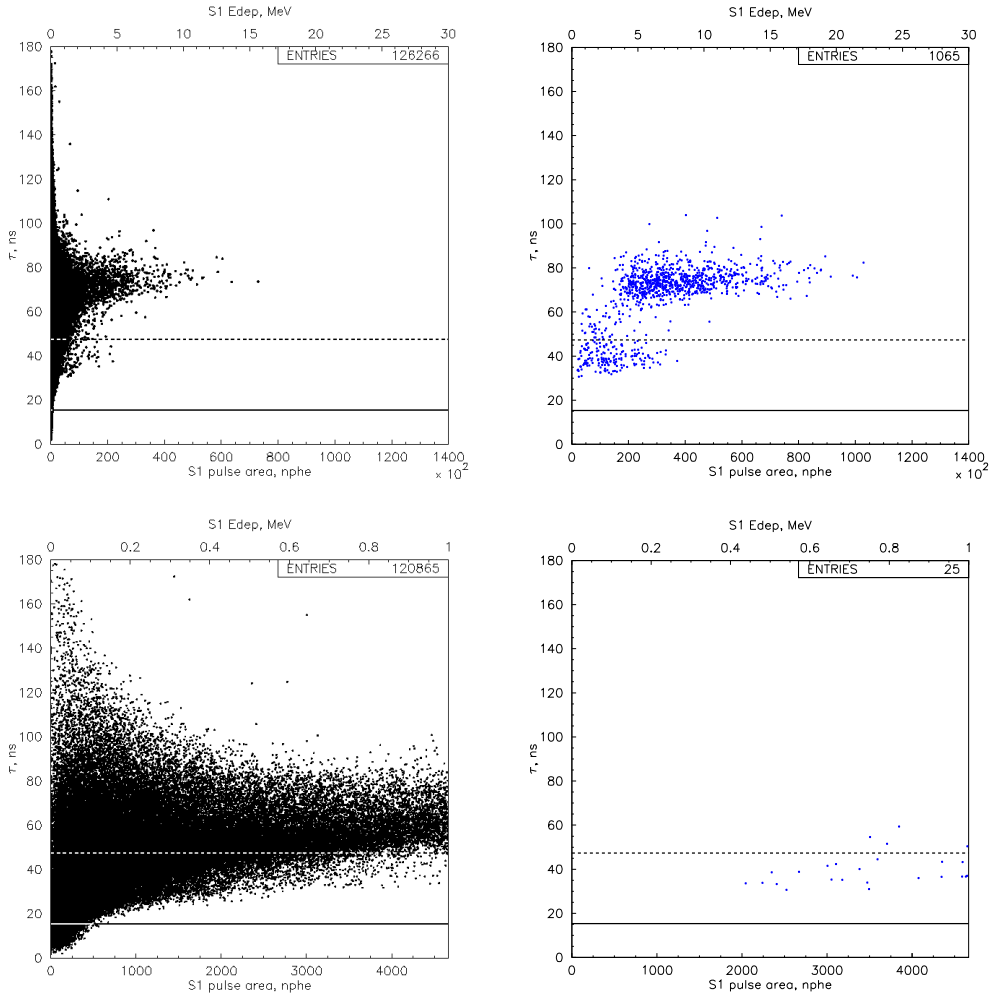

Figure 4.31: Scatter plots of τ vs S1 energy, E_{dep}, for all unsaturated, first pulses in the LS SUM channel. Expected τ_α and τ_γ values[150] are represented by the solid and broken lines, respectively. Distributions of events which are not distorted by the first stage amplifier in any of the readout channels are shown over two energy ranges (upper left and lower left panels). The γ population, with expected time constants of 47.4±0.4 ns[150], is clear. However, the population remains poorly defined, for E_{dep} <1 MeV, at large τ. Similarly, events which are distorted in one or more channels are also shown (upper right and lower right panels).

tion effect may prove useful when defining additional cuts to refine the τ vs E_{dep} scatter plots and to identify populations with more confidence.

The saturation algorithm implemented within ZE3RA is defined as: if the minimum value of a pulse in an individual readout channel is equal to -128, where the ACQIRIS amplitude digitized scale ranges from -128 to +127, with 256 discrete levels, then ZE3RA deems the pulse as 'saturated'; for the SUM channel the saturation check

is called in all thirty-one, individual, contributing channels and a pulse in the SUM is tagged as 'saturated' if any one or more of these are themselves 'saturated'. The ZE3RA reduction software does not quantify by what degree a pulse is 'saturated'.

It may be possible to quantify pulse saturation in terms of scatter around the $WIDTH50{=}\tau\ln(2)$ function. In a brief attempt to see how forcing symmetry about this line refines the scatter plot (Figure 4.30, left panel) an additional cut ($WIDTH50/\tau$ <1.04) was invoked. This cut corresponds to the modified function $WIDTH50{=}1.5{\times}\tau\ln(2)$, represented by the broken line. Following this additional cut the high-τ, low-energy population does appear to be significantly reduced (see Figure 4.32).

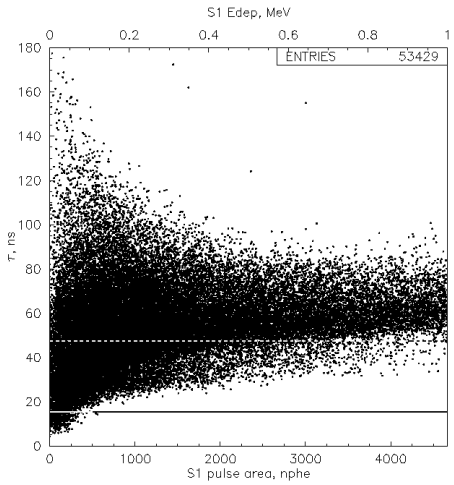

Figure 4.32: Scatter plot of τ vs S1 energy, E_{dep}, for all unsaturated, first pulses in the LS SUM channel which are not distorted by the first stage amplifier in any of the readout channels. Expected τ_α and τ_γ values[150] are represented by the solid and broken lines, respectively. The γ population is more tightly defined here, for E_{dep} <1 MeV, at large τ, following the $WIDTH50/\tau$ <1.04 correction cut.

Cosmic Ray Muon Events

When attempting to identify the high-τ events seen in this data-set all possible sources of background components should be considered. In the surface laboratories internal sources of background, by which one means those due to the natural radioactivity in the operating environment, include instrument components and the construction materials of the laboratory itself (such as ^{40}K within concrete). External sources of background signal recorded by the instrument will be due to cosmic secondary radiation; cosmic ray muons.

Cosmic ray interactions in the Earth's atmosphere produce particle showers of photons, electrons, heavy ions and high-energy neutrinos, yielding an assortment of muons, pions, electrons, protons, neutrons and photons, with energies up to ∼GeV. At sea level muons dominate the charged particle secondary flux from cosmic ray interactions with a flux of ∼1 $cm^{-2}min^{-1}$.[151] The next most abundant particles at sea level are neutrons.

The events recorded from cosmic rays are comprised of a series of many, narrow events, each depositing small amounts of energy and generating a wide, overall signal. This is due to the time between each one being very small since their kinetic energy is very high. The energy loss of muons, E_{loss}, ranges from about 1.1 to 1.8 MeV g^{-1} cm^{-2} in absorber materials with high (e.g. Xe) to low atomic number, respectively.[151] Using the following relationship, the energy deposited by a cosmic ray muon in LXe, with density ρ=2.953 g cm^{-3}[116], can be estimated:

$$E_{dep} = E_{loss} \cdot x \cdot \rho \tag{4.21}$$

where x (cm) is the interaction track length in the LXe volume. Assuming the cosmic ray particles interacting in the Xe are 'minimum ionising' (i.e. with velocity $\nu \sim c$=3×10^{10} cm s^{-1}) the interaction time (or pulse rise time), t, can be estimated employing $t = x/\nu$.

Events from the upper, high-τ, extended population were sampled in order to investigate their nature within a selection box defined by 2≤ E_{dep} ≤18 MeV and 50≤ τ ≤100 ns (see Figure 4.33, left panel). The corresponding energy spectrum, with a peak centred at ∼10.5 MeV, is also shown (right panel). If one assumes the events comprising this peak are cosmic secondary particles such an energy corresponds to a track length of 3.2 cm which is only a few millimetres short of the full 4.0 cm LXe depth; these particles would be travelling almost vertically through the target volume.

An experimentally obtained track length of 3.28 MeV/cm (=10.5 MeV/3.2 cm) does show good agreement with the purely theoretical value of 3.25-5.32 MeV/cm, calculated according to Equation 4.21.

The geometry shown in Figure 4.34 gives an example of 5 cm track from a cosmic ray induced muon, depositing ∼16 MeV in the LXe (the highest energy event detected in Figure 4.33) for a simplified, 2-dimensional approximation. This means, if the high-τ population, with τ ∼70 ns are cosmic secondary particles their interaction

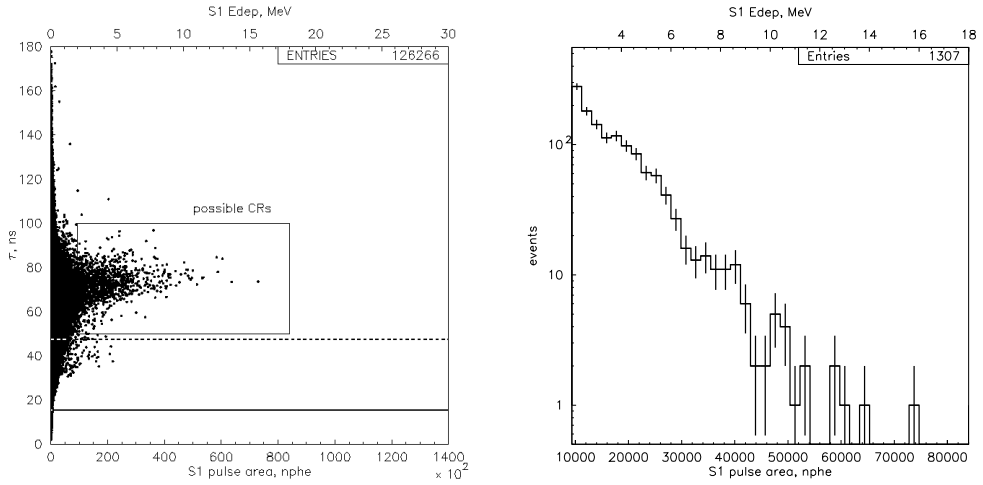

Figure 4.33: Scatter plot of τ vs S1 energy, E_{dep}, for all unsaturated, first pulses in the LS SUM channel for events which are not distorted by the first stage amplifier in any of the readout channels (left panel). Expected τ_α and τ_γ values[150] are represented by the solid and broken lines, respectively. It is not clear what type of events the 1307 contained within the box, defined by $2 \leq E_{dep} \leq 18$ MeV and $50 \leq \tau \leq 100$ ns, are. The energy spectrum of these events is also shown with a peak centred at ∼10.5 MeV (right).

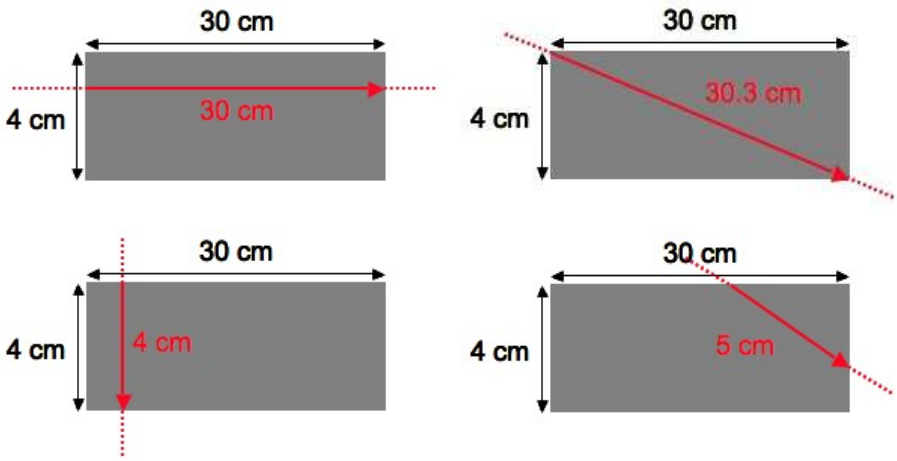

Figure 4.34: Schematic of the LXe region (shaded area) showing various paths cosmic ray particles interactions can take. Track lengths of 30.0 cm (t ∼1.00 ns, E_{dep} ∼97 MeV), 30.3 cm (t ∼1.01 ns, E_{dep} ∼98 MeV), 4.0 cm (t ∼0.13 ns, E_{dep} ∼13 MeV) and 5.0 cm (t ∼0.17 ns, E_{dep} ∼16 MeV) are shown in the panels (clockwise from upper left), respectively. The geometry depicted in the upper right panel clearly gives rise to the longest track length and therefore the largest deposited energy.

track lengths are <5 cm and the rise times of the pulses are <0.17 ns. In order to get just a fraction of their ∼GeV energy deposited into the LXe the incident cosmic ray particles would have to just clip the edge of the target volume. However, the path of these events are estimated to be approximately vertical. Therefore, it is unlikely that the wide events observed are energetic enough to be associated with cosmic ray interactions.

It is possible to assess where, in the PMT array, energy is deposited for a particular event by viewing signals in each individual channel within ZE3RA. Thus, this (early and unrefined) position reconstruction approach may be used to identify the incoming particle. A few events were selected from within the box shown on Figure 4.33 (left panel) and viewed within ZE3RA in order to further investigate the cosmic ray origins of these outliers. Figures 4.35 & 4.36 are composed of ZE3RA screenshots of events (#s 1112 and 1534, respectively) acquired in the LS channels, for example. Although these events are high-τ events (consistent with a cosmic ray scenario) the interaction tracks shown here are not linear but appear clustered. This, again, reinforces the idea that cosmic ray muon interactions do not explain the observed high-τ population.

In conducting this study, a 'double feature' in the peak of the pulse shapes was discovered (see Figures 4.35 & 4.36). This effect was found to exist in both individual and SUM channels, suggesting it is independent of the relative time delay of each PMT. Also, the 'double feature' was not necessarily seen in the same channels for different events. For instance, event #1112 occurred in the central region while event #1534 was located around the lower half of the array. Evidence of this feature is typically seen in all six surrounding PMTs for any event. On occasions, a 'triple feature' can even be seen where the separation between the three peaks, ∼10ns, is comparable (event #1112, PMTs #4 & 6). Two signals, acquired within the same PMT but for low- and high-τ events, were overlaid and the 'double features' in both were seen to coincide. This is suggestive of the effect and pulse shape being characteristic of each channel and may be evidence for electronic ringing (or after-pulsing) in the BNC signal cables. Furthermore, the 'double feature' was observed in low-amplitude pulses, well below the saturation or distortion voltage, while being absent in pulses of relatively higher amplitude: ruling out the acquisition or reduction processes as being the underlying cause.

It should be noted that the underground data (see Chapter 5, Section 5.1) do not seem to show the high-τ distribution seen within the surface data, suggesting it was

perhaps due to some, probably software, artefact or cosmic-ray effect.

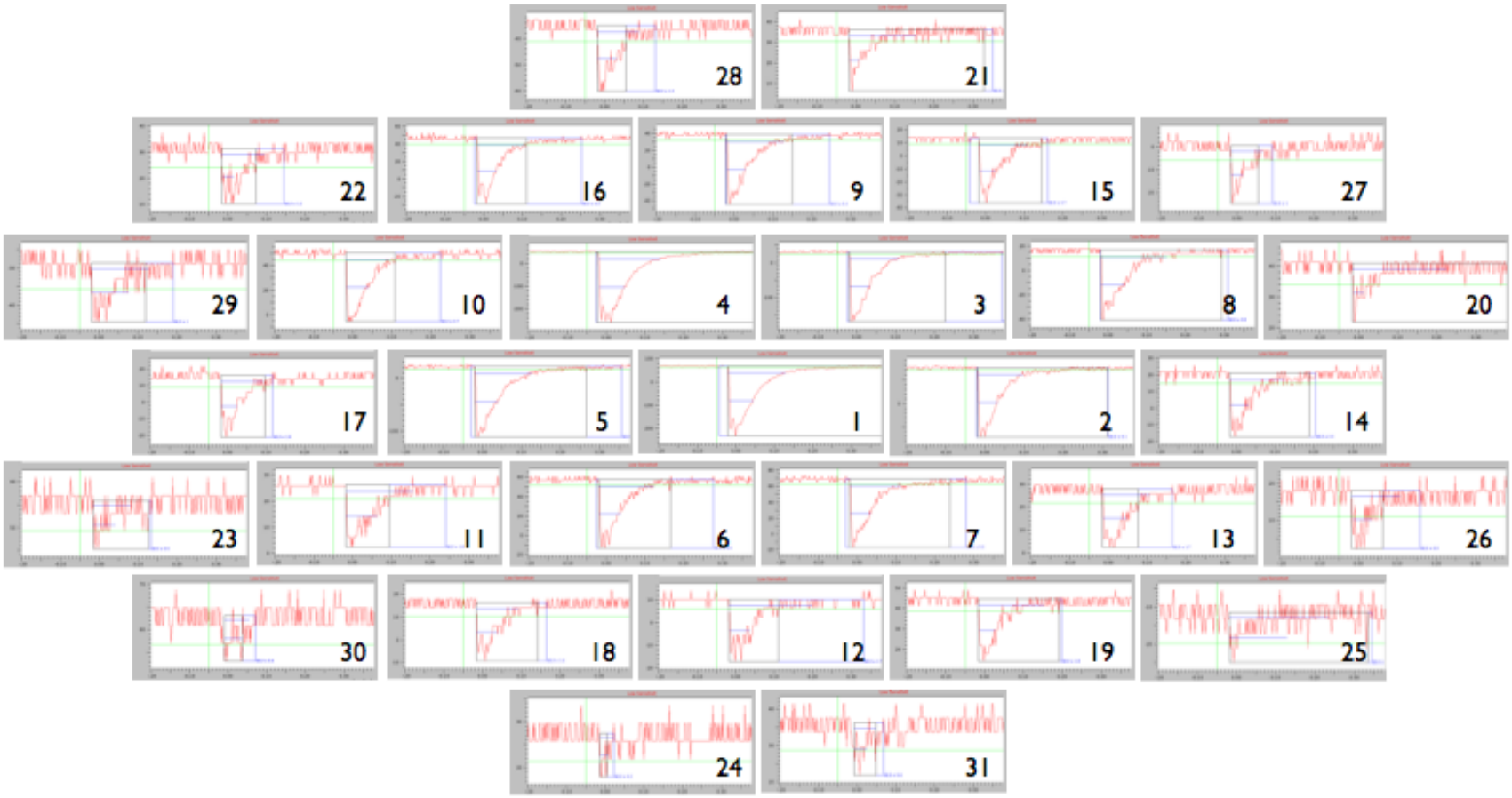

Figure 4.35: S1 signals (pulse amplitude (mV) vs time (μs)) as seen in individual LS channels across the array for event #1112. Pulse amplitude, τ and E_{dep} characteristics in the LS SUM channel are 1.77 V, 77.55 ns and 5.12 MeV, respectively.

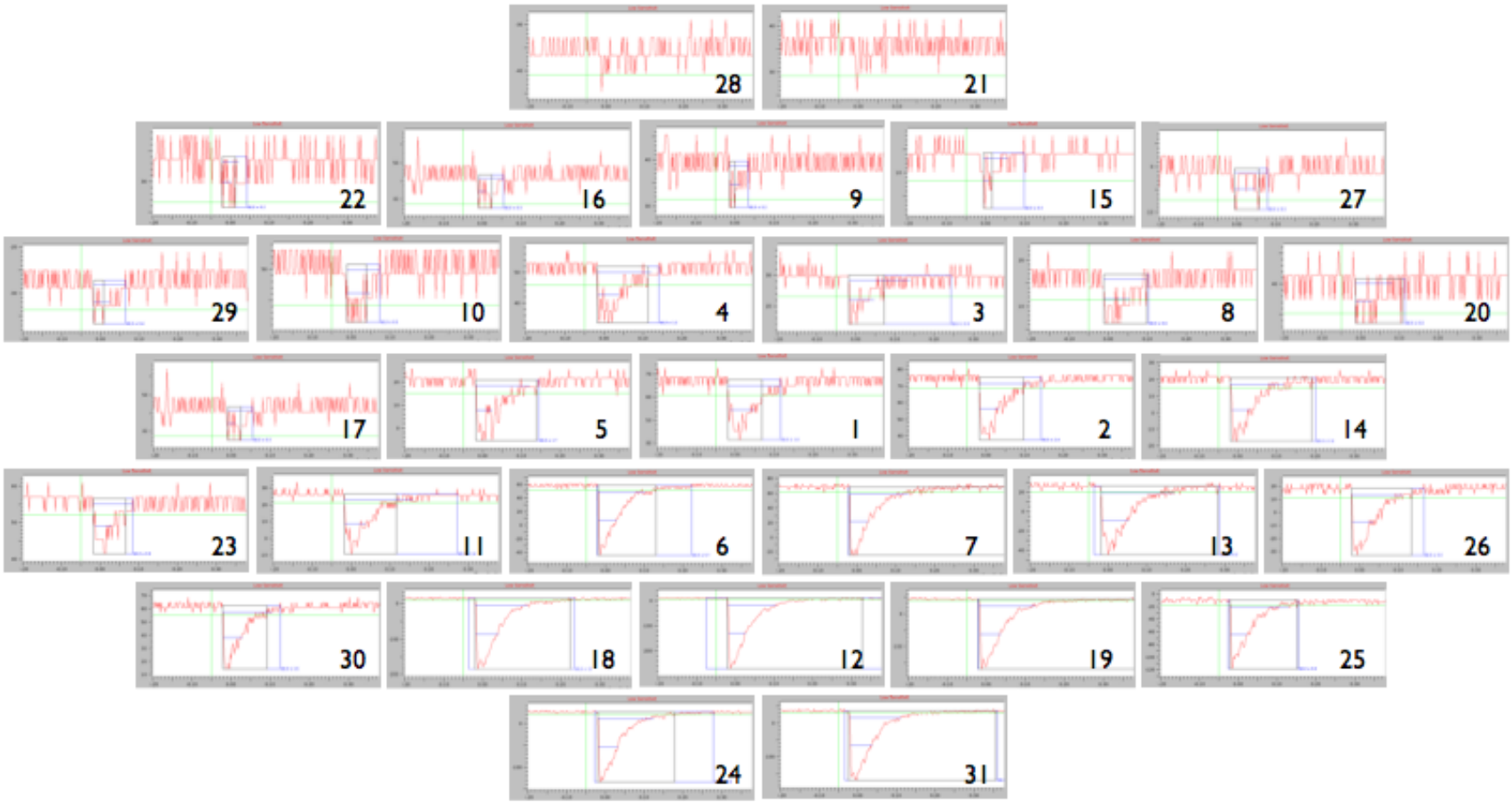

Figure 4.36: S1 signals (pulse amplitude (mV) vs time (μs)) as seen in individual LS channels across the array for event #1534. Pulse amplitude, τ and E_{dep} characteristics in the LS SUM channel are 1.67 V, 71.82 ns and 4.84 MeV, respectively.

Energy-Slicing

The true nature of the heavily-populated γ distribution in Figure 4.31 (lower left panel), around τ ~47 ns, was studied further by slicing in energy, below 0.3 MeV (see Figure 4.37). After being sliced in the energy the τ histograms are consistent with a γ-population, centred around τ ~47 ns and a clear systematic change in mean τ value with S1 energy is observed. Although the events in each slice do extend up to large τ it is clear that the number of such events is small relative to those within the peak bin.

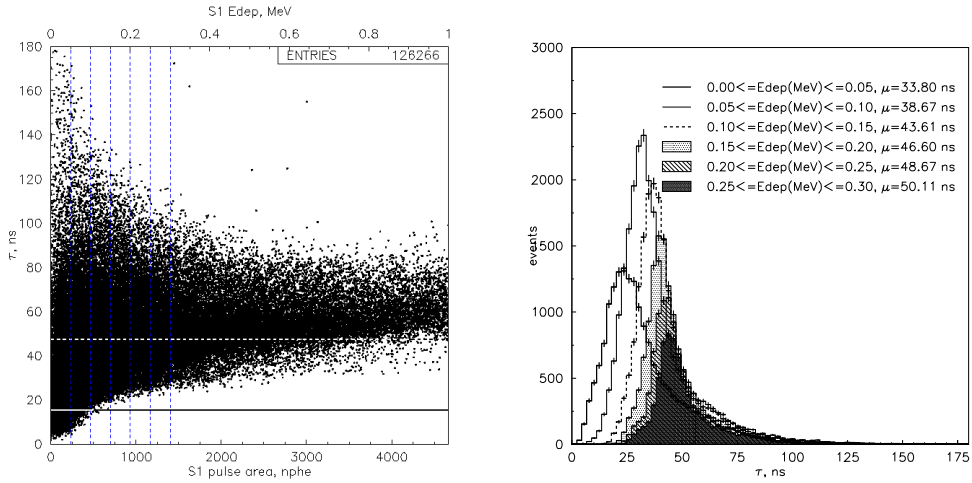

Figure 4.37: Scatter plot of τ vs S1 energy, E_{dep}, for all unsaturated, first pulses in the LS SUM channel which are not distorted by the first stage amplifier in any of the readout channels (left panel). The six energy slices used to histogram the γ distribution are clearly marked. Expected τ_α and τ_γ values[150] are represented by the solid and broken lines, respectively. Resulting τ histograms, corresponding to the six energy slices are also shown (right).

Decay Time Constant Comparisons

The decay time constants calculated by the ZE3RA reduction software were verified by fitting single exponential functions (with a baseline consideration), assuming a single dominant decay component to the scintillation pulse shape, to the right-hand tail of the sample pulses (as described in Section 4.2.4). This was done to check the values output by a very preliminary version of ZE3RA but also to possibly explain the presence of very wide (τ >70 ns) events, or the 'upper, high-τ' population (as seen in Figure 4.23). Figure 4.38 demonstrates that the time constants (and pulse widths) computed by the two described methods are consistent for the LS SUM

channel, for event #2092 (with LS SUM pulse amplitude of 0.15 V and E_{dep} of 0.26 MeV) and for the HS SUM channel. After evaluating numerous events in this way, ZE3RA was found to be, if anything, under-estimating the decay time constants in the LS.

The range over which the fit is performed varies between pulses and the start of the fit is defined by the maximum pulse amplitude. Hence, the time constant value obtained by the exponential fit is defined from the pulse maximum. In contrast, ZE3RA defines the start of the fit by the pulse start, that is the time at which the pulse first crosses the set threshold. This inconsistency in establishing the start of the calculation implies that the τ determined by the fit will disagree with that computed by ZE3RA by an amount roughly equal to the pulse rise time ($\lesssim \pm 2$ ns).

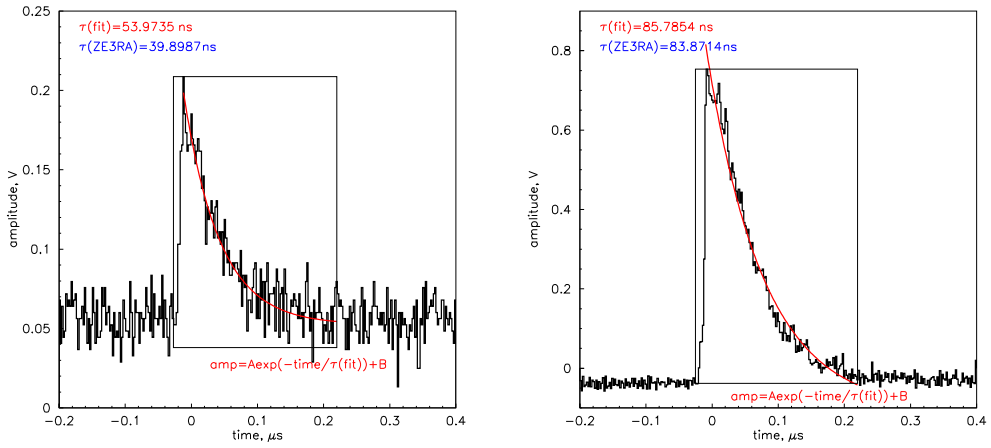

Figure 4.38: The S1 signal of event #2092 in the LS (left panel) and HS (right) SUM channel. For the LS channel a single exponential fit to the pulse rise-time yields a decay time constant, $\tau(fit)$, of 53.9735$\lesssim \pm 5$ ns while ZE3RA returns $\tau(ZE3RA)$=39.8987 ns. Similarly, for the HS channel $\tau(fit)$=85.7854$\lesssim \pm 5$ ns and $\tau(ZE3RA)$=83.8714 ns. The uncertainties in $\tau(fit)$ here are estimated neglecting systematic considerations.

Although analysis of the 060519 zero-field background surface data did not yield any firm conclusions regarding the presence of a ^{222}Rn contaminant nor an α-particle population in general, critical development of the ZE3RA and DAQ software and investigations into the hardware configuration did follow as a direct result. Upper limits on α-particles showed it was not likely to be a major issue. Revision of the DAQ circuit was proposed and later implemented, as a result of this work on amplifier distortion and decay time constants, specifically. The modifications are described in relation to the acquisition of underground data in Section 5.1.3 and

illustrated in Figures 3.13 and 3.14. With iterative studies, the issue of the high-τ and 'upper' and 'lower' populations was eventually resolved.

4.3.3 Unshielded Surface Background Run at Field: ^{222}Rn α Contamination

The with-field (3.01 kV/cm in the liquid) 060520 data-set was acquired for all read-out channels, with no external calibration source present, over a period of ∼60 minutes, with -1.8 kV applied to the PMTs, a total applied voltage of 13.05 kV and a GXe gap estimated to be approximately 3-4 mm. It was subsequently reduced with ZE3RA v1.3.

Many of the analysis tools exploited in Section 4.3.2 to investigate a potential α-particle population, possibly attributable to a ^{222}Rn contaminant, such as probing decay time constant distributions and event identification, have been repeated here in a continuation of the previous studies, but now in the context of two signals: S1 and S2.

As before, the quality of the data was confirmed and a check to see that most events are not saturated in the LS dynamic range was conducted. The S1 amplitude in an individual LS channel (not the SUM) was histogrammed showing some degree of saturation in the LS channels; with 0.6% of events being saturated in the LS SUM. Thus, confirming the need for the saturation cut ($nsaturated(64) = 0$) to be applied.

The time constant distribution, in the LS SUM channel is shown in Figure 4.39. Three analysis cuts employed here demand one or two unsaturated pulses (3> $npulses(64)$>0, $nsaturated(64)$=0, the first of which with $WIDTH50(1, 64)$ <50 ns. The cut on the pulse $FWHM$ <50 ns is applied to remove wider events in order to focus on low-energy S1 pulses and has a visible effect in Figure 4.39.

In order to identify α-particle interactions a plot of τ vs S1 E_{dep} was produced (see Figure 4.40). The data-set was calibrated in energy using the ^{57}Co 060520 with-field (3.01 kV/cm in the liquid) data (see Section 4.3.6) and the measured S1 (and S2) pulse area value of the ∼125 keV photopeak, for the inner 7 PMTs, at 222.50±0.76 phe (and 17394±71 phe). Comparisons can be made between these dual-phase data (LXe and GXe gap) and previous single-phase data (LXe only) since the S1 time constant, τ, does not change with the presence, or not, of a GXe gap

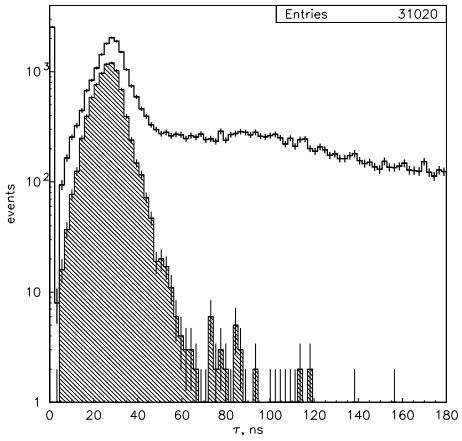

Figure 4.39: Histogram of the first pulses in the LS SUM channel of the time constants, τ, ns. The bold line corresponds to all reduced data with no applied cuts. Only events satisfying the demand for one or two unsaturated pulses, the first of which with $FWHM$ <50 ns, are plotted in the shaded region.

and is only affected by the field applied across the LXe layer, that is the *extraction field*. Previous single-phase measurements with no GXe gap (see Reference [150]) found the with-field (at 1.4 kV/cm in the liquid) τ_γ and τ_α to be 27.0±0.5 ns and 15.40±0.08 ns, respectively: with τ_α remaining approximately constant over an increase in field of 1.4 kV/cm in the liquid. Due to the higher applied extraction and electroluminescence fields at which the 060520 data were acquired, time constants of τ_γ <27.0±0.5 ns and τ_α ≥15.40±0.08 ns are expected.

The upper left panel of Figure 4.40 shows how a high-τ population of events appear extended over this energy range, up to ∼25 MeV. This with-field population appears markedly different from the equivalent zero-field data-set (shown previously in Section 4.3.2, Figure 4.23). This is probably because the with-field data provide an additional signal, both the S1 and S2, for selecting well-behaved events more reliably. The plot shown in the upper right panel, equivalent to the upper left, is redefined with τ in log space to demonstrate the two, separate population components of the distribution. This is shown more clearly in Figure 4.41 where the distribution is subdivided into events with just one pulse in the timeline ($npulses(64) = 1$, green data-points) and those with just two pulses ($npulses(64) = 2$, blue data-points). From this, its highly probable that the upper green population, events with τ >100 ns, are probably S2 signals, not S1s, that have triggered the system. Furthermore, the blue S1 population is seen to migrate from the expected S1 τ_γ value up to

τ ~10000 ns, perhaps due to the pulse integration time being over-estimated in ZE3RA.

The lower left panel suggests that the main population seen here are γ events and is reinforced by the $FWHM$ <50 ns cut removing the high-τ, extended population (blue data-points). No population, separate in S1 energy from the main, γ-population is visible in the upper right panel, particularly within the expected E_α region of ~4.9-5.5 MeV and τ_α ~15.40±0.08 ns.

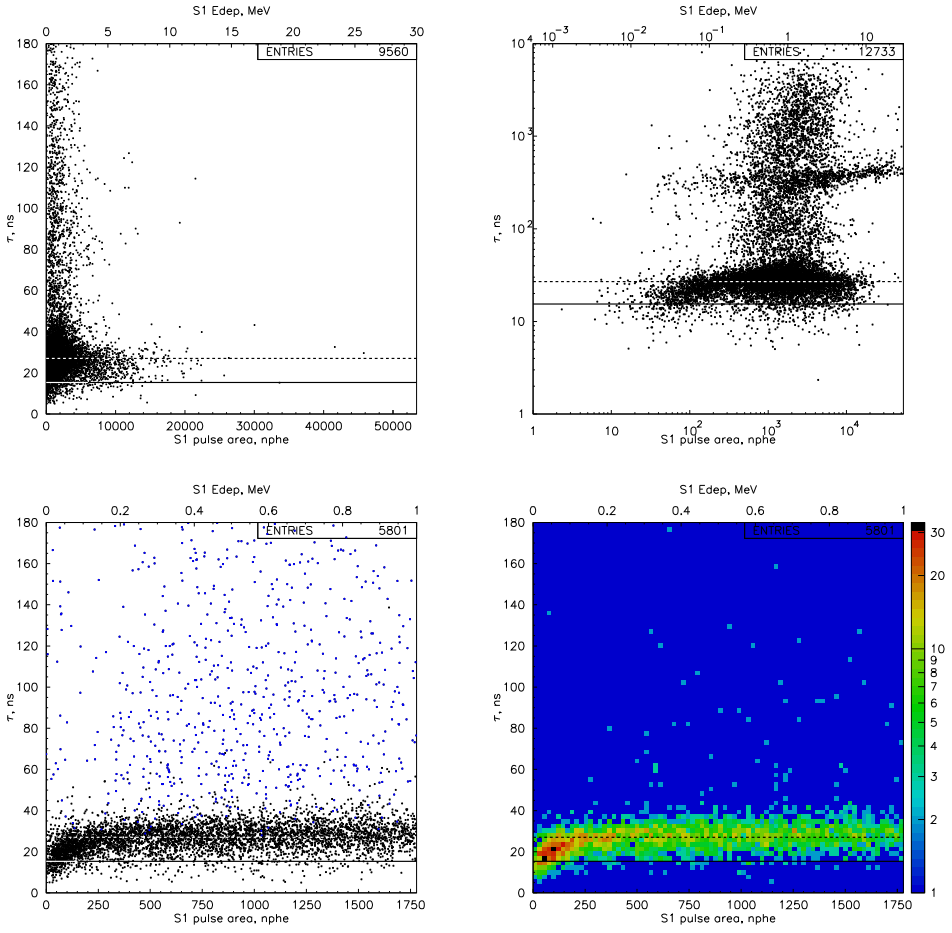

Figure 4.40: Scatter plots of τ vs S1 energy, E_{dep}, for all unsaturated, first pulses in the LS SUM channel, with each S1 energy scale successively zoomed (upper left and lower left panel). The plot shown in the upper right panel is equivalent to the upper left but redefined with τ and E_{dep} in log space. Events which may be removed by the $FWHM$ <50 ns cut are superposed on the plot in the lower left (blue data-points). The density plot (lower right, equivalent to the lower left panel) is also shown for clarity, revealing the structure of the distribution. Expected τ_α and τ_γ values, at a lower applied field than employed here,[150] are represented by the solid and broken lines, respectively.

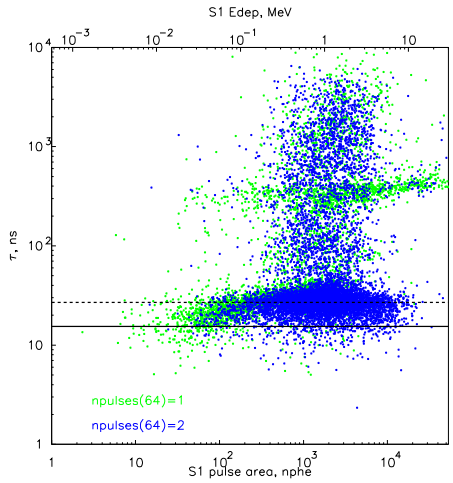

Figure 4.41: Scatter plot of τ vs S1 energy, E_{dep}, for all unsaturated, first pulses in the LS SUM channel with τ and E_{dep} in log space. The full distribution is comprised of two, separate event types: those with just one pulse in the timeline ($npulses(64) = 1$, green data-points); and those with just two pulses ($npulses(64) = 2$, blue data-points). Expected τ_α and τ_γ values, at a lower applied field than employed here,[150] are represented by the solid and broken lines, respectively.

4.9-5.5 MeV Events

If a significant α-particle population is present in the data it should be readily identifiable from the S1 energy spectrum (see Figure 4.42) but there does not appear to be a feature around 4.9-5.5 MeV, to within errors. The $FWHM$ cut seems to remove high-E_{dep} events with a peak at $\sim$7.5 MeV.

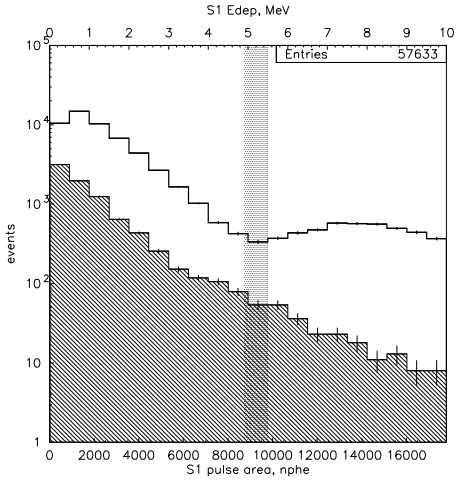

Figure 4.42: Histogram of S1 energy, E_{dep}, for the first pulses in the LS SUM channel up to 10 MeV. The bold line corresponds to all reduced data with no applied cuts. Only events satisfying the demand for one or two unsaturated pulses, the first of which with $FWHM$ <50 ns, are plotted in the shaded region. No α population can be identified in the expected 4.9-5.5 MeV energy band here, to within errors.

Event Identification

In attempting to identify the origin, or types of event comprising the populations in Figure 4.40, four boxes (labelled A-D) were strategically placed to sample events of different decay time constants and energies in order to investigate the diversity (or not) of pulse shapes being observed (see Figure 4.43). Boxes A-D are defined by: 4.7≤ E_A(MeV)≤5.7 and 10≤ τ_A(ns)≤20; 0.27≤ E_B(MeV)≤0.30 and 26.5≤ τ_B(ns)≤27.5; 0.9≤ E_C(MeV)≤1.1 and 35.0≤ τ_C(ns)≤38.0; 3.0≤ E_D(MeV)≤5.0 and 65.0≤ τ_D(ns)≤85.0. Thirty-two events were found within the expected α region, as defined by box A. Boxes B, C and D were found to contain 8, 38 and 21 events, respectively. A typical event, sampled within each box (A-D), was individually viewed in ZE3RA to assist in event identification and those corresponding to boxes C and D are presented in Figure 4.44.

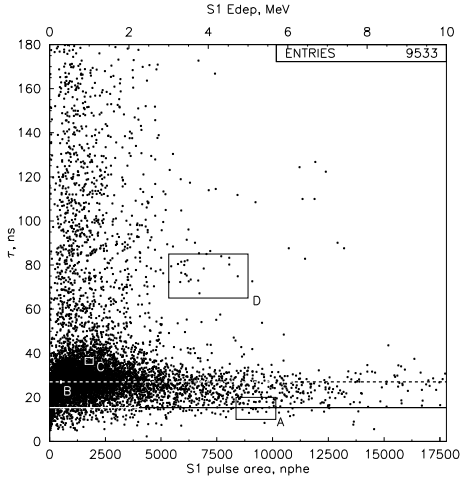

Figure 4.43: Scatter plot of τ vs S1 energy, E_{dep}, for all unsaturated, first pulses in the LS SUM channel with four, event sampling boxes positioned (A-D). Expected τ_α and τ_γ values[150] are represented by the solid and broken lines, respectively.

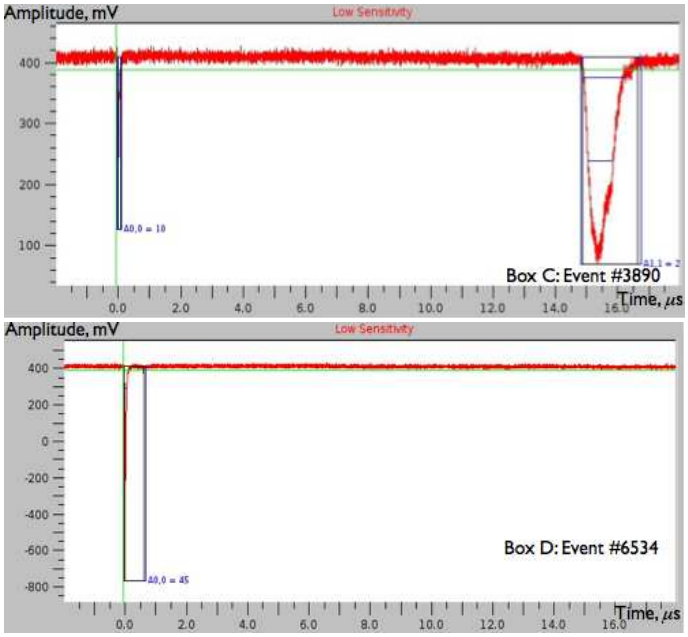

Figure 4.44: Pulse screenshots taken from the ZE3RA v1.3 reduction software in the LS SUM channel (pulse amplitude, mV vs time, μs) for boxes C (upper panel) and D (lower panel), respectively.

Alpha & Gamma S2/S1 Ratios

The S2 amplitude of an electron recoil (γ-ray interaction) is approximately 10 times larger than the S1 at 2.8 kV/cm in the liquid. In contrast, the S2 amplitude of an α signal is approximately equal to that of the S1.[150]

The S2 pulse area of an electron recoil is significantly larger than that of a nuclear recoil. The ratio of S1 pulse area to S2 pulse area (S1/S2) is a powerful with-field, two-phase discrimination parameter which can be used to distinguish nuclear recoils from electron recoils, with $(S2/S1)_{e^-recoils} >> (S2/S1)_{nucl.recoils}$.

Previous measurements of S1/S2 ratios in the ZEPLIN prototype detector, operated in two-phase mode (with 30 mm GXe gap) with 6 kV applied and an extraction field of 2.5 kV/cm in the liquid yielded a skewed, non-gaussian $(S2/S1)_\gamma$ area distribution with a modal value $\sim$100 and a symmetric $(S2/S1)_\alpha$ distribution with a mean value $\sim$10. Furthermore, an investigation of these ratios as a function of applied electric field indicated that $(S2/S1)_\alpha$ and $(S2/S1)_\gamma$ both *increase* with increasing electric field. At applied electric field, above 3.2 kV/cm in the liquid, the α ratios were found to be approximately 100 times smaller than that of the γ ratios.[150] Therefore α and γ ratios seen in this data-set, acquired at 3.01 kV/cm in the liquid, are expected to be $(S2/S1)_\alpha \geq 10$ and $(S2/S1)_\gamma \geq 100$. The distribution of S1/S2 ratios is shown in Figure 4.45 (left panel), where a skewed, non-gaussian γ population is indeed visible around $(S2/S1) \geq 100$ ($(S1/S2) \leq 0.01$). However, no separate population, a symmetric peak, due to α-particle events, expected at $(S2/S1) \geq 10$ ($(S1/S2) \leq 0.1$) can be identified here providing further evidence that no α events have been detected.

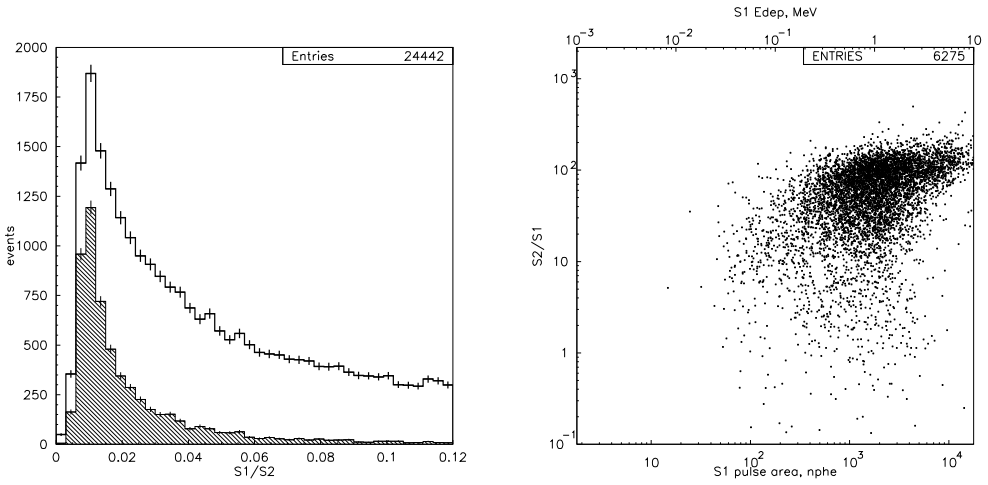

Figure 4.45: Histogram of the ratios of integrated pulse area of the first and second pulses in the LS sum channel, S1/S2 (left panel). The bold line corresponds to all reduced data while only events satisfying the saturation, width and *npulses* cuts are plotted in the shaded region. Just a single peak, characteristic of γ-ray events, appears in this distribution at a modal value of ∼0.01. The corresponding scatter plot of S2/S1 area vs S1 energy, MeV is also shown (right). No population, separate in energy from the main (γ-ray) population is visible here, particularly within the expected α region (E_{dep} ∼4.9-5.5 MeV).

Electron Drift Time

The electron drift time through the LXe phase, from the interaction point, to the GXe phase, t_d (or the time delay between the S1 and S2 signals), is proportional to the LXe depth at which the interaction happened. With an applied electric field, the t_d of an α-particle interaction is dependent on the LXe depth and the electric field strength. At 9 kV, with an electric field strength of 3.7 kV/cm in the liquid, the t_d of an α signal was previously measured as 6.7±0.1 μs [150].

From Figure 4.46 (left panel) it is clear the maximum measured t_d is ∼17.9 μs. This corresponds to electrons drifted across a maximum distance, the LXe depth, of 36.5 mm. Therefore, the maximum measured drift velocity in the LXe, at 3.01 kV/cm in the liquid, is ∼2.04 mm μs^{-1}. In Figure 4.46 (right panel) the poor LXe purity is quantified, with the electron lifetime being ∼8.0 μs.

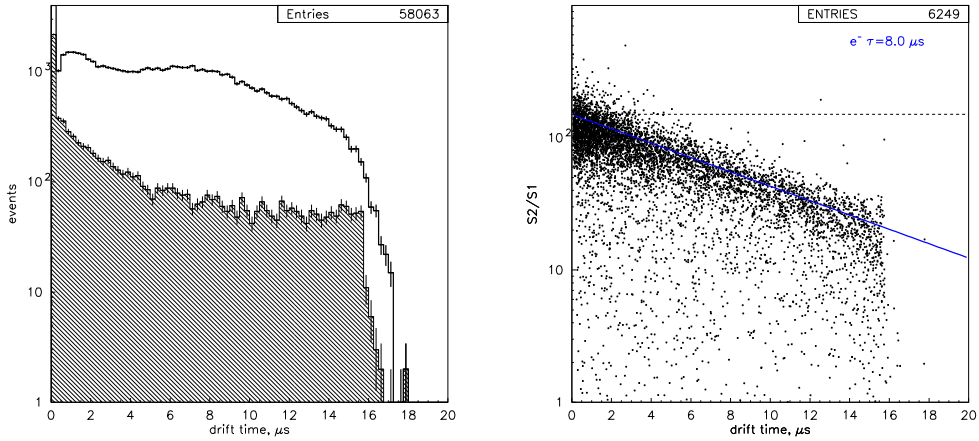

Figure 4.46: Drift time, t_d ($time(S2) - time(S1)$, μs), histogram of events (left panel) where the shaded plot corresponds to events unsaturated in the LS SUM, with the width cut applied. The scatter plot of S2/S1 area vs t_d (right panel) contains events from the shaded histogram. No population, separate from and lower with respect to the main, γ population (defined by a modal value of S2/S1$\sim$100) is visible here. The function S2/S1=150$\times$exp(-t_d/8.0) is added to this distribution (not fitted) in order to quantify the LXe purity implying an electron lifetime, $e^{-}\tau$, of $\sim$8.0 μs. For comparison, the ideal, pure LXe case is also shown (broken line).

4.3.4 ^{57}Co Run at Zero-Field: S1 Light Yield

With no applied electric field ^{57}Co γ-ray spectra were recorded for all readout channels with an uncollimated 100 μCi (3.7 MBq) ^{57}Co source located centrally above the detector for $\sim$30 minutes and an applied PMT HV of -1.8 kV. The xenon in the target was filled to its nominal depth and the LXe level was monitored to sub-mm accuracy. The ^{57}Co source delivered low-energy photons (14.41 keV, 122.06 keV and 136.47 keV[152] with 9.2%, 85.6% and 10.7% relative intensities, respectively) and higher-energy photons (692.03 keV[152] with 0.16% intensity) to the target volume. Since the decay products of ^{57}Co are of low energy the event interaction sites are constrained in depth to the upper few mm of the LXe.

Neither the DAQ, nor the ZE3RA reduction software identifies pulses i.e. distinguishing an S1 from noise or, for the with-field scenario, an S2 signal. Therefore, the S1 is identified within up to ten recorded pulses (per timeline) at the analysis, post-acquisition stage. This involves defining a cut on the time constant, 30$\leq \tau$(ns)$\leq$65, as shown in Figure 4.47, and implementing this constraint within a PAW function.

Each of the pulses in the timeline are scanned through until the pulse, with the minimum time stamp, satisfies the cut. From the distributions in Figure 4.47 it is clear a significant number of events are saturated in the HS SUM channel (#32) due to the choice of full scale (FS). For this reason, the analyses that follow, involve the LS (#33-63) and LS SUM (#64) channels.

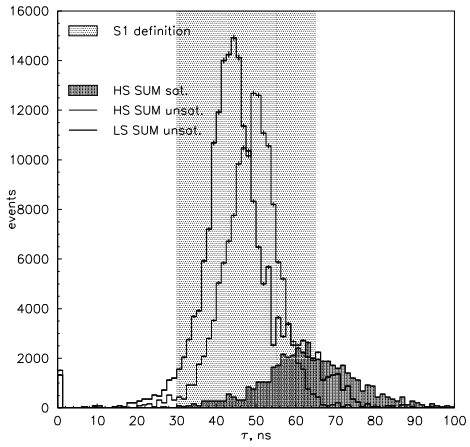

Figure 4.47: Zero-field ^{57}Co 060519 time constant, τ (ns), distributions for the first of the ten recorded pulses per event in the LS and HS SUM channels (with and without a cut on pulses saturating the FS acquisition range). Comparison of the distributions enable the τ parameter to define an S1: $30 \leq \tau(\text{ns}) \leq 65$.

The 060519 ^{57}Co zero-field data-set, reduced with ZE3RA v1.1, was used in conjunction with the 060707 SPE data to calculate an S1 photoelectron (light) yield (see Section 4.3.1). The S1 pulse area (nphe) distribution for all thirty-one PMTs in the LS SUM channel is shown in Figure 4.48.

The conversion from pulse area (Vns) to pulse area (nphe) was done within a PAW function, on a channel-by-channel basis using the mean of the SPE pulse area distribution values, not using the fits to the distributions. The $\sim$125 keV ^{57}Co 'collimated' photopeak distribution, corresponding to the central events (those with the highest light collection), from the inner 7 PMTs is also shown. The broad shoulder on the low side of the uncollimated spectrum (for all PMTs in the array) is purely due to light collection variations towards the edge of the xenon volume. Most of these fall outside the fiducial volume and the remainder can be corrected using 3-D position reconstruction information. The ^{57}Co distribution generated at this stage was done without QE corrections, which were applied in later analyses following 'flat-fielding' of the array. The energy calibration is determined by a single Gaussian fit to the

^{57}Co photopeak, a combination of the unresolved 122.06 keV and 136.47 keV γ-ray lines, with a mean of 583.17±0.34 phe (and 27.2% FWHM resolution). The distribution for the inner 7 PMTs is constructed by invoking a PAW function to search for events where the maximum energy deposited is seen in any of the inner 7 PMTs, or LS channels #33-39. This is done in terms of the pulse area ntuple parameter, *AREA*, on an event-by-event basis. Thus, an S1 LY of 4.67±0.54 phe/keV for the centre of the chamber was derived where the error is calculated conservatively, using the standard deviation, not the error on the mean. For comparison, this calculated LY exceeds that predicted by MC simulations (3.4-4.0 phe/keV[97]) with the most optimistic being ∼5 phe/keV, assuming 60 photons/keV with no grid. A higher LXe scintillation yield than considered in those simulations (60 photons/keV, W_{ph}=16.7 eV) could explain this difference. A corresponding decrease in energy threshold, a key parameter of WIMP detectors, is expected.[97]

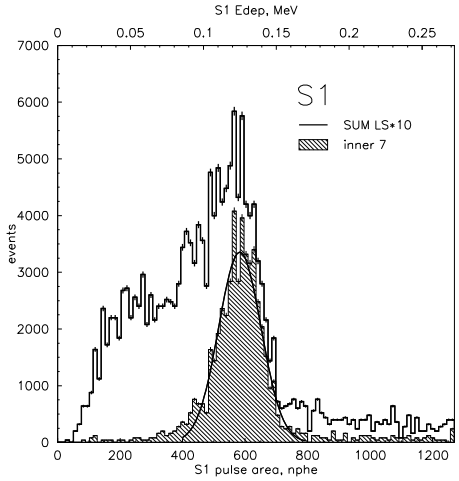

Figure 4.48: S1 zero-field ^{57}Co 060519 pulse area (nphe), or energy (MeV), spectrum for the LS*10 SUM channel (equivalent to the HS SUM) using LS SPE pulse area values from the 060707 data-set. A Gaussian function is fitted to the LS SUM distribution for the inner 7 PMTs - the ∼125 keV 'photopeak' - with a mean of 583.17±0.34 phe (27.2% FWHM). From this an S1 zero-field LY of 4.67±0.54 phe/keV is derived.

An equivalent plot to Figure 4.48, but in log space, is shown in Figure 4.49 with some indication of the 692 keV γ-ray line. A potential 'backscatter peak' due to Compton scattering in the LXe phase with the scattered photon escaping upwards, i.e photon backscattering, is also expected. The energy of the scattered electron, E_{max}, is continuous up to a maximal kinematically possible value, for a single scatter - the Compton edge energy. This occurs for maximum energy loss of the γ-ray and

minimum electron energy, via Compton scattering when the incident angle of the interaction, θ, is 180°. The backscatter peak can effectively be considered as the Compton edge. Since θ can take any value in practice, the location of the Compton edge can be calculated according to:

$$E_{max} = E_{\gamma} - \frac{E_{\gamma}}{1 + \frac{(1-\cos\theta)E_{\gamma}}{E_e}} \tag{4.22}$$

where E_{γ} is the γ-ray energy (122.06 keV or 136.47 keV) and E_e is the electron rest mass energy (511 keV).[151] According to Equation 4.22 the energy deposited in the LXe from the two ^{57}Co γ-ray lines following photon backscattering is 39.46 keV and 47.51 keV, respectively. No clear indication of these can be seen in Figure 4.49.

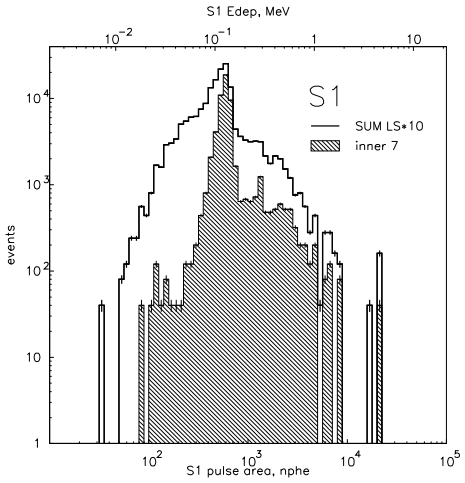

Figure 4.49: S1 zero-field ^{57}Co 060519 pulse area (nphe), or energy (MeV), spectrum for the LS*10 SUM channel (equivalent to the HS SUM). The x-axis is normalised with respect to the ∼125 keV 'photopeak' which corresponds to the central events, within the inner 7 PMTs. The position of the 692 keV 'shoulder' is clear.

Figure 4.50 shows the density distribution of the LS peak PMT frequency as a function of PMT location within the array. The peak PMT is defined as the channel with the largest deposited energy response, $AREA$, for each event and is implemented using a PAW function. The peak PMT parameter provides a useful cross-check: the PMTs are all responsive; the ^{57}Co source is positioned centrally; the inner PMTs demonstrate higher light collection. Figure 4.50 indeed confirms the expected behaviour, although the peak PMT is not #1 but is #4 (LS channel #36). This suggests the source may have been positioned slightly off-centre during the ^{57}Co 060519 zero-field run.

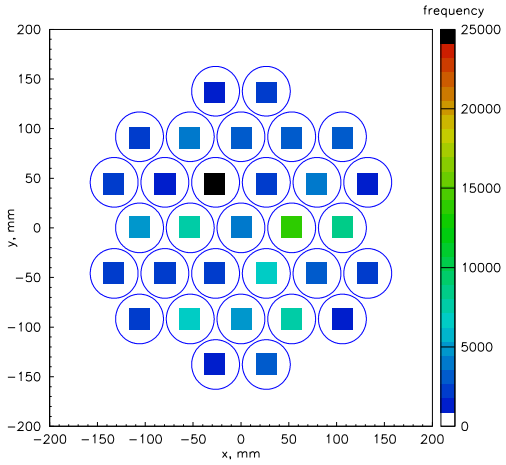

Figure 4.50: S1 zero-field ^{57}Co 060519 density distribution of the LS peak PMT frequency (z-axis): the number of times the channel is the peak PMT of the array, for an event i.e. the PMT with the largest deposited energy response, *AREA*. Here the LS channel peak PMT is #4. The square bins do not reflect the true, circular response areas of the PMT photocathodes and are an artefact of the histogram plotting.

4.3.5 ^{137}Cs Run at Zero-Field: S1 Light Yield

With the same setup as described previously in Section 4.3.4, with no applied electric field, but using a uncollimated 100 μCi (3.7 MBq) ^{137}Cs source instead, located centrally above the detector for ∼30 minutes, ^{137}Cs γ-ray spectra were recorded for all channels. The ^{137}Cs source delivered high-energy photons (661.66 keV[153] with 85.1% intensity) to the target volume. In addition, the source spectrum includes 31.82 keV and 32.19 keV X-rays[153] with 2.0% and 3.8% relative intensities, respectively. Since the emitted γ-rays of ^{137}Cs are of higher energy than for ^{57}Co the event interaction sites are not constrained in depth to the upper few mm of the LXe but are expected to propagate further.

In the same manner as described in Section 4.3.4 a cut on the time constant, $40 \leq \tau(\text{ns}) \leq 65$, was defined (see Figure 4.51). As before, the analyses that follow, involve the LS (#33-63) and LS SUM (#64) channels.

The S1 pulse area (nphe) distribution for all thirty-one PMTs in the LS SUM channel is shown in Figure 4.52. The conversion from pulse area (Vns) to pulse area (nphe) was done as described in Section 4.3.4. The 662 keV ^{137}Cs photopeak from the inner 7 PMTs is also shown and is fitted with a Gaussian function with a mean

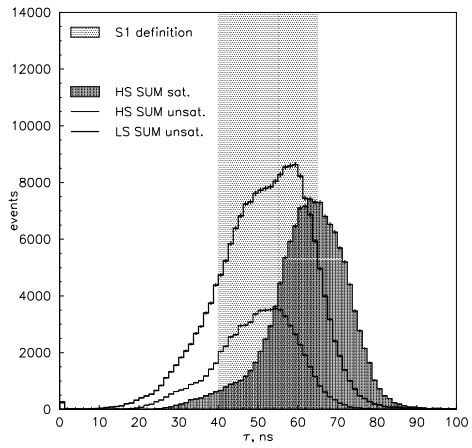

Figure 4.51: Zero-field ^{137}Cs 060519 time constant, τ (ns), distributions for the first of the ten recorded pulses per event in the LS and HS SUM channels (with and without a cut on pulses saturating the FS acquisition range). Comparison of the distributions enable the τ parameter to define an S1: $40 \leq \tau(\text{ns}) \leq 65$.

of 3053.5±13.0 phe (21.2% FWHM). Thus, an S1 LY of 4.61±0.42 phe/keV for the centre of the chamber was derived. The broad shoulder on the low side of the uncollimated spectrum (for all PMTs in the array) is also evident, as for the ^{57}Co case, and is purely due to light collection variations towards the edge of the xenon volume.

An equivalent plot to Figure 4.52, but in log space, is shown in Figure 4.53 in order to identify the ^{137}Cs Compton edge, at $E_{max} \lesssim 478$ keV (according to Equation 4.22), in addition to the photopeak. The distribution does turn-up at approximately the right energy. Although weak, some small suggestion of the ^{137}Cs low-energy X-ray lines can be seen at $\lesssim$35 keV in Figure 4.53. The sharp fall-off in the inner 7 PMT distribution, down to $E_{dep} \sim 0$, can be attributed to the absorption length of 662 keV γs in LXe. An approximation, using the mass attenuation coefficient, μ/ρ, as $8.28 \times 10^{-2} cm^2 \text{g}^{-1}$[154] for γs at 600 keV and the density of LXe, ρ, as 2.953 gcm^{-3}[116], yields the absorption length of 600 keV γ-rays in LXe as ∼41 mm. This length is comparable to the liquid Xe depth.

Figure 4.54 shows the density distribution of the LS peak PMT frequency as a function of PMT location within the array. Figure 4.54 indeed confirms the PMTs are all responsive and the inner PMTs demonstrate higher light collection, as expected, although the peak PMT is not #1 but is #4 (LS Channel #36). As with the ^{57}Co 060519 zero-field run, this suggests the source may have been positioned slightly

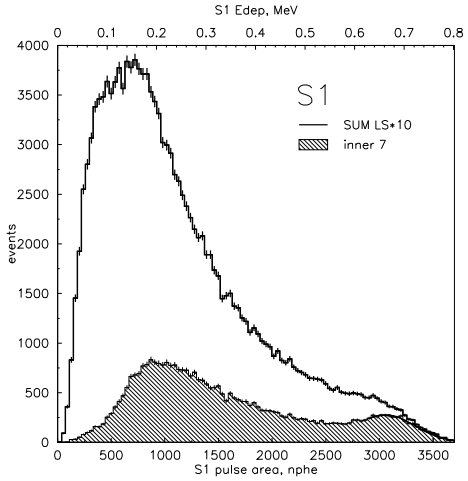

Figure 4.52: S1 zero-field ^{137}Cs 060519 pulse area (nphe), or energy (MeV), spectrum for the LS*10 SUM channel (equivalent to the HS SUM) using LS SPE pulse area values from the 060707 data-set. A Gaussian function is fitted to the LS SUM distribution for the inner 7 PMTs - the 662 keV 'photopeak' - with a mean of 3053.5±13.0 phe (21.2% FWHM). From this an S1 zero-field LY of 4.61±0.42 phe/keV is derived.

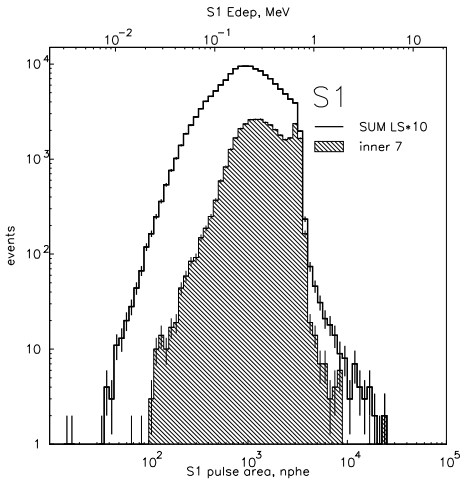

Figure 4.53: S1 zero-field ^{137}Cs 060519 pulse area (nphe), or energy (MeV), spectrum for the LS*10 SUM channel (equivalent to the HS SUM). The x-axis is normalised with respect to the 662 keV 'photopeak' which corresponds to the central events, within the inner 7 PMTs. The position of the Compton edge at $\lesssim$478 keV is also clear. Although weak, a trace of the ^{137}Cs low-energy X-ray lines can be seen at $\lesssim$35 keV.

off-centre during data acquisition.

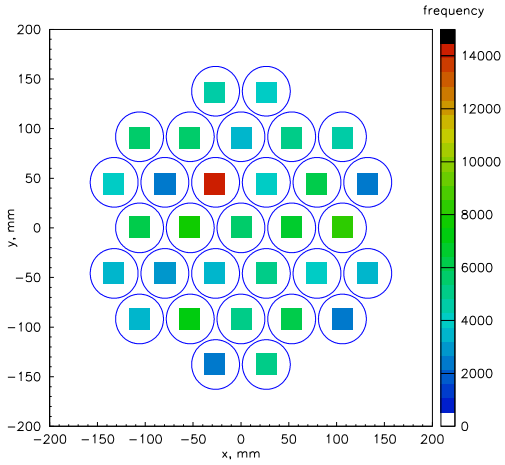

Figure 4.54: S1 zero-field ^{137}Cs 060519 density distribution of the LS peak PMT frequency (z-axis): the number of times the channel is the peak PMT of the array, for an event. Here the LS channel peak PMT is #4. The square bins do not reflect the true, circular response areas of the PMT photocathodes and are an artefact of the histogram plotting.

4.3.6 ^{57}Co Run at Field: S1 and S2 Light Yield

Following successful completion of the zero-field tests 13.05 kV were applied between the cathode grid and the anode mirror, setting up a field of 3.01 kV/cm in the liquid - two-phase operation. Data were acquired at this field, with -1.8 kV on the PMTs and the 100 μCi (3.7 MBq) ^{57}Co source placed on top of the instrument for ∼30 minutes, and were subsequently reduced using ZE3RA v1.1.

The scintillation (S1) signal is identified from within up to ten recorded pulses (per timeline) at the analysis, post-acquisition stage. This involves defining a cut on the time constant, $10 \leq \tau_{S1}(\text{ns}) \leq 50$ in the HS SUM channel, as shown in Figure 4.55, and implementing this constraint within a PAW function. If the first pulse in the timeline satisfies this S1 τ cut it is deemed the primary. The secondary, ionisation (S2) signal is defined after checking for saturation of pulse area in the HS SUM channel, and more specifically, pulse amplitude in individual HS channels. Then, each pulse in the timeline is scanned through, in reverse (in time), until the pulse with the minimum time stamp which satisfies the S2 τ cut ($300 \leq \tau_{S2}(\text{ns}) \leq 600$) is identified as the secondary. Since saturation of the S2 signal was evident in the HS readout, the S2 cut was defined in the LS SUM channel (see Figure 4.56).

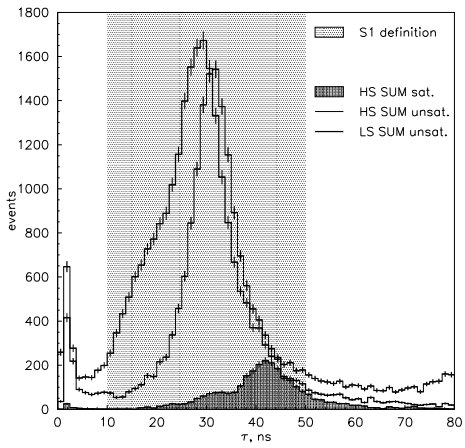

Figure 4.55: With-field (3.01 kV/cm in the liquid) ^{57}Co 060520 S1 time constant, τ(1,32), distributions for the first of the ten recorded pulses per event in the LS and HS SUM channels (with and without a cut on pulses saturating the FS acquisition range). Comparison of the distributions enable the τ parameter to define an S1: $10 \leq \tau(\text{ns}) \leq 50$.

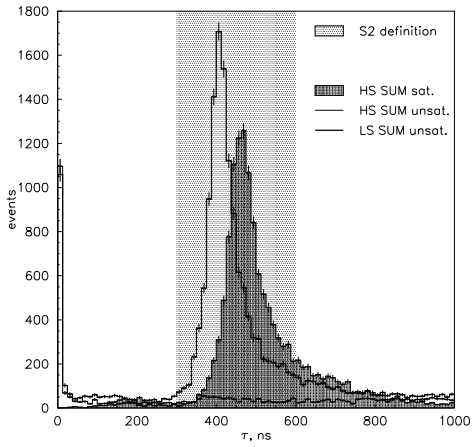

Figure 4.56: With-field (3.01 kV/cm in the liquid) ^{57}Co 060520 S2 time constant, τ(2,64), distributions for the pulse with the lowest time stamp, which is not necessarily pulse #2, out of the recorded 10. These are shown in the LS and HS SUM channels (with and without a cut on pulses saturating the FS acquisition range). Comparison of the distributions enable the τ parameter to define an S2: $300 \leq \tau(\text{ns}) \leq 600$.

The 060520 ^{57}Co with-field (3.01 kV/cm in the liquid) data-set was used in conjunction with the 060707 SPE data to calculate an S1 and S2 photoelectron yield.

The associated S1 pulse area (nphe) distribution for all thirty-one PMTs in the HS SUM channel is shown in Figure 4.57. This 'uncollimated' spectrum is reconstructed using all thirty-one PMTs. In order to eliminate an unidentified feature in the HS SUM* distribution (centred at ∼150 phe) only evident in the with-field data from the full array, the S1 and S2 were defined in terms of τ and then the S2 was used to 're-select' the S1. This 're-selection' was done by enforcing the S2 τ cut in addition to the S1 τ cut when plotting the S1 energy spectrum in the HS SUM channel. The conversion from pulse area (Vns) to pulse area (nphe) was done as previously described in Section 4.3.4. The 125 keV ^{57}Co S1 'collimated' photopeak from the inner 7 PMTs is also shown and is fitted with a Gaussian function with a mean of 222.50±0.76 phe (42.4% FWHM). The corresponding S2 distribution, in the LS SUM, is presented in Figure 4.58. Similarly, a Gaussian fit to the S2 distribution from the inner 7 PMTs returns a mean of 17394±71 phe (52.0% FWHM). The 060520 acquired data indicate a LY of 1.78±0.32 phe/keV and 139.2±30.8 phe/keV for the S1 and S2 channels of the inner 7 PMTs, respectively. For comparison, the ZEPLIN II instrument demonstrated an S1 with-field LY of ∼0.55 phe/keV.[57] The derived S1 photoelectron yield is approximately 35%[87] of the zero-field value previously determined and the FWHM for both distributions are consistent with the degradation of the zero-field energy resolution due to photoelectron statistics. Furthermore, the S2/S1 ratio is ∼80, as expected at this field.[87]

Note that the array had been 'externally' flat-fielded prior to the acquisition of these data, in that the PMT gains and cold photocathode QEs were equalised as accurately as possible. Corrections to the data were applied post-acquisition to account for SPE and QE considerations and involved: incorporating the means of the individual SPE distributions into the S1 and S2 LY calculations within a PAW function, as opposed to using an SPE pulse area value averaged across the array; software QE flat-fielding applied within a PAW function, whereby the individual QE values at -100°C are normalised to 30%, accounting for variation in QE across the array. Ideally, an additional correction, for LXe purity - compensating for the increasing loss of charge at larger drift times due to poor LXe purity (∼7-8 μs) - would have also been applied at this stage, thus increasing the S2 LY and the resulting measured S2/S1 ratio accordingly.

Figure 4.59 shows the depth of the S1 interaction, z (mm), as a function of the energy deposited in the LXe and in the GXe, corresponding to the HS SUM* spectrum in Figure 4.57. For comparison, Figure 4.60 is an equivalent plot, but for the HS SUM spectrum (with the S1 're-selected' using the S2). Clearly, the population

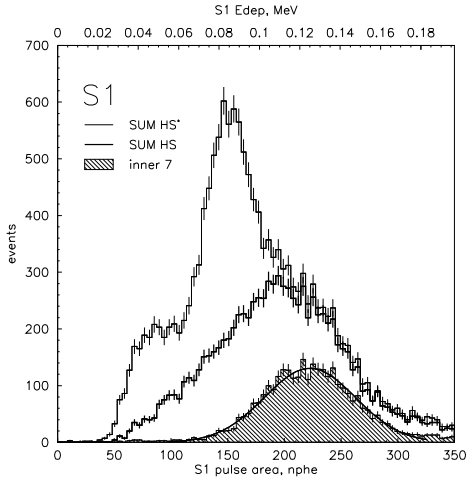

Figure 4.57: S1 with-field (3.01 kV/cm in the liquid) ^{57}Co 060520 pulse area (nphe), or energy (MeV), spectrum for the final HS SUM channel (post- 're-selection' of the S1) using HS SPE pulse area values from the 060707 data-set. A Gaussian function is fitted to the HS SUM distribution for the inner 7 PMTs - the ∼125 keV 'photopeak' - with a mean of 222.50±0.76 phe (42.4% FWHM). From this an S1 LY, at this field, of 1.78±0.32 phe/keV is derived. Also shown is the HS SUM* distribution (pre- 're-selection' of the S1), exhibiting an additional, spurious 'feature' centred at ∼150 phe.

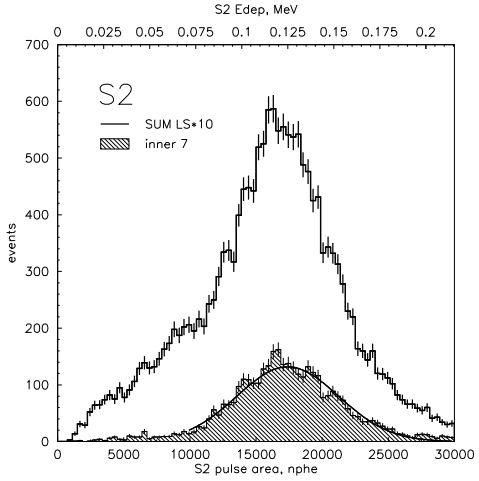

Figure 4.58: S2 with-field (3.01 kV/cm in the liquid) ^{57}Co 060520 pulse area (nphe), or energy (MeV), spectrum for the LS*10 SUM channel (equivalent to the HS SUM) using HS SPE pulse area values from the 060707 data-set. A Gaussian function is fitted to the HS SUM distribution for the inner 7 PMTs - the ∼125 keV 'photopeak' - with a mean of 17394±71 phe (52.0% FWHM). From this an S2 LY, at this field, of 139.2±30.8 phe/keV is derived.

constituting the additional peak, centred around ∼150 phe, prior to the S1 being 're-selected', propagates throughout the LXe volume to depths of z <0 mm and is probably due to a random coincidence of some sort. As expected, the 125 keV photopeak and restriction of the interaction sites to the upper few mms (z ∼30-36.5 mm) of the LXe target volume are seen in Figure 4.60. For this particular data-set, the GXe gap was estimated to be ∼3.5 mm, implying a total LXe depth of ∼36.5 mm. Using this, and a maximum t_d of 17.6 μs from the data, an electron drift velocity of ∼2.07 mm μs^{-1} is estimated in the LXe, at this field. This is consistent with the value provided by Reference [155].

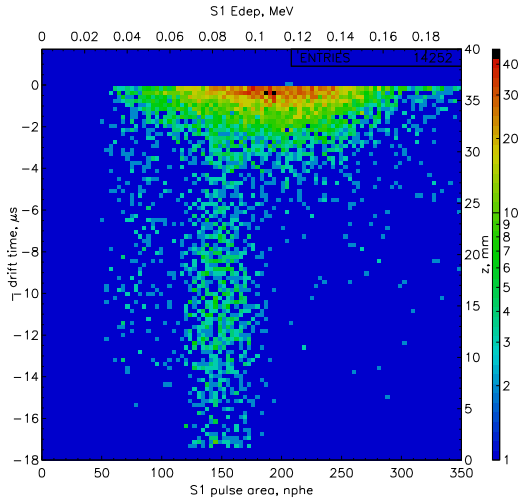

Figure 4.59: Depth of the S1 interaction, z (mm), as a function of the energy deposited in the LXe and in the GXe (layer between ∼36.5-40.0 mm) for the HS SUM* channel, using with-field (3.01 kV/cm in the liquid) ^{57}Co 060520 data. The additional peak, centred around ∼150 phe, seen prior to the S1 being 're-selected', propagates throughout the LXe volume to depths of z <0 mm.

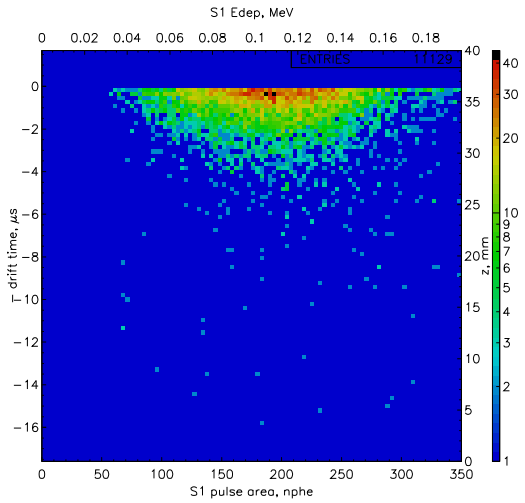

Figure 4.60: Depth of the S1 interaction, z (mm), as a function of the energy deposited in the LXe and in the GXe (layer between ∼36.5-40.0 mm) for the HS SUM channel, using with-field (3.01 kV/cm in the liquid) ^{57}Co 060520 data. The 125 keV photopeak and restriction of the interaction sites to the upper few mms (z ∼30-36.5 mm) of the LXe target volume, are clear.

4.3.7 ^{137}Cs Run at Field: Higher Energy Calibration & Xe Purity

Two-phase calibration data were acquired with 13.05 kV applied (3.01 kV/cm in the liquid) with -1.8 kV on the PMTs and the 100 μCi (3.7 MBq) ^{137}Cs source positioned, externally, on top of the instrument. The data were later reduced with ZE3RA v2.0.

The S1 and S2 signals are identified from within the five recorded pulses per timeline (or event) in the same way as described in Section 4.3.6. An S1 time constant cut, 15$\leq \tau$(ns)$\leq$60, is invoked in the HS SUM channel (Figure 4.61). Similarly, an S2 time constant cut, 200$\leq \tau$(ns)$\leq$800, is implemented in the LS SUM channel (Figure 4.62). Both the S1 and S2 signals show significant saturation in the HS and LS SUM channels, respectively. This is because the HS and LS full scales were later realised to have been set too small. Thus, all are events classed as 'saturated' when looking at the pulse areas of events within the 662 keV photopeak.

The 060520 ^{137}Cs with-field (3.01 kV/cm in the liquid) data-set was used in conjunction with the 060707 SPE data to calculate an S1 and S2 photoelectron yield.

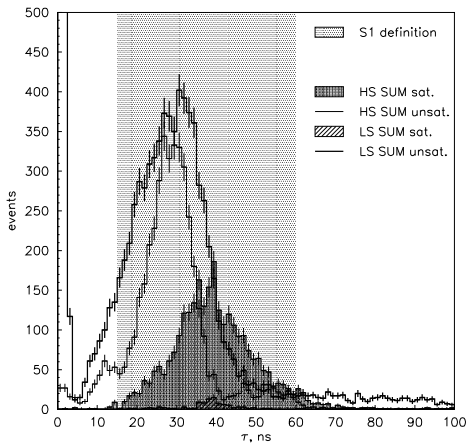

Figure 4.61: With-field (3.01 kV/cm in the liquid) ^{137}Cs 060520 time constant, τ(1,32), distributions for the first of the ten recorded pulses per event in the LS and HS SUM channels (with and without a cut on pulses saturating the FS acquisition range). Comparison of the distributions enable the τ parameter to define an S1: $15 \leq \tau(\text{ns}) \leq 60$.

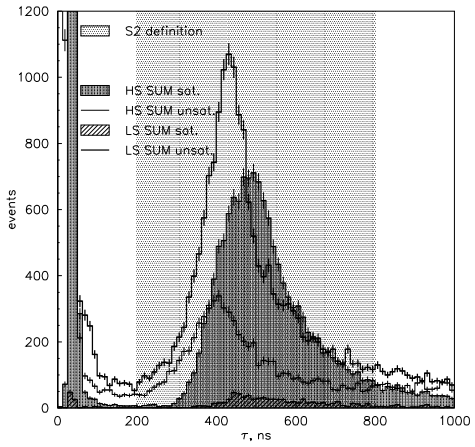

Figure 4.62: With-field (3.01 kV/cm in the liquid) ^{137}Cs 060520 time constant, τ(2,64), distributions for the pulse for the second of the ten recorded pulses per event in the LS and HS SUM channels (with and without a cut on pulses saturating the FS acquisition range). These are shown in the LS and HS SUM channels (with and without a cut on pulses saturating the FS acquisition range). Comparison of the distributions enable the τ parameter to define an S2: $200 \leq \tau(\text{ns}) \leq 800$.

The associated S1 pulse area (nphe) distribution for all thirty-one PMTs in the HS SUM channel is shown in Figure 4.63. This 'uncollimated' spectrum is recon-

structed using all thirty-one PMTs. The conversion from pulse area (Vns) to pulse area (nphe) was done as previously described in Section 4.3.4. The 662 keV ^{137}Cs S1 'collimated' photopeak from the inner 7 PMTs is also shown and is fitted with a Gaussian function with a mean of 818.80±23.13 phe (39.5% FWHM). The corresponding S2 distribution, in the LS SUM, is presented in Figure 4.64. Similarly, a Gaussian fit to the S2 distribution from the inner 7 PMTs returns a mean of 64629.0±1107.6 phe (84.4% FWHM). The 060520 acquired data indicate a LY of 1.24±0.21 phe/keV and 97.6±35.1 phe/keV for the S1 and S2 channels of the inner 7 PMTs, respectively. This is consistent with the ^{57}Co with-field S1 and S2 derived LYs for the inner 7 PMTs (detailed in Section 4.3.6), to within errors. The derived S2/S1 ratio is ∼80, as expected at this field.[87]

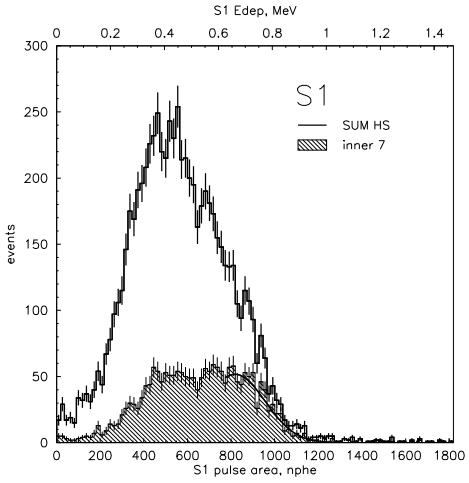

Figure 4.63: S1 with-field (3.01 kV/cm in the liquid) ^{137}Cs 060520 pulse area (nphe), or energy (MeV), spectrum for the HS SUM channel using HS SPE pulse area values from the 060707 data-set. A Gaussian function is fitted to the HS SUM distribution for the inner 7 PMTs - the 662 keV 'photopeak' - with a mean of 818.80±23.13 phe (39.5% FWHM). From this an S1 LY, at this field, of 1.24±0.21 phe/keV is derived.

As described in Section 4.3.6 the array had been 'externally' flat-fielded prior to the acquisition of these data and corrections were applied to the data post-acquisition to account for SPE and QE considerations. Ideally, an additional correction, for LXe purity would have also been applied at this stage, thus increasing the S2 LY and the resulting measured S2/S1 ratio accordingly. The effect of poor LXe purity at this time is demonstrated, and the purity level quantified, in Figure 4.65 with the electron lifetime in the LXe being ∼8.0 μs.

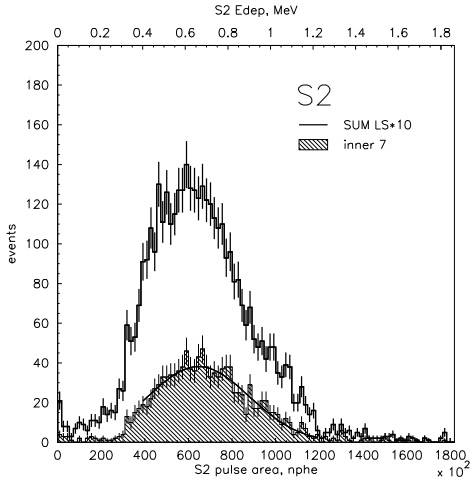

Figure 4.64: S2 with-field (3.01 kV/cm in the liquid) ^{137}Cs 060520 pulse area (nphe), or energy (MeV), spectrum for the LS*10 SUM channel (equivalent to the HS SUM) using HS SPE pulse area values from the 060707 data-set. A Gaussian function is fitted to the HS SUM distribution for the inner 7 PMTs - the 662 keV 'photopeak' - with a mean of 64629.0±1107.6 phe (84.4% FWHM). From this an S2 LY, at this field, of 97.6±35.1 phe/keV is derived.

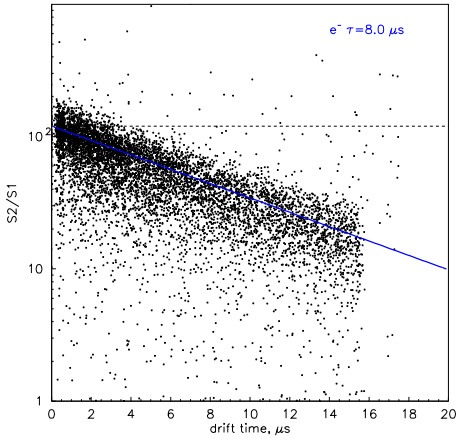

Figure 4.65: Purity plot of the S2/S1 pulse area ratios (in log space) versus the electron drift time in the LXe, t_d, for the 060520 ^{137}Cs with-field (3.01 kV/cm in the liquid) data-set, for the inner 7 PMTs. The drift time is defined as the difference in the time stamps of the S2 signal and the preceding S1. The function S2/S1=120×exp(-t_d/8.0) is added to this distribution (not fitted) in order to quantify the LXe purity implying an electron lifetime, $e^{-}\tau$, of ∼8.0 μs. For comparison, the ideal, pure LXe case is also shown (broken line).

Figure 4.66 shows the depth of the S1 interaction, z (mm), as a function of the energy deposited in the LXe and in the GXe. As expected, the 662 keV 'shoulder' (of the photopeak) and propagation of the interaction sites throughout the full LXe target volume are clear. Figure 4.67 provides a zoom of Figure 4.66 at low energies, for E_{dep} <100 keV, demonstrating some indication of the 8 keV Cu X-rays. For this particular data-set, the GXe gap was estimated to be ∼3.5 mm, implying a total LXe depth of ∼36.5 mm. Using this, and a maximum t_d of 17.8 μs from the data, an electron drift velocity of ∼2.05 mm μs^{-1} is estimated in the LXe, at this field. This is consistent with the value provided by Reference [155].

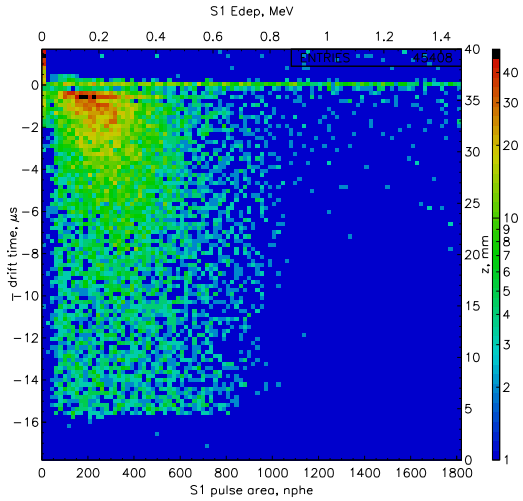

Figure 4.66: Depth of the S1 interaction, z (mm), as a function of the energy deposited in the LXe and in the GXe (layer between ∼36.5-40.0 mm) for the HS SUM channel, using with-field (3.01 kV/cm in the liquid) ^{137}Cs 060520 data. The 662 keV 'shoulder' (of the photopeak) and propagation of the interaction sites throughout the LXe target volume, for a range of energies, are clear.

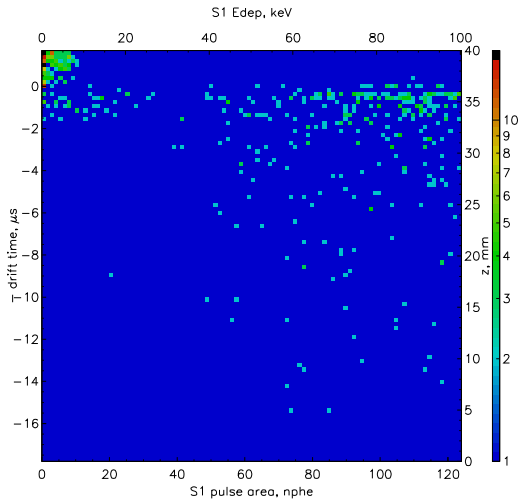

Figure 4.67: Depth of the S1 interaction, z (mm), as a function of the energy deposited in the LXe and in the GXe (layer between ∼36.5-40.0 mm) for the HS SUM channel, using with-field (3.01 kV/cm in the liquid) ^{137}Cs 060520 data. There is some suggestion of the 8 keV Cu X-rays, in the GXe and/or upper few mms of the LXe phase. Events with negative drift times are suspected to be due to an artefact of the ZE3RA software code.

4.3.8 Am-Be Neutron Run at Field: Particle Discrimination

As discussed before, in Section 3.1, it is, ultimately, the ability of a dark matter detector to discriminate between nuclear and electron-recoil interactions which determines its performance. Demonstrating this key feature, Figure 3.5 shows how the S2/S1 ratio varies with S1 energy when a 10 mCi (370 MBq) Am-Be (α,n) source is placed externally, above the detector for ∼60 minutes, during the acquisition of the 060520 with-field (3.01 kV/cm in the liquid) data-set.[87] The data were subsequently reduced with ZE3RA v2.0.

In Figure 3.5 (Section 3.1) there are three distinct and relatively tight populations: nuclear recoils from neutron elastic scattering (A); the de-excitation of the 40 keV ^{129}Xe inelastic level (B); the γ-ray population (C), also associated with the source. Here, only single scatter events (events with a single S1 interaction site in the LXe), within the inner 7 PMTs are plotted. The distributions of the individual populations are expected to tighten further, being more well-defined, when the instrument is operated at the proposed, higher field.

Figure 3.5 has been produced with a purity (or electron lifetime, $\tau(e^-)$) correction implemented: compensating for the loss of charge at longer drift times (or larger

LXe depths). In order for such a correction to be applied the LXe purity was first assessed and then accounted for via the inclusion of a '$1/\exp(-t_d/\tau(e^-))$' correction factor to the S2/S1 quantity (y-axis) and is demonstrated in Figure 4.68.

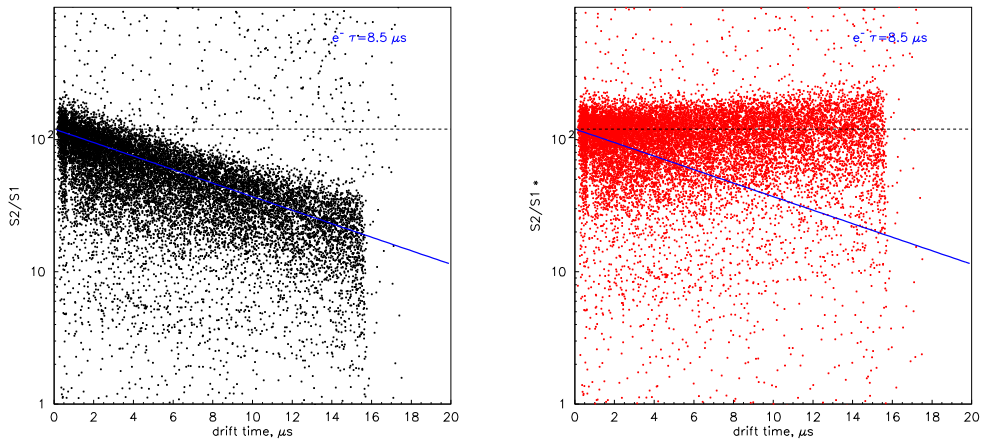

Figure 4.68: Purity plots of the S2/S1 pulse area ratios (in log space) versus the electron drift time in the LXe, t_d, for the 060520 Am-Be with-field (3.01 kV/cm in the liquid) data-set, for the inner 7 PMTs, without any correction (left panel). The drift time is defined as the difference in the time stamps of the S2 signal and the preceding S1. The function S2/S1=120×exp(-t_d/8.5) is added to this distribution (not fitted) in order to quantify the LXe purity implying an electron lifetime, $\tau(e^-)$, of ∼8.5 μs. For comparison, the ideal, pure LXe case is also shown (broken line). An equivalent plot, but for the post- purity corrected case, S2/S1 $*$, is also shown (right).

4.4 Summary

Data acquired during the first two surface commissioning stages has demonstrated the successful completion of construction of ZEPLIN III. In addition, the high light collection, the 3-D position reconstruction sensitivity and the ability to separate nuclear recoils from electron recoils has been verified.[87]

A discussion on Phase I (zero-field operation) has been presented in this Chapter. With regards to the data analysis and reduction software this included the development of code, although preliminary, being crucial in establishing an early form of the data pipeline, and vital testing and development of iterative versions of ZE3RA. Data acquired with the ACQIRIS setup during this phase provided the first indication of non-linearity in the S1 response of the LXe target to γ-rays at low energies.

A study of the enhanced light yield, LY, was conducted with thirty-one ^{241}Am γ-sources mounted internally. A factor of $\sim \times 2$ improvement in the dual-phase (LXe and GXe phases, with an estimated GXe gap of ∼2-5 mm) LY with respect to the single-phase (LXe only) LY being observed: 18.12±0.91 phe/keV and 7.42±0.37 phe/keV, respectively, for PMT #11 operated at 2.0 kV. The single-phase value was consistent with that predicted by MC simulations (∼7.1 phe/keV, PMTs at 1.9 kV[130]). The dual-phase value was confirmed by an alternative approach, using data acquired with the MCA, giving ∼18.0 phe/keV. A separate study of pulse shapes or decay time constants was carried out with Am-Be n-run data in which the computed τ values were independently verified. When compared with background data and subsequently sliced in energy, a small, but inconclusive, excess of events with $E(keV) \lesssim 15$ was seen in the Am-Be data, suggesting any small indication of a n-population was in fact 'masked' by the internal, thirty-one ^{241}Am sources.

The second commissioning phase, Phase II (with-field operation), following the removal of the thirty-one ^{241}Am internal γ-sources, has also been described here.

Dedicated SPE data-sets were used to propose attenuation adjustments to each readout channel, equalising the signals, as well as to characterise the zero-field and with-field S1 and S2 LYs for the inner 7 PMTs. Furthermore, several different, phyiscally-motivated functions were fitted to the SPE spectra when considering the best method of estimating of the SPE peak value. The average SPE area, calculated across the full array, ranged from 41.78±1.55 Vps to 52.37±1.59 Vps, depending on the method employed.

Zero-field background data were looked at in order to investigate a potential ^{222}Rn α contamination at low energies, as seen previously with ZEPLIN II. No significant population separate in energy from the main γ-ray population was observed, particularly within the expected E_α ∼4.9-5.5 MeV and τ_α ∼15.40±0.08 ns region. This α-search led to the identification of an observed high-τ population (τ ∼70 ns) whereby the interaction sites were confined to the outer edge of the PMT array. In turn, three spin-off studies were conducted into the origin of these events, relating to: saturation of the signal in the DAQ/ZE3RA and distortion by the amplifiers, with the latter effect shown to not fully account for the high-τ events; event sampling of the high-τ population in order to rule out a cosmic ray association, exploiting geometrical, timing and position reconstruction arguments; and an independent verification of the calculated decay time constants, as output by ZE3RA, via fitting single exponential functions to individual pulse shapes. Although no firm

conclusions regarding the presence of a ^{222}Rn contaminant could be drawn, critical development of the ZE3RA and DAQ software did follow as a direct result of this work. Also investigations into the hardware configuration followed, with the DAQ circuit revised for future data acquisition.

In order to continue the α-search, the analysis approached used on the zero-field data-set was repeated on the with-field data-set together with additional investigations into the S2/S1 pulse area ratios. No α population, with expected S1/S2$\leq$0.1 was identified.

A zero-field S1 LY of 4.67$\pm$0.54 phe/keV was calculated using the $\sim$125 keV ^{57}Co 'collimated' (inner 7 PMTs) S1 photopeak and the status of all PMTs within the array was confirmed as responsive. For comparison, this calculated LY exceeds that predicted by MC simulations (3.4-4.0 phe/keV[97]) with the most optimistic being $\sim$5 phe/keV, assuming 60 photons/keV with no grid. Similarly, a zero-field S1 LY of 4.61$\pm$0.42 phe/keV for the centre of the chamber, was measured with the $\sim$662 keV ^{137}Cs photopeak.

With-field (3.01 kV/cm in the liquid) S1 and S2 LYs of 1.78$\pm$0.32 phe/keV and 139.2$\pm$30.8 phe/keV, respectively, were calculated using the $\sim$125 keV ^{57}Co collimated photopeak, including QE flat-fielding and SPE corrections. An S2/S1 ratio of $\sim$80 was found, as expected at this field. As predicted, the interaction sites of events in the $\sim$125 keV photopeak were restricted to the upper few mms (z $\sim$30-36.5 mm) of the LXe target volume. Similarly, with-field (3.01 kV/cm in the liquid) S1 and S2 LYs of 1.24$\pm$0.21 phe/keV and 97.6$\pm$35.1 phe/keV, respectively, were calculated using the $\sim$662 keV ^{137}Cs photopeak. For both ^{57}Co and ^{137}Cs with-field studies the LXe purity (or electron lifetime, $\tau(e^-)$ was measured to be $\sim$7.0-8.0 μs.

Successful particle discrimination was demonstrated with the with-field (3.01 kV/cm in the liquid) Am-Be (α,n) source data, following application of a LXe purity correction ($\sim$8.5 μs) in which three distinct populations of nuclear recoils, 40 keV ^{129}Xe inelastics and γ-rays were observed.

Fuller characterisation of ZEPLIN III as a dark matter detector, in particular generating more accurate energy calibration factors, establishing an effective flat-fielding method and further refinement of the ZE3RA and DAQ software, were conducted underground, post-deployment, in a lower background environment and are described in the following Chapters.

Chapter 5

ZEPLIN III Underground Data

ZEPLIN III was deployed underground, commencing a lower-background, shielded phase following the initial, surface commissioning phase. In preparation for the first science run, the detector was reassembled and verified as fully operational, running at high field, in situ. These underground commissioning studies constituted more rigorous instrument testing. The data were analysed, aiming to re-validate the detector functioning and identify and resolve any operational issues in advance of the science runs.

Comparative studies of different methods of obtaining single photoelectron distributions were conducted. Also, the origin of the previously identified long-τ events was probed in the context of an amplifier distortion effect. The instrument's energy resolution was assessed and an early 'flat-fielding' method was designed. The effectiveness of this was demonstrated by minimising the energy resolution obtained in ^{57}Co calibration runs. Finally, timing offsets, correcting for the difference in pulse start times in each active channel, were evaluated and applied within the reduction code.

5.1 Neutron-Shielded Underground Background Run at Zero Field

Due to the signal saturation and amplifier distortion effects observed during the ZEPLIN III surface runs, and an improvement in the photoelectron response be-

ing sought, significant revision of the DAQ configuration followed to coincide with deployment of the instrument underground (see Figure 3.13). These included modifying the voltage divider box design and the number of amplifiers used per readout channel. Removing an amplification factor of $\times 10$ and increasing the PMT gain was designed to maintain the same overall gain and not worsen the impedance mismatch.[156]

With all six faces of the n-shielding in place, fully surrounding the instrument, and the PMTs operated at -2.15 kV, an overnight run of underground, zero-field, 070717 background data was acquired.

5.1.1 Comparison of Surface & Underground Data: ZE3RA Evolution

The data reduction and analysis software was continuously evolving simultaneously with the detector commissioning process, during the surface and underground runs. Thus, distributions and pulse parameters were compared and contrasted for background data-sets acquired on the surface (060519, PMT applied voltage=-1.8 kV) and underground, neutron-shielded (070717, PMT applied voltage=-2.15 kV), and reduced with various ZE3RA codes (v1.3, v2.0 and v2.1). For reference, the key modifications made in iterative releases of ZE3RA were mentioned in Section 3.5.

The effect of the changing ZE3RA reduction software on resulting pulse parameter distributions was explored; with particular emphasis placed on observation (or not) of the long-τ events. Figure 5.1 presents density plots of τ as a function of S1 pulse area (or energy) for the LS and HS SUM channels for data reduced with ZE3RA version 1.3, 2.0 and 2.1. Here, the energy-calibration value corresponding to the $\sim$125 keV photopeak, previously obtained with the ^{57}Co 060519 zero-field surface data, of 583.17$\pm$0.34 phe was used (see Section 4.3.4). Although the two data-sets were acquired with different applied PMT voltages, the aim here is not to calibrate the 070717 underground data precisely, but to compare the shape of the surface and underground τ distributions in the context of the long-τ population. The migration of the long-τ population with successive ZE3RA releases is clear. Similarly, Figures 5.2 and 5.3 also log the development of the reduction code, but in terms of pulse width as a function of τ and histogramming τ for all unsaturated events, respectively. The structure (three features) seen within the τ $\approx$20-60 ns main peaks of the τ distributions in the latter, is unaffected by decreasing the bin

width and is therefore believed to be real. Implementing ZE3RA v2.1 is shown to significantly suppress the long-τ population, relative to earlier versions.

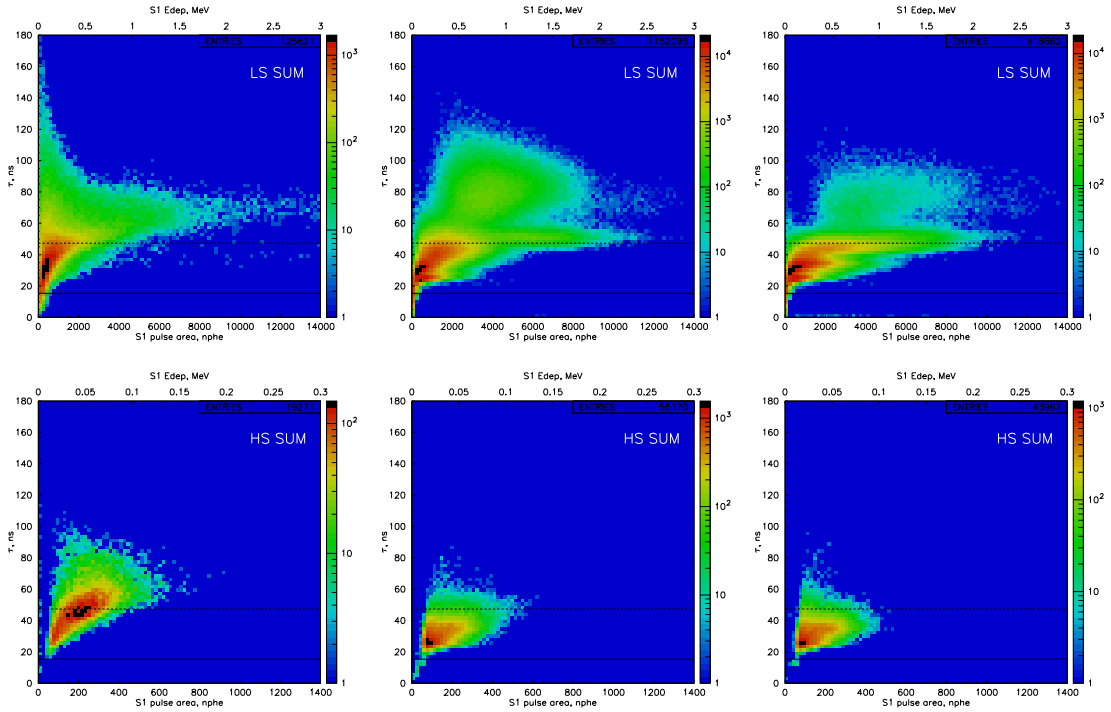

Figure 5.1: Density plots of τ (ns) vs $S1$ pulse area (Vns) or deposited energy, E_{dep}, for the first pulse of unsaturated events within surface 060519 (ZE3RA v1.3), n-shielded underground 070717 (ZE3RA v2.0) and 070717 (ZE3RA v2.1) data-sets, from left to right, in the LS SUM (upper panels) and HS SUM (lower panels) channels. Expected τ_α and τ_γ values[150] are represented by the solid and broken lines, respectively.

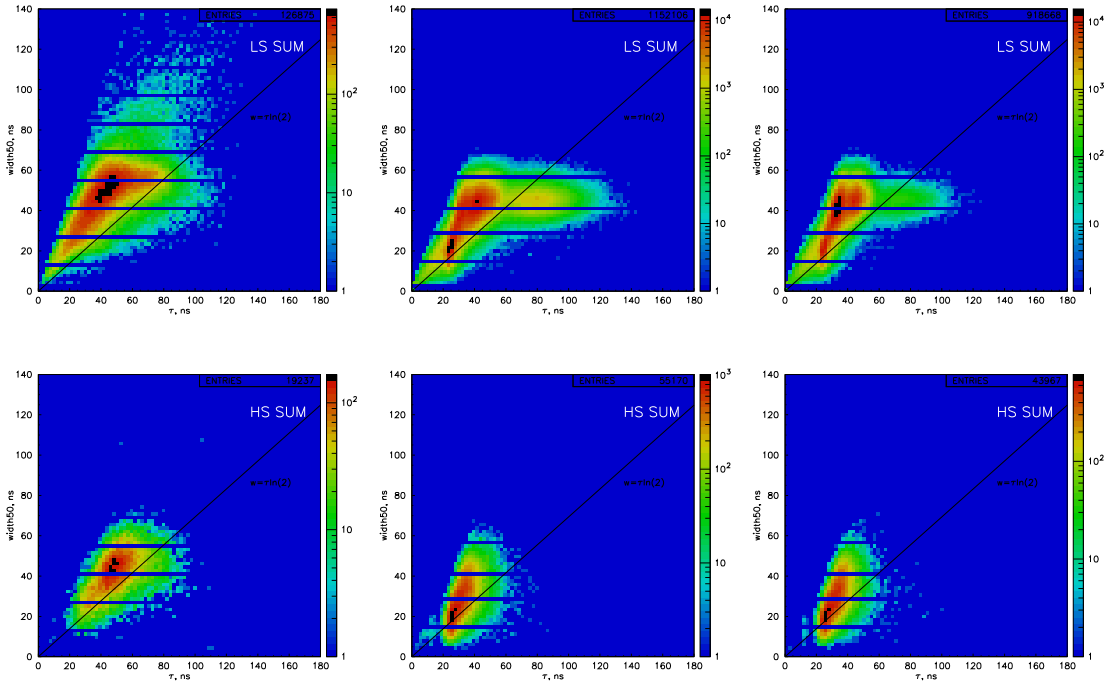

Figure 5.2: Density plots of $S1$ pulse $WIDTH50$ (ns) vs τ (ns), for the first pulse of unsaturated events within surface 060519 (ZE3RA v1.3), n-shielded underground 070717 (ZE3RA v2.0) and 070717 (ZE3RA v2.1) data-sets, from left to right, in the LS SUM (upper panels) and HS SUM (lower panels) channels. The solid line shows how the pulse FWHM varies with τ for a well-behaved exponential pulse shape obeying $WIDTH50{=}\tau\ln(2)$. The $WIDTH50$ axis exhibits some structure due to the digitisation of the pulse shape in the DAQ software.

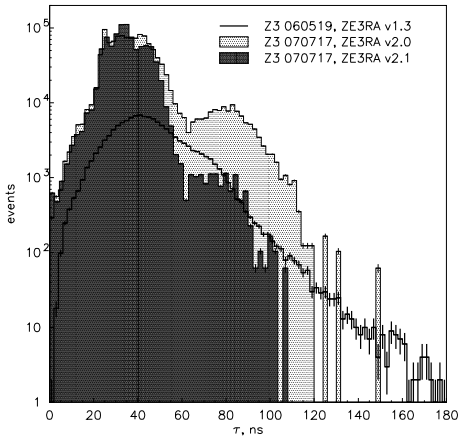

Figure 5.3: Histograms of $S1$ τ (ns) for the first pulse of unsaturated events within the surface 060519 (ZE3RA v1.3), n-shielded underground 070717 (ZE3RA v2.0) and 070717 (ZE3RA v2.1) data-sets, in the LS SUM channel. The long-τ population is significantly suppressed with ZE3RA v2.1. Note that the y-axis here is unnormalised with considerably fewer events are plotted in the 060519 than in the 070717 data-set.

5.1.2 Long-τ Events: Event Identification

In order to better understand the long-τ events and diversity of pulse shapes, in the same way as the approach described in Section 4.3.2, four boxes (labelled A-D) were strategically places on the plot shown in the upper, central panel of Figure 5.1 to sample events of different decay time constants and energies (see Figure 5.4). Boxes A-D are defined by: $0.7 \leq E_A(\text{MeV}) \leq 0.8$ and $70 \leq \tau_A(\text{ns}) \leq 80$; $1.1 \leq E_B(\text{MeV}) \leq 1.2$ and $50 \leq \tau_B(\text{ns}) \leq 55$; $0.20 \leq E_C(\text{MeV}) \leq 0.25$ and $22 \leq \tau_C(\text{ns}) \leq 28$; $0.20 \leq E_D(\text{MeV}) \leq 0.25$ and $32 \leq \tau_D(\text{ns}) \leq 38$. Boxes A, B, C and D were found to contain 5518, 2129, 17506 and 32120 events, respectively.

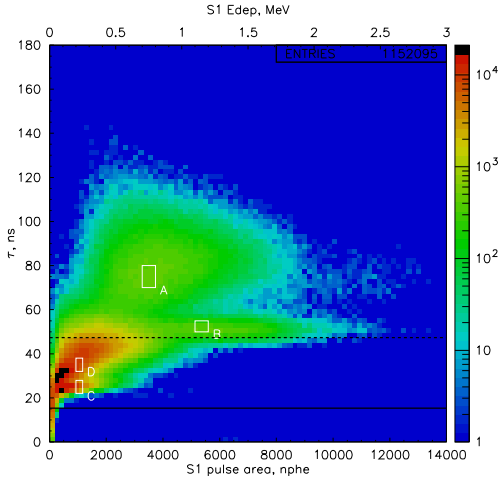

Figure 5.4: Density plot of τ (ns) vs $S1$ pulse area (Vns) or deposited energy, E_{dep}, for the first pulse of unsaturated events within n-shielded underground 070717 (ZE3RA v2.0) data-set in the LS SUM channel. The positioning of four, event sampling boxes is also shown (A-D). Expected τ_α and τ_γ values[150] are represented by the solid and broken lines, respectively.

A typical event, sampled within each box (A-D), was individually viewed in ZE3RA to assist in event identification and is presented in Figure 5.5. Event #s 8 and 156 suggest the integration time (or defined pulse window) is being set too long by ZE3RA while event # 178 may be indicative of a hardware problem with the pulse already appearing to suffer distortion, prior to reduction.

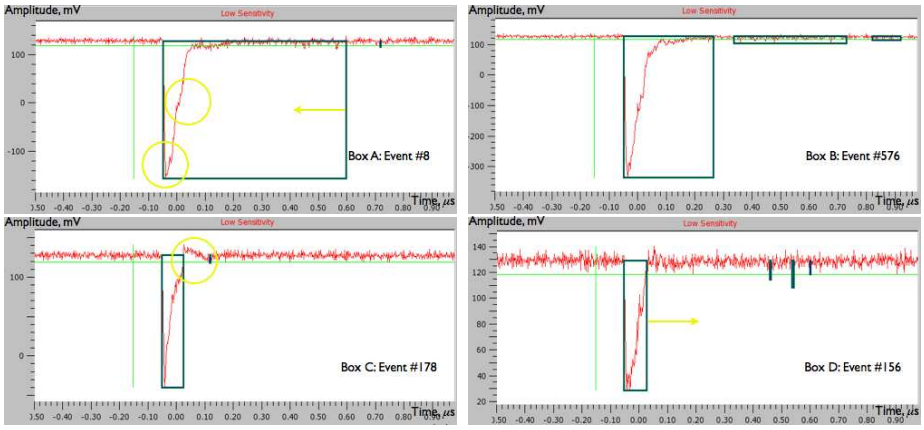

Figure 5.5: Pulse screenshots taken from the ZE3RA v2.0 reduction software in the LS SUM channel (pulse amplitude, mV vs time, μs) for example, 'problematic' pulses within boxes A (upper left panel), B (upper right), C (lower left) and D (lower right). Potential problems associated with the ZE3RA integration time or hardware setup are highlighted in yellow.

5.1.3 Long-τ Events: Amplifier Distortion Tests

An amplifier distortion effect within the ZEPLIN III DAQ setup has been identified and discussed in Chapter 4 (Section 4.3.2). However, it was shown that amplifier distortion effects do not fully account for the observed high-τ events. Nevertheless, further investigation into these events was conducted and analysed by the author to: determine the voltage at which the two PS-770 amplifiers distort; investigate whether distortion in the high sensitivity (HS) channel affects the signal seen in the low sensitivity (LS) channel in anyway; investigate the origin of the long time constants seen for some events in surface data.[157]

Pulse parameters of the amplifier output LS (or HS) signal were measured as a function of the amplitude of the input signal for three different setups: without an attenuator present; with an attenuator (A=0.5); and with an attenuator (A=1.0).

The first and second stage amplifiers may distort above output signal amplitudes of 2.5 V and 2 V, respectively.[117] This is because the bipolar outputs are designed to deliver over $\pm$ 2.5 V across a single 50 Ω load and $\pm$ 2 V across two 50 Ω loads. Above these values the linearity of the amplifiers is not guaranteed and is characterised by $\pm$0.1% for $\pm$2.0 V across one 50 Ω load and $\pm$1.5 V across two 50 Ω loads. Channels 3 and 4 of the amplifiers were used and the disused outputs were terminated with 50 Ω loads. Prior to testing the amplifier offsets were checked and adjusted to zero.

For these tests a Thandar TG503 5 MHz Function Generator[158] was used with the generated square wave differentiated to give a fast signal with the following settings: 1.0 Hz; x1 k freq; 5μs delay range; width x100; symmetry max; start/stop phase 0; run mode; 50 ns width range; norm pulse mode; complimentary and positive pulse output; 0 or 20 dB output.

A LeCroy 9430 10 bit 150 MHz Oscilloscope[159] was used to measure the signal parameters (using the E and F functions) with the following settings: DC 50 Ω coupling; source Ch1 ($P0$); automatic mode; negative slope; bandwidth limiter off. The pulse amplitude was measured using the cursors together with the absolute voltage function. Measured parameters were obtained from an averaged pulse, averaged over 200 waveforms. Channel 2 of the PS-804 manual attenuator[118] was used in two of the three tests with the attenuation either set at 0.5 or 1.0.

The e*Scope function on a Tektronix TDS3032B 300 MHz 2.5 GS/s Oscilloscope[160] was used to capture example pulse waveforms (as both binary data and images). It was also used to measure the signal amplitude, width, rise time and fall time, averaged over 256 traces, with the 'snapshot' function. These parameters are shown schematically in Figure 5.6 and are defined, between the cursors, respectively as: the difference between the baseline signal value and the minimum, peak value; the width of the first pulse (either positive or negative), averaged for all similar pulses; duration of the pulse waveform's rising transition from 10% to 90% of the amplitude, averaged for all rising transitions; duration of the waveform's falling transition from 90% to 10% of the amplitude, averaged for all rising transitions.

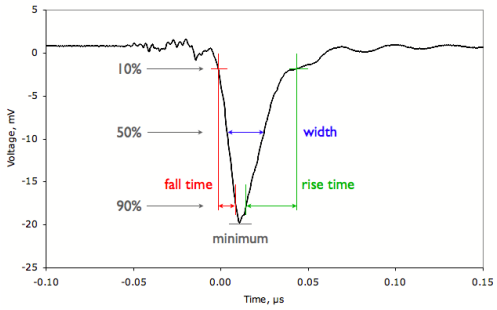

Figure 5.6: Schematic of a typical pulse shape annotated with some of the parameters measured using the LeCroy 9430 and Tektronix TDS3032B oscilloscopes.

The signals at different stages ($P0$, $P1$, $P2$ and $P3$) are as defined previously, in Section 4.3.2, with the exception of $P2$ which is re-defined here as $P2{=}(P1 \times A)/F$ where A is the attenuation and F is some 'splitting factor', no longer necessarily

equal to two which, for future reference, should be experimentally determined.

The error analysis does not include systematic errors and only considers statistical errors i.e. the standard deviation, σ, in the spread of the mean. For the amplitude, width and rise time measurements no σ associated with these is given by the oscilloscope. Therefore twenty, repeat readings were taken, at $P0$=150 mV with $G1$ and $G2$=10 and A=1.0 (averaged over 200 waveforms) to determine the spread on these distributions, for this particular $P0$. Gaussians were fitted to these distributions and the error in the mean of the input amplitude, $e(inputamplitude)$, was found to be $\pm$1.79 mV; $e(LSamplitude)\pm$0.006 V; $e(LSwidth)\pm$0.15 ns; $e(LSrisetime)\pm$0.25 ns; $e(HSamplitude)\pm$0.029 V; $e(HSwidth)\pm$0.075 ns; and $e(HSrisetime)\pm$0.11 ns. These were scaled accordingly to be applied to all other measurements in the data-sets. This method was then applied to the $P0$=156 mV, $G1$ and $G2$=10 and A=1.0 Tektronix TDS3032B data-set, with each measurement averaged over 256 waveforms. The following measurements were made: $e(inputamplitude)\pm$0.14 mV; $e(LSamplitude)\pm$0.007 V; $e(LSwidth)\pm$0.059 ns; $e(LSrisetime)\pm$0.097 ns; $e(HSamplitude)\pm$0.016 V; $e(HSwidth)\pm$0.058 ns; and $e(HSrisetime)\pm$0.16 ns.

On each plot of input amplitude ($P0$) versus output amplitude ($P2$ or $P3$) trendlines are fitted to the data and their functions displayed (Figures 5.8, 5.11 and 5.13). Also the data's departure from linearity at 1% and 10% are indicated by the broken lines, centred around the trendlines and defined in terms of the output. These are not shown at the 0.1% level (as defined by the manufacturer) as they would be indistinguishable from the trendlines themselves.

Configuration With No Attenuation

The LS (or HS) output pulse parameters were monitored as a function of input amplitude according to the setup shown in Figure 5.7 and the results are presented in Figure 5.8.

The signal in the LS channel is expected to distort above $P2$=2.00 V and the HS above $P3$=1.50 V. These are shown by the solid red circular data-points in Figure 5.8 (upper panel). Both of these values appear consistent with the acquired data.

The gradients of the LS$\times$10 and HS LeCroy data-sets are approximately equal at 68.6$\pm$1.1 and 64.0$\pm$3.3 respectively, with a factor of 9.33$\pm$0.50 between the HS and LS (see Figure 5.8). This implies that the gain of the first and second stage amplifiers, $G1$ and $G2$ are not equal to 10 but are infact 6.86$\pm$0.11 and 9.33$\pm$0.50,

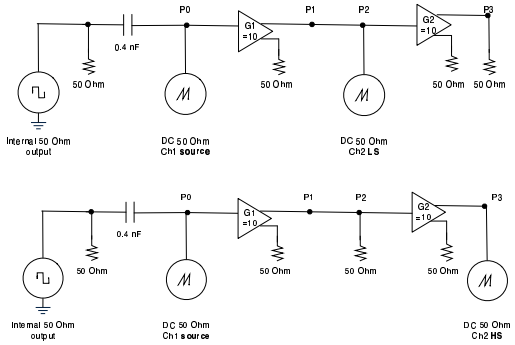

Figure 5.7: Circuit diagram of the experimental configurations used for measuring parameters in the LS channel ($P2$, upper panel) and HS channel ($P3$, lower panel) with no attenuator present in the setup and $G1$, $G2$=10. This configuration is designed to mimic the real data-taking scenario.

respectively.

Figure 5.8 (upper panel) also demonstrates the apparent variation in measurements made by different oscilloscopes. The gradients of the data acquired with the Tektronix TDS3032B oscilloscope are systematically higher than those with the LeCroy 9430 in all three of these studies (see Figures 5.11 & 5.13).

From Figure 5.8 (central panel) it is clear that the pulse width in the LS channel does not distort. Note that this holds even when the HS channel is distorted. Comparison of Figure 5.8 (central and lower panels) suggests the pulse width parameter is considerably more reliable across this range of input amplitudes than the rise time, when looking for significant changes in signal shapes under distortion. Furthermore the pulse width measured in the LS channel is comparable to the input pulse width.

For completion, some example pulses are shown below in Figures 5.9. These correspond to the open circular data-points (Tektronix values) on Figure 5.8. The LS and HS examples with $P0$=20 mV show well-behaved input, LS and HS signals. However, there is some evidence of 'ringing' in the input and LS channels for $P0 \geq$75 mV. With $P0 \geq$75 mV, distortion effects in the HS channels are shown.

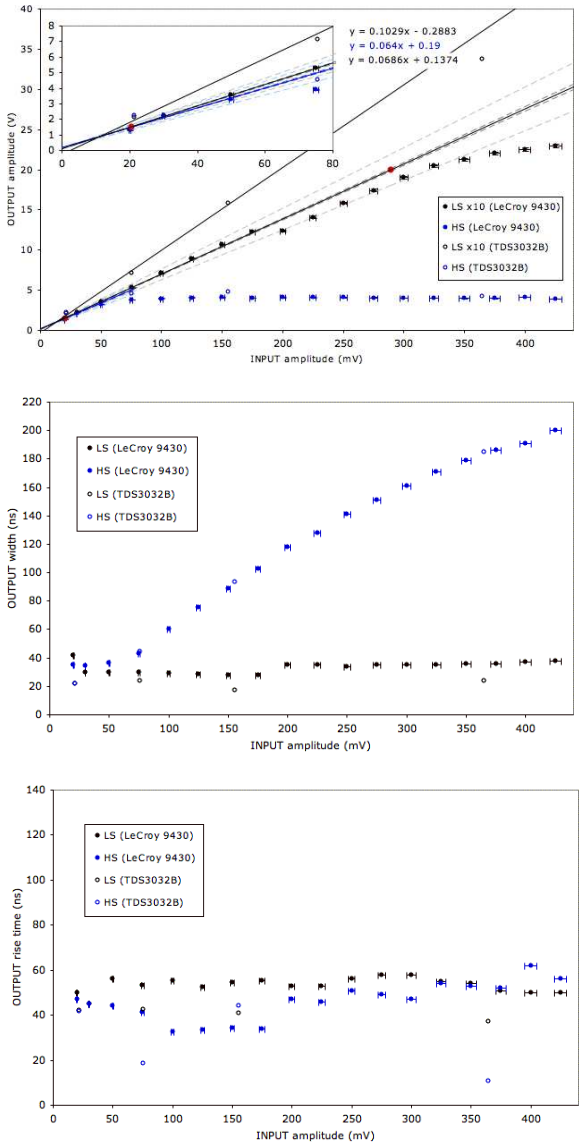

Figure 5.8: Input pulse amplitude, ($P0$) vs output pulse amplitude (upper panel), width (central) and rise time (lower) for LS ($P2$) and HS ($P3$) channels with no attenuator present in the setup and $G1$, $G2$=10. The upper panel shows the LS and HS LeCroy data fitted up to $P0$=275 mV ($P2$=1.89 V) and $P0$=30 mV ($P3$=2.11 V) respectively, and the LS Tektronix TDS3032B data up to $P0$=155 mV ($P2$=1.58 V).

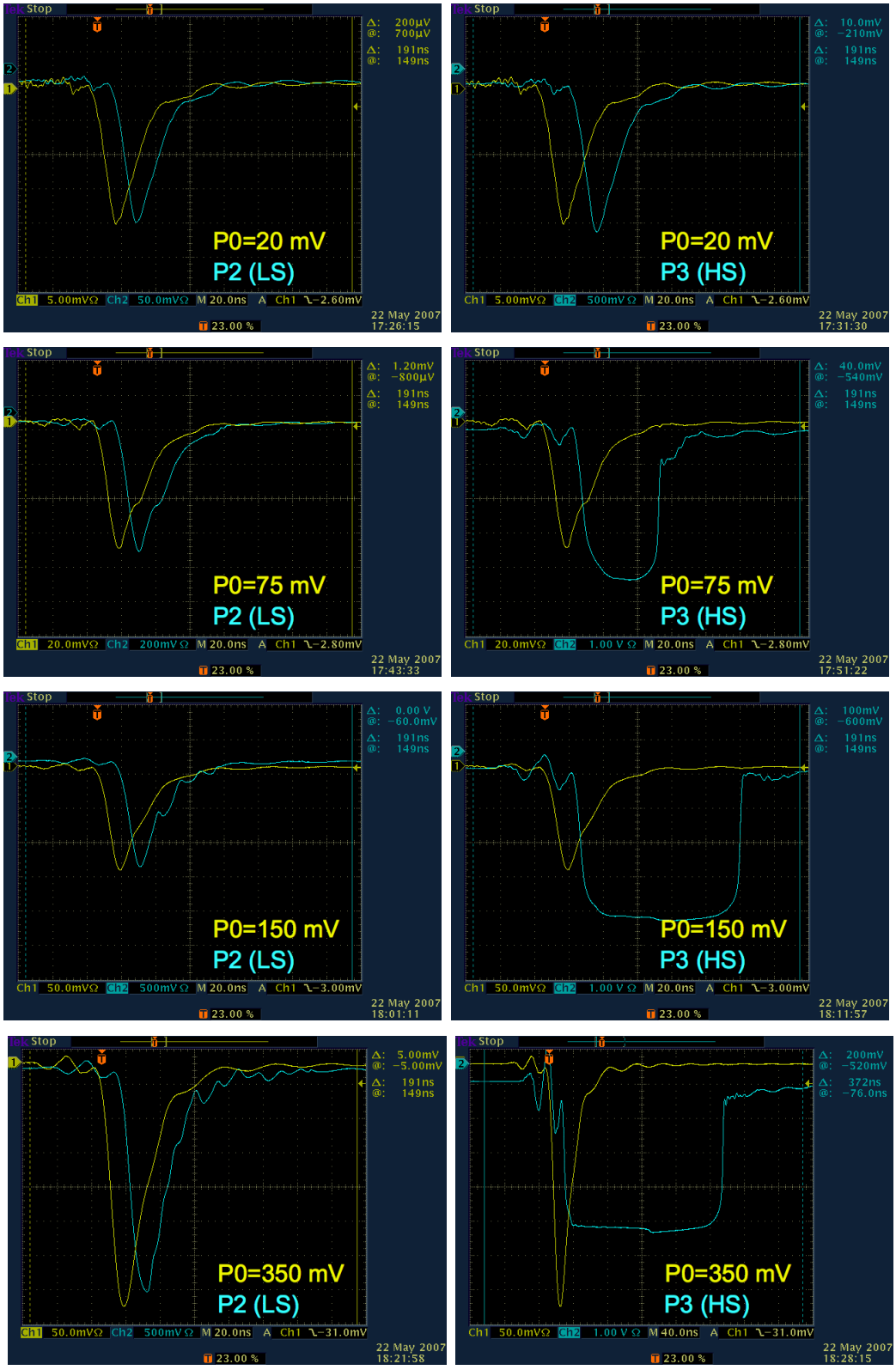

Figure 5.9: Screenshots of pulses from Tektronix TDS3032B oscilloscope for the input ($P0$), LS ($P2$) and HS ($P3$) channels with no attenuator present in the setup and $G1$, $G2$=10.

Configuration With Attenuation: A=0.5

The LS (or HS) output pulse parameters were monitored as a function of input amplitude according to the setup shown in Figure 5.10, where A=0.5, and the results are presented in Figure 5.11.

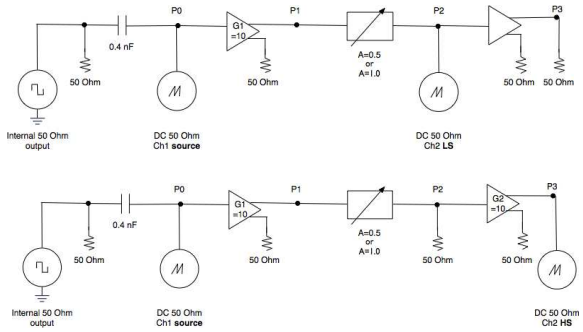

Figure 5.10: Circuit diagram of the experimental configurations used for measuring parameters in the LS channel ($P2$, upper panel) and HS channel ($P3$, lower panel) with the attenuator present in the setup (A=0.5 or 1.0) and $G1$, $G2$=10. This configuration is designed to mimic the real data-taking scenario.

For A=0.5, the signal in the LS channel is expected to distort above $P2$=1.00 V and the HS above $P3$=1.50 V (solid red circular data-points in Figure 5.11, upper panel). The LS channel appears to distort above $P2$=0.80 V (the open red circular data-point).

The gradients of the LS×10 and HS LeCroy data-sets are approximately equal at 23.3±0.3 and 23.6±0.3 respectively, with a factor of 10.13±0.21 between the HS and LS (see Figure 5.11). This implies that the gain of the first and second stage amplifiers, $G1$ and $G2$ are not equal to 10 but are infact 4.66±0.07 (=2.33/A) and 10.13±0.21, respectively.

Figure 5.11 (upper) also demonstrates the apparent variation in measurements made by different oscilloscopes. Again, the gradient of the data acquired with the Tektronix TDS3032B oscilloscope are higher than those with the LeCroy 9430.

From Figure 5.11 (central), the pulse width in the LS channel does not distort even when the HS channel is distorted and the pulse width measured in the LS channel is comparable to the input pulse width.

Example pulses are shown below in Figures 5.12 (corresponding to the open circular data-points, Tektronix values, of Figure 5.11). The LS and HS examples with $P0$=20

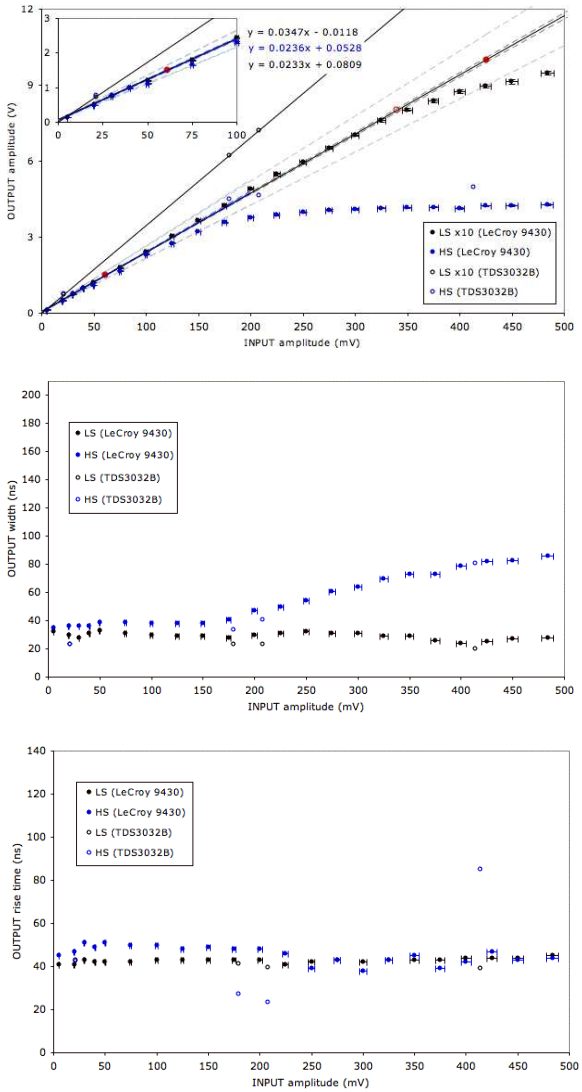

Figure 5.11: Input pulse amplitude, ($P0$) vs output pulse amplitude (upper panel), width (central) and rise time (lower) for LS ($P2$) and HS ($P3$) channels with the attenuator present in the setup (A=0.5) and $G1$, $G2$=10. The upper panel shows the LS and HS LeCroy data fitted up to $P0$=350 mV ($P2$=0.80 V) and $P0$=125 mV ($P3$=0.30 V) respectively, and the LS Tektronix TDS3032B data up to $P0$=208 mV ($P2$=0.70 V).

mV show input and LS signals with a 'double peak' feature, or perhaps the presence of 'ringing' or after-pulsing. With $P0 \geq$400 mV and $P0 \geq$175 mV, distortion effects in the LS and HS channels, respectively, are shown.

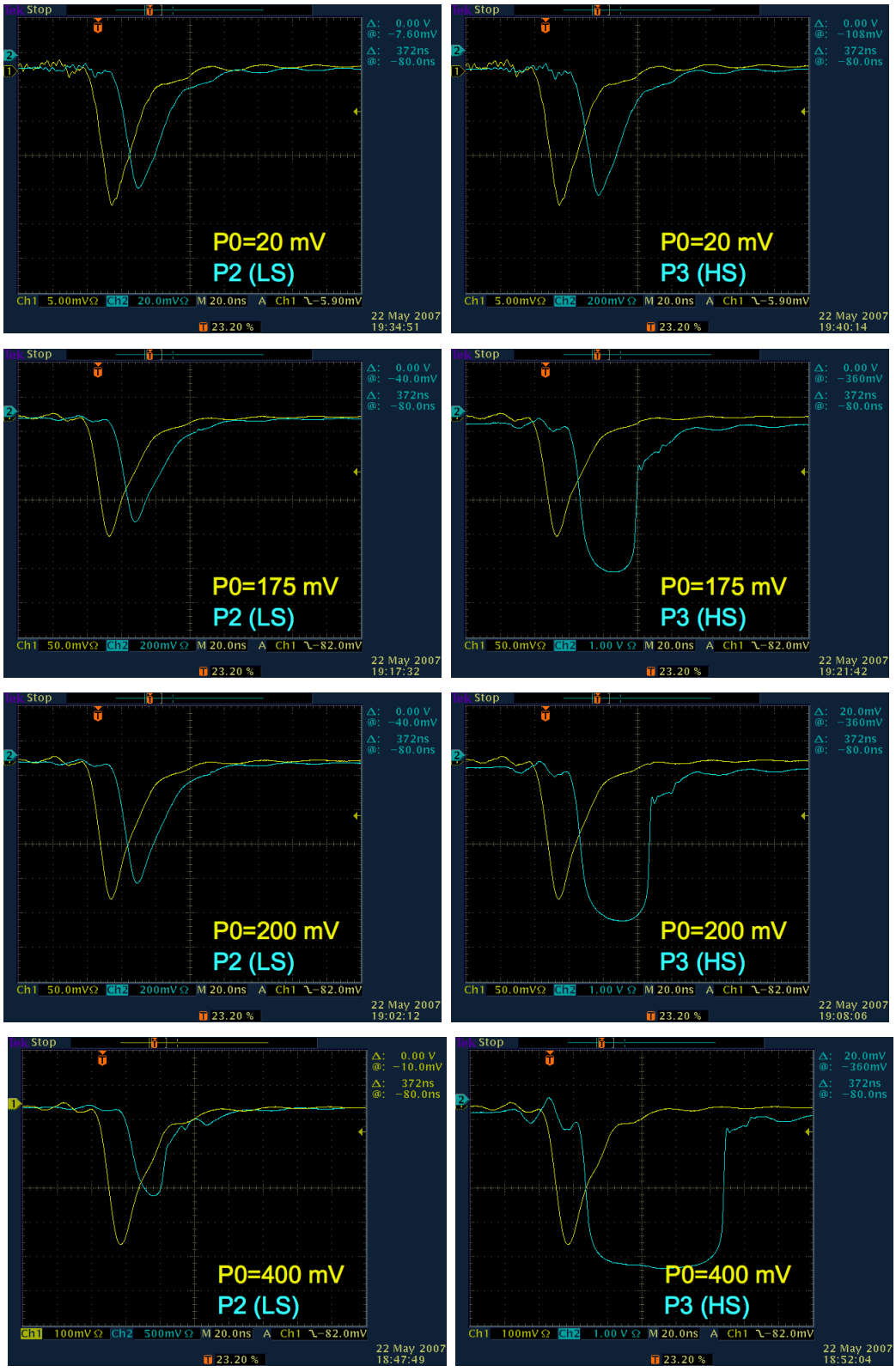

Figure 5.12: Screenshots of pulses from Tektronix TDS3032B oscilloscope for the input ($P0$), LS ($P2$) and HS ($P3$) channels with the attenuator present in the setup (A=0.5) and $G1$, $G2$=10. Signal saturation is shown to broaden the pulse shape (in the LS channel for $P0$=400 mV and the HS channel for $P0$=175-400 mV).

Configuration With Attenuation: A=1.0

The LS (or HS) output pulse parameters were monitored as a function of input amplitude according to the setup shown in Figure 5.10, where A=1.0, and the results are presented in Figure 5.13.

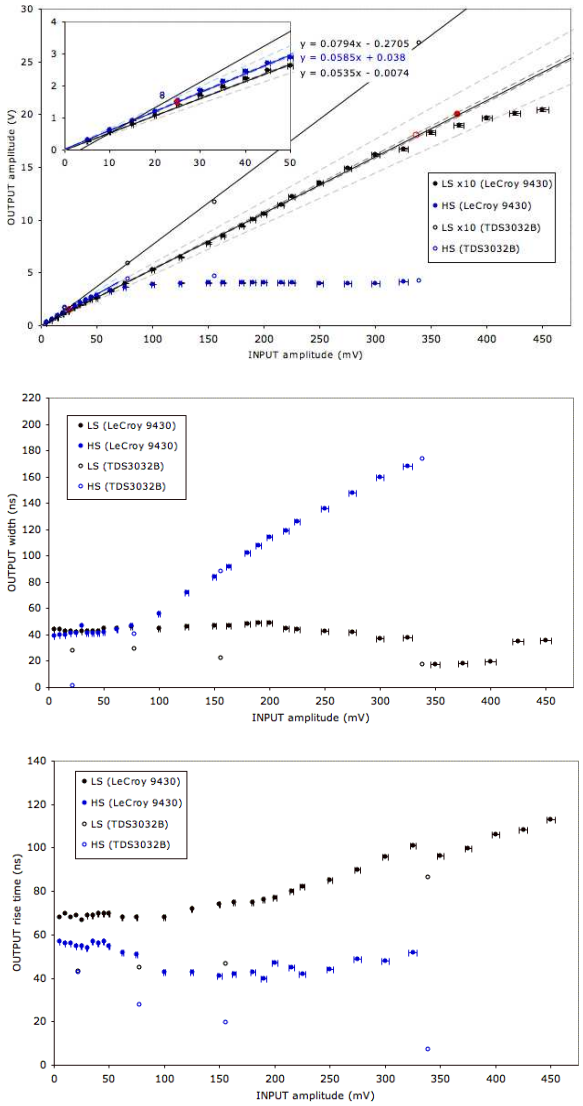

Figure 5.13: Input pulse amplitude, ($P0$) vs output pulse amplitude (upper panel), width (central) and rise time (lower) for LS ($P2$) and HS ($P3$) channels with the attenuator present in the setup (A=1.0) and $G1$, $G2$=10. The upper panel shows the LS and HS LeCroy data fitted up to $P0$=300 mV ($P2$=1.62 V) and $P0$=20 mV ($P3$=1.21 V) respectively, and the LS Tektronix TDS3032B data up to $P0$=339 mV ($P2$=2.68 V).

For A=1.0, the signal in the LS channel is expected to distort above $P2$=2.00 V and the HS above $P3$=1.50 V (solid red circular data-points in Figure 5.13, upper

panel). The LS channel appears to distort above $P2$=1.80 V (the open red circular data-point).

The gradients of the LS×10 and HS LeCroy data-sets are approximately equal at 53.5±0.8 and 58.5±1.1 respectively, with a factor of 10.93±0.26 between the HS and LS (see Figure 5.13). This implies that the gain of the first and second stage amplifiers, $G1$ and $G2$ are not equal to 10 but are infact 5.35±0.08 (=5.35/A) and 10.93±0.26 respectively.

The apparent variation in measurements made by different oscilloscopes is shown in Figure 5.13 (upper panel). Again, the gradient of the data acquired with the Tektronix TDS3032B oscilloscope are higher than those with the LeCroy 9430.

From Figure 5.13 (central) it is clear that the pulse width in the LS channel does not distort, even when the HS channel is distorted. Furthermore, this is the only configuration (A=1.0) which yields an increase in the LS pulse rise time (up to ∼100 ns) at large input amplitudes (see Figure 5.13 lower panel).

Some example pulses are shown below in Figures 5.14 (corresponding to the open circular data-points, Tektronix values, of Figure 5.13). The input, LS and HS examples with $P0$=20 mV are all shown to exhibit a 'double peak' feature, or potential 'ringing' effect. Also, large rise times in the LS and HS channels are already seen here at this relatively small input amplitude. With $P0 \geq$325 mV and $P0 \geq$75 mV, distortion effects in the LS and HS channels, respectively, are shown. 'Ringing' in the LS channel continues to be present with $P0 \geq$75 mV and by $P0$=150 mV the migration to higher rise times, longer τs, has clearly begun.

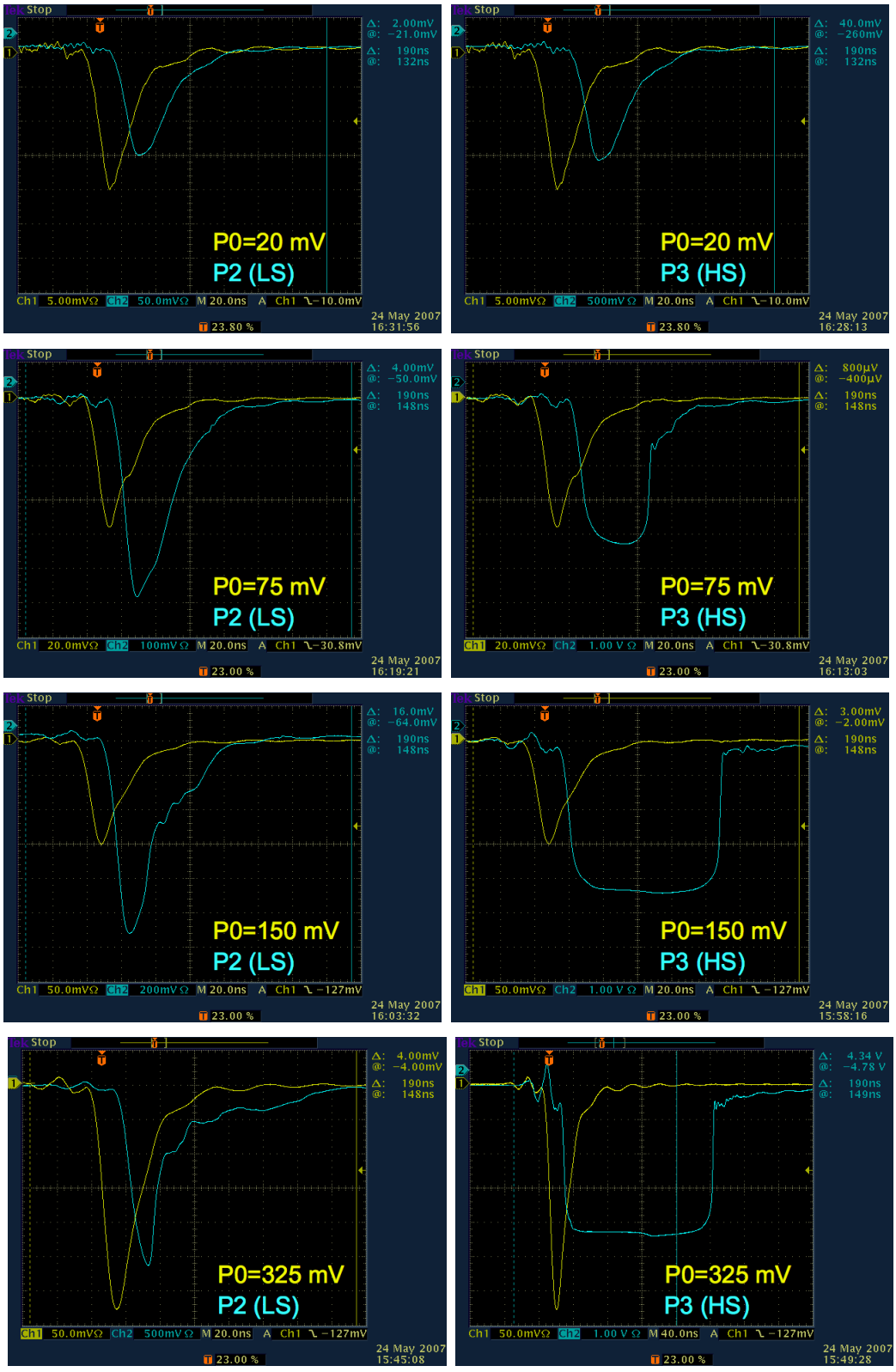

Figure 5.14: Screenshots of pulses from Tektronix TDS3032B oscilloscope for the input ($P0$), LS ($P2$) and HS ($P3$) channels with the attenuator present in the setup (A=1.0) and $G1$, $G2$=10. Signal saturation is shown to broaden the pulse shape (in the LS and HS channels for $P0$=75-325 mV).

From these studies of output amplitude, pulse width and rise time as a function of input amplitude there is no evidence to suggest that the pulse width in the LS channel changes in anyway at the onset of distortion in the HS channel and beyond. This means that no 'feedback' mechanism in which distortion in the HS channel affects the pulse shape in the LS channel is occurring and therefore does not explain the origin of events with long time constants seen in the surface data-sets.

The LS pulse amplitude ($P2$) at which distortion begins without the manual attenuator is 2.00 V ($P0$=289.5 mV). However, when the attenuator is used (A=1.0) the LS pulse amplitude ($P2$) at which distortion begins is 1.80 V ($P0$=336.3 mV). These two values should be equivalent if the attenuator is a passive device as originally believed to be the case.

Including the manual attenuator in the acquisition configuration and altering the attenuation, A, changes the experimentally determined gain of the first stage amplifier, $G1$. This is shown below in Table 5.1 and, once again, implies the attenuator is not acting as a passive device. Not only is $G1$ found to vary as a function of A but $G1$ is not equal to $\sim\times10$, as initially believed. This may be due to loading of the output since the measured gain is inconsistent with the estimate by factor of $\sim$2. However, the gain of the second stage amplifier, $G2$, was consistently measured as 10.13±0.20 across all three configurations.

	A	$G1$	$G2$
	0.5	4.66±0.07	10.13±0.21
	1.0	5.35±0.08	10.93±0.26
	1.0†	6.86±0.11	9.33±0.50
Mean		5.62±0.05	10.13±0.20

Table 5.1: Comparison of measured gains $G1$ and $G2$ of the first and second stage amplifiers, respectively, which are not consistent with both amplifiers having gains of $\sim\times10$. †When no attenuator is present in the setup A=1.0, effectively.

With A=1.0 the LS pulse rise time was shown to increase significantly. In contrast, no such increase was seen in the A=0.5 data-set where both the pulse rise time and width remained approximately constant across the range of input amplitudes.

Finally, examples of 'ringing', the origin of which is unknown, were observed to some degree in all data-sets where the shapes of the pulses demonstrating this effect were found to be similar to those seen in the surface data analysis.

Further revision of the hardware configuration and DAQ circuit followed as a direct

result of the amplifier distortion tests presented here. This involved implementing the changes illustrated in Figures 3.13 and 3.14.

5.1.4 Verifying ZE3RA τ Calculation

The pulse shape of and the mean arrival time, τ, returned by ZE3RA v2.0 for event #8 identified from within box A (see Figure 5.4, Section 5.1.2), was studied to establish the implications, if any, of the software pulse integration time (or 'pulse duration window') on τ.[161]

The first, unsaturated pulse of event #8 in the LS SUM channel was plotted, its decay time constant computed within PAW, $\tau(int)$, and an exponential function of known τ, $\tau(func)$, superposed (not fitted) for comparison (see Figure 5.15). The $\tau(int)$ value was calculated according to the mean arrival time method described in Section 3.5, over a range defined by the pulse duration in ZE3RA. In addition, a pulse from a different, individual event (#92187) was also added. Event #92187 was selected due to its pulse shape, amplitude, $\tau(int)$ and area being comparable with that of event #8. Neither event is shown to be similar in shape to the superposed function, with $\tau(func)$=77.7404 ns. Furthermore, regardless of the similarities in pulse shape and other parameters for these two events, ZE3RA justifies v2.0 integrating out to very different times in each case.

Figure 5.16 shows an exponential function fitted to the pulse rise time of event #8, as a function of varying pulse integration time: 100% integration time corresponds to the pulse duration window set by ZE3RA. Pulse areas calculated through the integration method and by ZE3RA are comparable for 100%, 75% and 50% of the window size. However, for the 25% window case the shorter tail starts to affect the integrated pulse area. The resulting decay time constants are inconsistent for all cases, suggesting ZE3RA v2.0 may have been artificially shifting similar events (box A) to longer τs, from $\tau \sim$50 ns to $\tau \sim$80 ns.

Further investigations (not shown) subsequently followed: this procedure was repeated for event #s 8 and 576 (box B), in both the LS and HS SUM channels; the integration method was adapted to disregard all negative contributions to the pulse area i.e. those above the baseline; and a new method was introduced, calculating $\tau(wsa)$ from the weighted sum average for all amplitude values above the baseline. The latter assumes no particular pulse shape, is equivalent to the algorithm invoked by ZE3RA[162] and returns a $\tau(wsa)$ consistent with that of ZE3RA.

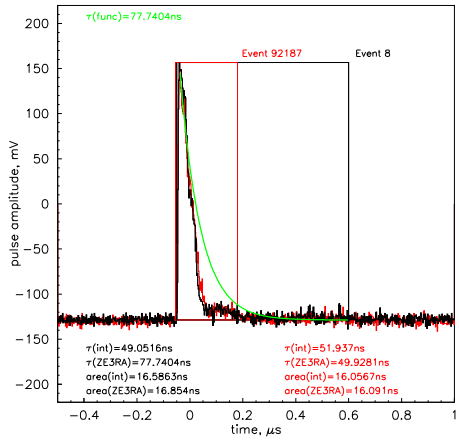

Figure 5.15: Comparable $S1$ unsaturated pulses for event #s 8 and 92187 in the LS SUM channel with characteristic decay time constants computed from the integrated pulse area, $\tau(int)$, and as given by ZE3RA, $\tau(ZE3RA)$, shown. A theoretical, exponential function of known τ, $\tau(func)$, is also shown (not fitted) for comparison.

The variation of $\tau(wsa)$ as a function of pulse integration time is presented in Figure 5.17 for various events in LS and HS SUM channels. For all events sampled here, except event #25 in HS SUM, when the integration time is $\lesssim$75% of the identified pulse duration the increase in calculated τ with increasing integration time is approximately constant (left panel). Therefore, contributions from the pulse tail, i.e. the latter $\sim$25% of the identified pulse, significantly affect the calculated τ and its dependence on pulse duration. Above $\sim$500 ns the increase in calculated τ with increasing pulse duration appears to be disjointed for event #8 in the LS and HS SUM (right panel). This then raises the question: if the identified S1 pulse has a pulse duration exceeding $\sim$500 ns then should the ZE3RA pulse definition be forced to stop at 500 ns?

The decay time constants calculated by ZE3RA v2.0 are successfully reproduced by a weighted sum averaging method, excluding all negative contributions to the total pulse area, employed in PAW. However, an exponential function, with $\tau(func)$=77.7404 ns, superposed does not mimic the pulse shape of event #8. As a result of this study, it was suggested that the pulse integration time defined within ZE3RA, should be revised, perhaps forcing the pulse area calculation to stop at $\sim$500 ns, for particularly long pulses.

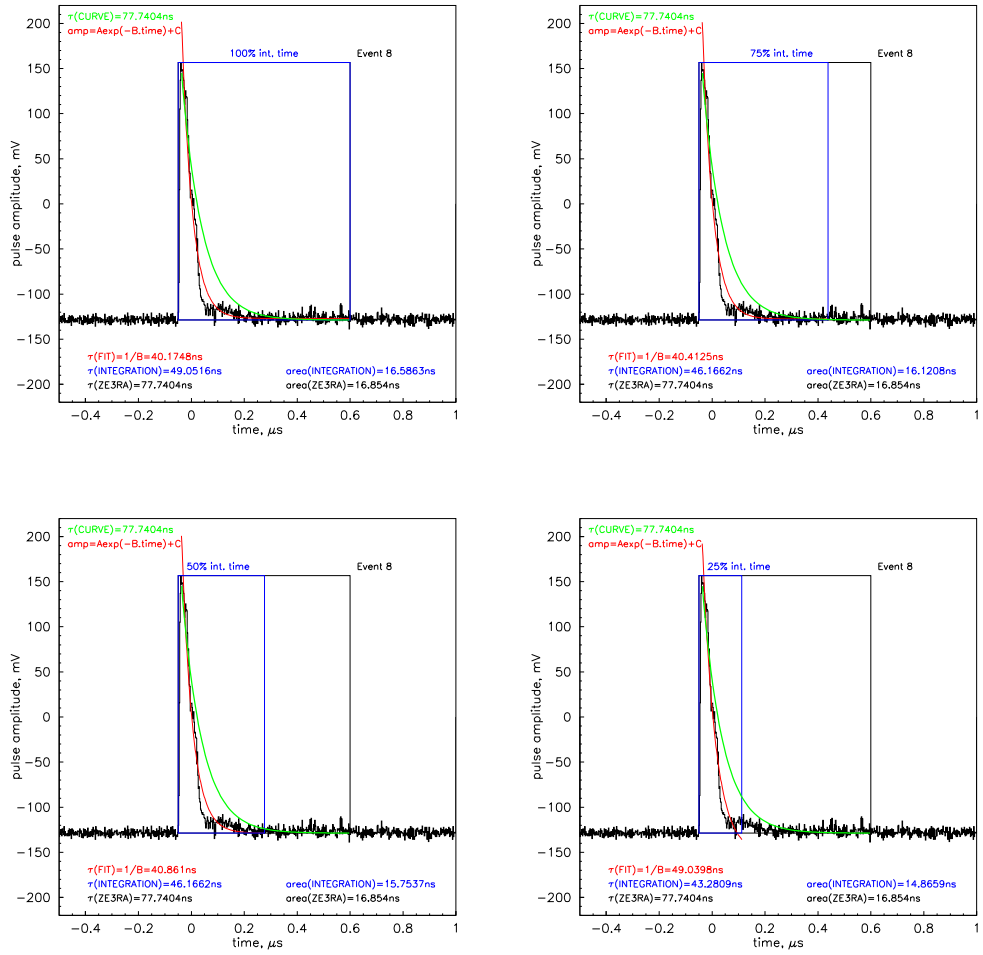

Figure 5.16: $S1$ unsaturated pulse for event #8 in the LS SUM channel with characteristic decay time constants computed from the integrated pulse area, $\tau(int)$, an exponential fit, $\tau(fit)$, and as given by ZE3RA, $\tau(ZE3RA)$, as functions of varying pulse integration time (100%, 75%, 50% and 25% of the ZE3RA setting) shown. A theoretical, exponential function of known τ, $\tau(func)$, is also shown (not fitted) for comparison.

Following re-reduction of this data-set with a revised ZE3RA, v2.1, the number of events in the long-τ population is significantly decreased, by at least a factor of one hundred and the $\tau(ZE3RA)$s are more clearly defined. This migration in the $\tau(ZE3RA)$ values, due to improved handling of pulses, particularly after-pulsing, although marked, requires additional study with the long-τ population still remaining at this stage.

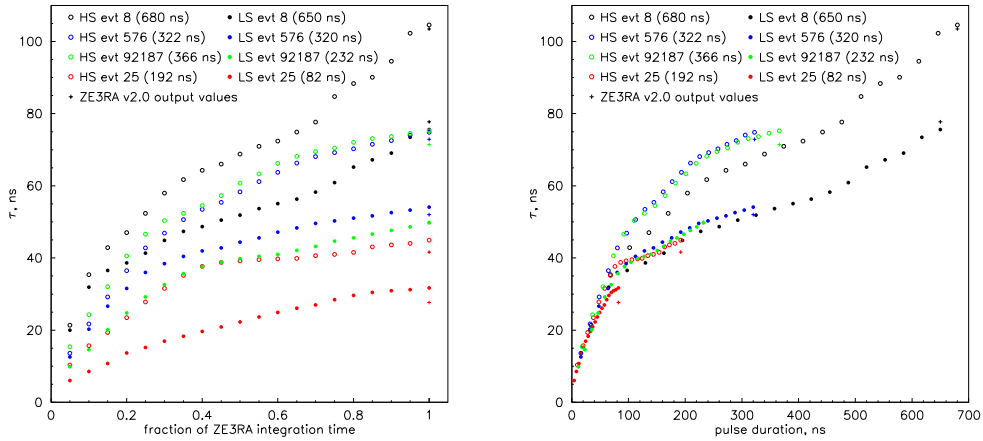

Figure 5.17: Comparison of computed characteristic decay time constants, $\tau(wsa)$, as a function of fraction of ZE3RA pulse integration time (left panel) and absolute pulse duration (right panel) for various events in the LS and HS SUM channels, with ZE3RA v2.0 output values, $\tau(ZE3RA)$. The full pulse duration, or integration times, are indicated inside the brackets of the legends.

5.2 Single Photoelectron Response

The single photoelectron response can be measured in two ways: with continuous light so attenuated that the average interval between successive photoelectrons is much greater than the least interval the measuring setup is able to resolve making it possible to count pulses from individual photoelectrons, well separated in time, which show very large amplitude fluctuations; and with light pulses so attenuated that the probability of each pulse giving rise to only one photoelectron is much greater than the probability of its giving rise to more than one.[163] The former description is deemed the 'conventional' approach, while the latter is defined as an 'alternative' one from here onwards.

The conventional approach to obtaining single photoelectron response spectra and SPE measurements (described in Sections 4.2.2.1 and 4.3.1) could not be invoked for the thirty-one 070706-070717 SPE, underground data-sets (acquired with an applied PMT voltage of 1.95 kV or 2.15 kV and reduced with ZE3RA v1.3). This was due to the trigger/threshold being set too high, incorrectly triggering, and only realised post-acquisition and analysis. Consequently, an alternative method was developed by the collaboration, demanding no specific data-sets or dedicated SPE runs instead using long, ^{137}Cs or ^{57}Co runs with good statistics, to calibrate the detector. It was

also deemed possible to utilise an SPE pulse from within the after-pulsing for calibration. However, this potentially useful cross-check, has not yet been implemented.

Alternative Poisson Approach

The alternative, Poisson approach to retrieving the SPE values for each PMT is based on the principle of plotting the pulse area spectrum in one PMT for a particular event, where a different PMT registers the largest deposited energy (*peakpmt*) for that same event. Hence, by doing this on an event-by-event basis a gate or time window is applied. The PMT in which the distribution is observed is required to be far enough away from the *peakpmt* for a sufficiently small (*nphe*=1) signal to be identified i.e. non-adjacent PMTs should be selected. Conversely, the observed PMT should not be too far from the *peakpmt* location - its probable that there is an optimum separation. For a more thorough account of this method, see Reference [164].

Since *nph* per light pulse follows a Poisson distribution, the spectrum of *nphe* produced in the PMT photocathode due to light pulses with constant intensity also does so:

$$P(\mu, nphe) = \frac{\mu^{nphe} \exp(-\mu)}{nphe!} \tag{5.1}$$

where μ is the mean of the distribution. It therefore follows that the probability of zero photoelectrons being emitted is:

$$\frac{P(\mu, 0)}{\sum_{k=0}^{+\infty} P(\mu, k)} = \exp(-\mu) \tag{5.2}$$

$$\Rightarrow \mu = -ln(\frac{N_0}{N_{total}}) \tag{5.3}$$

where N_0 is the frequency of zero photoelectrons being produced during some gate time window and N_{total} is the total number of events (or counts) in the spectrum.[163][165] Thus, by plotting the pulse area distribution for each PMT independently, with some gated cut in the reconstructed *nphe* applied, the number of events in the pulse area=0 bin (corresponding to the frequency characterising the absence of any signal and defined using a sample of pure noise in the same waveform) can be compared with the total number of events to compute μ according to Equation 5.3 and the mean of the pulse area spectrum, $< A >$ (Vns), can be found. Iterating this for all reconstructed *nphe* values, over say $\sim$10 keV energy bins, the

reciprocal of the gradient of a straight-line fit to the plot of μ as a function of $< A >$, for all gate values for a particular PMT i, returns the average SPE value, $< SPE_i >$ (Vns). For example, the case of the central PMT, PMT #1, is presented in Figure 4, Reference [124]. Ultimately, this procedure is repeated for each PMT (i=1,31) in turn, generating thirty-one $< SPE_{i=1,31} >$ values in the range 47±12 Vps. Note that the treatment of the errors in $\mu_{i=1,31}$ (and hence $< SPE_{i=1,31} >$) remains, at present, statistical only neglecting errors associated with the reconstructed event co-ordinates and energy and are therefore underestimated.

This robust, alternative approach has many strengths in that: any, non-specific data-set may be used, making this method extremely flexible; no threshold on the pulse area spectra is observed since the pulse is triggered in a separate PMT; and no appropriate fit function is required since fitting to the SPE distribution is not necessary.

Comparison of SPE Approaches

All, historical measured mean SPE area values are compared in Table 5.2. The different analyses were carried out by three members of the ZEPLIN III collaboration (referred to as A-C, where 'A' denotes work conducted by the author).

Mean SPE area measurements from the first science run (FSR) data, analysed by 'C', were derived by selecting short pulses with $area$(Vps)>0 and 3< tau(ns)<8 (as in Reference [166]). The resulting pulse area distribution, histogrammed for each channel, was then fitted with a Gaussian function (to the peak of the distribution) with the 'error on the mean' returned by the fit itself.

The measured mean SPE areas for the individual readout channels are presented in Figure 5.18. These were obtained using the different methods outlined in Table 5.2. Since the experimental configurations varied significantly, the general trends can be analysed however the absolute values can not be. If however 'true' SPE area values from these data-sets were compared instead of the measured mean SPE pulse areas, this would be valid. Across the data-sets the true SPE pulse areas would allow for: the acquisition at different applied PMT voltages, changing the potential difference across the PMTs; acquisition with distinct voltage dividers, altering the distribution of voltages across each dynode within the PMT; QE factors across the array.

Generally, the 080605 ^{137}Cs and FSR values, analysed by 'B' and 'C' respectively, are shown to be systematically lower than those derived from the SPE-specific 060707

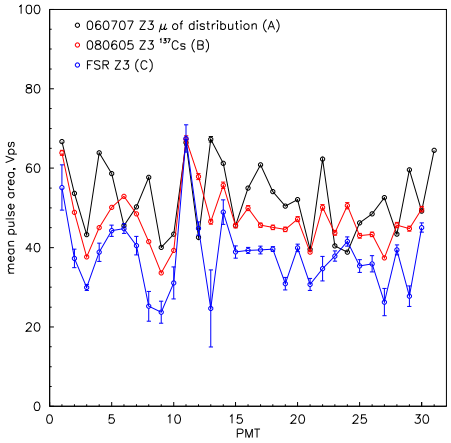

Figure 5.18: Plot summarising the measured mean SPE pulse areas for various studies conducted by different individuals (labelled A-C), using varied approaches (as outlined in Table 5.2). The author is referred to as 'A' and FSR corresponds to the first science run data.

data-set invoking the 'mean of the distribution' analysis approach. Additionally, as expected, there are particular data-points which are not consistent with the earlier analysis, namely for PMT channel #s 6, 13, 17, 24, 27, 28 and 29.

configuration	**A**	**B**[167]	**B**[165]	**C**
data-set	060707 SPE	060520 ^{57}Co	080605 ^{137}Cs	FSR
ZE3RA	v1.2	v2.2	v2.5	v2.5.2
# PMTs operational	31	31	30	30
voltage divider #	1	1	2	2
attenuation setup	surface	surface	underground	underground
Channels with 2 amplifiers	1-31	1-31	1, 8, 11, 13, 22	1, 8, 11, 13, 22
PMT V (- kV)	1.80	1.80	2.15	2.15
applied HV (kV)	0.00	13.05	17.00	17.00
E in liquid (kV/cm)	0	3.01	3.79	3.79
analysis method	mean of distribution	Poisson	Poisson	G fit to peak
SPE mean area (Vps)	52.37±1.59	-	47.13±1.32	37.97±1.67
analysis method	G+G fit, $g(x)$			
SPE mean area (Vps)	44.70±1.40			
analysis method	Polya fit, $p(x)$			
SPE mean area (Vps)	49.06±1.71			
analysis method	Wolfs fit, $w(x)$			
SPE mean area (Vps)	41.78±1.55			

Table 5.2: Comparison of SPE measurement approaches and the mean SPE area (Vps) values yielded. The analyses compared here were carried out by three members of the ZEPLIN III collaboration (labelled A-C). The author is referred to as 'A' and FSR corresponds to the first science run, underground data-set. The measured mean SPE areas of the individual readout channels are presented in Figure 5.18.

5.3 ^{57}Co Run at Zero Field

With no applied electric field 070711 ^{57}Co γ-ray data were acquired (with an applied PMT HV of -2.15 kV), with an uncollimated 3.7 MBq (100 μCi) ^{57}Co source located centrally on top of the instrument, for all readout channels. This data-set was subsequently reduced with ZE3RA v2.0.

The S1 is identified within all of the five recorded pulses (per timeline) at the analysis, post-acquisition stage. This involves defining a cut on the time constant, $\tau(ns) \geq 15$, as shown in Figure 5.19. It is clear a significant number of events are saturated in the HS SUM channel (#32) due to the choice of FS (where FS=0.2 V). Thus, a larger FS setting is recommended for future data-taking to ensure events with large amplitudes (and areas equivalent to the energy of the photopeak) are not saturated.

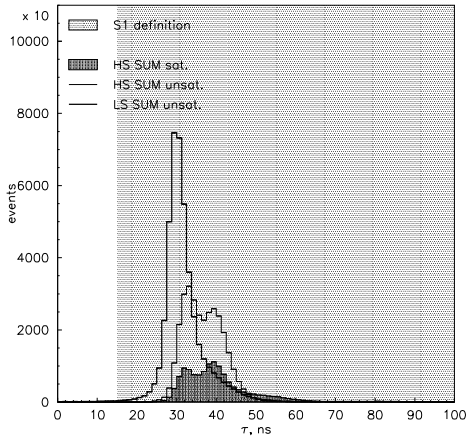

Figure 5.19: Zero-field ^{57}Co 070711 time constant, τ (ns), distributions for the first recorded pulse per event in the LS and HS SUM channels (with and without a cut on pulses saturating the FS acquisition range). Comparison of the distributions enable the τ parameter to define an S1: $\tau(ns) \geq 15$.

Amplifier Distortion

The S1 τ distributions in all thirty-one individual LS and HS channels were plotted and compared to investigate evidence of time constant distortion, noting those particular channels with two amplifiers in the DAQ chain.

The τ LS and HS distributions for PMT #s 1, 8, 11, 13 and 22, i.e. those with

two amplifiers, were found to be less symmetric than for single amplifier channels. The LS and HS τ values were systematically longer in channels with two amplifiers ($\sim$38 ns and $\sim$42 ns, respectively) than with a single amplifier ($\sim$30 ns and $\sim$40 ns), with the HS channels always yielding longer time constants than the LS regardless of the acquisition setup. Also, HS distributions for the outermost PMTs (#s 23-31) exhibited an additional 'feature' at τ $\sim$10-15 ns. Ultimately this brief study confirmed that the time constants in readout channels with two amplifiers do suffer some degree of distortion and four noteworthy examples are presented in Figure 5.20 for PMT #s 1, 2, 13 and 31.

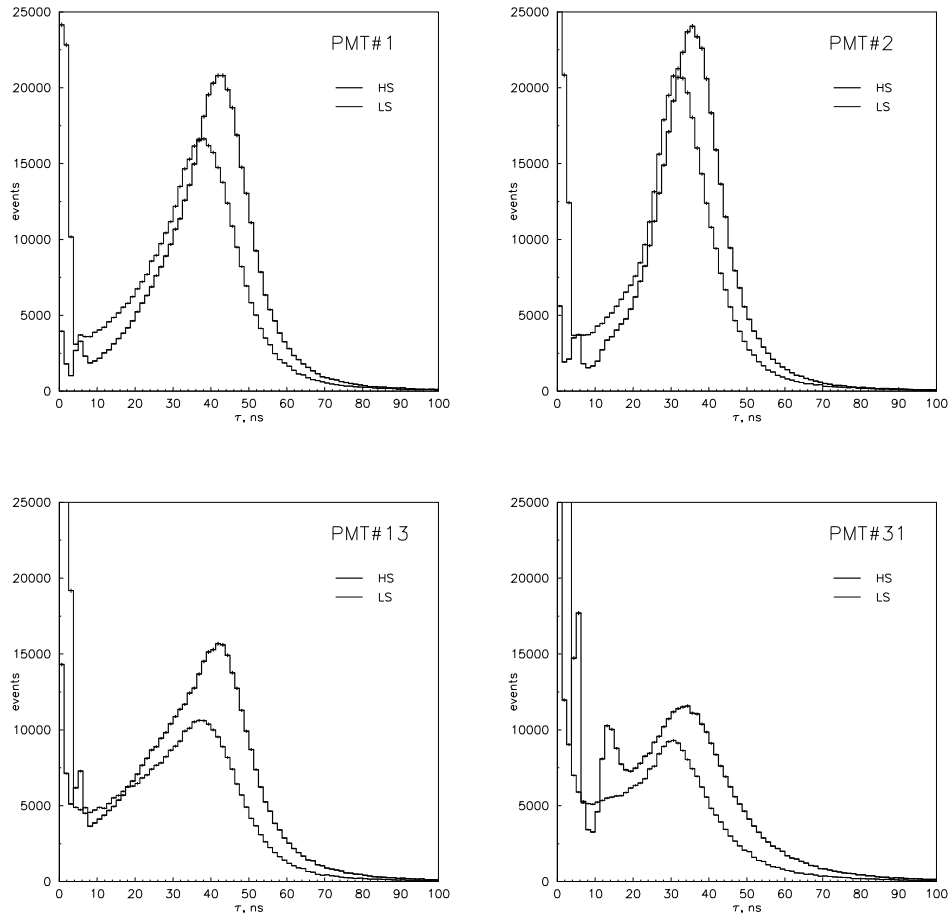

Figure 5.20: Zero-field ^{57}Co 070711 τ (ns) distributions for the first recorded pulse per event in the LS and HS SUM channels of PMT #s 1, 2, 13 and 31. The asymmetry of the distributions with two amplifiers is clear when comparing PMT #s 1 and 13 (two amplifiers) with #2 (a single amplifier). For each PMT the HS channel yields higher time constants than the LS. The additional 'feature' at τ $\sim$10-15 ns is evident in the HS distribution corresponding to PMT #31. This PMT was later shown to not be connected properly (see Section 5.4).

S1 Light Collection

The 070711 ^{57}Co zero-field data-set was used in conjunction with the equivalent 070716/17 SPE data to calculate an S1 LY. The S1 pulse area (nphe) distribution for all thirty-one PMTs in the HS SUM channel, without QE corrections, is shown in Figure 5.21. The ∼125 keV ^{57}Co 'collimated' photopeak distribution corresponding to the central events from the inner 7 PMTs is also shown.

The conversion from pulse area (Vns) to pulse area (nphe) was done using the average SPE pulse area distribution value from a zero-field 070716/17 data-set of 58.06±1.18 Vps in the HS SUM. This value was obtained by averaging the means of the inner 7 distributions, without invoking a fit function, and the error quoted is derived from the 'standard error of the mean'. The energy calibration is determined by fitting four Gaussian functions to the ^{57}Co photopeak distribution, returning a mean of 589.51±1.04 phe (28.6% FWHM). Thus, an S1 LY of 4.72±0.10 phe/keV for the centre of the chamber was derived. The S1 LY measured here is consistent with that presented in Section 4.3.4 using the 060519 zero-field ^{57}Co data-set, acquired with a slightly more conservative PMT voltage of -1.8 kV.

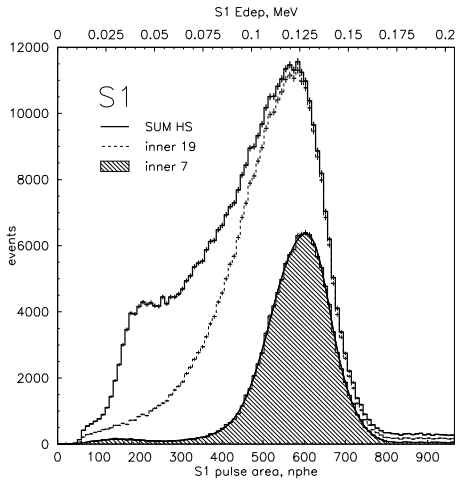

Figure 5.21: S1 zero-field ^{57}Co 070711 pulse area (nphe), or energy (MeV), spectrum for the HS SUM channel using an averaged HS SPE pulse area value from the 070716/17 data-set. Four Gaussian functions are fitted to the HS SUM distribution for the inner 7 PMTs - the ∼125 keV photopeak - with a mean of 589.51±1.04 phe (28.6 % FWHM). From this an S1 zero-field LY of 4.72±0.10 phe/keV is derived.

The distributions shown in Figure 5.21 corresponding to the inner 7, 19 and all PMTs in the array can provide additional information on light collection in the

chamber by comparing the areas under the distributions themselves, the number of events detected or intensity, defined as I_7/I_{19}, I_7/I_{31} and I_{19}/I_{31}. The values of these dimensionless ratios will be determined by (at least) two competing effects in that: above the central PMTs the γ-rays will interact in a smaller thickness of the Cu (pressure) vessel, due to the reduced angle, depositing more energy above the central PMTs and hence increasing the I_7/I_{31} ratio; an outer PMT will collect additional contributions of light from events happening beyond the physical edge of the PMT array, but within the LXe volume, actively decreasing the I_7/I_{31} ratio.

The expected intensity ratios were estimated using a simplistic, geometrical approach (see Figure 5.22), solely modelling the former effect, by considering: the thickness and density of the Cu vessel (t ~0.3 cm and ρ_{Cu}=8.96 g cm^{-3}, respectively) in the emitted ^{57}Co 122.06 keV γ-ray's path; the dimensions of the LXe target (total Xe depth, l=4.0 cm); the mass attenuation coefficient for 122.06 keV ^{57}Co γ-rays ($\mu/\rho_{(E_\gamma,Cu)}$=0.30882 cm^2 g^{-1}[168]); the PMT position co-ordinates (x_i (cm), y_i (cm)) with respect to the central PMT (i=1); the (non-vertical) thickness of the Cu vessel between the ^{57}Co source and each PMT (or distance travelled) along the line of sight, d_i (cm); and the angle of propagation with respect to the central PMT, θ_i (°). These parameters are applied to the following equations in order to determine the predicted intensity ratios:

$$\frac{I_j}{I_k} = \frac{\sum_{i=1}^{j} I_{PMTi}}{\sum_{i=1}^{k} I_{PMTi}} \tag{5.4}$$

and where

$$I_{PMTi} = \exp\{\ln(E_\gamma) - (\mu/\rho_{(E_\gamma,Cu)} \times \rho_{Cu} \times d_i)\} \tag{5.5}$$

$$d_i = \frac{t}{\cos\theta_i} \tag{5.6}$$

$$\theta_i = \arctan\frac{x_i}{(l+t)} \tag{5.7}$$

$$\tag{5.8}$$

The results of this study, compared with measured values extracted from Figure 5.21, are summarised in Table 5.3. Although simplistic in its treatment, this model does successfully reproduce the measured intensity ratios. This suggests that the

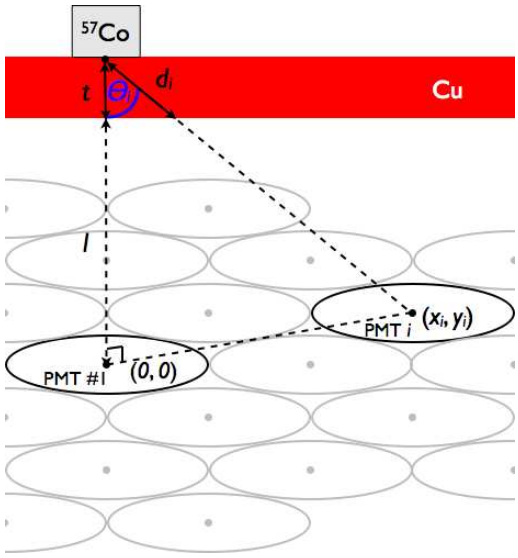

Figure 5.22: Schematic representing the simplified geometrical model used to estimate the expected intensity ratios, only modelling the effect of ^{57}Co γ-ray absorption in the Cu vessel on light collection at PMT i.

(considered) effect of attenuation by the Cu vessel is more dominant than the (unconsidered) effect of extra light contributions from beyond the array. Also, the I_7/I_{31} ratio is not simply found to be equal to 7/31=0.23. In future, this approach may be extended to include modelling of the second, inner Cu (target) vessel and, ultimately, of the unconsidered effect in some way.

	modelled	070711 data
I_7/I_{31}	0.33	0.31
I_7/I_{19}	0.46	0.41
I_{19}/I_{31}	0.71	0.75

Table 5.3: Comparison of modelled and measured (070711 ^{57}Co data) event intensity ratios for the inner 7, 19 and all 31 PMTs, considering the effect of ^{57}Co 122.06 keV γ-ray absorption in the Cu (pressure) vessel.

Low-Energy Spectral Feature

An equivalent plot to Figure 5.21, but in log space, is shown in Figure 5.23 providing some indication of the 692 keV γ-ray line as well as evidence of 'photon backscattering' peaks, or a Compton shoulder, below ~50 keV, expected at 39.46 keV and 47.15 keV.

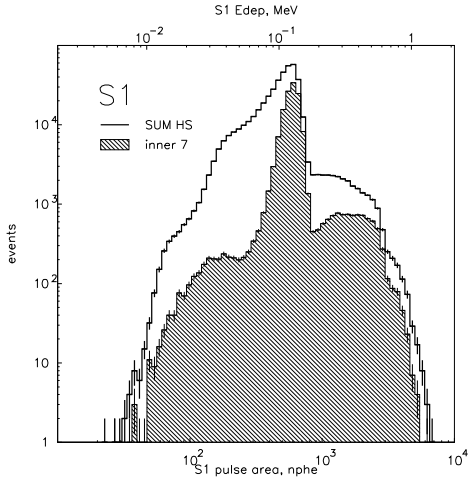

Figure 5.23: S1 zero-field ^{57}Co 070711 pulse area (nphe), or energy (MeV), spectrum for the HS SUM channel. The x-axis is normalised with respect to the ∼125 keV 'photopeak'. The position of the 692 keV 'shoulder' is clear and, although weak, there is some suggestion of the 122.01 keV and 136.46 keV backscatter peaks here at $\lesssim$50 keV and a possible Cu X-ray peak at ∼8 keV, although statistics are very poor here.

5.3.1 Energy Resolution Parameterisation: Gaussian Fitting & Comparison with MC Simulation

The zero-field 070711 ^{57}Co energy distribution shown in Figure 5.21, recovered from the inner 7 PMTs, was compared with an equivalent GEANT4 MC simulated spectrum in order to investigate and parameterise the energy resolution of ZEPLIN III.

In order to accurately employ this method the y-axis of ^{57}Co spectrum (0.02275 days exposure) was converted to rates and the complementary zero-field 070717/18 normalised background spectrum (0.6212 days exposure) was then subtracted, treating the errors in each bin appropriately (see Figure 5.24). The resulting 'data' spectrum, i.e. purely due to ^{57}Co energy deposits with no background contribution, was attempted to be fitted with four Gaussian functions, corresponding to: the 122.06 keV and the 136.47 keV photoelectric ^{57}Co γ-ray absorption lines; the escape peak from the 136.47 keV incident γ-ray, at 96.46 keV (=136.47-34.56-5.45 keV, where 34.56 keV is the Xe K shell binding energy[133]); and the Compton edge ($\lesssim$40 keV) centred at ∼30 keV. Although this was possible within a PAW function, following normalisation to 1 sec exposure and the background subtraction, this was problematic due to the total fit function containing 12 free parameters and proving ultra-

sensitive to the initial parameters. Therefore, the fit parameters produced from a fit to the ^{57}Co spectrum, prior to background subtraction, were temporarily adopted for further analysis. Values were retrieved for the width, σ, and mean energy, E_{dep}, values for each line or feature, including: $\sigma(E_{dep}$=124.68±0.18 keV)=15.41±0.15 keV, $FWHM$=29.0% (χ^2=1.08). This was done with a view to developing an alternative approach for establishing the energy resolution without requiring such a fit to be performed.

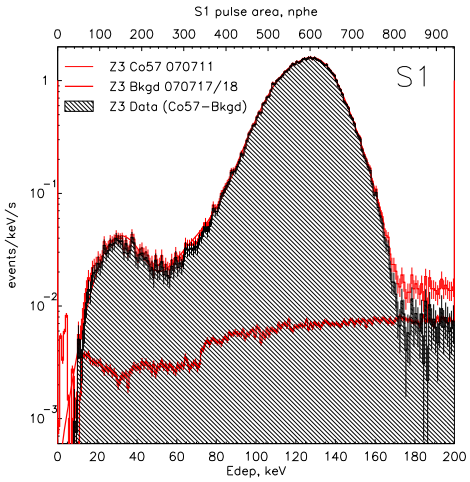

Figure 5.24: Comparison of S1 pulse area (nphe) or energy, E_{dep} (keV), spectra for ZEPLIN III 070711 acquired ^{57}Co calibration data and the complementary 070717/18 background data-set, for the inner 7 PMTs. The difference between these two is also shown. Subtraction of the background has a significant impact on the ^{57}Co distribution at higher energies, $E_{dep} \gtrsim$150 keV.

Note that the obvious, sharp step observed in the background spectrum at $E_{dep} \sim$70 keV in Figure 5.24 is no longer present when the same background data-set is re-reduced with ZE3RA v2.1 (see Figure 5.25).

In parallel to the ^{57}Co normalisation, the deposited energy output spectrum generated by GEANT4 was smeared with an energy resolution Gaussian function with σ(keV)=1.10$\sqrt{(}E_{dep}$(keV)) implemented within PAW (see Figure 5.26). Here this particular σ value was selected merely as a reasonable physics-motivated starting point. The smeared MC spectrum was then fitted with four Gaussian functions, yielding σ' and E_{dep} values for each line or feature in the same way as for the real data scenario with $\sigma'(E_{dep} = 121.50 \pm 0.11$keV)=14.67±0.11, $FWHM$=28.4% (χ^2=1.08). The final MC and data spectra are superposed for comparison. Thus, the eight determined σ, σ' and E_{dep} values, four from the MC and four from the real

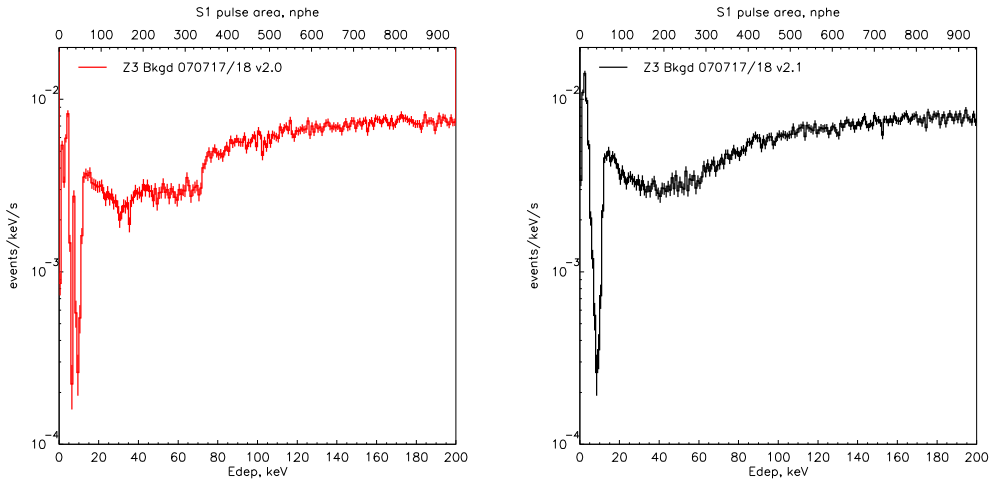

Figure 5.25: Comparison of S1 pulse area (nphe) or energy, E_{dep} (keV), spectra for ZEPLIN III 070717/18 acquired background data-set, for the inner 7 PMTs, reduced with ZE3RA v2.0 (left panel) and v2.1 (right panel). There was a marked improvement in the shape of the background distribution with the later version, v2.1, removing the sharp 'step' feature around E_{dep} ~70 keV.

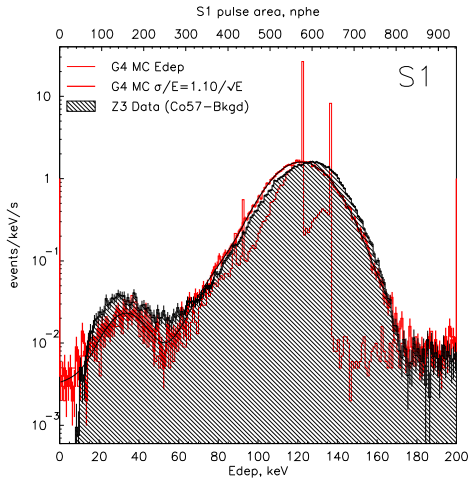

Figure 5.26: Comparison of S1 pulse area (nphe) or energy, E_{dep} (keV), spectra for ZEPLIN III 070711 acquired 'data' (background subtracted ^{57}Co calibration data) for the inner 7 PMTs and the GEANT4 ^{57}Co MC data-set (without background contributions), smeared with energy resolution σ/E_{dep}=1.10/$\sqrt{E_{dep}}$.

ZEPLIN III data, could be used to plot σ/E_{dep} (or σ'/E_{dep}) as a function of E_{dep} (see Figure 5.27), parameterising the energy resolution of the instrument.

Superposing the ^{57}Co spectrum (with background subtraction) and the smeared

output from the MC in Figure 5.26 demonstrates consistency in amplitude and width of the photopeak. However, the energy-calibration factor (and thus the peak position returned by the fit and/or the measured SPE value) is not exactly correct since each of the photopeak positions, of the G4 MC and data spectra, do not coincide. Also, the peak-to-valley ratios of the lines and features show less agreement. This suggests that the MC input parameters and modelled physics may require some refinement or further considerations, i.e. with regards to the grid model, reflectivity values, etc.

Instrument energy resolution, σ/E, may be parameterised by:

$$\left(\frac{\sigma}{E}\right)^2 = \left(\frac{A}{\sqrt{E}}\right)^2 + \left(\frac{B}{E}\right)^2 + C^2 \tag{5.9}$$

where C is a constant.[151] The most dominant term is the first, A (keV$^{1/2}$) term which is stochastic, representing statistical fluctuations in sampling. Statistical processes e.g. photoelectron statistics, limit the detector accuracy with this term dominating the overall energy resolution. The second, B (keV), (electronic) noise term, or that due to instrumental effects which are mainly attributable to amplifier noise is energy-dependent. The relative contribution of this decreases with increasing E and this limiting accuracy is more significant in the low-E regime. The final, C, constant term is energy-independent and is due to non-uniformities i.e. operating drift, or non-linearities in the detector components, setting the limit for detector performance at high energies. Aside from these three main contributions, the intrinsic PMT resolution - uniformity of photoelectron collection from the photocathode and statistical fluctuations in the PMT gain, or electron multiplication - may also factor in the overall detector resolution.

Using 070711 ^{57}Co calibration data (prior to background subtraction), with four Gaussians fitted to the energy spectrum, the energy resolution, σ/E_{dep}, as a function of energy, E_{dep}, is shown in Figure 5.27. The results of fitting to GEANT4 MC generated data (with no background contributions), smeared with a Gaussian of σ/E_{dep}=1.10/$\sqrt{E}_{dep}$, are also shown for comparison. Trendlines are added for both data and simulation, neglecting an anomalous data-point in each case along with a curve corresponding to all features of the GEANT4 MC input spectrum, smeared with resolution σ/E_{dep}=1.10/$\sqrt{E}_{dep}$.

Figure 5.27 suggests that the instrument energy resolution (with A=1.08 keV$^{1/2}$, B=0 keV and C=0.03) is worse than the input G4 MC energy resolution (A=1.10 keV$^{1/2}$, B=0 keV and C=0), with a more accurate description requiring a second,

constant term. Note that the apparent shift in the photopeak data-points for data with respect to simulation is due to the performed fit, not the GEANT4 MC modelling. The GEANT4 MC fitted data-points do not reproduce that of the GEANT4 MC input resolution, with smearing. Furthermore, the low-energy feature is not a line, but is a distribution prior to smearing. Therefore, when plotting the GEANT4 MC fitted data-points a correction was required for the low-energy feature.

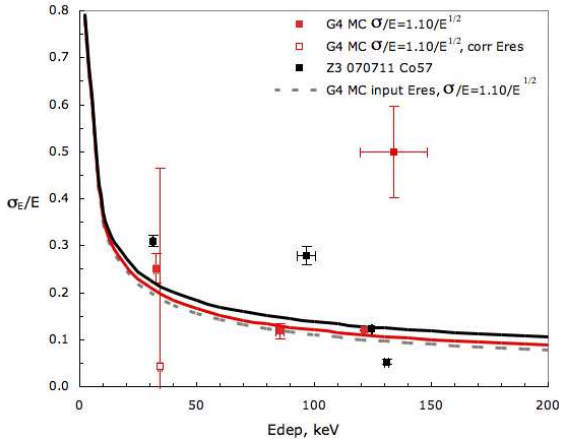

Figure 5.27: Parameterising the ZEPLIN III energy resolution using 070711 ^{57}Co calibration data (prior to background subtraction), with four Gaussians fitted to the energy spectrum with a superposed trendline (A=1.08 keV$^{1/2}$, B=0 keV and C=0.03). For comparison, the results of fitting to GEANT4 MC generated data, smeared with a Gaussian of σ/E_{dep}=1.10/$\sqrt{E}_{dep}$, and the corresponding trendline (A=1.10 keV$^{1/2}$, B=0 keV and C=0.01) are also shown. Since the low-energy feature at E_{dep} ~32 keV is not a line, but a distribution the corrected data-point has been indicated. Finally, a function for each G4 MC input line/feature, smeared with σ/E_{dep}=1.10/$\sqrt{E}_{dep}$ (A=1.10 keV$^{1/2}$, B=0 keV and C=0), is displayed for completeness (broken line).

The corrected energy resolution of the GEANT4 MC low-energy feature, σ_{eres}/μ_{eres}, was found by deconvolving the energy resolution intrinsic in the smeared and fitted mean E_{dep} value, σ_f/μ_f, from that of the fitted mean E_{dep} value, σ_i/μ_i, prior to smearing according to the prescription in Figure 5.28.

Correcting for the low-energy feature in this way, as well as the two data and simulated outlying data-points due to the fit sensitivity, demands a new method of parameterising the energy resolution to be developed. Preferably, this method would eliminate dependence on any fit procedure.

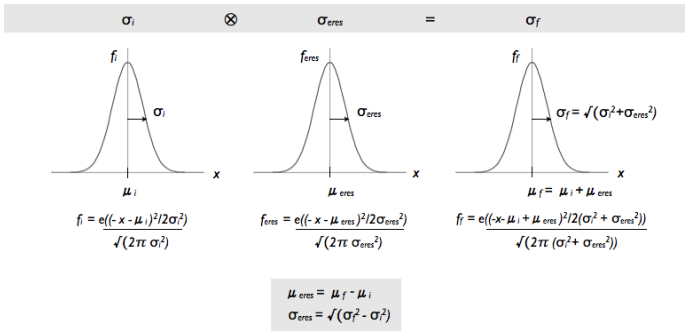

Figure 5.28: Procedure to deconvolve the energy resolution of the low-energy feature in the smeared and fitted GEANT4 MC energy spectrum, f_f, from that of the initial GEANT4 MC input (unsmeared) energy spectrum, f_i to allow the 'corrected' energy resolution data-point, σ_{eres}/μ_{eres}, to be plotted in Figure 5.27.

Photo-Fractions and Cross Sections

The photo-fraction, P (%), is a direct measure of the probability that a γ-ray, that undergoes interaction of any kind within a detector, ultimately deposits its full energy. It is defined as the ratio of the total area under the photopeak, $R_{p.p}$ (events/s), to that of the entire response function, R_{total} (events/s), in the energy spectrum[151]:

$$P = 100 \times \frac{R_{p.p}}{R_{total}} \tag{5.10}$$

Here, evaluation of the photo-fraction is used to interpret the energy spectrum and large values of P are sought to minimise the complicating effects of Compton continua and escape peaks in the spectra with numerous lines and features.[151] Furthermore, $R_{p.p}$ can be used to estimate the dimensionless photoelectric and Compton continuum cross section ratio in Xe: $(\sigma_{p.e}/\sigma_C)_{Xe}$. For a 'small' detector (i.e. where only single interactions take place) this relationship can be expressed in the following way:

$$\left(\frac{\sigma_{p.e}}{\sigma_C}\right)_{Xe} = \frac{R_{p.p}}{R_C} \tag{5.11}$$

where R_C (events/s) is the area under (or event rate of) the Compton continuum, i.e. with $E_{dep} \lesssim$50 keV.[151]

Applying Equation 5.10 to the data (^{57}Co minus background) energy spectrum in Figure 5.24 yields $P \sim$98% when integrating $R_{p.p}$ for 50$\lesssim E_{dep} \lesssim$170 keV and R_{total} for 170$\lesssim E_{dep} \lesssim$200 keV. Similarly, the derived cross section ratio, $(\sigma_{p.e}/\sigma_C)_{Xe}$, is

found to be ∼59.6. This is consistent with the theoretical value, quoted as 58.6 using attenuation and scattering cross sections of $\sigma_{p.e}/\rho_{Xe} = 1.0101$ cm^2 g^{-1}[133] and $\sigma_C/\rho_{Xe} = 0.17241$ cm^2 g^{-1}[133] at E_γ=122 keV.

5.3.2 Energy Resolution Parameterisation: Iterative χ^2 Testing

An alternative method of parameterising the energy resolution of ZEPLIN III was developed. As in Section 5.3.1 the zero-field 070711 ^{57}Co energy distribution shown in Figure 5.21, recovered from the inner 7 PMTs, and an equivalent GEANT4 MC simulated spectrum were used throughout application of this method.

The novel approach adopted did not demand any fit procedure and actively sought to eliminate this requirement. This was achieved by defining an energy resolution function in PAW ('eres.f' according to Equation 5.9) which was allowed to vary, accompanied by an iterative minimum χ^2 test, comparing each smeared energy spectrum (counts/keV) to the real, data spectrum (purely due to ^{57}Co energy deposits with no background contribution). Note that within eres.f a vector 'dgauss' of single-precision random numbers in a Gaussian distribution, with mean=0 and variance=1, is generated by the 'rnorml' CERN program library. 'rnorml' invokes the uniform generator 'ranmar'. Thus, each time the E_{dep} is smeared (with fixed A, B and C) the shape of the resulting spectrum will inevitably vary since eres.f contains a random number generator.

The total χ^2 value, summed over n bins in the energy range E=10-200 keV, is defined as:

$$\chi^2 = \sum_{i=1}^{n} \frac{(OBS_i - EXP_i)^2}{EXP_i} \tag{5.12}$$

where OBS_i and EXP_i are the number of observed and expected counts in the i^{th} bins, respectively. The reduced χ^2 value, summed over n bins, is defined as:

$$red.\chi^2 = \frac{\chi^2}{m} \tag{5.13}$$

where m is the number of degrees of freedom, m=n-1. The reduced χ^2 values were then averaged over all runs to find the physical minimum of the average reduced χ^2 value and its corresponding A_0, B_0 and C_0 values. In order to be computationally- and time-efficient this procedure was designed to be conducted in two, distinct steps:

an initial, coarse scan; and a later, refined scan.

The coarse scan consisted of sampling A, B and C during a run, r, of 20000 iterations, with: r=1, 10, +1; A=0.00, 2.00, +0.10; B=0.00, 1.00, +0.10; and C=0.00, 1.00, +0.10. This located a physical minimum with output values of A_0=1.10, B_0=0.70 and C_0=0.00 with average reduced χ^2=12.8901. Thus, the run conditions for the refined scan, with 130000 iterations, were set as: r=1, 10, +1; A=0.00, 1.30, +0.02; B=0.00, 1.00, +0.05; and C=0.00, 0.10, +0.01. Final, generated output values of A_0=1.08, B_0=0.95 and C_0=0.00, with an average reduced χ^2 of 12.4407, were generated.

The resulting physical minimum was checked by plotting the 'valleys' in the average reduced χ^2 for A, B and C in turn whilst keeping the other two parameters fixed, to ensure it was not merely a local minimum (see Figure 5.29).

The errors in the final, output A_0, B_0 and C_0 values were calculated using these distributions, specifically the valley widths. However, the distribution of reduced χ^2 as a function of A was found to be asymmetric about A_0, no obvious physical minimum was found for B and there appeared to be an insufficient number of data-points sampled for C <0 to establish a lower error on C_0, δC_{0-}. Therefore, an additional, third stage was introduced into the procedure, allowing even more refined sampling of A, B and C, in turn. Effective evaluation of A_0 and re-calculation of the associated error, δA_0, required 650 iterations with: r=1, 10, +1; A=1.00, 1.30, +0.02; B=0.95; and C=0.00 (see Figure 5.30). Similarly, for further analysis of B_0 (and δB_0) 2000 iterations were performed, with: r=1, 10, +1; A=1.08; B=0.00, 100.00, +0.05; and C=0.00 (see Figure 5.31). Finally, C_0 (and δC_0) was re-sampled with 100 iterations and: r=1, 10, +1; A=1.08; B=0.95; and C=0.00, 0.10, +0.01 (see Figure 5.32). The resulting distributions of reduced χ^2 as a function A (or B, or C) were then fitted with a polynomial function to locate the minima (A_{0fit}, B_{0fit} and C_{0fit}) precisely. Note that plots of the reduced χ^2 as a function of two parameters simultaneously (fixing the third) although challenging to interpret visually would have more tightly constrained A_{0fit}, B_{0fit} and C_{0fit}.

The polynomial fit to the refined A distribution has a minimum at A_{0fit}=1.08±0.06 (Figure 5.30, right panel). The large error bars on B_{0fit}, shown in Figure 5.31 (right panel), demonstrate the insensitivity of the reduced χ^2 to B_{0fit}. In this case it is only really possible to place an upper limit on the value of B_{0fit}: B_{0fit} <1.94±1.70. This suggests that B_{0fit} should be optimised first and that the order in which these three parameters are optimised may matter. Figure 5.32 (right panel) shows the

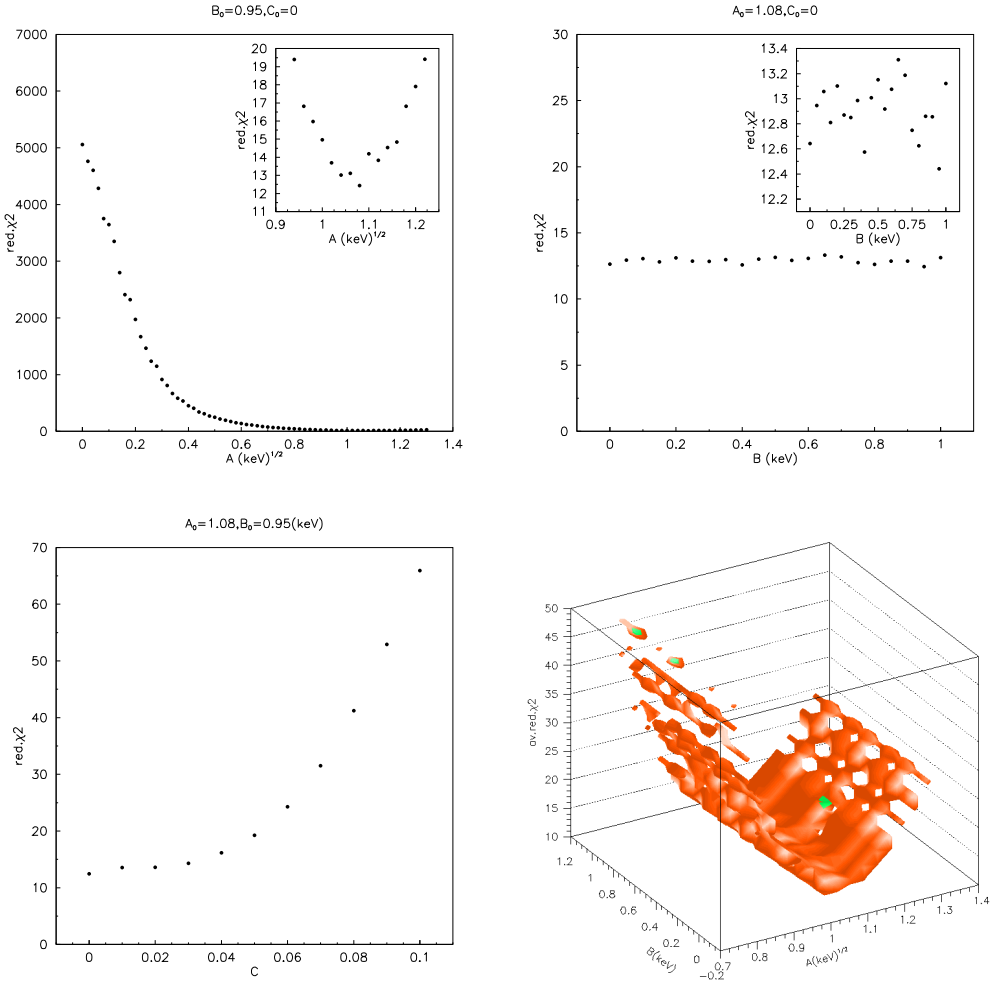

Figure 5.29: The reduced χ^2 as a function of A (with fixed B and C), B (with fixed A and B) and C (with fixed A and B) following both the coarse (20000 iterations) and refined (130000 iterations) scans shown in the upper left, upper right and lower left panels, respectively. The average reduced χ^2 as a function of A and B is also shown in 3-D parameter space (lower right panel). The insert shown in each upper panel is a zoomed version of the distribution.

reduced χ^2 is also insensitive to the fitted C_{0fit} value, with only an upper limit able to be placed on it: C_{0fit} <0.02±0.01. As expected, the energy resolution parameter A (stochastic term) dominates the behaviour of χ^2.

The resulting GEANT4 energy spectrum (smeared with A=1.08, B=0.00 and C=0.00) along with the ^{57}Co data spectrum, is shown in Figure 5.33 (left panel). Inconsistencies in the peak-to-valley ratios of the two spectra remain. As previously mentioned (see Section 5.3.1), the MC input parameters and modelled physics may require some refinement. The residuals of these two spectra are plotted in Figure

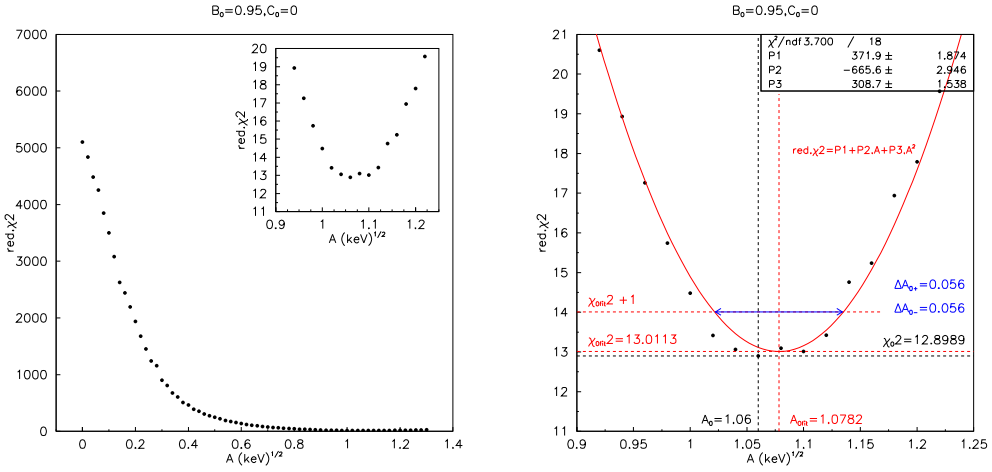

Figure 5.30: The reduced χ^2 as a function of A (with fixed B and C) following all three iterative stages, the coarse, refined and additional third stage scans, (left panel). A polynomial fit to the zoomed distribution, inset in the left panel, is also shown, displaying the fitted minimum, A_{0fit}, and associated errors, δA_{0fit}, (right).

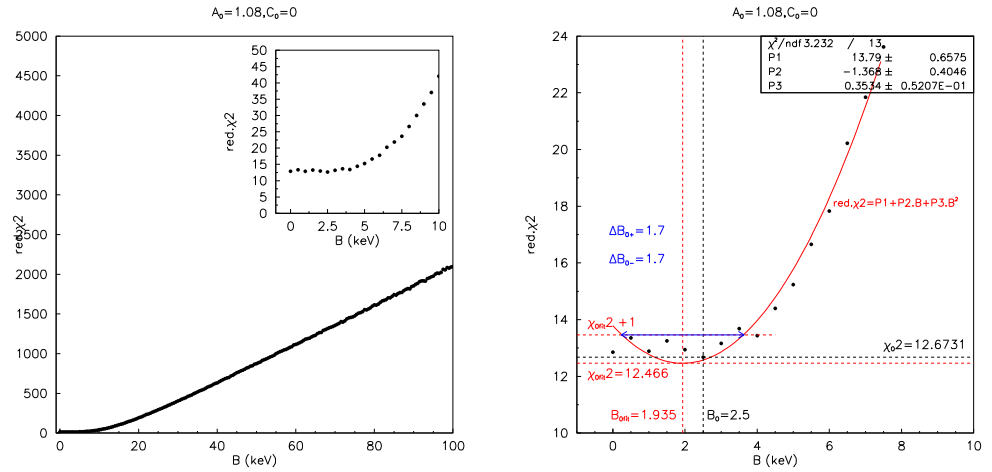

Figure 5.31: The reduced χ^2 as a function of B (with fixed A and B) following all three iterative stages, the coarse, refined and additional third stage scans, (left panel). A polynomial fit to the zoomed distribution, inset in the left panel, is also shown, displaying the fitted minimum, B_{0fit}, and associated errors, δB_{0fit}, (right).

5.33 (right panel). The large residuals observed indicate that the photopeaks were not exactly aligned during the energy calibration, contributing significantly to the large average reduced χ^2 returned.

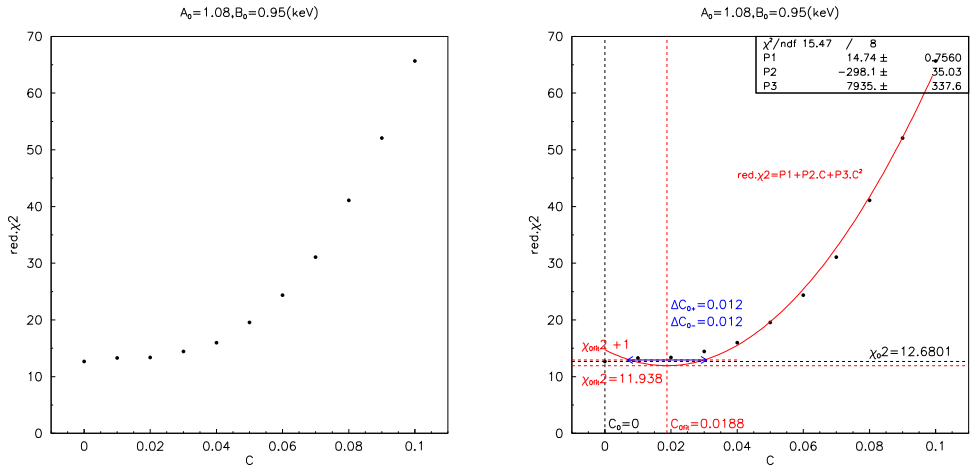

Figure 5.32: The reduced χ^2 as a function of C (with fixed A and B) following all three iterative stages, the coarse, refined and additional third stage scans, (left panel). A polynomial fit to the zoomed distribution, inset in the left panel, is also shown, displaying the fitted minimum, C_{0fit}, and associated errors, δC_{0fit}, (right).

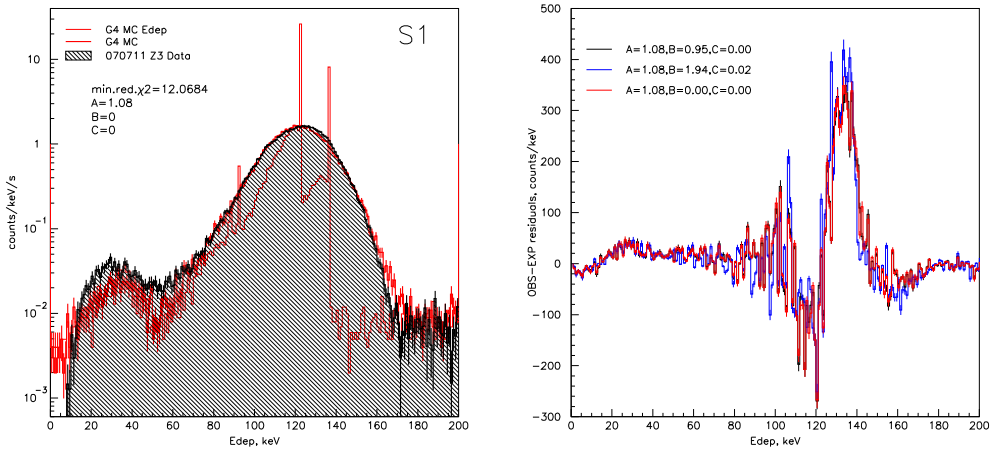

Figure 5.33: Comparison of S1 pulse energy, E_{dep} (keV), spectra for ZEPLIN III 070711 acquired 'data' (with background subtraction) for the inner 7 PMTs and the GEANT4 ^{57}Co MC data-set (without background contributions), smeared with energy resolution σ=1.08$\sqrt{E_{dep}}$ (left panel). The observed, OBS, and expected, EXP, residuals as a function of E_{dep} are also shown (right) for three distinct cases: with values of A, B and C found prior to implementation of the additional, third stage scan; using upper limits for B and C following the third stage; and the scenario where the reduced χ^2 is insensitive to B and C.

Ultimately, knowing $A_{0fit}\pm\delta A_{0fit}$, $B_{0fit}\pm\delta B_{0fit}$ and $C_{0fit}\pm\delta C_{0fit}$ enabled the energy resolution to be parameterised as σ=1.08±0.06$\sqrt{E(keV)}$, $\delta\sigma$ to be determined and σ/E to be plotted as a function of E(keV) for the full energy range (see Figure 5.34). Here the error in A_{0fit}, δA_{0fit}, is propagated through to compute the error in σ/E, $\delta(\sigma/E)$, according to:

$$\delta\left(\frac{\sigma}{E}\right) = \frac{\sigma}{E}\sqrt{\left(\frac{\delta(A)}{A}\right)^2 + \left(\frac{\delta(E)}{2E}\right)} \tag{5.14}$$

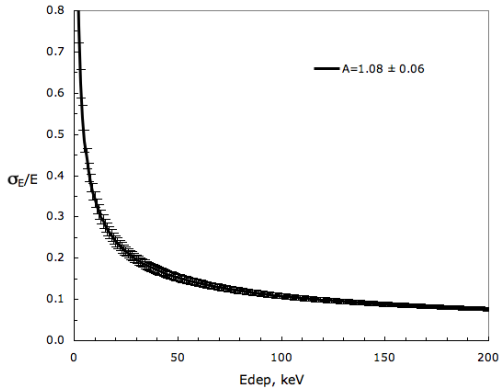

Figure 5.34: Parameterising the ZEPLIN III energy resolution using 070711 ^{57}Co calibration data (with background subtraction) compared with the GEANT4 MC generated data, smeared with a Gaussian of σ=1.08$\sqrt{E(keV)}$.

The first method of parameterising the energy resolution required four Gaussian functions to be fitted to the ZEPLIN III data (with background contributions) over a 14-164 keV energy range. An alternative, novel method was successfully developed whereby the resolution parameters A, B and C were varied and the reduced χ^2 minimised on the data spectrum (without background contributions) over 10-200 keV. The former returns a smaller reduced χ^2 value than the latter. However, it is not strictly valid to directly compare the two approaches when subtracting background (or not) and computing over different energy ranges. Note that even when the fitting procedure of the first method is performed over 10-200 keV the returned χ^2 remains lower than that of method two. This suggests the difference in the χ^2 values may only be explained through systematics in the background estimation.

The work presented here may be extended by: repeating the above analysis with a re-reduced data-set, reduced with ZE3RA v2.1; running the GEANT4 MC simula-

tion code with 'optical tracking' to generate a more complete data-set (but with a significantly longer run time); invoking the *golden code* adapted for zero-field analysis.

5.4 ^{57}Co Run at Field

Whilst analysing the with-field (2.5 kV/cm in the liquid) 070705 ^{57}Co data-set the author identified a misbehaving PMT during data acquisition. Event position scatter plots and pulse area (or gain) distributions as a function of ntuple file# (or event#) clearly indicated that PMT#30 was failing to detect S1 (and S2) signals effectively throughout the run (see Figures 5.35 & 5.36). Gain distributions, in HS and LS channels, were constructed in this way for all PMTs within the array. Only the HS channel of PMT#30 was shown to be affected, with a sudden decrease in pulse area (or deposited energy) pin-pointed to within ntuple file#23, after event#1132.

Although unfortunate this was not deemed a critical failure due to the location of PMT#30 in the outer radii and there not being a complete loss of gain. Note that it was only with the use of the golden code that this issue was revealed since the additional event parameters it generates (e.g. ntuple file# and event#) provide much more information than non-golden code is able to.

No large or irregular signal was seen in or around the vicinity of PMT#30 immediately before event#1132. Since the LS channel remains unaffected the cause of the loss of gain must be due to amplifier performance. To account for this, a single gain correction scale factor (of $\times$4.5-5.0), applied to the HS channel of PMT#30 only, was included inside the *golden code*.

Figure 5.35 shows a significant asymmetry in the number of events reconstructed in the upper and lower halves of the array. However, since no obvious variation in the S2 pulse widths for events in the two halves was observed, and the asymmetry exists for both S1 and S2 signals, this is not believed to be due to detector levelling.

In addition to the loss of gain exhibited by PMT#30, an issue with PMT#31 was raised during Phase II. PMT#31 was shown to be inactive, apparently 'switching off' with no output at all (not even a loss of gain) at which stage the cause was unknown. Therefore, thirty PMTs in the array are considered 'live'. Following the first science run (FSR) the detector was opened up. Close inspection of the internal PMT pin connections revealed that the cathode pin of PMT#31 (only) had, at some

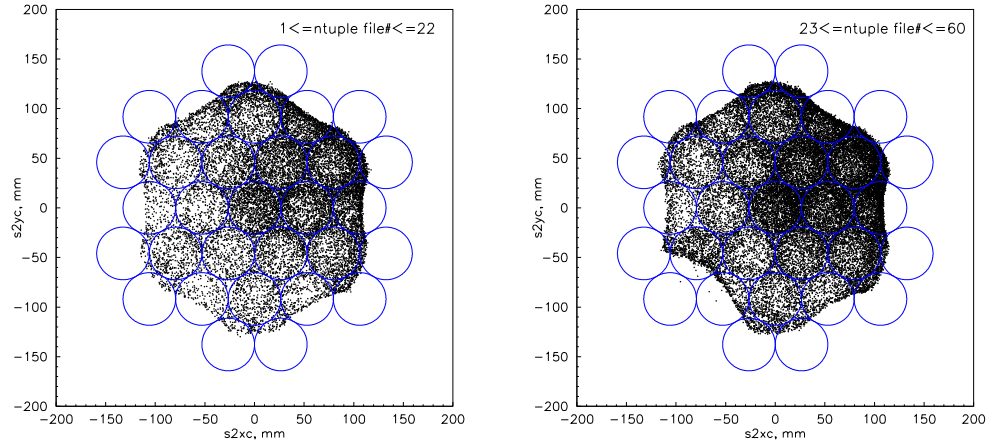

Figure 5.35: Centroid reconstructed S2 event positions, $s2[x, y]c$ (mm), for ntuple file#s 1-22 inclusive (left panel) and 23-60 inclusive (right) for the ^{57}Co 070705 with-field data-set in the HS channel. The event distributions clearly exhibit some time dependence: the population around PMT#30 (centred at $s2xc$=-106.0 mm, $s2yc$=-91.8 mm) differs when plotting events from the first 22 ntuple files and the remaining 38 files.

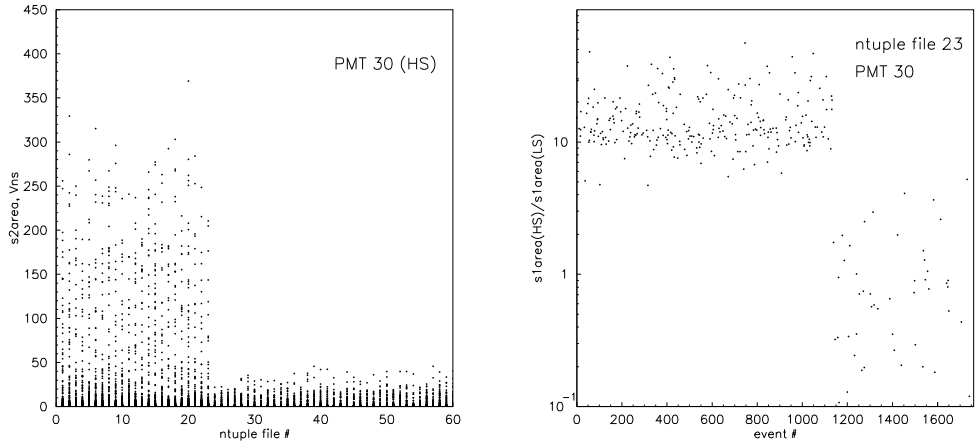

Figure 5.36: The S2 pulse area, in the HS channel of PMT#30, as a function of ntuple file# is shown (left panel). There is a marked, sudden decrease in area during the acquisition of ntuple file#23. Within this ntuple file, the gain distribution in the same PMT as a function of event# is also presented (right). After event#1132, signals are still being detected but the area in the HS channel is approximately equal to that in the LS, not a factor of 10 higher.

point, become disconnected. The stainless steel tubular 'sleeve' (spring contact) that usually connects the Cu pin on the Cu plate to the PMT cathode pin had slipped

downwards, leaving the PMT cathode pin exposed and thus disconnected. This may have happened due to cryo-cycling, during normal operation, or it is possible that the sleeve was not made tight enough when originally mounting the PMT pins. For the second science run (SSR) this will be remedied, by which point the PMTs are expected to be upgraded (with the same pin configuration).

5.4.1 Normalising the PMT Array: 'Flat-Fielding'

'Flat-fielding', or normalisation of the optical response, of the PMT array is a required step in the analysis of low-light level signals. It is a standard calibration technique, correcting for any variation in response over the array, which can be applied as a post-acquisition software correction and once performed promises to enhance the detector performance, signal-to-noise ratio and quality of the resulting spectra.

With compensation for different gains and QEs in a flat-fielded detector, a uniform signal consistently yields a uniform output, removing the light sensitive characteristics of individual PMTs within the array. Thus any flat-fielded signal is due solely to the detection phenomenon not systematic error.

The following method was developed in order to provide an S1 and S2 flat-fielding matrix for the PMT array which includes SPE (or gain) response, QE variation and additional correction factors for light collection across the array (a separate effect). Ultimately, the aim was to minimise the energy resolution of ZEPLIN III. The 080210 ^{57}Co calibration underground data-set, acquired with a partially neutron-shielded and level detector, with an applied electric field of 3.8 kV/cm in the liquid and reduced with ZE3RA v2.1 was used here. In principle this recipe can be performed on any calibration data-set acquired with a source of known type providing there is little saturation of the S1 and S2 pulses in the HS and LS channels, respectively.

The flat-fielding method described here is very much an iterative process with monitoring and analysis performed at regular intervals before cuts and correction coefficients are modified or implemented into the *golden code* and the data re-processed. Eventually four independent correction factor matrices (S1ETA(30), S2ETA(30), S1LCF(30), S2LCF(30)) are derived. These matrices each contain only thirty array elements since PMT #31 was not live (as previously mentioned).

Firstly, a non-golden time constant analysis of the data provides baseline cuts (identifying the S1 and S2 signals using τ, $width50$ and $area$) to establish values input into the golden code (v14). At this stage, the recovered spectrum from the 122.06 keV line was fitted with a single Gaussian, of resolution 67.0% for the S1 full volume energy spectrum and 25.8% for S2. The golden code was subsequently applied to the reduced data files with all correction factors provisionally set to 1.00. The main effect of this was to remove all signals which did not appear to be good, two-phase, single interactions. Gaussian fit functions return an energy resolution of 20.6%, 13.4% and 13.7% for the fiducialised ($s[1,2]rhoc$ <100 mm) S1, S2 and anti-correlated energy channel, E^*, spectrum, respectively. Introduced in Section 3.1, E^* consists of a linear combination of the two signals channels, where the fraction of the total charge going into each is described by:

$$\eta_2 = (1-\eta_1) \tag{5.15}$$

$$E^* = \eta_1 S1 + \eta_2 S2 \tag{5.16}$$

on an event-by-event basis, with η_1=0.3 and thus (by definition) η_2=0.7, at this particular electric field[169].

Next the S1ETA and S2ETA, the coefficients corresponding to each PMT's response, are calculated. A well-defined region, here chosen to be a circle, concentric with respect to the PMT, with a radius of 26.5 mm is selected and the S1 (or S2) signal from events occurring only within this region are considered. To decide where events were above a particular PMT a centroid reconstruction algorithm was initially used, determining the x and y event co-ordinates, $s[1,2][x,y]c$. This had an inherent limitation at larger radii and it was necessary to use a re-mapping function to improve the reconstruction beyond ∼100 mm[1] (see Figure 5.37). The re-mapping parameterisation is given by: $s[1,2][x,y]c'$=$s[1,2][x,y]c/(A\cdot s2rhoc^2+B\cdot s2rhoc+C)$ where A=-1.30×10^{-5}, B=3×10^{-4} and C=0.9937. The Geant4 ZepIII simulation indicates that the actual hit positions extend out to this larger radius.

The re-mapping parameterisation was established using the actual PMT ($\#i$) radial position, ρ_i, as a function of the mean centroid reconstruction, $s[1,2]rhoc$, performed

[1]Eventually, this was extended further, out to ≲193 mm using a template (not centroid) event position reconstruction. The centroid reconstruction algorithm is the simpler and faster method, using signals from the 'peak PMT', it is independent of assumptions and simulations. However, its accuracy is strongly dependent on the amount of light collected and is limited to the central PMTs. Conversely, the template algorithm uses G4 MC simulation data to estimate event positions and thus, the results are highly dependent on the accuracy of the simulation. See Reference [108] for further details.

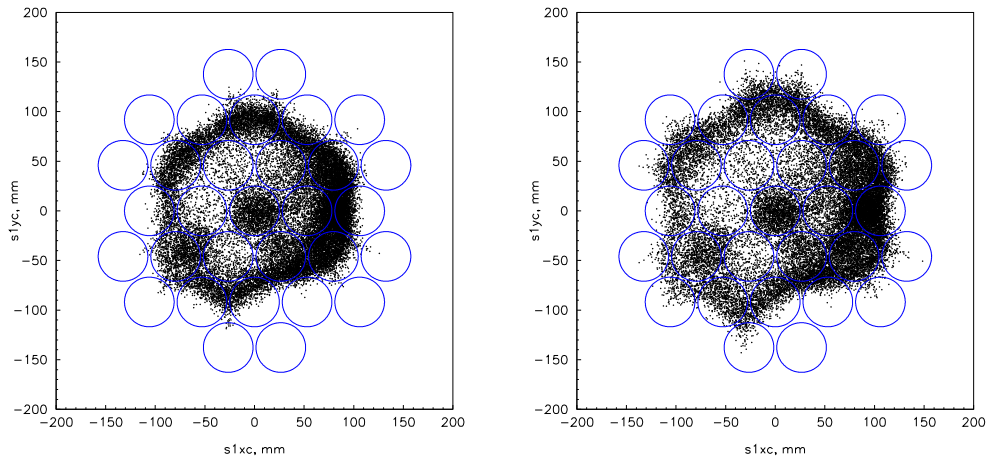

Figure 5.37: Centroid reconstructed ^{57}Co S1 event interaction co-ordinates, $s1[x,y]c$ without (left panel) and with re-mapping (right). The event positions were re-mapped according to the parameterisation: $s[1,2][x,y]c'$=$s[1,2][x,y]c/(A\cdot s2rhoc^2+B\cdot s2rhoc+C)$ where A=-1.30×10^{-5}, B=3×10^{-4} and C=0.9937. With re-mapping the events are seen to be more locally uniform and extend out to $s1[x,y]c \lesssim$150 mm.

by looking at the largest signals in each PMT (the 'peak PMT') and plotting the x, y and radial positions.

Not incorporating the re-mapping function into the event selection prescription during flat-fielding would result in associating the event with the wrong PMT (see Figure 5.38, left panel). The re-mapping function not only provided a corrected central position for each PMT but also described how the circular face was distorted into an ellipse by the centroiding procedure. This needed to be used to determine more accurately whether events really are above a particular PMT. This re-mapping provides a more accurate event interaction position and increases the event statistics detected in the outer PMTs. The reconstruction was verified through an 'inverse mapping' procedure in which the actual (physical) PMT positions are used to reproduce the reconstructed (measured) PMT position, and is detailed in Figure 5.38 (right panel).

After calling the re-mapping function the S1 (and S2) distributions above each PMT in turn, with positions reconstructed above that *same* PMT, are plotted and fitted with a single Gaussian function. In most PMTs this resulted in well-defined peaked distributions where the fitted mean areas, μ_i (Vns), provide normalisation factors, f_i, for each PMT #i (see the example given for S1s in PMT #1 in Figure 5.39).

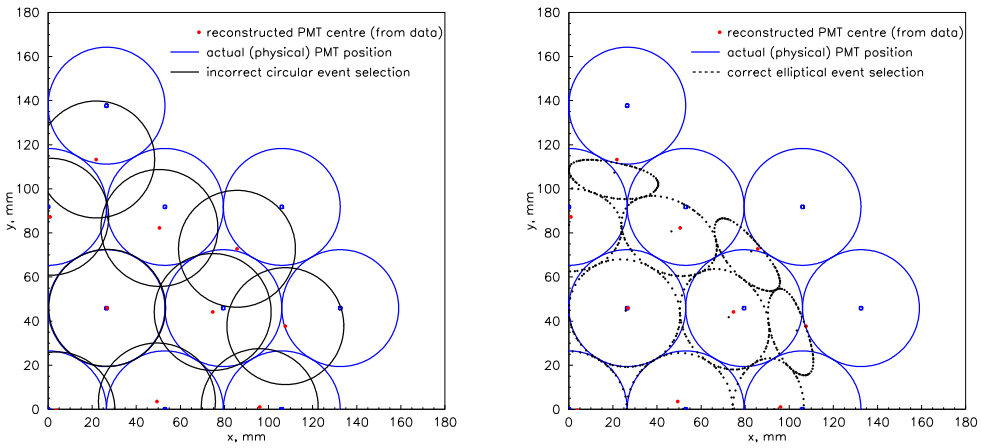

Figure 5.38: Event position reconstruction for the first quardrant of the PMT array assuming a circular, incorrect selection with no re-mapping applied (left panel) and an elliptical selection with an applied non-linear re-mapping function (right panel). The known actual (physical) PMT positions have been taken and the inverse mapping applied, generating event selection areas. These should then be compared with the reconstructed PMT central positions (from data), demonstrating good agreement.

The flat-fielding correction factors S1ETA (and S2ETA) scale as the reciprocal of the fitted mean values normalised with respect to the central PMT according to:

$$< \mu_{S[1,2]} > = \frac{\sum_{i=1}^{30} \mu_{S[1,2]}(i)}{30} \tag{5.17}$$

$$f_{S[1,2]}(i) = \frac{\mu_{S[1,2]}(i)}{< \mu_{S[1,2]} >} \tag{5.18}$$

$$S[1,2]ETA(i) = \frac{f_{S[1,2]}(1)}{f_{S[1,2]}(i)} \tag{5.19}$$

where $< \mu_{S[1,2]} >$ (Vns) is the mean response area averaged over all thirty (live) PMTs.

In order to investigate whether the variation in PMT response is largely due to QE values a plot of fitted mean response area as a function of the previously measured QE[136] is shown in Figure 5.40 (left panel). From this, no obvious correlation is identified. Similarly, Figure 5.40 (right panel) (μ/QE as a function of PMT radial position) suggests that light collection variations are not dominant either. The most likely culprit is thus variation in the gain of the PMT-amplifier combinations.

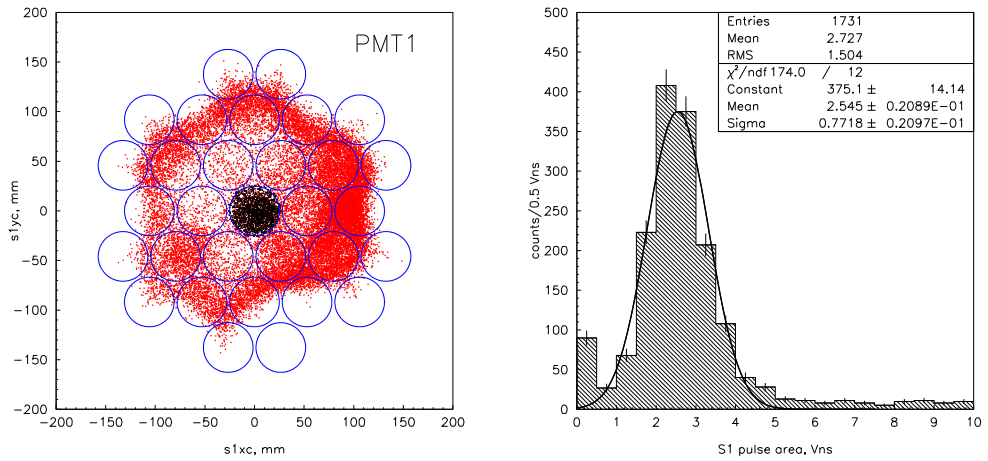

Figure 5.39: An example of the (re-mapped) S1 event selection for PMT #1 (left panel), defined by a circle of radius 26.5 mm. The corresponding S1 area histogram for selected, unsaturated events is fitted with a Gaussian function (right), yielding an S1 correction factor for PMT #1: S1ETA(1)=1.00 ($\mu_{S1}(1)$=2.545 Vns; $<\mu_{S1}>$=1.700 Vns; $f_{S1}(1)$=1.50). All events histogrammed are the PMT #1 HS readout channel with reconstructed positions above the *same* PMT.

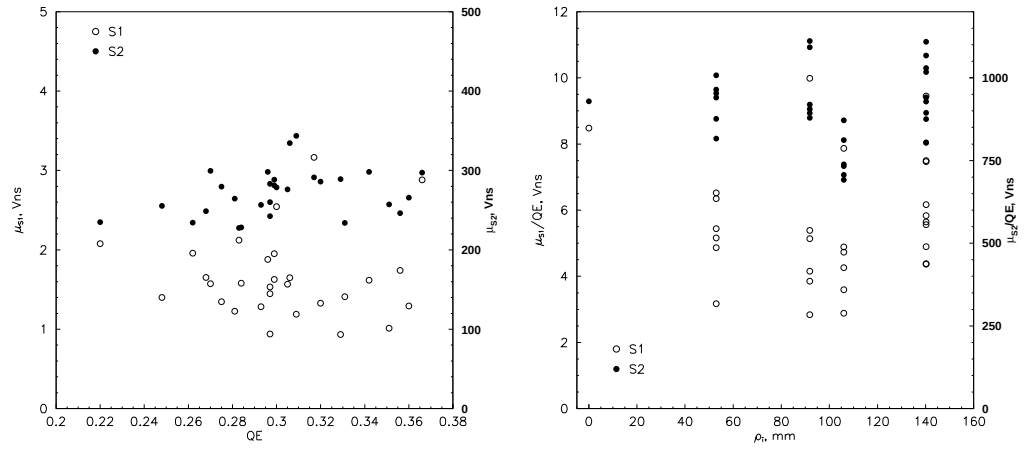

Figure 5.40: S1 and S2 fitted mean response area, $\mu_{S[1,2]}$ (Vns), as a function of QE (left panel) and $\mu_{S[1,2]}/QE$ as a function of (actual) radial position, ρ_i (mm), (right). These plots do not show any obvious correlations.

The S1ETA and S2ETA correction factors (see Figure 5.41, left panel) impacting on both the area and position reconstruction, are input into the analysis code and the data re-processed. At this stage, the spectra recovered from the complete instrument were fitted with a single Gaussian, of resolution 19.8% for the S1 fiducial

volume energy spectrum, 13.9% for S2 and 14.2% for E^*. As an aside, a brief, similar study was performed in which just a single ETA correction factor (using S1) was employed. This yielded a final energy resolution of 13.7% (for the 122.06 keV line) in the fiducialised anti-correlated energy channel. Unless the correction factors were amplitude dependent the use of two correction factors were suspected to be conceptually wrong but mathematically viable.

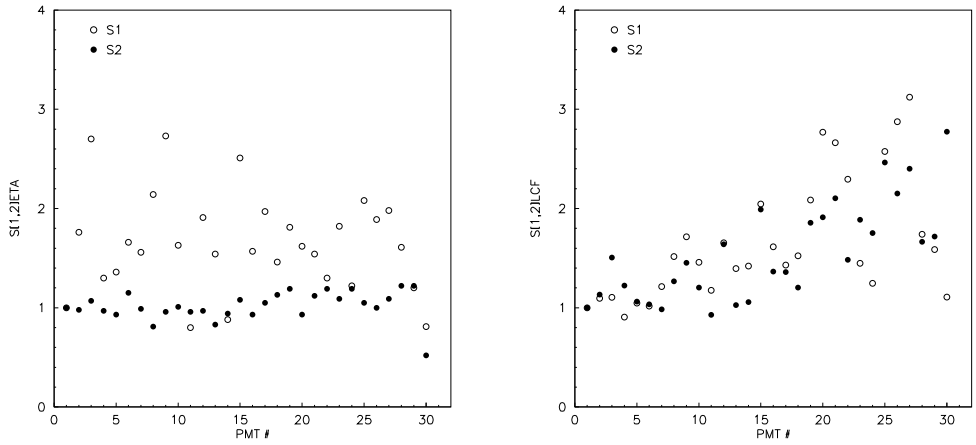

Figure 5.41: Derived S[1,2]ETA flat-fielding (left panel) and S[1,2]LCF light collection correction (right panel) factors, with respect to the central PMT, as a function of PMT #.

A depth correction, that is compensation for the xenon purity and the electron lifetime of ∼15.5 μs, is next applied using a multiplicative scale factor (exp($dtime/lifetime$)) to the S2 pulse area. This corrects the S2/S1 values, for all LXe depths (or drift times, *dtime*s), to the ideal, pure Xe case, i.e. the datapoints shown previously in Figure 4.68 (S2/S1 as a function of *dtime*) would be scaled to the horizontal line (pure case) by the applied correction factor. The data are then re-processed and the resulting energy spectrum demonstrating further improvement in energy resolution of the 122.06 keV line: 19.8% for the S1 fiducial volume energy spectrum, 13.2% for S2 and 13.4% for the anti-correlated channel.

The second phase of the flat-fielding procedure is to derive the S1 and S2 light collection corrections S1LCF and S2LCF, respectively. This is not a radial light collection approach but is performed on a PMT-by-PMT basis and as before, the reconstructed x and y co-ordinates are subject to the 'standard' re-mapping.

Initially, the complete flat-fielding method described here involved two different light

collection correction factors: S[1,2]LCR and S[1,2]LCC. The former was derived from a radial light collection approach whilst the latter was on an additional, PMT-by-PMT basis. The PMT-by-PMT correction used the whole instrument response, summed from all PMTs but only for events occurring above the particular PMT for which that correction applies. The S[1,2]LCR values are computed by plotting the mean (Gaussian-fitted) S1, or S2, positions from the data as a function of centroid radius as returned within the *s2rhoc* parameter, in 20 bins (0-200 mm). However, upon revisiting this study it was decided that a single light collection correction factor would be optimal.

S1 pulse area distributions are plotted from the HS SUM channel for events centred above each PMT in turn and fitted with a single Gaussian. Similarly, S2 pulse area distributions in the LS*10 SUM channel are analysed. The S1LCF and S2LCF (geometrical) light collection correction factors (see Figure 5.41, right panel), scaling as reciprocal of the fitted mean values, normalised with respect to the central PMT, are input into the analysis code and the data once again re-processed. The resulting energy spectrum demonstrates further improvement in energy resolution of the 122.06 keV line: 24.2% for the S1 fiducial volume energy spectrum, 11.6% for S2 and 11.7% for the anti-correlated channel.

The 122.06 keV ^{57}Co photopeak is used to provide an accurate reference point for the S1 (and S2) energy calibration, correlating pulse area (Vns) with deposited energy (keV). Once this is performed, inside the golden code, the resulting fiducialised anti-correlated energy spectrum is shown in Figure 5.42. A single Gaussian function is fitted to the low-energy feature at $\sim$34 keV (49.1% resolution). The origin of which can be attributed to backscatter events. Furthermore, two combined Gaussian functions, with fixed intensity, μ and σ of the 136.47 keV line with respect to the 122.06 keV, were simultaneously fitted to the anti-correlated energy spectrum's region of interest. The recovered 1-σ energy resolution ($\sigma(E)/E$) of the 122.06 keV and 136.47 keV fiducialised photopeaks were found to be 8.6% and 7.3 %, respectively.

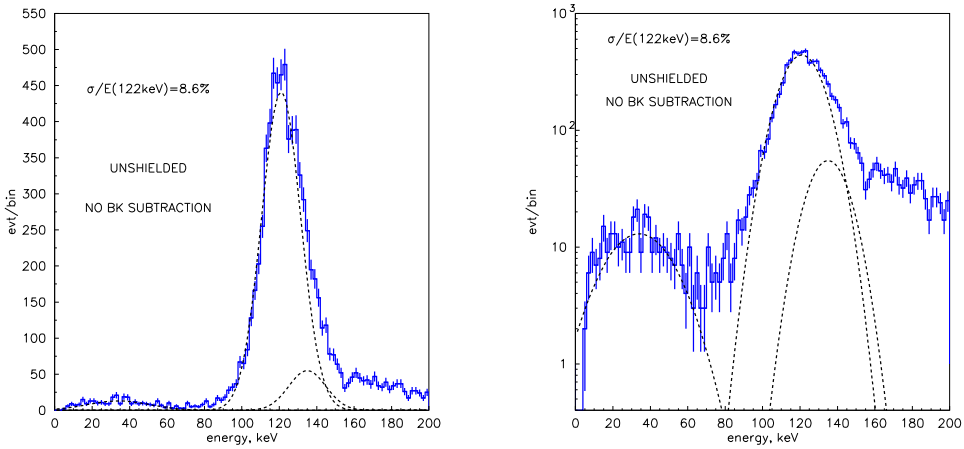

Figure 5.42: The final, ^{57}Co fiducialised anti-correlated energy spectrum, E^*, following the depth correction in linear (left panel) and logarithmic space (right). The spectrum is fitted with three Gaussian functions (a single one to the low-energy feature and two, combined to the two photopeaks) shown here as the broken lines, to determine the energy resolution, σ/E, in E^*. Following flat-fielding and light collection corrections, improvement in the energy resolution is seen with $\sigma(E{=}122.06\text{ keV})/E{=}8.6\%$.

A summary of the flat-fielding and light collection correction method developed here is outlined in Figure 5.43. On completion of (one iteration of) the full procedure the energy resolution of the 122.06 keV photopeak, in the anti-correlated energy channel, is shown to improve: recovering a final value of 8.6%.

Prior to this analysis the most significant contributing factor to variation in optical response across the array, of the three obvious ones discussed here (SPE, QE and light collection), was believed to be light collection. This study of the 080210 data-set confirmed this.

Later analysis of the FSR data eventually adopted a more refined flat-fielding method, based on this initial study. Just a single matrix of flat-fielding coefficients, ETA, was incorporated into the golden code since, neglecting light losses at the edge of the PMT array would lead to identical S1ETA and S2ETA values (see Figure 5.44, left panel). These were obtained through an iterative, multi-stage process in which: the highest amplitude events in PMT#i are identified and assumed to be located directly above the centre of that PMT#i, providing a first approximation for ETA; for each PMT in turn (e.g. PMT#1) event positions were reconstructed using all PMTs (except e.g. PMT#1), selecting events occurring directly above the centre

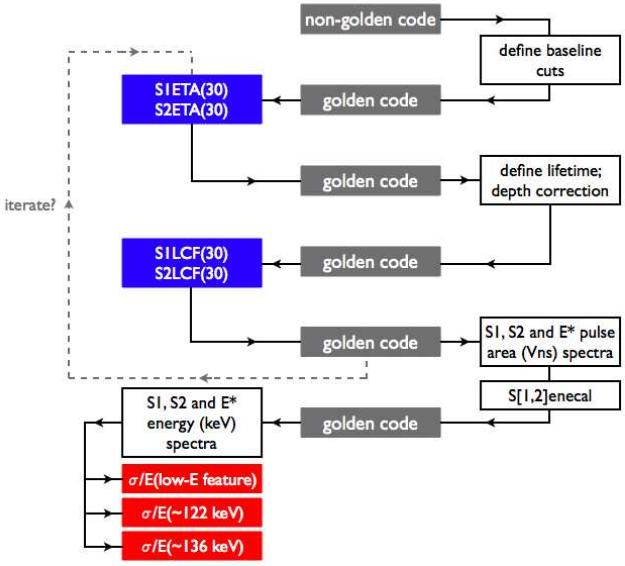

Figure 5.43: Schematic summarising the final approach employed to flat-field and adjust for light collection across the array, iteratively invoking the golden code, generating the correction factors S[1,2]ETA and S[1,2]LCF, respectively. The energy resolution of the 122.06 keV and 136.47 keV ^{57}Co γ-ray lines and the low-energy feature, for the anti-correlated energy spectrum E^*, are ultimately determined.

of that PMT (e.g. PMT#1). This second stage generates a second, improved approximation for ETA, and may be repeated if necessary. Furthermore, the method used to construct S[1,2]LCF matrices was extracted directly, without any modification, from the work presented here but iterated and fine-tuned for a light collection correction treatment of the FSR data (see Figure 5.44, right panel).

There are several key areas in which the method described here could be developed further. These include: improving the re-mapping parameterisation (and the event selection process) when flat-fielding; subtracting the commensurate background energy spectrum from the ^{57}Co spectrum, proving particularly important for long calibration runs; iterating the full routine multiple times, enabling the flat-fielding and light collection correction values, if unstable, to converge; applying this method to other (^{137}Cs, etc) calibration data-sets; and optimising the analysis for very small signals.

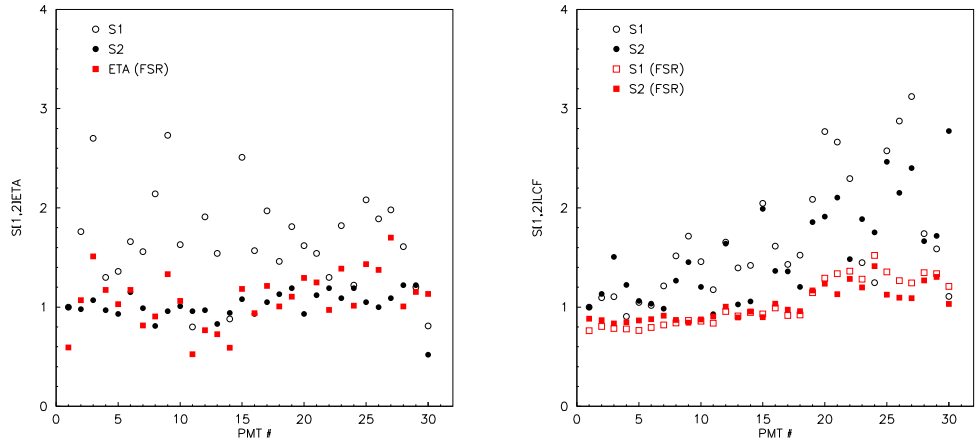

Figure 5.44: Derived S[1,2]ETA flat-fielding (left panel) and S[1,2]LCF light collection correction (right panel) factors, with respect to the central PMT, as a function of PMT #. Coefficients derived from this work are shown with those generated from subsequent work and applied to the FSR analysis, for completion.

5.4.2 Timing Corrections: Coincidence Spectra

A timing correction, or offset applied to an individual HS (and LS) readout channel, is required in order to synchronise pulse start times in different PMTs. Incorporating this timing correction matrix, normalised with respect to the central PMT, into the ZEPLIN III reduction software, ZE3RA, was expected to result in more well-defined pulse shapes in the HS and LS SUM channels. Consequently tighter timing cuts, with lower associated efficiencies, may be applied in order to identify the S1 and S2 signals leading to improved discrimination, as demonstrated by ZEPLIN II.

The same 080210 ^{57}Co (3.8 kV/cm in the liquid) calibration underground data-set, reduced with ZE3RA v2.1 and the golden code (v14), used in the flat-fielding analysis (previously described) was also operated on here.

The process of determining the offsets in each channel was initially carried out during the ZEPLIN III surface data run. However, following deployment underground the voltage divider box, powering the PMT array, was changed. The characteristic time-response of a PMT is dependent on the electron multiplier stage: specifically, the dynode structure and the applied voltage. Thus, the output signal (and the offset) was altered. This modification required that the offsets be re-calculated and applied in a software correction, as detailed below.

The time difference between pulses seen in two PMTs or the offset, Δt, with respect to the HS channel of the central PMT, HS01, is defined as:

$$\Delta t(Ch) = t_s(Ch) - t_s(01) \tag{5.20}$$

where $t_s(Ch)$ and $t_s(01)$ are the S1 (or S2) pulse start times in HS (or LS) PMT Channel 1(2,...,31) and the central, reference PMT, respectively. This is shown schematically in Figure 5.45.

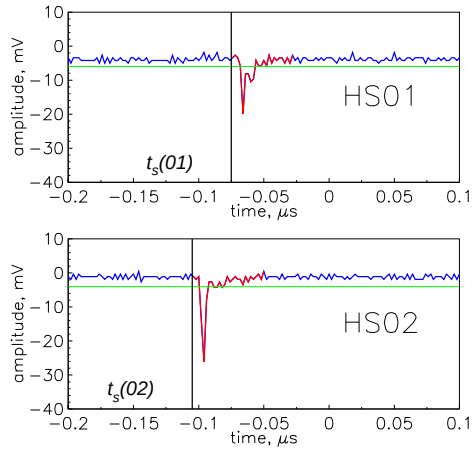

Figure 5.45: A schematic representation of the time difference between PMT#2 and the HS channel of the central PMT (HS01), $\Delta t(02)$. According to this definition (given in Equation 5.20) with $\Delta t(02)$ <0 the pulse in this channel occurred prior to that in HS01.

When investigating a potential timing offset, distributions of $\Delta t(Ch)$ were histogrammed for all PMTs, preserving information relating to individual events. Only unsaturated S1 (or S2) events depositing sufficient charge were considered. For example, the deposited S1 (or S2) energy E_{dep} was constrained around the ^{57}Co photopeak, to be 110 < E_{dep}(keV)< 150. An additional constraint - that both channels being compared coincidentally detect the event - was also applied in order to prevent events where a null, zero default $t_s(Ch)$ and/or $t_s(01)$ value was input by ZE3RA and propagated throughout from being analysed. This was implemented by defining some charge threshold, exceeding noise, above which events are accepted, e.g. $s1area$ >2 phe. The resulting Δt distributions (or coincidence spectra) were shown to be symmetric and Gaussian-like since the PMTs (separate detectors), timing electronics and triggering conditions are nearly identical in the two branches. A Gaussian function was then fitted to each distribution in turn to characterise a HS

(and similarly a LS) 'jitter' in each tube. Example HS distributions for S1 and S2 signals in PMT#6 are provided in Figure 5.46.

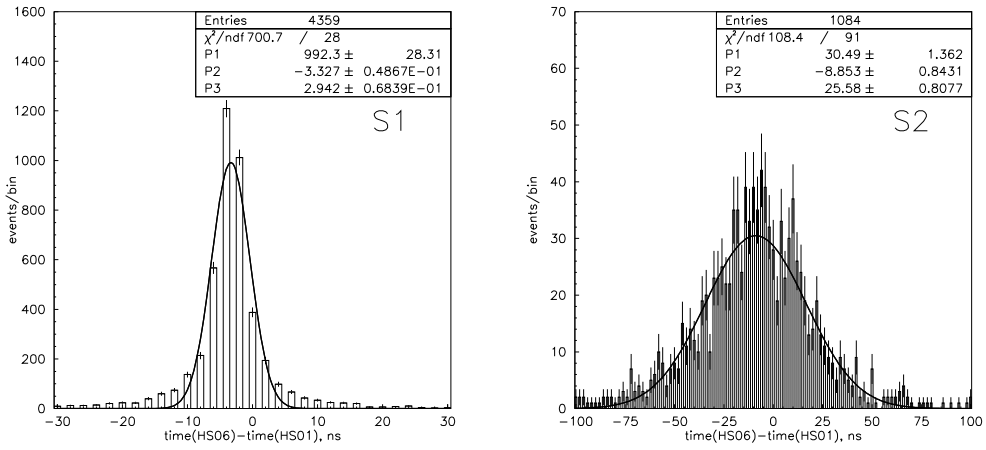

Figure 5.46: Example HS Δt (ns) distributions (or coincidence spectra), with respect to PMT#1, for S1 (left panel) and S2 (right) unsaturated signals in PMT#6. A Gaussian function has been fitted to each distribution to determine the mean value (P2) and σ (P3).

Here the term signal 'jitter', a timing inaccuracy due to random fluctuations in signal size and shape, refers to both time jitter - occurring when input pulse amplitudes are constant - and also to time slewing - an effect seen when input pulses are of variable amplitudes. Amongst others, signal time jitter may be attributed to electronic noise or the discrete nature of the electronic signal.[151]

Since the post-signal processing trigger time in the DAQ software is placed at $t = 0$ the Δt distributions (see Figure 5.46) offer no information on the PMT *transit time*: the characteristic time taken for charge to travel from the PMT photocathode to the anode. This is quoted as 41 ns, with 2.2 ns single electron jitter, for the similar ETL 9829QB PMTs.[170] One would expect the Δt distributions to be centred around zero though, since this is where the trigger is set, with any deviation of the mean of the distribution from this being the jitter. The spread of the distribution corresponds to the error on the mean.

The measured mean time jitter, $\mu_{\Delta t}$ (ns), for S1 and S2 signals as a function of PMT number and QE were plotted. No obvious correlation between the jitter and QE was observed (not shown). Figure 5.47 demonstrates how the measured S1 and S2 mean jitter was shown to vary as a function of PMT#.

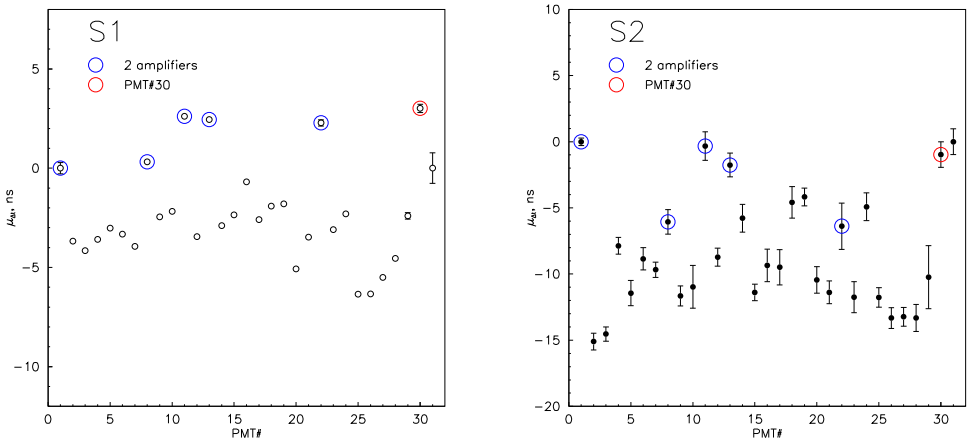

Figure 5.47: Measured mean time jitter, $\mu_{\Delta t}$ (ns), for S1 (left panel) and S2 (right) signals as a function of PMT #. Channels with two amplifiers along with PMT#30 (with questionable response due to loss of gain) are highlighted. The S1 signals are more strongly correlated with PMT# than the S2 signals.

In Figure 5.47 readout channels with not one, but two amplifiers are highlighted - the central PMT being one such channel. It is clear that the presence of a second amplifier significantly affects the S1 timing offset. Furthermore, the data-point corresponding to PMT#30 may be considered anomalous since this PMT is known to have lost gain during the acquisition of these data, no doubt leading to distorted signal shapes and thus a possible additional timing offset.

As PMT#31 was known to be inactive at this stage only the noise contribution to the jitter would be seen in this channel. However, since only sufficiently large signals are considered in this analysis, cutting on the noise, the observed jitter should be negligible.

Four obvious effects may account for an observed variation in jitter: aforementioned electronic noise and the discrete nature of the electronic signal; variations in the coaxial signal cable lengths; and a difference in the light propagation time simply due to the finite time it takes light from an event to travel to two PMTs which are not necessarily equidistant from the interaction point.

The light propagation effect was parameterised via a simplified and purely geometrical argument, utilising: the known co-ordinates of the PMT array; the speed of light, c; the theoretical refractive index of LXe ($\eta_{LXe} = 1.69 \pm 0.02$[171]); and the fact that the interaction points of ^{57}Co γ-rays are restricted to the upper few mms

of the LXe target.

A uniform distribution of events across the array was considered by calculating Δt_{calc} (ns) from the difference in distance, d (mm), travelled by light from the event location, (x_e, y_e, z_e) (mm), (assumed to be directly above PMT#i) to PMT#1 and to PMT#i, for $i = 1, 30$. The event was then 'moved' around, over all PMTs in turn (assuming uniformly distributed events across the array) and this process repeated. Averaging the Δt_{calc} values allowed the parameterisation to be plotted as a function of radial position for comparison with the normalised real data points, $norm.\mu_{\Delta t}$ (see Figure 5.48). The amplifier 'typical insertion delay' quoted by the manufacturer is 3.5 ns[117]. This has been accounted for when normalising the response of each PMT channel with two amplifiers to the central one.

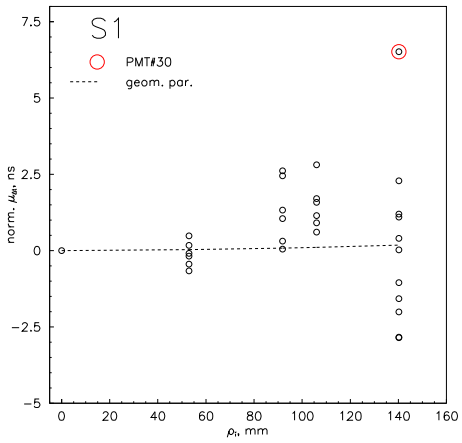

Figure 5.48: Normalised measured mean time jitter, $\mu_{\Delta t}$ (ns), for S1 signals as a function of (actual) radial position, ρ_i (mm). The geometrical parameterisation for the light propagation effect (assuming a uniform distribution of events) is shown and the channel corresponding to PMT#30 is highlighted.

This parameterisation is described by:

$$\Delta t_{calc}(i) = \frac{1}{-30}\sum_{e=1}^{30}\left(\frac{d_1(e) - d_i(e,i)}{\nu_{LXe}}\right) \tag{5.21}$$

where ν_{LXe} (mm ns^{-1}) is the speed of light in LXe ($=c/\eta_{LXe}$) and

$$d_1 = \sqrt{(x_e - x_1)^2 + (y_e - y_1)^2 + z_e^2} \tag{5.22}$$

$$d_i = \sqrt{(x_e - x_i)^2 + (y_e - y_i)^2 + z_e^2} \tag{5.23}$$

Here all x and y coordinates used are from the (actual) physical positions of the PMT centres and z_e is set at 249 mm, i.e. 1 mm below the LXe surface.

A difference in coaxial cable length, Δl, of 1 cm would only account for a Δt of ~0.05 ns.[151] Hence, a Δl of ~20 cm would be required to explain the scatter in the data points of Figure 5.48. Furthermore a variation of this order would be noticeable in the hardware configuration.

The discrete nature of the signal with 2 ns sampling may well contribute, almost entirely, to the deviation of observed time jitter from the geometrical parameterisation seen in Figure 5.48.

Since the amplifier insertion delay offset is only specified as a typical, not exact, value it too may well account for the observed deviation of $norm.\mu_{\Delta t}$ from the geometrical parameterisation. Symmetry of the events distributed about the parameterisation is seen in Figure 5.48, with events below it ($norm.\mu_{\Delta t}$ <0) corresponding to PMTs mounted in the upper half of the array, described by positive x coordinates. This suggests the ^{57}Co source was located off-centre, in the positive x-direction.

The data presented in Figure 5.47 (left panel) has been re-plotted as a function of ρ_i (mm) where ρ_i is re-defined relative to PMT#27 (see Figure 5.49). This particular PMT#27 was chosen since the channel has a single amplifier and is located in the outer radius of the array. The latter reason takes the reference PMT out from the centre, removing symmetry effects, as seen in the similar plot of Figure 5.48. In Figure 5.49 a linear function has been fitted to the data generating an 'inverse velocity' gradient of 0.0103±0.0036 ns mm^{-1}. Considering the delay due to the approximate transit time in coaxial cables involves subtracting 0.005 ns mm^{-1} from this, yielding a corrected velocity, $\nu_{LXecalc}$, of 188.68±65.95 mm ns^{-1}. When comparing this with c, a refractive index of LXe, $\eta_{LXecalc}$, is calculated as 1.59±0.56, proving consistent with the theoretical value, η_{LXe}. Agreement between the theoretical and calculated refractive index values would imply that only light propagation through the target medium (a geometrical effect) accounts for the observed signal time delays, with no contribution due to other, perhaps light collection, effects.

The mean S1 jitter values determined in this study (those shown in Figure 5.47, left panel) were incorporated into the ZE3RA reduction code, from v2.2 onwards, as a correction to the S1 pulse start time. As a result, the output τ distributions, or pulse shapes, were observed to be significantly more well-defined.

In principle, it will not be necessary for these corrections to be edited in future,

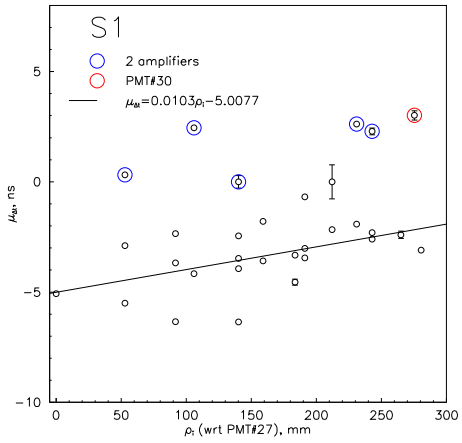

Figure 5.49: Measured mean time jitter, $\mu_{\Delta t}$ (ns), for S1 signals as a function of (actual) radial position, ρ_i (mm). Here ρ_i is re-defined to be with respect to PMT#27, located on the edge of the array. Channels with two amplifiers along with PMT#30 are highlighted. A linear fit to the data (neglecting the highlighted data-points) is also shown. This yields a calculated refractive index of LXe, $\eta_{LXecalc}$, of 1.59±0.56.

provided the current setup remains. Practically, this will not be the case since an imminent PMT upgrade is planned and the Xe purity and LXe level are presently stable but subject to change.

From a simple, purely geometrical argument the time difference in pulse start times observed in PMTs#1 and #25, when the S1 event is occurring on the opposite side of the array, above PMT#22 and say, ∼1 mm below the LXe surface, is estimated to be 0.50 ns. PMT#1 would register a signal in approximately 1.61 ns whereas PMT#25 would do so in 2.11 ns. If however the event is located directly above PMT#25 the observed $\Delta t(25)$ should be -0.21 ns if light propagation times are the only, or at least the dominant, time delay factor. These two scenarios are shown schematically in Figure 5.50.

An alternative, simpler method was pursued in an attempt to investigate the effect of the geometry of the array or light propagation on the time delays and to provide a single χ^2 value quantifying how well the model describes the observed data. Again, this involved a basic and purely geometrical calculation but looked at the response of just two PMTs to an event, as opposed to that of the entire array. Also PMT#2 was chosen to be the reference PMT, removing any systematics due to the central channel's inherent, double amplifier insertion delay. In effect, an event was 'placed'

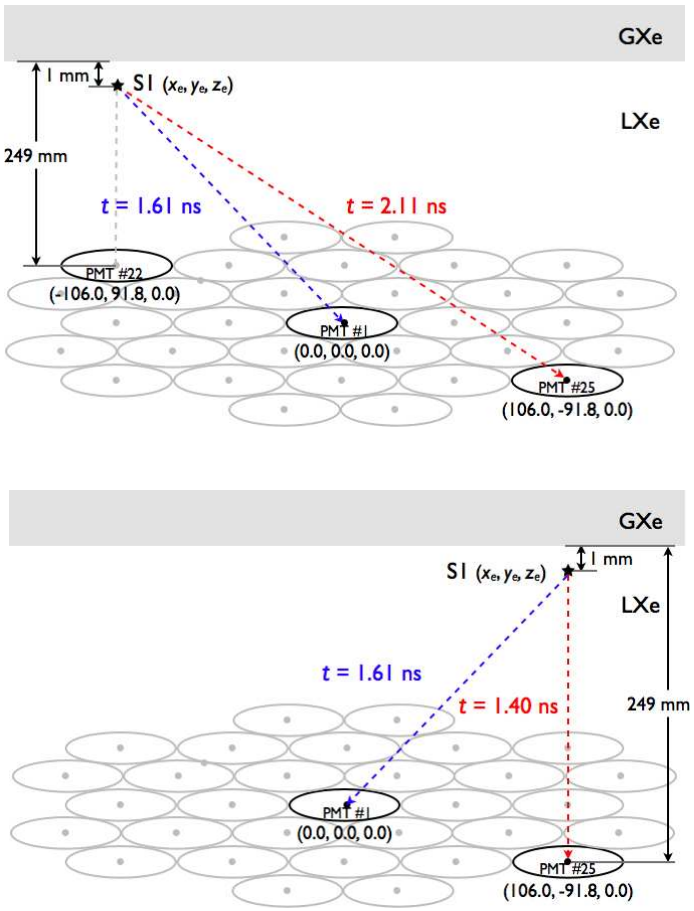

Figure 5.50: Schematic of the simple geometrical model for the light propagation time effect. Two scenarios are shown where an event is 'placed' above PMT#22 (upper panel) and PMT#25 (lower panel). The difference in the response times of PMT#1 and PMT#25 are estimated in each case.

above PMT#i and the time difference between the signal detected in PMT#i and PMT#2 calculated. The event was then 'relocated' to be above each PMT in turn with the response of that particular PMT compared to that of the reference one.

It was assumed that the event occurred directly above the centre of PMT#i and that the light was detected at the centre of the photocathodes of PMT#i and PMT#2, i.e. a point-like photocathode. The S1 event location x, y co-ordinates could be extracted from real data and it was assumed interaction always occurred 1 mm below the LXe surface.

For all channels with a single amplifier histograms of $\Delta t_{meas}/\Delta t_{calc}$ could be plotted and fitted to give a final χ^2 measurement. This could then, in theory, be repeated for all readout channels with two amplifiers. If the geometrical model (Δt_{calc}) could ex-

plain the observed data (Δt_{meas}) well one would expect a Gaussian-like distribution with mean μ of ~ 1.

From Figure 5.51, the mean values of the Δt_{meas} and Δt_{calc} distributions are not consistent: the proposed geometrical model did not fully account for the measured time delay effect. Either this simplified approach underestimated the light propagation time across the array, a separate and non-geometrical factor was required or the discrete nature of the signal binning could explain the time delays. The latter is believed to be the most significant with the relatively coarse 2 ns sampling severely limiting the accuracy with which Δt_{meas} could be determined.

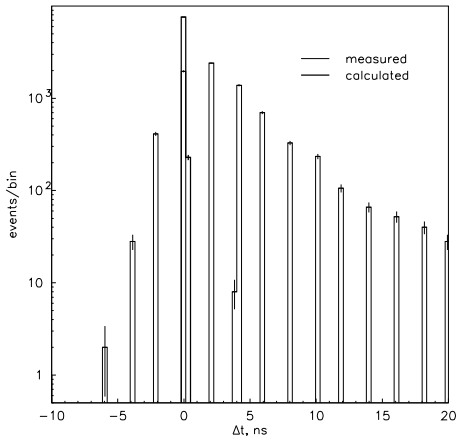

Figure 5.51: Comparison of Δt_{meas} and Δt_{calc} distributions, demonstrating inconsistency in their mean values. Unsaturated signals, in all channels with a single amplifier are considered, using PMT#2 as the reference channel. The coarse 2 ns sampling for Δt_{meas} is shown to limit the accuracy with which the mean of the distribution is determined.

5.5 The ELM: ZEPLIN III Underground Data Measurements

During the underground data-taking phase the target LXe was sampled and its purity continuously monitored using the ELM (see Section 3.2). In preparation for the FSR the Xe purity was required to be optimised. With the ZEPLIN III Xe purity believed to be $\lesssim 10^2$ μs and clear degradation over time previously observed, the 071228-080120 data-sets were acquired to assess how to proceed. More specifically,

this study was designed to finalise the decision to retain the existing gas system, with passive GXe purification via the SAES getters or to replace this with an alternative, active re-circulation system. Although the latter, proved to be highly effective in ZEPLIN II, it would entail a full redesign and installation of the purification system.

The purity of both the ZEPLIN II and ZEPLIN III Xe supplies were sampled on each respective gas system, independently and tested with the ELM. The ELM was operated with an applied voltage of 1.0 kV, a LXe depth of 25 mm and a GXe gas gap of 5 mm. The underground data were acquired, and subsequently analysed, by the author. The results of this study are presented in Figure 5.52. On each day the target Xe was sampled and the ELM filled twice. As expected, Figure 5.52 clearly demonstrates improvement in the Xe purity (∼21-76 %) with the second runs.

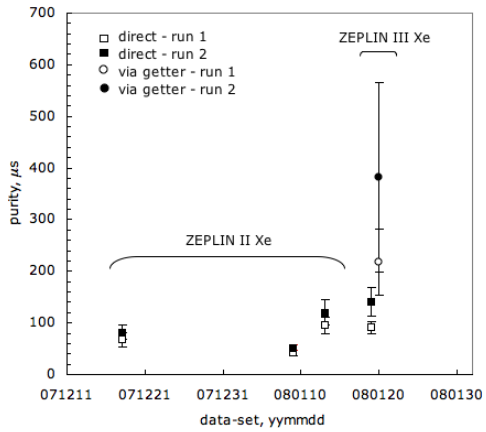

Figure 5.52: LXe purity measurements made over several weeks for samples of ZEPLIN II and ZEPLIN III Xe supplies using the ELM (with 1.0 kV applied, 25 mm LXe depth and 5 mm GXe gap). Following passage through the getters the ZEPLIN III Xe purity is shown to increase.

The 080120 data differ from all other sets in that the Xe was transferred from one bottle on the gas system to the other, not directly, but via the two getters. Comparing results from the second runs of the 080119 and 080120 data, the Xe purity was measured as 141±27 μs and 382±184 μs, respectively. This proved encouraging, confirming that the ZEPLIN III Xe supply was capable of achieving significant improvement in purity (to the order of a few $\times 10^2$ μs although the error bars are large). As a consequence of this study the decision was made to continue with the current purification gas system configuration, with a view to installing an active re-circulation system prior to the second science run (SSR).

5.6 Summary

The ZEPLIN III instrument and auxiliary systems were deployed underground prior to the first science run (FSR). Data acquired at this stage were analysed, demonstrating successful operation in situ and, crucially, the ability to run at high-field (up to 3.79 kV/cm in the liquid). Development of the DAQ, ZE3RA reduction code and analysis procedures, were demanded in preparation for the FSR.

Migration of the long-τ population (where τ $\sim$70 ns) with successive ZE3RA releases (v1.3, 2.0 and 2.1) was observed for S1 events during comparison of surface and underground background data. With respect to earlier versions, ZE3RA v2.1 was shown to significantly suppress the long-τ population through improved pulse handling by, at least, a factor of 100. Events of different decay time constants and energies were sampled and their pulse shapes assessed, in an attempt to identify and establish the origin of the long-τ population. This was suggestive of the defined pulse window, or integration time, assigned by ZE3RA being elongated (as confirmed by the implementation of v2.1). A series of experimental tests into amplifier distortion were conducted. The LS (or HS) output signal parameters (pulse amplitude, width and rise time) were monitored as a function of the input parameters, in a setup with (attenuation A=0.5 and A=1.0) and without an attenuator present. The pulse amplitude values at which the LS and HS channels were expected to distort proved consistent with the acquired data-sets. Also, the pulse width in the LS channel remained unchanged when the signal in the HS channel underwent distortion. This eliminated the concept of a 'feedback' mechanism whereby the HS channel could influence that of the LS. For each experimental configuration the difference in the HS and LS pulse amplitudes was determined and shown to be inconsistent with a supposed first stage amplifier gain of 10; an approximate factor of 2 disagreement between the expected and observed gain was shown to vary as a function of A. The gain of the second stage amplifier however was measured as 10.13$\pm$0.20 for all three configurations.

The pulse shapes of particular long-τ events were studied in detail to deduce the relationship between the ZE3RA pulse integration times and the ZE3RA-calculated time constants. A weighted sum average method, implemented within PAW, was invoked to reproduce the τ values calculated by ZE3RA v2.0 and did so successfully. As a consequence of this study, revision of the ZE3RA pulse integration time was advised and a forced maximum integration time of $\sim$500 ns was recommended in

the case of particularly long signals.

Since the trigger/threshold was set too high during acquisition of the 070706-070717 SPE, underground data-sets, the conventional approach of obtaining SPE measurements had to be abandoned and an alternative method developed. A novel, Poisson approach was used, with the 080605 ^{137}Cs data-set (acquired at 3.79 kV/cm in the liquid), to determine the mean SPE area in each readout channel. These were then compared, along with mean SPE areas derived using FSR data, with the previously-described SPE-specific 060707 values. Although the absolute SPE mean areas could not be directly contrasted, due to the significant modifications made to the acquisition setup, the general trends could be and exhibited good agreement.

LS and HS τ distributions, using zero-field ^{57}Co 070711 data, were analysed, investigating evidence of time constant distortion. A notable difference in τ-distribution shapes for channels with a single and with two amplifiers was observed with signals in the latter suffering some degree of distortion. Using this data-set, in conjunction with the 070716/17 SPE data, an S1 light yield (LY) for ^{57}Co photopeak from the inner 7 PMTs was determined to be 4.72±0.10 phe/keV.

An effort to parameterise the energy resolution of ZEPLIN III using 070711 ^{57}Co calibration data (prior to background subtraction) has been presented in this Chapter. This was achieved by fitting four Gaussian functions to the ^{57}Co spectrum over the 14-164 keV energy range and through comparison with a fitted G4 MC simulated spectrum (resolution $\sigma/E_{dep} = 1.10\sqrt{E_{dep}(keV)}$, without background contributions). The resulting parameterisation was shown to be worse than anticipated, with an additional, second, constant term proposed. A direct estimate of the photoelectric and Compton continuum cross section ratio in Xe, $(\sigma_{p.e.}/\sigma_C)_{Xe}$ ~59.6, was obtained with the 070711 ^{57}Co data proving consistent with the known, published value of $(\sigma_{p.e.}/\sigma_C)_{Xe}$ ~58.6. The sensitivity of the four Gaussian fit function to the 12 free parameters and their initial input values demanded the development of an alternative approach for parameterising the instrument's energy resolution. This was realised through defining an energy resolution function in PAW which was allowed to vary, and by a minimum χ^2 test comparing each smeared energy spectrum to the real, data spectrum over the 10-200 keV energy range. This yielded values of the three coefficients in the energy resolution function, A, B and C, of A_{0fit}=1.08±0.06, B_{0fit} <1.94±1.70 and C_{0fit} <0.02±0.01 whereby the reduced χ^2 is insensitive to both the fitted B_{0fit} and C_{0fit} values. As expected, the stochastic term, A, was demonstrated to dominate the behaviour of χ^2. Ultimately, the energy

resolution was parameterised as $\sigma = 1.08 \pm 0.06\sqrt{E(keV)}$ over the full energy range.

Analysis of the with-field (2.5 kV/cm in the liquid) 070705 ^{57}Co data-set led to the identification of an ineffective readout channel (HS of PMT#30), losing gain during acquisition. Following this, an appropriate correction could be applied inside the *golden code*. Also, evidence of both HS and LS channels for PMT#31 being inactive was provided. On subsequent disassembly of the target vessel, this issue was explained by loss of contact between the cathode pin of the PMT and the Cu plate.

In addition, the development and application of a 'flat-fielding' method, exploiting the with-field (3.8 kV/cm in the liquid) 080210 ^{57}Co data to minimise the instrument's energy resolution, has been described. This involved constructing an S1 and S2 matrix of four independent correction factors for the thirty active PMTs in the array. Also, an elliptical event selection was generated via a position re-mapping function and a depth (or Xe purity) correction was applied. Before invoking this routine, a Gaussian fit to the 122.06 keV ^{57}Co line giving rise to an S1 energy resolution of 67.0% for the full volume. Application of the flat-fielding recipe significantly improved this, yielding an S1 and S2 resolution of 8.6% and 7.3%, respectively in the fiducialised anti-correlated energy, E^*, channel. This study confirmed light collection as a significant contributing factor to variation in optical response across the array.

In analysis of the FSR data, the method for constructing the light collection correction matrices was identical to that developed by the author. Also, although the recipe for generating the flat-fielding coefficients was later modified, the FSR approach capitalised on the main principles and techniques presented in this initial work.

Timing corrections, or offsets, for each HS and LS readout channel were required in order to synchronise S1 pulse start times across the array. Thus, an investigation was conducted on the with-field (3.8 kV/cm in the liquid) 080210 ^{57}Co data whereby these offsets were deduced and later implemented with the ZE3RA reduction code (v2.2). The differences in pulse start times (or 'jitter') for each PMT with respect to the central PMT, with coincident detection, were histogrammed and fitted with single Gaussian functions. The presence of an additional, second-stage amplifier was clearly shown to significantly affect the measured offsets, with the discrete, coarse 2 ns signal sampling potentially contributing to the observed variation in jitter as a function of PMT#. As an aside, the refractive index of LXe, η_{LXe}, was

experimentally derived: $\eta_{LXecalc}$=1.59±0.56, consistent with the published value and indicative of the light propagation time through the target medium (or geometrical effect) accounting for the observed time delays.

A simplified geometrical model was employed to estimate the light propagation time for an S1 event located ∼1 mm below the LXe surface, directly above an outer PMT (#22) and detected at an outer PMT on the opposite side of the array (#25). This was found to be 2.11 ns.

An alternative method of probing this geometrical effect, by monitoring the response of just two PMTs to an event, was also carried out. The aim was to ultimately provide a χ^2 value quantifying how well the simplified geometrical model describes the data. However, the coarse signal binning severely limited the accuracy with which the time delays could be measured.

During the underground science runs the GXe purity was believed to be $\lesssim 10^2 \mu$s. Therefore, seeking higher purity, a decision had to be made to either continue with the existing GXe purification system, or to install an active re-circulation system, prior to the FSR. Following a series of ELM GXe purity tests whereby the Xe was passed through the getters, it was deemed possible to achieve significant improvement in purity with the ZEPLIN III Xe supply and the existing purification configuration.

In Chapter 6, conclusions from the author's work are presented and findings from the FSR, including the corresponding limit result, are described.

Chapter 6

Conclusions

As introduced in Chapter 1, the lightest supersymmetric particle, namely the neutralino - and more specifically the WIMP - is currently the favoured candidate for non-baryonic, cold dark matter within a supersymmetric framework and extension to the standard model of particle physics. The two prevailing, experimental approaches attempting to yield a dark matter discovery were also outlined. The direct detection approach was allotted particular emphasis, where, in Chapter 2, the operating principles of single and dual channel detectors were described.

ZEPLIN III is a liquid xenon (LXe) dark matter detector, exploiting liquid noble gas technology and operation at high-field to seek a positive WIMP direct detection in advance of its worldwide competitors (see Chapter 3). After demonstrating successful proof-of-principle during the surface and underground commissioning phases, the ZEPLIN III first science run (FSR) commenced. This took place underground, at the Boulby Underground Laboratory, North Yorkshire, UK in a low-background, shielded environment. Full details of this can be found in Reference [124]. This FSR excluded a WIMP-nucleon elastic scattering spin-independent cross section, with 847 kg·days exposure, above 7.7×10^{-8} pb at 55 GeV c^{-2} with a 90% confidence limit (see Reference [124], Figure 17). This makes ZEPLIN III a real contender for first detection amongst competitive experiments, especially with the expected improvement in sensitivity following the photomultiplier (PMT) upgrade to a significantly lower-background array prior to the start of the extended, second science run (SSR).

The results of the FSR undoubtedly hinge on knowledge accrued by the collaboration during the construction of ZEPLIN III, its commissioning and its installation in situ: from the details of performing preliminary energy calibrations and optimising

methods for retrieving single photoelectron (SPE) spectra; crucial development and testing of the DAQ, analysis and reduction software; to the intricacies of equalising the response of the PMT array through 'flat-fielding' procedures, and more. The work presented in this thesis is limited to studies conducted during these commissioning phases - proving integral to the characterisation of ZEPLIN III, the understanding of LXe physics, the development of its auxiliary systems and, ultimately, the published exclusion limit.

Results of calibration runs, conducted during the first two commissioning stages, at the Imperial College London laboratories, were presented in Chapter 4. These included: characterising the instrument's response in terms of the light yield (LY) and single photoelectron (SPE) spectra; and demonstration of key operating principles such as 3-D position reconstruction and particle discrimination.

In Phase I an enhanced S1 zero-field LY, with thirty-one ^{241}Am γ-sources mounted internally, was measured as 7.42±0.37 phe/keV and 18.12±0.91 phe/keV in single- and dual-phase, respectively. The single-phase value was consistent with GEANT4 MC simulations (∼7.1 phe/keV[130]) and the dual-phase value was confirmed by an alternative approach (∼18.0 phe/keV). Phase I was completed and the internal ^{241}Am γ-sources were removed.

In Phase II several functions were fitted to acquired SPE spectra, estimating the SPE peak value, including a combination of Gaussian functions, and Polya and Wolfs functions. Depending on the method employed the measured SPE values ranged from 41.78±1.55 Vps to 52.37±1.59 Vps. A study into potential ^{222}Rn α-contamination at low energies (previously observed in ZEPLIN II) was performed on zero-field background data with no convincing population identified in the region of interest. Repetition of this analysis applied to the commensurate with-field dataset identified no α population with expected S1/S2≤0.1. Investigation into the saturation of signals in software and their distortion by the amplifiers followed. This lead to critical development of the acquisition and reduction software and revision of the hardware configuration for future data acquisition. S1 zero-field LYs of 4.61±0.42 phe/keV and 4.67±0.54 phe/keV, calibrated with ^{137}Cs (662 keV photopeak) and ^{57}Co (∼125 keV photopeak) external sources respectively, were measured for the centre of the chamber. These exceed that predicted by G4 MC simulations (3.4-4.0 phe/keV[97]). S1 with-field (3.01 kV/cm in the liquid) LYs of 1.24±0.21 phe/keV and 1.78±0.32 phe/keV and S2 LYs 97.6±35.1 phe/keV and 139.2±30.8 phe/keV were also determined. Furthermore, three distinct populations

of nuclear recoils, 40 keV ^{129}Xe inelastics and γ-rays were observed in the with-field (3.01 kV/cm in the liquid) Am-Be (α,n) source data, verifying effective particle discrimination.

Following deployment underground the instrument was re-calibrated, it demonstrated successful operation at high field (up to 3.79 kV/cm in the liquid) and further studies were undertook in preparation for the FSR (reported in Chapter 5).

Various methods of obtaining SPE distributions and retrieving mean values were investigated: the SPE mean pulse areas generated by the conventional and alternative, Poisson approaches exhibited good agreement. The previously identified long-τ population (events with S1 τ $\sim$70 ns) was experimentally probed in the context of an amplifier distortion effect and in relation to iterative reduction software version releases. The origin of these events was ultimately resolved and attributed to some software or cosmic-ray artefact. An S1 zero-field LY of 4.72$\pm$0.10 phe/keV, calibrated with a ^{57}Co external source, was recovered for the inner 7 PMTs.

A direct estimate of the photoelectric and Compton continuum cross section ratio in Xe, $(\sigma_{p.e.}/\sigma_C)_{Xe}$ $\sim$59.6, was obtained with a zero-field ^{57}Co data-set proving consistent with the known, published value of $(\sigma_{p.e.}/\sigma_C)_{Xe}$ $\sim$58.6. The instrument's energy resolution was assessed and a novel parameterisation approach yielded σ=1.08$\pm$0.06$\sqrt{E(keV)}$ over the full energy range (0-200 keV), with a dominant stochastic term.

The HS PMT#30 readout channel was identified as ineffective following analysis of a with-field (2.5 kV/cm in the liquid) ^{57}Co data-set. Following this, an appropriate correction could be applied inside the *golden code* which remained in place throughout the FSR analyses. Also, evidence of both HS and LS channels for PMT#31 being inactive was provided and subsequently explained by loss of contact between the cathode pin of the PMT and the Cu plate.

The 'flat-fielding' method presented in Chapter 5 was designed to minimise the characteristic energy resolution. Indeed, an improvement in the instrument's S1 energy resolution from 67.0% for the full volume to 8.6% and 7.3% for S1 and S2, respectively in the fiducialised anti-correlated energy channel was observed. This flat-fielding recipe, along with construction of the light collection correction matrices, formed the basis of the approach subsequently applied to the FSR data.

Timing corrections, or offsets, for each HS and LS readout channel were deduced through pulse start time histograms. The presence of an additional, second-stage

amplifier was shown to significantly affect the resulting delays. These were implemented within the reduction code, further contributing to its refinement and development.

A series of LXe purity tests were conducted by the author to assess whether the ZEPLIN III Xe supply and the existing purification configuration were capable of achieving the required high purity levels. Significant improvement in the purity was realised by passing the Xe supply through the getters. Thus proving the proposed active re-circulation system could be installed prior to the FSR as an advantageous, but non-essential, upgrade.

The SSR is due to commence soon. Following an upgraded PMT array, this lower-background, extended run is expected to advance the exclusion limit achieved with the FSR to higher sensitivities, with the possibility of the first direct WIMP discovery.

Glossary

AMANDA Antarctic Muon Neutrino Detector Array
AMS Alpha Magnetic Spectrometer
ANTARES Astronomy With A Neutrino Telescope And Abyss Environmental Research
BBN Big Bang Nucleosynthesis
BNC Bayone Neill Concelman
BOOMERanG Balloon Observations Of Millimetric Extragalactic Radiation and Geophysics
CANGAROO Collaboration Of Australia and Nippon For A Gamma Ray Observatory In The Outback
CMB Cosmic Microwave Background
CDM Cold Dark Matter
CDMS Cryogenic Dark Matter Search
CRESST Cryogenic Rare Event Search With Superconducting Thermometers
DAMA Dark Matter
DAQ Data Acquisition
DRIFT Directional Recoil Identication From Tracks
DUSEL Deep Underground Science And Engineering Laboratory
EDELWEISS Experience Pour Detecter Les Wimps En Site Souterrain
EGRET Energetic Gamma Ray Experiment Telescope
ELIXIR European Liquid Xenon Identication Of Recoils
ELM Electron Lifetime Monitor
FS Full Scale
FSR First Science Run
FWHM Full Width Half Maximum
GLAST Gamma-Ray Large Area Space Telescope
GXe Gaseous Xenon
HESS High Energy Stereoscopic System

HS High Sensitivity
KIMS Korea Invisible Mass Search
LAr Liquid Argon
ΛCDM Λ-Cold Dark Matter
LET Linear Energy Transfer
LHC Large Hadron Collider
LIBRA Large Sodium Iodide Bulk For Rare Processes
LN_2 Liquid Nitrogen
LS Low Sensitivity
LSB Low Surface Brightness
LSS Large Scale Structure
LSP Lightest Supersymmetric Particle
LUX Large Underground Xenon
LXe Liquid Xenon
LY Light Yield
MACHOs Massive Astronomical Compact Halo Objects
MAXIMA Millimeter Anisotropy Experiment Imaging Array
MC Monte Carlo
MCA Multi-Channel Analyser
MOND Modied Newtonian Dynamics
MSSM Minimal Supersymmetric Standard Model
MWPCs Multi-Wire Proportional Chambers
NEWAGE New Generation WIMP Search With An Advanced Gaseous Tracking Device Experiment
OFHC Oxygen-Free High Conductivity
PAW Physics Analysis Workstation
PHA Pulse Height Analysis
PMT Photomultiplier Tube
PTFE Polytetrafluoroethylene
P/V Peak-To-Valley
QE Quantum Efficiency
ROSEBUD Rare Objects Search With Bolometers Underground
SM Standard Model
SNe Supernovae
SNO Sudbury Neutrino Observatory
SPE Single Photoelectron
SSR Second Science Run

SUPER-Kamiokande Super-Kamioka Nucleon Decay Experiment
SUSY Supersymmetry
TPC Time Projection Chamber
UKDMC UK Dark Matter Collaboration
VUV Vacuum Ultra-Violet
WARP Wimp Argon Programme
WIMP Weakly Interacting Massive Particle
WMAP Wilkinson Microwave Anisotropy Probe
W-SPTs Tungsten Superconducting Phase Transition Thermometers
ZE3RA ZEPLIN III Reduction And Analysis Software
ZEPLIN Zoned Proportional Scintillation In Liquid Noble Gases

References

[1] E. E. Ltd, "52 mm (2") photomultiplier 9829B series data sheet." http://www.et-enterprises.com/pdf/9829QB.pdf, 2007.

[2] E. Komatsu *et al.*, "Five-Year Wilkinson Microwave Anisotropy Probe (WMAP) Observations: Cosmological Interpretation," *arXiv:astro-ph/0803.0547v1* (2008).

[3] S. V. den Bergh, "A Short History of the Missing Mass and Dark Energy Paradigms," *arXiv:astro-ph/0005314* (2000).

[4] V. C. Rubin, "Galaxy Dynamics and the Mass Density of the Universe," *Proceedings of the National Academy of Science* **90** (1993) 4814–4821.

[5] H. W. Babcock, "The rotation of the Andromeda Nebula," *Lick Observatory Bulletin* **19** (1939) 41–51.

[6] J. H. Oort, "Some Problems Concerning the Structure and Dynamics of the Galactic System and the Elliptical Nebulae NGC 3115 and 4494," ApJ **91** (1940) 273.

[7] M. Schwarzschild, "Mass distribution and mass-luminosity ratio in galaxies," AJ **59** (1954) 273.

[8] V. C. Rubin and W. K. J. Ford, "Rotation of the Andromeda Nebula from a Spectroscopic Survey of Emission Regions," ApJ **159** (1970) 379.

[9] H. V. Klapdor-Kleingrothaus and K. Zuber, *Particle Astrophysics, Revised Edition.* IoP, 2000.

[10] J. P. Ostriker and P. J. E. Peebles, "A Numerical Study of the Stability of Flattened Galaxies: or, can Cold Galaxies Survive?," ApJ **186** (1973) 467–480.

[11] V. C. Rubin, "Galaxy Dynamics and the Mass Density of the Universe," *Proceedings of the National Academy of Science* **90** (1993) 4814–4821.

[12] J. Kormendy and K. C. Freeman, "Scaling Laws for Dark Matter Halos in Late-Type and Dwarf Spheroidal Galaxies," *Bulletin of the American Astronomical Society* **30** (1998) 1281.

[13] J. H. Oort, "The force exerted by the stellar system in the direction perpendicular to the galactic plane and some related problems," Bulletin of the Astronomical Institutes of the Netherlands **6** (1932) 249.

[14] J. H. Oort, "Note on the determination of K_z and on the mass density near the Sun," Bulletin of the Astronomical Institutes of the Netherlands **15** (1960) 45.

[15] S. Khalil and C. Muñoz, "The enigma of the dark matter," *Contemporary Physics* **43** (2002) 51–61.

[16] F. Zwicky, "Die Rotverschiebung von extragalaktischen Nebeln," *Helvetica Physica Acta* **6** (1933) 110–127.

[17] S. Smith, "The Mass of the Virgo Cluster," ApJ **83** (1936) 23.

[18] F. D. Kahn and L. Woltjer, "Intergalactic Matter and the Galaxy," ApJ **130** (1959) 705.

[19] K. M. Ashman, "Dark matter in galaxies," Publications of the Astronomical Society of the Pacific **104** (1992) 1109–1138.

[20] V. Springel *et al.*, "The large-scale structure of the Universe," Nature **440** (2006) 1137–1144.

[21] S. Perlmutter *et al.*, "Measurements of Omega and Lambda from 42 High-Redshift Supernovae," ApJ **517** (1999) 565–586.

[22] G. Bertone *et al.*, "Particle dark matter: evidence, candidates and constraints," Physics Reports **405** (2005) 279–390.

[23] A. Melchiorri *et al.*, "A Measurement of Ω from the North American Test Flight of Boomerang," ApJL **536** (2000) L63–L66.

[24] S. Hanany *et al.*, "MAXIMA-1: A Measurement of the Cosmic Microwave Background Anisotropy on Angular Scales of 10'-5°," ApJL **545** (2000) L5–L9.

[25] M. Milgrom, "A modification of the Newtonian dynamics as a possible alternative to the hidden mass hypothesis," ApJ **270** (1983) 365–370.

[26] M. Milgrom, "A modification of the Newtonian dynamics - Implications for galaxies," ApJ **270** (1983) 371–389.

[27] K. G. Begeman *et al.*, "Extended rotation curves of spiral galaxies - Dark haloes and modified dynamics," MNRAS **249** (1991) 523–537.

[28] J. Bekenstein, "The modified Newtonian dynamics - MOND and its implications for new physics," *Contemporary Physics* **47** (2006) 387–403.

[29] D. Clowe *et al.*, "A Direct Empirical Proof of the Existence of Dark Matter," ApJL **648** (2006) L109–113.

[30] M. J. Jee *et al.*, "Discovery of a Ringlike Dark Matter Structure in the Core of the Galaxy Cluster Cl 0024+17," ApJ **661** (2007) 728–749.

[31] J. W. Moffat, "Gravitational Lensing in Modified Gravity and the Lensing of Merging Clusters without Dark Matter," *arXiv:astro-ph/0608675v1* (2006).

[32] B. Famaey *et al.*, "The wedding of modified dynamics and non-exotic dark matter in galaxy clusters," *arXiv:astro-ph/0706.1279* (2007).

[33] N. Werner *et al.*, "Detection of hot gas in the filament connecting the clusters of galaxies Abell 222 and Abell 223," A&A **482** (2008) L29–L33.

[34] P. I. P. Kalmus, "Particle physics at the turn of the century," *Contemporary Physics* **41** (2000) 129–142.

[35] G. Kane, "Supersymmetry: what? why? when?," *Contemporary Physics* **41** (2000) 359–367.

[36] L. Bergstrom and A. Goobar, *Cosmology and Particle Astrophysics*. Wiley, 1999.

[37] H. Goldberg, "Constraint on the photino mass from cosmology," PhysRevLett **50** (1983) 1419–1422.

[38] S. V. den Bergh, "The Early History of Dark Matter," Publications of the Astronomical Society of the Pacific **111** (1999) 657–660.

[39] K. Hagiwara *et al.*, "Review of Particle Properties," PhysRevD **66** (2002) 010001.

[40] P. F. Smith, "Direct Detection of Weakly Interacting Massive Particles Using Non-Cryogenic Techniques," *Philosophical Transactions: Mathematical, Physical and Engineering Sciences* **361** (2003) 2591–2606.

[41] R. Bernabei *et al.*, "Dark Matter search," *Nuovo Cimento Rivista Serie* **26** (2003) 1–74.

[42] Y. Ramachers, "WIMP direct detection overview," *arXiv:astro-ph/0211500* (2002).

[43] P. D. J. Barnes *et al.*, "Installation of the Cryogenic Dark Matter Search (CDMS)," NIMPA **370** (1996) 233–236.

[44] A. de Bellefon *et al.*, "Dark matter search in the Frejus Underground Laboratory EDELWEISS experiment," NIMPA **370** (1996) 230–232.

[45] U. Oberlack, "XENON: A 1 tonne liquid Xenon Detector for a sensitive WIMP dark matter search," *34th COSPAR Scientific Assembly, COSPAR, Plenary Meeting* **34** (2002).

[46] W. G. Jones *et al.*, "The "ZEPLIN" Detector - a Proposed High Sensitivity Dark Matter Detector in the Boulby Mine Based on Proportional Scintillation in Liquid Xenon," in *Identification of Dark Matter*, N. J. C. Spooner, ed., p. 428. 1997.

[47] R. Bernabei *et al.*, "First results from DAMA/LIBRA and the combined results with DAMA/NaI," *arXiv:astro-ph/0804.2741* (2008).

[48] H. S. Lee *et al.*, "Limits on Interactions between Weakly Interacting Massive Particles and Nucleons Obtained with CsI(Tl) Crystal Detectors," PhysRevLett **99** (2007) 091301.

[49] R. F. Lang, "The CRESST-II Experiment," *arXiv:astro-ph/0805.4705v1* (2008).

[50] S. Cebrián *et al.*, "First results of the ROSEBUD dark matter experiment," ASP **15** (2001) 79–85.

[51] C. Cozzini *et al.*, "CRESST cryogenic dark matter search," *New Astronomy Review* **49** (2005) 255–258.

[52] J. Amaŕe *et al.*, "Recent developments on scintillating bolometers for WIMP searches: ROSEBUD status," in *Proc. Ninth Int. Conf. on Topics in Astroparticle and Underground Physics*, vol. 39, pp. 133–135. 2005.

[53] J. Angle *et al.*, "First Results from the XENON10 Dark Matter Experiment at the Gran Sasso National Laboratory," PhysRevLett **100** (2008) 021303.

[54] R. Brunetti *et al.* in *The Identification of Dark Matter*, N. J. C. Spooner and V. Kudryavtsev, ed., p. 348. 2005.

[55] Z. Ahmed *et al.*, "A Search for WIMPs with the First Five-Tower Data from CDMS," *arXiv:astro-ph/0802.3530* (2008).

[56] I. Ivaniouchenkov and others, "ZEPLIN-I: A Single Phase Liquid Xe Detector for Dark Matter Search," in *Identification of Dark Matter*, N. J. C. Spooner and V. Kudryavtsev, ed., p. 433. 2001.

[57] G. J. Alner *et al.*, "First limits on WIMP nuclear recoil signals in ZEPLIN-II: A two-phase xenon detector for dark matter detection," ASP **28** (2007) 287–302.

[58] T. J. Sumner, "The ZEPLIN III dark matter project," *New Astronomy Review* **49** (2005) 277–281.

[59] C. Spiering, "Status and Perspectives of ASP in Europe," *arXiv:astro-ph/0804.1500* (2008).

[60] R. Gaitskell, "LUX: DUSEL Multi-tonne LXe TPCs." http://neutrino.lbl.gov/∼dusel/HomestakeWorkshopApril2008/Physics/LUX_1_overview_Gaitskell.pdf, 2008.

[61] ANTARES Collaboration, "A Deep Sea Telescope for High Energy Neutrinos," *arXiv:astro-ph/9907432v1* (1999).

[62] D. Huberta, "Neutralino dark matter searches with neutrino telescopes: AMANDA results and IceCube prospects," *Nuclear Physics B Proceedings Supplements* **173** (2007) 87–90.

[63] The SNO Collaboration, "The Sudbury Neutrino Observatory," *arXiv:nucl-ex/9910016v2* (1999).

[64] S. Desai *et al.*, "Search for dark matter WIMPs using upward through-going muons in Super-Kamiokande," PhysRevD **70** (2004) 083523.

[65] G. Kanbach *et al.*, "The project EGRET (Energetic Gamma-Ray Experiment Telescope) on NASA's Gamma-Ray Observatory (GRO)," *Space Science Reviews* **49** (1988) 69–84.

[66] E. Nuss, "Dark Matter searches with GLAST," *Advances in Space Research* **41** (2008) 2029–2031.

[67] T. Hara *et al.*, "A 3.8 m imaging Cherenkov telescope for the TeV gamma-ray astronomy collaboration between Japan and Australia," NIMPA **332** (1993) 300–309.

[68] D. Horns, "Indirect search for Dark Matter with H.E.S.S.," *Advances in Space Research* **41** (2008) 2024–2028.

[69] S. Ahlen *et al.*, "An antimatter spectrometer in space," NIMPA **350** (1994) 351–367.

[70] H. Baer and X. Tata, "Dark matter and the LHC," *arXiv:hep-ph/0805.1905v2* (2008).

[71] P. F. Smith and J. D. Lewin, "Dark Matter Detection," Physics Reports **187** (1990) 203–280.

[72] J. D. Lewin and P. F. Smith, "Review of mathematics, numerical factors, and corrections for dark matter experiments based on elastic nuclear recoil," ASP **6** (1996) 87–112.

[73] S. Golwala, *Exclusion limits on the WIMP-nucleon elastic-scattering cross-section from the Cryogenic Dark Matter Search.* PhD thesis, University of California, Berkeley, 2000.

[74] J. L. Feng, "Supersymmetry and cosmology," *Annals of Physics* **315** (2005) 2–51.

[75] R. Bernabei *et al.*, "Searching for WIMPs by the annual modulation signature," *Physics Letters B* **424** (1998) 195–20.

[76] A. Morales, "Direct detection of WIMP dark matter," *Nuclear Physics B* **87** (2000) 477–488.

[77] R. Bernabei *et al.*, "Results from DAMA/NaI and perspectives for DAMA/LIBRA," *arXiv:astro-ph/0311046* (2003).

[78] R. Bernabei *et al.*, "First results from DAMA/LIBRA and the combined results with DAMA/NaI," *arXiv:astro-ph/0804.2741v1* (2008).

[79] S. Burgos *et al.*, "Track reconstruction and performance of DRIFT directional dark matter detectors using alpha particles," NIMPA **584** (2008) 114–128.

[80] M. J. Lehner *et al.*, "The DRIFT project: searching for WIMPs with a directional detector," in *Dark matter in Astrophysics and Particle Physics*, H. V. Klapdor-Kleingrothaus and L. Baudis, ed., p. 767. 1999.

[81] G. J. Alner *et al.*, "The DRIFT-I dark matter detector at Boulby: design, installation and operation," NIMPA **535** (2004) 644–655.

[82] G. J. Alner *et al.*, "The DRIFT-II dark matter detector: Design and commissioning," NIMPA **555** (2005) 173–183.

[83] C. Ghag, *Simulation, Calibration & Exploitation of the DRIFT-II Directional Dark Matter Detector*. PhD thesis, University of Edinburgh, 2006.

[84] K. Miuchi *et al.*, "Detector performance of the NEWAGE experiment," *arXiv:physics/0701118* (2007).

[85] K. Miuchi *et al.*, "Direction-sensitive dark matter search results in a surface laboratory," *Physics Letters B* **654** (2007) 58–64.

[86] A. Hitachi *et al.*, "Effect of ionization density on the time dependence of luminescence from liquid argon and xenon," PhysRevB **27** (1983) 5279–5285.

[87] D. Yu. Akimov *et al.*, "The ZEPLIN-III dark matter detector: Instrument design, manufacture and commissioning," ASP **27** (2007) 46–60.

[88] Jochum, "Astroparticle Physics." http://www.desy.de/desy-hs/zeuthen2001/presentations/students/jochum.pdf, 2005.

[89] R. Bernabei *et al.*, "Search for WIMP annual modulation signature: results from DAMA/NaI-3 and DAMA/NaI-4 and the global combined analysis," *Physics Letters B* **480** (2000) 23–31.

[90] G. Gerbier *et al.*, "Note on a 'hint' for an annual modulation signature of a 60 GeV WIMP," *arXiv:astro-ph/9710181* (1997).

[91] R. Abusaidi *et al.*, "Exclusion Limits on the WIMP-Nucleon Cross Section from the Cryogenic Dark Matter Search," *Physical Review Letters* **84** (2000) 5699–5703.

[92] C. Seife, "Dark-Matter 'Sighting' Returns to Shadows," *Science* **296** (2002) 1782–1783.

[93] S. K. Kim *et al.*, "KIMS : Dark Matter Search Experiment in Korea," in *Particles, Strings, and Cosmology*, K. Choi and J. E. Kim and D. Son, ed., vol. 805 of *American Institute of Physics Conference Series*, pp. 75–81. 2005.

[94] J. G. Alner *et al.*, "First limits on nuclear recoil events from the ZEPLIN I galactic dark matter detector," ASP **23** (2005) 444–462.

[95] S. Scorza, "The EDELWEISS-II experiment," *arXiv:astro-ph/0806.3147v1* (2008).

[96] P. Benetti *et al.*, "First results from a Dark Matter search with liquid Argon at 87 K in the Gran Sasso Underground Laboratory," ASP **28** (2008) 495–507.

[97] H. M. Araújo *et al.*, "The ZEPLIN-III dark matter detector: Performance study using an end-to-end simulation tool," ASP **26** (2006) 140–153.

[98] T. J. Sumner *et al.*, "ELIXIR - A direct dark matter search facility." FP7-INFRASTRUCTURES-2007-1 Coordination & Support Action proposal, 2007.

[99] G. Gerbier, "Status of the EDELWEISS-II experiment," *Journal of Physics Conference Series* **120** (2008) 042017.

[100] G. Angloher *et al.*, "Commissioning Run of the CRESST-II Dark Matter Search," *arXiv:astro-ph/0809.1829* (2008).

[101] S. Cebrián *et al.*, "The ROSEBUD experiment at Canfranc : 2001 report," *Nuclear Physics B Proceedings Supplements* **110** (2002) 97–99.

[102] N. J. T. Smith, "UKDMC Dark Matter Search: Liquid Xenon Scintillation Mechanism." http://hepwww.rl.ac.uk/ukdmc/iop98njts/sld012.htm, 1998.

[103] L. S. Miller *et al.*, "Charge Transport in Solid and Liquid Ar, Kr, and Xe," *Physical Review* **166** (1968) 871–878.

[104] E. Conti *et al.*, "Correlated fluctuations between luminescence and ionization in liquid xenon," PhysRevB **68** (2003) 054201.

[105] D. Cline *et al.*, "A WIMP detector with two-phase xenon," ASP **12** (2000) 373–377.

[106] E. Aprile *et al.*, "Scintillation response of liquid xenon to low energy nuclear recoils," PhysRevD **72** (2005) 072006.

[107] V. Chepel *et al.*, "Scintillation efficiency of liquid xenon for nuclear recoils with the energy down to 5 keV," ASP **26** (2006) 58–63.

[108] A. Lindote *et al.*, "Preliminary results on position reconstruction for ZEPLIN III," NIMPA **573** (2007) 200–203.

[109] H. A. Araújo, "ZEPLIN-III Backgrounds Summary." http://www.hep.ph.ic.ac.uk/ZEPLIN-III/analysis/Z3Backgrounds.htm, 2008.

[110] IconMedialab, "SAES Getters." http://www.saesgetters.com.

[111] I. SAES Pure Gas, "Micro Torr." http://www.chell.co.uk/SAES/pdfs/microtorr.pdf, 2001.

[112] R. J. Walker *et al.*, "A Portable Xenon Purity Monitor using Electron Drift in Two-Phase Xenon," *In preparation.*

[113] J. C. Barton, "basic physics & statistics of photomultipliers: technical reprint R/P063." http://www.et-enterprises.com/pdf/rp063colour.pdf.

[114] H. M. Araújo *et al.*, "Low-temperature study of 35 photomultiplier tubes for the ZEPLIN III experiment," NIMPA **521** (2004) 407–415.

[115] H. M. Araújo, "Specifications for ETL/D766Q photomultipliers for the ZEPLIN-III Detector," *ZEPLIN III Note: D766Q_specs_070709_v5* (2007).

[116] E. Conti, "Collection of xenon properties." http://www.pd.infn.it/∼conti/images/LXe/xe_properties.txt.

[117] P. Scientific, "Quad CD-300 MHz Amplifier: NIM Model 770, 771." http://www.phillipsscientific.com/pdf/770ds.pdf.

[118] Phillips Scientific, "Quad Rotary Attenuator: NIM Model 804." www.phillipsscientific.com/pdf/804ds.pdf .

[119] H. M. Araújo, "DAQ & Trigger Setup," *ZEPLIN III Note: ZEPLIN-III Idiot's Guide #9* (2007).

[120] F. Neves, "Fast Start Manual for ZE3RA v2.0," *ZEPLIN III Note* (2007).

[121] O. Couet, "PAW Physics Analysis Workstation." http://wwwasd.web.cern.ch/wwwasd/paw/, 2006.

[122] M. Robinson *et al.*, "Measurements of muon flux at 1070m vertical depth in the Boulby underground laboratory," NIMPA **511** (2003) 347–353.

[123] P. F. Smith *UKDMC Note* (2005).

[124] V. N. Lebedenko *et al.*, "Result from the First Science Run of the ZEPLIN-III Dark Matter Search Experiment," *arXiv:astro-ph/0812.1150v1* (2008).

[125] E. E. Ltd, "78 mm (3") photomultiplier 9302B series data sheet." http://www.et-enterprises.com/pdf/9302KB.pdf, 2007.

[126] D. Davidge, *Development of a two phase xenon detector for use in direct dark matter searches*. PhD thesis, Imperial College London, University of London, 2003.

[127] V. Lebedenko, "Z3 Orientation in Castle." ZEPLIN III Note: Documents Database # 37, z3_RepHrd_4_v1_070227, 2007.

[128] V. Solovov, "Slow Control Software." ZEPLIN III Note: z3wiki/Slow_Control_Software, 2008.

[129] LBNL Isotopes Project, "WWW Table of Radioactive Isotopes: 241Am." http://ie.lbl.gov/toi/nuclide.asp?iZA=950241, 2008.

[130] H. M. Araújo, "Note on G4 simulations of Am-241 tests (v2)." ZEPLIN III Note, 2006.

[131] LBNL Isotopes Project, "WWW Table of Radioactive Isotopes: 64Cu." http://ie.lbl.gov/toi/nuclide.asp?iZA=290064, 2008.

[132] T. Y. Voronova *et al.*, "Ionization yield from electron tracks in liquid xenon," *Sov. Phys. Tech. Phys* **34** (1989) 825–827.

[133] NIST, "Form Factors, Attenuation and Scattering Cross-sections." http://physics.nist.gov/cgi-bin/ffast/ffast.pl?Z=54.+XenonFormula=gtype =4range=4upper=Ulower=upper=density, 2008.

[134] H. M. Araújo, "Measurements with 31x Am-241 disk (Nov/Dec 2005)." ZEPLIN III Presentation: Resources Page http://www.hep.ph.ic.ac.uk/ZEPLIN-III/organisation/meetings/Moscow_2008/ZeroFieldLinearity_HA.ppt, 2008.

[135] D. Akimov *et al.*, "Measurements of scintillation efficiency and pulse shape for low energy recoils in liquid xenon," *Physics Letters B* **524** (2002) 245–251.

[136] H. M. Araújo, "Zeplin3 phototubes type D730QA/9829QA: EMI DATA." ZEPLIN III Spreadsheet: Resources Page http://www.hep.ph.ic.ac.uk/ZEPLIN-III/instrument/PMT/Z3pmts.xls, 2008.

[137] V. Chepel, "Light Yield and Ws value (v1)." ZEPLIN III Note: Ws_report_v1.doc, 2006.

[138] V. Solovov, "private communication."

[139] T. J. Sumner, "Interim Report to PPARC Oversight Committee: 6th Meeting." ZEPLIN II Presentation: UKDMC_OsC6.ppt, 2006.

[140] H. M. Araújo, "private communication."

[141] V. Chepel *et al.*, "Primary scintillation yield and α/β ratio in liquid xenon," *Radiation Physics and Chemistry* **74** (2005) 160–167.

[142] C. Thorne, "Light Yield Discrepancy." ZEPLIN III Note: PulseRefCheck.pdf, 2006.

[143] F. Wolfs, "Monitoring the SPE Area Distributions." ZEPLIN II Note: SPEAreas042506.pdf, 2006.

[144] J. R. Prescott, "A Statistical Model For Photomultiplier Single-Electron Statistics," NucIM **39** (1966) 173–179.

[145] T. Asch *et al.*, "Single Photoelectron Resolution for the Calibration of Photomultiplier-Systems," 2005.

[146] B. Edwards, "Alpha Rate Investigation." ZEPLIN II Note, 2006.

[147] K. Mavrokoridis *et al.*, "Alpha Events in ZEPLIN II." ZEPLIN II Note, 2006.

[148] NIST, "astar: stopping-power and range tables for helium ions." http://physics.nist.gov/PhysRefData/Star/Text/ASTAR.html.

[149] LBNL Isotopes Project, "WWW Table of Radioactive Isotopes: 222Rn." http://ie.lbl.gov/toi/nuclide.asp?iZA=860222, 2008.

[150] J. Dawson, *ZEPLIN III: A Two-Phase Xenon WIMP Detector*. PhD thesis, University of London, 2003.

[151] G. F. Knoll, *Radiation Detection and Measurement*. John Wiley & Sons, 2000.

[152] LBNL Isotopes Project, "WWW Table of Radioactive Isotopes: 57Co." http://ie.lbl.gov/toi/nuclide.asp?iZA=270057, 2008.

[153] LBNL Isotopes Project, "WWW Table of Radioactive Isotopes: 137Cs." http://ie.lbl.gov/toi/nuclide.asp?iZA=550137, 2008.

[154] NIST, "X-ray Mass Attenuation Coefficients: Z=54, Xenon." http://physics.nist.gov/PhysRefData/XrayMassCoef/ElemTab/z54.html.

[155] L. S. Miller *et al.*, "Charge Transport in Solid and Liquid Ar, Kr, and Xe," *Physical Review* **166** (1968) 871–878.

[156] H. M. Araújo, "Do we change DAQ circuit?." ZEPLIN III Note: Documents Database, z3_RepHrd_2_v1_070125, 2007.

[157] C. Thorne, "Amplifier Distortion Tests." ZEPLIN III Note: Documents Database, z3_RepAnl_6_v1_070604, 2007.

[158] T. T. Instruments, "Function Generator Range." http://www.tti-test.com/products-tti/generator/gens-function.htm.

[159] LeCroy, "Digital Oscilloscope Selection Guide." http://www.lecroy.com/tm/products/default.asp.

[160] T. Communications, "Tektronix Test and Measurement Equipment: Oscilloscope Home." http://www.tek.com/products/oscilloscopes/.

[161] C. Thorne, "Background Data Analysis & Long Taus." ZEPLIN III Note: Documents Database, z3_RepAnl_17_v3_071127, 2007.

[162] F. Neves, "ZE3RA v2.0 Manual." ZEPLIN III Resources Page: http://mars.fis.uc.pt/∼neves/ZE3RA/manual.pdf, 2007.

[163] P. Photonis, "Photomultiplier tubes: Principles and applications." www.photonics.com/industryscience/products/photomultipliers_assemblies/application_book_1, 2002.

[164] F. Neves *et al.*, "Calibration of Photomultiplier Arrays," *arXiv:0905.2523v1* (2009).

[165] F. Neves, "ZE3RA Status & SPE Analysis." ZEPLIN III Presentation: Resources Page, Moscow08_FN.pdf, 2007.

[166] P. Majewski, "Single photoelectron distribution studies using science run data." ZEPLIN III Note: Documents Database, z3_RepAnl_28_v1_080624, 2008.

[167] F. Neves, "ZE3RA upgrades & SPE analysis." ZEPLIN III Presentation: Resources Page, Boulby.pdf, 2008.

[168] NIST, "X-ray Form Factor, Attenuation and Scattering Tables." http://physics.nist.gov/cgi-bin/ffast/ffast.pl?Z=29Formula=gtype=3lower=upper=density=, 2008.

[169] B. Edwards, "ZEPLIN Anti-Correlation." ZEPLIN III Presentation: Resources Page, BE_AntiCorrelation.pdf, 2008.

[170] Electron Tubes Limited, "52 mm (2") photomultiplier 9829B series data sheet." www.saetong.co.kr/products/ETL/forms/pdf/9829B.pdf, 2002.

[171] V. N. Solovov *et al.*, "Measurement of the refractive index and attenuation length of liquid xenon for its scintillation light," NIMPA **516** (2004) 462–474.